



Virginia Commonwealth University  
**VCU Scholars Compass**

---

Theses and Dissertations

Graduate School

---

2007

## Structures and Reactivities of Ionized and Metal Cation-Containing Acetylene Clusters

Paul O. Momoh  
*Virginia Commonwealth University*

Follow this and additional works at: <https://scholarscompass.vcu.edu/etd>

 Part of the [Chemistry Commons](#)

© The Author

---

Downloaded from

<https://scholarscompass.vcu.edu/etd/1000>

This Dissertation is brought to you for free and open access by the Graduate School at VCU Scholars Compass. It has been accepted for inclusion in Theses and Dissertations by an authorized administrator of VCU Scholars Compass. For more information, please contact [libcompass@vcu.edu](mailto:libcompass@vcu.edu).

© Paul O. Momoh, 2007

All Rights Reserved

STRUCTURES AND REACTIVITIES OF IONIZED AND METAL CATION-  
CONTAINING ACETYLENE CLUSTERS

A Dissertation submitted in partial fulfillment of the requirements for the degree of  
Doctor of Philosophy at Virginia Commonwealth University.

by

PAUL O. MOMOH  
B.Sc., Fort Valley State University, Georgia, 2002

Director: M. SAMY EL-SHALL  
PROFESSOR, DEPARTMENT OF CHEMISTRY

Virginia Commonwealth University  
Richmond, Virginia  
May 2007

## Acknowledgements

This dissertation is dedicated to Veronica Momoh, whose ideals and principles serve as the roadmap guiding my daily journey through life. Your patience, compassion, and selflessness, even at the peril of your own wellbeing cannot be appreciably articulated. Though you are gone, you will remain in my heart forever. I love you mom. Thanks to my wife, Rovianne C. Momoh, for her loving support and encouragement over the past five years and “high-fives” to Branden and Chelsea, my angels. I also want to recognize and thank Prof. M. Samy El-Shall for his scientific aptitude and academic guidance. To Drs. Michael Moet-Ner and Samuel A. Abrash, I will like to say a big thank you. Working with these brilliant yet humble men amplified the joy and raw gratification derived from the scientific process and collaborative work. Also, thanks to Dr. Yehia M. Ibrahim for his tremendous contribution to my understanding of the ion-mobility technique and finally, thanks to Dr. Edreese Alsharaeh who helped with my initial training at the lab.

## Table of Contents

	Page
Acknowledgements .....	ii
Table of Contents .....	iii
List of Tables .....	vi
List of Figures .....	viii
CHAPTER 1 Introduction .....	1
CHAPTER 2 Experimental Setup .....	6
2.1 Ion Generation .....	6
2.1.1 Laser Vaporization Ionization (LVI) .....	6
2.1.2 Electron Impact (EI) Ionization .....	8
2.2 Cluster Formation .....	8
2.3 QMS-IM-QMS .....	9
2.3.2 Ion Energy and Injection Energy .....	19
2.4 Reflectron Time-of-Flight Mass Spectrometer (RTOF-MS) .....	23
2.5 Static Time-of-Flight Quadrupole Mass Spectrometer (STOF-QMS) .....	30
CHAPTER 3 Experimental Techniques .....	37
3.1 Mobility Measurements .....	37
3.2 Structure Determination .....	41
3.3 Kinetic Measurements .....	46
3.4 Thermochemical Measurements (van't Hoff Plots) .....	48
CHAPTER 4 Structures of Small Acetylene Cluster Ions $(C_2H_2)_n^+$ , where $n = 1-3$ ...	52
4.1 Introduction .....	52
4.2 Experimental Section .....	56
4.3 Theoretical Section .....	56
4.4 Results and Discussion .....	57

4.4.2	Dissociation of the Acetylene Dimer and Trimer Ions .....	58
4.4.3	DFT Structures of Neutral Acetylene Dimer and Trimer Clusters .....	63
4.4.4	DFT Structures of the Acetylene Dimer and Trimer Cations .....	67
4.4.4.2	DFT Structures of the Acetylene Dimer Cation .....	67
4.4.4.3	DFT Structures of the Acetylene Trimer Cation.....	69
4.4.5	Mobilities of the Acetylene Dimer and Trimer Cations .....	69
4.4.5.2	Mobility of the Acetylene Dimer Cation .....	76
4.4.5.3	Mobility of the Acetylene Trimer Cation .....	80
4.5	Infrared Determination of Cluster Ion Structures .....	82
CHAPTER 5	Reactivity of Small Acetylene Cluster Ions, $(C_2H_2)_{1-3}^+$ , with Water ....	90
5.1	Introduction.....	90
5.2	Ionic Reactions between $C_2H_2^+$ and $H_2O$ : The $C_2H_3O^+$ and $C_2H_4O^{\bullet+}$ Ions .....	91
5.2.1	Experimental and Computational Method .....	91
5.2.2	Results and Discussion .....	94
5.2.2.1	The $C_2H_2^{\bullet+}/H_2O$ Reaction System and Proposed Mechanism.....	94
5.2.2.2	Thermochemistry and Structure of the $C_2H_4O^{\bullet+}$ Adduct Ion .....	104
5.2.2.3	Formation and Deprotonation of the $C_2H_3O^+$ Product Ion .....	105
5.2.2.4	Interstellar Reaction of the Acetylene-Water System.....	107
5.2.2.5	Theoretical Calculations .....	107
	$C_2H_4O^{\bullet+}$ .....	109
	$C_2H_3O^+$ .....	110
5.2.2.6	Comparison with Experimental Thermochemistry .....	112
5.2.2.7	Predicted Geometries for the $C_2H_nO^+ \cdot H_2O$ Complexes ( $n = 3$ and $4$ ). .....	117
	$C_2H_4O^{\bullet+} \cdot H_2O$ .....	117
	$C_2H_3O^+ \cdot H_2O$ .....	121
	Conclusion .....	123
5.3	Stepwise Hydration of Ionized Acetylene Dimer and Trimer Cations. ....	128
	Experimental and Theoretical section.....	128
5.4	Results and Discussion .....	129
5.4.1	Dimer Ion Hydration.....	129
5.4.1.1	Binding Energies and Thermochemistry of the Dimer Ion.....	130
5.4.1.2	Calculated $C_4H_4^+ \cdot (H_2O)_{1-2}$ Structures for Select $C_4H_4^+$ Isomers .....	131
	$C_4H_4^+ \cdot H_2O$ : .....	131
	$C_4H_4^+ \cdot (H_2O)_2$ : .....	133
5.4.2	Trimer Ion Hydration. Further Evidence for the Formation of Benzene Radical Cation.....	135
5.4.3	Conclusions.....	145

Chapter 6	Interaction of the $\text{Fe}^+$ , $\text{Co}^+$ , and $\text{Ni}^+$ Cations with Acetylene Clusters .....	153
6.1	Introduction.....	153
6.2	Experimental and Theoretical Methodology. ....	154
6.3	Results and Discussion .....	155
6.3.2	DFT Predicted Structures and Energies of $\text{Fe}^+$ , $\text{Co}^+$ , and $\text{Ni}^+(\text{C}_2\text{H}_2)_n$ clusters 161	
	$\text{Fe}^+\text{C}_2\text{H}_2$ , $\text{Co}^+\text{C}_2\text{H}_2$ , and $\text{Ni}^+\text{C}_2\text{H}_2$ .....	161
	$\text{Fe}^+(\text{C}_2\text{H}_2)_2$ , $\text{Co}^+(\text{C}_2\text{H}_2)_2$ , and $\text{Ni}^+(\text{C}_2\text{H}_2)_2$ .....	167
	$\text{Fe}^+(\text{C}_2\text{H}_2)_3$ , $\text{Co}^+(\text{C}_2\text{H}_2)_3$ , and $\text{Ni}^+(\text{C}_2\text{H}_2)_3$ .....	176
6.3.3	Investigation of Suspect $\text{Co}^+$ -mediated $\text{C}_2\text{H}_2$ Cyclotrimerization Reaction 181	
6.3.4	Conclusion .....	189
	Summary and Future Work.....	190
	List of References .....	193
	Appendix.....	206
	VITA.....	249

## List of Tables

	Page
Table 1: Pressure and temperature effects on the rate coefficients and product ratios in the $C_2H_2^{+\bullet} + H_2O$ system.....	102
Table 2: G3(MP2) and DFT calculated structures and energies of $C_2H_4O^{+\bullet}$ isomers <sup>a</sup> .	114
Table 3: G3MP2 and DFT results on isomers of $C_2H_3O^{+}$ <sup>a</sup> .....	116
Table 4: G3(MP2) calculations on $C_2H_4O^{+\bullet} \cdot H_2O$ complexes <sup>a</sup> .....	125
Table 5: G3(MP2) calculations on $C_2H_3O^{+} \cdot H_2O$ complexes <sup>a</sup> .....	127
Table 6: Measured thermochemistry ( $\Delta H_{n-1,n}^o$ and $\Delta S_{n-1,n}^o$ ) of clustering reaction 5.6...	139
Table 7: Optimized structures of the $C_4H_4^{+\bullet} \cdot H_2O$ species for select $C_4H_4^{+\bullet}$ isomers. Energies are relative to the most stable species for a particular $C_4H_4^{+\bullet}$ isomer. Optimization and energies were performed using the G3(MP2) method. Binding energies are for removal of a water molecule, $C_4H_4^{+\bullet} \cdots H_2O$ . .....	140
Table 8: G3(MP2) structures of the $C_4H_4^{+\bullet} \cdot (H_2O)_2$ species for select $C_4H_4^{+\bullet}$ isomers. Energies are relative to the most stable species for a particular $C_4H_4^{+\bullet}$ isomer. Binding energies are for removal of a water molecule, $C_4H_4^{+\bullet} \cdot H_2O \cdots H_2O$ . .....	141
Table 9: Measured binding energies and association entropies for the stepwise hydration of the mass selected $(C_2H_2)_3^{+}$ ion compared to previously published results for the hydration of the $C_6H_6^{+}$ ion <sup>138</sup> .....	149



Table 10: Comparison of  $M^+(C_2H_2)$  binding energies, bond lengths and angles, and C-H frequency stretch to those from previous calculations. .... 174

Table 11: UB3LYP/Wachters+*f*/6-31+G\*\* predicted magnitude of C-H stretch frequency red shift compared to that of the neutral acetylene monomer, 3294  $cm^{-1}$  (A) and 3388  $cm^{-1}$  (S), (B3LYP/6-31+G\*\*). Notice the increasing degree of C-H red shift from  $Ni^+(C_2H_2)_n$  to  $Fe^+(C_2H_2)_n$  clusters. This trend indicates increasing C-H bond activation from the  $Ni^+(C_2H_2)_n$  to  $Fe^+(C_2H_2)_n$  species. .... 175

Table 12: Comparison of  $M^+(C_2H_2)_2$  binding energies, bond lengths and angles, and C-H stretch frequency to those from previous calculations. .... 178

Table 13: Comparison of  $M^+(C_2H_2)_3$  binding energies, bond lengths and angles, and C-H stretch frequency to those from previous calculations. Also included are geometric parameters predicted for  $Co^+(n-C_4H_4) + (C_2H_2)^*$ , intermediate for cyclotrimerization reaction and  $Co(C_6H_6)^+$ . .... 180

## List of Figures

	Page
Figure 1: The experiment setup for mass-selected ion mobility spectrometer. (1) pulsed nozzle (2) 5 mm skimmer (3) electron-impact ionizer (4) quadrupole mass filter (5) ions transport lenses (Einzel Lenses 1, 2 and 3) (6) steering lens/ion gate (7) drift cell (8) to manometer (9) ions transport lenses (Einzel Lenses 4, 5 and 6) (10) quadrupole mass filter (11) electron multiplier (detector).....	13
Figure 2: Technical drawing of the drift cell. Dimension in inches [mm]. .....	14
Figure 3: Side view drawing of new drift cell. (1) Endcap (copper) (2) Reaction cell body (copper) (3) Tapered entrance lens (4) Entrance lens (5) Entrance orifice (0.25 mm) (6) Drift rings (7) Exit orifice (8) Tapered exit lens (9) Cell body liquid nitrogen inlet (10) Baratron connector (11) Drift cell (12) Endcap liquid nitrogen inlet. Dimensions in inches.....	17
Figure 4: Diagram of endcap assembly. (1) Cooling connection (2) Heater cavity (3) Orifice retainer (4) Ceramic rods (5) Ceramic spacers (6) Drift rings (5 pieces) .....	18
Figure 5: Schematic diagram for the wiring of QMS-IM-QMS for laser vaporization/ionization setup.....	21
Figure 6: Timing sequence for electron impact ionization experiment. ....	22
Figure 7: Pre-modified time-of-flight (TOF) mass spectrometer .....	25
Figure 8: Modified reflectron time-of-flight (RTOF) mass spectrometer .....	26

Figure 9: Pictures of the RTOF acceleration source (A – D) and ion mirror structure (E and F). (1) Repeller plate (2) Ground plate (3) Flight tube plate (4) Field shield (5) Nickel mesh on the ground plate (6) Ion mirror ring (7) Sapphire bearings (8) Chain of 20 MΩ resistors (9) Manipulator screw for tilting acceleration source (note the source is upside down here). ..... 31

Figure 10: RTOF mass spectrum for  $\text{Pd}^+(\text{C}_2\text{H}_2)_n$  clusters. Multiplets are the result of palladium’s extensive isotopic matrix. Resolution = 1600 amu. See Figure 49 for comparison to spectrum obtained using the pre-modified instrument. .... 32

Figure 11: Timing sequence for LVI-TOF experiment. .... 33

Figure 12: Setup for the modified time of flight/quadrupole mass spectrometer. Dashed lines show trajectory of clusters. .... 35

Figure 13: Timing sequence for TOF/QMS experiment..... 36

Figure 14: The arrival time distributions (ATDs) of injecting 20  $\mu\text{s}$   $\text{C}_2\text{H}_2^+$  ion pulse into drift cell filled with 2.1 Torr He at decreasing cell voltages of 2V steps. The earlier ATD corresponds to a drift voltage of 34 V while the later ATD corresponds to a drift voltage of 22 V. .... 42

Figure 15: Comparison of measured ATD of the acetylene trimer cation  $(\text{C}_2\text{H}_2)_3^+$  with that predicted by the transport theory equation. The inset shows the linear plot of  $t_d$  vs  $P/V$  used in calculating the reduced mobility. .... 43

Figure 16: Plot of  $-\ln I/I_0$  vs. arrival time for the reaction of acetylene ions with water at 31°C. The least squares linear fit (solid line) gives a first order rate constant (slope) of  $14.12 \pm 0.04 \text{ s}^{-1}$  and  $R^2 = 0.9984$ . .... 50

Figure 17: van’t Hoff plots for the  $(\text{C}_2\text{H}_2)_3^+ / (\text{H}_2\text{O})_n$  association reaction. Here  $A^+ = (\text{C}_2\text{H}_2)_3^+$  and  $B = \text{H}_2\text{O}$ . .... 51

Figure 18: Structures of the experimentally observed $C_4H_4^+$ isomers .....	59
Figure 19: Mass spectrum of EI ionized (46eV) acetylene clusters in a vacuum. ....	60
Figure 20: Mass spectrum of mass selected dimer, trimer, and tetramer acetylene clusters injected into the drift cell at 300 K, with injection energy of 12 eV, and cell pressure of 1.5 Torr He. ....	61
Figure 21: Dissociation pattern resulting from injection of mass selected $(C_2H_2)_2^+$ into the drift cell containing 0.22 Torr of helium at 298 K using different injection energies. ....	62
Figure 22: (a) CID spectrum of the mass-selected $(C_2H_2)_3^+$ ions using water vapor at 0.018 Torr as a collision gas. (b) and (c): Mass spectra obtained following the injection of the mass-selected $(C_2H_2)_3^+$ ions into the drift tube containing 0.4 Torr He at 300 K using 43 and 62 eV injection energies. The observed fragments at m/z 77, 63, 52, 51, 50, 39, and 26 correspond to the $C_6H_5^+$ , $C_5H_3^+$ , $C_4H_4^+$ , $C_4H_3^+$ , $C_4H_2^+$ , $C_3H_3^+$ , and $C_2H_2^+$ ions are identical to the EI fragmentation of the benzene ion. ....	64
Figure 23: Mass spectra obtained following the injection of mass-selected $(C_2H_2)_3^+$ ions into the drift cell containing 0.4 Torr He at 300 K using injection energy of 62 eV ( <i>lab</i> ). (b) Electron impact (70 eV) mass of the benzene ion obtained from the NIST database. <sup>120</sup> .....	65
Figure 24: DFT predicted geometries for the neutral $C_2H_2$ , $(C_2H_2)_2$ and $(C_2H_2)_3$ clusters	70
Figure 25: Relative total energies (DFT / UPBEPBE/aug-cc-pVDZ relative to the energy of the methylenecyclopropene ion), structures and calculated collision integrals ( $\Omega$ , Å <sup>2</sup> ) of the $C_4H_4^+$ isomers. The collision integrals in helium at 300 K are calculated using the trajectory method. <sup>94</sup> .....	71

Figure 26: Relative total energies (DFT / UPBEPBE/aug-cc-pVDZ relative to the energy of the benzene ion), structures and calculated collision integrals ( $\Omega$ , $\text{\AA}^2$ ) of the $\text{C}_6\text{H}_6^+$ isomers. The collision integrals in helium at 300 K are calculated using the trajectory method. <sup>94</sup> .....	73
Figure 27: Relative energies and collision integrals of the $\text{C}_6\text{H}_6^+$ isomers.....	74
Figure 28: Comparison between the measured ATD of the mass-selected acetylene monomer ion with that predicted by transport theory. The inset shows the linear plot of arrival time ( $t_d$ ) vs. $P/V$ used to calculate the mobility. ....	77
Figure 29: Measured ATDs of $(\text{C}_2\text{H}_2)_n^+$ with $n = 1-3$ at 300 K using approximately similar field and collision conditions ( $E/N$ ). The increasing arrival time for $n = 1-3$ reflects the increase in collision cross section of the injected cluster from the monomer to the trimer. ....	83
Figure 30: Arrival time distribution of mass-selected acetylene dimer clusters injected into the drift cell with 5.0 Torr helium at 300 K using injection energy of 12 eV. $E/N = 4.37 \text{ Td}$ . ....	84
Figure 31: Comparison of experimental arrival time distribution (open circles) of mass-selected acetylene dimer clusters to the distribution predicted by the transport theory equation (solid line). The drift cell temperature and pressure were 300 K and 5.0 Torr (He) respectively and injection energy of 12 eV was utilized. $E/N = 4.37 \text{ Td}$ . ....	85
Figure 32: Arrival time distribution of injected acetylene dimer cluster fitted with distribution predicted by transport theory using a combination of two $\text{C}_4\text{H}_4^+$ isomers, cyclobutadiene (dotted line) and vinylacetylene (dashed line), at a ratio of 62:38 respectively. Experimental condition are the same as given in Figure 29 and Figure 30. ....	86
Figure 33: ATDs of the mass selected acetylene dimer ion at different drift voltages (decreasing from left to right) used in obtaining $t_d$ for the mobility measurements. ....	87

- Figure 34: Plot of  $t_d$  versus  $P/V$  (open circles) used in calculating reduced mobility for mass-selected acetylene dimer ions injected into the cell. The solid line represents the linear least square fit of the plot.  $R^2$  and slope values from this fit are 0.9999 and  $2.07 \pm 0.01$  respectively; corresponding to a  $K_0$  value of  $14.2 \text{ cm}^2 \text{ V}^{-1} \text{ s}^{-1}$ . This value represents the averaged mobility of the cyclobutadiene and vinylacetylene ions determined to be present in the molecular beam. .... 88
- Figure 35: Comparison of the experimental ATD of the acetylene trimer ion  $(\text{C}_2\text{H}_2)_3^+$  with that predicted by the transport theory equation. The inset shows the linear plot of  $t_d$  vs.  $P/V$  used in calculating the reduced mobility..... 89
- Figure 36: Mass spectrum obtained following the injection of  $\text{C}_2\text{H}_2^{+\bullet}$  ions into cell containing  $\text{H}_2\text{O}/\text{He}$  at 303 K, cell field 2.81 V/cm,  $P(\text{H}_2\text{O}) = 20$  mtorr,  $P(\text{He}) =$  (top) 358 mtorr and (bottom) 1441 mtorr..... 99
- Figure 37: Arrival time distributions (ATDs) of the ions observed following the injection of  $\text{C}_2\text{H}_2^{+\bullet}$  ions into  $\text{H}_2\text{O}/\text{He}$  at 303 K,  $P(\text{H}_2\text{O}) = 20$  mtorr,  $P(\text{He}) = 713$  mtorr, injection energy (lab) = 11.9 eV, cell field = 2.81 V/cm. Overlap in ATD of  $\text{C}_2\text{H}_3\text{O}^+$  and  $\text{C}_2\text{H}_4\text{O}^+$  is as a result of similar drift mobilities. .... 100
- Figure 38: Intensities of ion signals (integrated ATD peaks) as a function of reaction time after injection of  $\text{C}_2\text{H}_2^{+\bullet}$  ions into the mobility cell with  $P(\text{H}_2\text{O}) = 19.6$  mTorr (or  $N[\text{H}_2\text{O}] = 7.19 \times 10^{14} \text{ molecules/cm}^3$ ),  $T = 272$  K, and injection energy = 11.9 eV. Helium partial pressure was (a) 332.4 mTorr ( $N[\text{He}] = 1.22 \times 10^{16} \text{ molecules/cm}^3$ ) and (b) 1002.0 mTorr ( $N[\text{He}] = 3.68 \times 10^{16} \text{ molecules/cm}^3$ ). The time corresponds to the ion mobility time through the cell of the  $\text{C}_2\text{H}_2^{+\bullet}$  (26) ion plus the detection time of the ion after exiting the cell ( $\approx 24.7 \mu\text{s}$ ). In the graphs, "adduct" denotes the combined intensities of the  $\text{C}_2\text{H}_4\text{O}^{+\bullet}(\text{H}_2\text{O})_n$  ( $n = 0 - 4$ ) ions, " $\text{H(W)}_n$ " denotes the combined intensities of the  $(\text{H}_2\text{O})_n\text{H}^+$  ( $n = 0 - 4$ ) ions, and "T" denotes sum of intensities for the unreacted  $\text{C}_2\text{H}_2^+$  as well as all other observed products. .... 101
- Figure 39: Arrival time distribution (ATD) for the  $\text{H}^+(\text{H}_2\text{O})_3$  cluster produced upon injection of  $\text{C}_2\text{D}_2^{+\bullet}$  ions into cell containing  $\text{H}_2\text{O}/\text{He}$  at 304 K,  $P(\text{H}_2\text{O}) = 20$  mtorr,  $P(\text{He}) = 999$  mtorr, injection energy (lab) = 11.9 eV and cell field of (a) 3.9 V/cm and (b) 1.7 V/cm. .... 108

- Figure 40: Acetylene dimer ions injected into (504 mTorr at 299 K) pure H<sub>2</sub>O at 15.4 eV injection energy and 24 V drift voltage. .... 136
- Figure 41: ATDs of  $(C_2H_2)_2^+(H_2O)_n$  clusters obtained by injecting  $(C_2H_2)_2^+$  at 15.4 eV (*lab*) into 526 mTorr of H<sub>2</sub>O vapor and 24 V drift voltage at 307 K. .... 137
- Figure 42: van't Hoff plots of the temperature dependence of the equilibrium constant of the reaction:  $A_2^+(H_2O)_{n-1} + H_2O \rightleftharpoons A_2^+(H_2O)_n$ , where  $A_2^+ = (C_2H_2)_2^+$  ..... 138
- Figure 43: Mass spectrum obtained after injecting  $(C_2H_2)_3^+$  into water vapor (0.17 Torr at 249 K) in the drift-tube. Note the formation of hydrated  $(C_2H_2)_3^+(H_2O)_n$  (i.e.  $A_3W_n$ ) and the deprotonation products  $H^+(H_2O)_n$  (i.e.  $W_nH$ ). (b) Mass spectrum obtained after injecting  $C_6H_6^+$  into H<sub>2</sub>O vapor (0.12 Torr at 239 K) in the drift tube.<sup>138</sup> Note the formation of hydrated  $Bz^+(H_2O)_n$  (i.e.  $BW_n$ ) and the deprotonation products  $H^+(H_2O)_n$  (i.e.  $W_nH$ ). .... 146
- Figure 44: Arrival time distributions (ATDs) of  $(C_2H_2)_3^{\bullet+}(H_2O)_n$  clusters obtained by injecting  $(C_2H_2)_3^{\bullet+}$  at 11.9 eV (*lab*) into 166 mtorr of H<sub>2</sub>O vapor and 24 V drift voltage at 250 K. .... 147
- Figure 45: van't Hoff plots of the temperature dependence of the equilibrium constant of the reaction:  $(C_2H_2)_3^{\bullet+}(H_2O)_{n-1} + H_2O \rightleftharpoons (C_2H_2)_3^{\bullet+}(H_2O)_n$ . .... 148
- Figure 46: Equilibrium geometries for the  $C_6H_6^+(H_2O)_{1-4}$  clusters at the ROHF/6-31+G\*\* level extracted from previous work.<sup>138</sup> Bond lengths are in angstroms, while the molecular charges are in bold and the atomic charges are in parentheses. .... 150
- Figure 47: Cartoon representation of the overall trimerization reaction of ionized acetylene clusters and its reaction with water. .... 152
- Figure 48: Time of Flight (TOF) mass spectrum of  $Fe^+(C_2H_2)_n$  clusters at early arrival times (low mass range). A 3 % acetylene/helium (60 PSI) was used in cluster

generation. Laser intensity at the target surface was  $\sim 10^7 \text{ Wcm}^{-2}$ . Deflector voltages were adjusted to accommodate smaller clusters. .... 157

Figure 49: Time of Flight (TOF) mass spectrum for low mass products of  $\text{Co}^+(\text{C}_2\text{H}_2)_n$  clusters. The Nd: YAG laser was timed to fire  $578.7 \mu\text{s}$  after the nozzle opened ( $t_0$ ). The acceleration plates were pulsed  $1.08 \text{ ms}$  after  $t_0$ . Pressure of the first chamber was  $1.3 \times 10^{-4} \text{ Torr}$ . A 3 % acetylene/helium (60 PSI) was used in cluster generation. Laser intensity at the target surface was  $\sim 10^7 \text{ Wcm}^{-2}$ . Deflector voltages were adjusted to accommodate smaller clusters. .... 158

Figure 50: Time of Flight (TOF) mass spectrum and intensity plot (inset) for  $\text{Fe}^+(\text{C}_2\text{H}_2)_n$  clusters. Notice the  $n = 14$  magic number which was observed for all transition metals investigated. A 3% acetylene/helium (60 PSI) was used in cluster generation. Laser intensity at the target surface was  $\approx 10^7 \text{ Wcm}^{-2}$ . Deflector voltages were adjusted to accommodate larger clusters. .... 162

Figure 51: Time of Flight (TOF) mass spectrum and intensity plot (inset) for  $\text{Co}^+(\text{C}_2\text{H}_2)_n$  clusters. Intriguing cyclic magic numbers (3, 6, 9, and 12) suggest a multiple cyclization process mediated by the cobalt cation. A 3% acetylene/helium (60 PSI) was used in cluster generation. Laser intensity at the target surface was  $\approx 10^7 \text{ Wcm}^{-2}$ . Deflector voltages were adjusted to accommodate larger clusters. .... 163

Figure 52: TOF mass spectrum for  $\text{Ni}^+(\text{C}_2\text{H}_2)_n$  clusters. Notice the  $n = 14$  magic number as well as the  $n = 3$  magic number. A 3% acetylene/helium (60 PSI) was used in cluster generation. Laser intensity at the target surface was  $\approx 10^7 \text{ Wcm}^{-2}$ . Deflector voltages were adjusted to accommodate larger clusters. .... 164



- Figure 53: DFT optimized structures for the  $M^+C_2H_2$  cluster ( $M = Fe, Co, Ni$ ). Optimizations were performed with the B3LYP hybrid functional utilizing the Wachters+*f* basis set for the transition metals and the 6-31+G\*\* basis set for the C and H atoms. .... 170
- Figure 54: DFT optimized structures for  $M^+(C_2H_2)_2$  clusters ( $M = Fe, Co, Ni$ ). Optimizations were performed with the B3LYP hybrid functional utilizing the Wachters+*f* basis set for the transition metal ions and the 6-31+G\*\* basis set for the C and H atoms. .... 171
- Figure 55: DFT optimized structures for  $M^+(C_2H_2)_3$  clusters ( $M = Fe, Co, Ni$ ). Optimizations were performed with the B3LYP hybrid functional utilizing the Wachters+*f* basis set for the transition metal ions and the 6-31+G\*\* basis set for the C and H atoms. .... 173
- Figure 56: Relative energies of the UB3LYP/Wachter+*f*/6-31+G\*\* predicted isomers of the  $Co^+(C_2H_2)_2$  cluster. .... 179
- Figure 57: DFT (UB3LYP/Wachters+*f*/6-31+G\*\*) predicted geometry and parameters for the  $Co(C_6H_6)^+$  complex. Two views are presented for clarity. The predicted C-C and C-H bond lengths for the neutral benzene molecule is included in parenthesis. .... 186
- Figure 58: DFT (UB3LYP/Wachters+*f*/6-31+G\*\*) predicted intermediate for  $Co^+$ -mediated cyclotrimerization of acetylene. The intermediate consist of a  $Co^+(n-C_4H_4) + C_2H_2$ -type structure. The lower view is given due to disparity in bond lengths and angles. .... 187
- Figure 59: Relative energies (kcal/mol) corrected for ZPE for the  $Co^+$ -mediated cyclotrimerization reaction of acetylene in  $Co^+(C_2H_2)_n$  clusters. Reaction pathway assumes spin conservation. The energy levels with the numbers "1" and "5" represent the singlet and quintet multiplicities respectively. All attempts to optimized the  $Co^+(c-C_4H_4) + C_2H_2$  and  $Co^+(n-C_6H_6)$  (metallahexadienyl) species failed. .... 188

- Figure 60: Mass spectrum of photoionized (193 *nm*) benzene/naphthalene heterogeneous clusters. Benzene and naphthalene were contained in bubblers arranged in series. Helium pressure was 40 PSI and stagnation temperature was 27° C. .... 206
- Figure 61: Mass spectrum of photoionized (193 *nm*) benzene/naphthalene heterogeneous clusters. Benzene and naphthalene were contained in bubblers arranged in series. Helium pressure was 40 PSI and stagnation temperature was 27° C. Raising the naphthalene temperature to increase its partial pressure in the line or cooling the benzene to reduce its relative partial pressure showed no effect on cluster distribution. .... 207
- Figure 62: Mass spectrum of mass selected EI ionized acetylene ion,  $C_2H_2^+$ , injected into the cell containing 468 mTorr of  $C_2H_2$  only using an injection energy of 11.9 eV. The temperature of the drift cell was 31° C and the cell voltage was 24 V. Note some of the peaks represent the acetylene/acetone cluster due to the acetone impurity. .... 208
- Figure 63: Mass spectrum of mass selected EI ionized acetylene ion,  $C_2H_2^+$ , injected into the cell containing 70 mTorr of  $C_2H_2$  only using an injection energy of 11.9 eV. The temperature of the drift cell was 31° C and the cell voltage was 24 V. Note some of the peaks represent the acetylene/acetone cluster due to the acetone impurity. .... 209
- Figure 64: Mass spectrum of mass selected EI ionized acetylene ion,  $C_2H_2^+$ , injected into the cell containing 24 mTorr of  $C_2H_2$  only using an injection energy of 11.9 eV. The temperature of the drift cell was 31° C and the cell voltage was 24 V. Note some of the peaks represent the acetylene/acetone cluster due to the acetone impurity. .... 210
- Figure 65: Mass spectrum of mass selected EI ionized acetylene ion,  $C_2H_2^+$ , injected into the cell containing 22 mTorr of  $C_2H_2$  and 1.206 Torr He using an injection energy of 11.9 eV. The temperature of the drift cell was 31° C and the cell voltage was 24 V. Note some of the peaks represent the acetylene/acetone cluster due to the acetone impurity. .... 211

- Figure 66: Mass spectrum of mass selected EI ionized acetylene ion,  $\text{C}_2\text{H}_2^+$ , injected into the cell containing 22 mTorr of  $\text{C}_2\text{H}_2$  and 311 mTorr He using an injection energy of 11.9 eV. The temperature of the drift cell was  $31^\circ\text{C}$  and the cell voltage was 24 V. Note some of the peaks represent the acetylene/acetone cluster due to the acetone impurity..... 212
- Figure 67: Static TOF mass spectrum of photoionized (193 nm)phenylacetylene clusters,  $(\text{C}_8\text{H}_6)_n^+$ . 30 PSI of Argon was passes overed phenylacetylene held at a temperature of  $60.1^\circ\text{C}$ ..... 213
- Figure 68: Static TOF mass spectrum of photoionized binary phenylacetylene/acetylene clusters,  $(\text{C}_8\text{H}_6)_m^+(\text{C}_2\text{H}_2)_n$ . The major series observed was of the form,  $(\text{C}_8\text{H}_6)_m^+(\text{C}_2\text{H}_2)_n$ . Ionization was achieved by photoionization (193 nm) with phenylacetylene acting as a chromophore. 2 PSI of acetylene seeded in helium, 60 PSI, was passed over phenylacetylene held at  $0^\circ\text{C}$  to reduce vapor pressure. .... 214
- Figure 69: Static TOF mass spectrum of photoionized (193 nm) binary bezene/phenylacetylene clusters,  $(\text{C}_6\text{H}_6)_m^+(\text{C}_8\text{H}_6)_n$ . The major series observed was the homogeneous benzene clusters,  $(\text{C}_6\text{H}_6)_m^+$ . 70 PSI of helium was passed over benzene held at  $27^\circ\text{C}$ . Phenylacetylene used was that desorbed in inside surface of line. .... 215
- Figure 70: Static TOF mass spectrum of photoionized binary benzene/acetylene clusters,  $(\text{C}_6\text{D}_6)_m^+(\text{C}_2\text{H}_2)_n$ . The major series observed was of the form,  $(\text{C}_6\text{D}_6)_m^+(\text{C}_2\text{H}_2)_n$  (where  $m=1-4$ ). Most of the unmarked peaks represent reactions of acetone, an impurity in the acetylene tank. Ionization was achieved by photoionization (193 nm) with benzene acting as a chromophore. 5 PSI of acetylene seeded in helium, 60 PSI, was passed over benzene held at  $-78.5^\circ\text{C}$  to reduce vapor pressure, (0.10 mmHg)..... 216

Figure 71: Mass spectrum and intensity plots for electron impact ionized (EI) binary benzene/acetylene clusters of the form,  $(C_6D_6)_m^+(C_2H_2)_n$ . Notice the acetylene cluster series  $(C_2H_2)_n^+$ . In PI (193 nm), the benzene molecules acted as a chromophore because acetylene absorbs at VUV. Charge transfer was undetectably low or absent as benzene has a lower ionization potential (9.24 eV) than acetylene (11.4 eV). On the other hand, in EI ionization, both molecules were ionized and as a result, a substantial proportion of the observed acetylene series is likely the result of EI ionization rather than fragmentation of binary acetylene/benzene clusters. Also interesting was the observation of  $C_3H_3^+$  fragment. Since deuterated benzene was utilized in this experiment, this complex can only be the result of acetylene isomerization reaction. .... 217

Figure 72: TOF mass spectrum of  $Ti^+(H_2O)_n$  clusters using low laser power. The metal target was ablated 619  $\mu s$  after the nozzle opened ( $t_0$ ) and the accelerating plates were pulsed 1.12  $ms$  after  $t_0$ . Stagnation helium pressure was 12 PSI and the water temperature was 27° C. .... 218

Figure 73: TOF mass spectrum of  $Pt^+(H_2O)_n$  clusters. Stagnation helium pressure was 21 PSI and the water temperature was 27° C. .... 219

Figure 74: TOF mass spectrum of  $Pd^+(H_2O)_n$  clusters. Stagnation helium pressure was 16 PSI and the water temperature was 27° C. .... 220

Figure 75: TOF mass spectrum of  $Ni^+(H_2O)_n$  clusters. Stagnation helium pressure was 13 PSI and the water temperature was 27° C. .... 221

Figure 76: TOF mass spectrum of  $Fe^+(H_2O)_n$  clusters. Stagnation helium pressure was 21 PSI and the water temperature was 27° C. .... 222

Figure 77: TOF mass spectrum of  $Fe^+(H_2O)_n$  clusters. Stagnation helium pressure was 30 PSI and the water temperature was 23° C. .... 223

Figure 78: TOF mass spectrum of  $Co^+(H_2O)_n$  clusters. Stagnation helium pressure was 16 PSI and the water temperature was 27° C. .... 224

Figure 79: TOF mass spectrum of $\text{Co}^+(\text{H}_2\text{O})_n$ clusters. ....	225
Figure 80: TOF mass spectrum of $\text{Al}^+(\text{H}_2\text{O})_n$ clusters. Stagnation helium pressure was 20 PSI and the water temperature was 27° C. ....	226
Figure 81: TOF mass spectrum of $\text{Ca}^+(\text{H}_2\text{O})_n$ clusters. ....	227
Figure 82: TOF mass spectrum of $\text{Cr}^+(\text{H}_2\text{O})_n$ clusters. Stagnation helium pressure was 30 PSI and the water temperature was 27° C. ....	228
Figure 83: TOF mass spectrum of $\text{K}^+(\text{H}_2\text{O})_n$ clusters. ....	229
Figure 84: TOF mass spectrum of $\text{Mn}^+(\text{H}_2\text{O})_n$ clusters. ....	230
Figure 85: TOF mass spectrum of $\text{Na}^+(\text{H}_2\text{O})_n$ clusters. ....	231
Figure 86: TOF mass spectrum of $\text{Sc}^+(\text{H}_2\text{O})_n$ clusters. ....	232
Figure 87: TOF mass spectrum of $\text{Si}^+(\text{H}_2\text{O})_n$ clusters. Stagnation helium pressure was 30 PSI and the water temperature was 48° C. ....	233
Figure 88: TOF mass spectrum of $\text{V}^+(\text{H}_2\text{O})_n$ clusters. ....	234
Figure 89: TOF mass spectrum of $\text{Au}^+(\text{C}_2\text{H}_2)_n$ clusters. Stagnation pressure was 50 PSI (helium) and 1.5 PSI acetylene (3%). Pressure of the source chamber was $5.3 \times 10^{-5}$ Torr. ....	235
Figure 90: TOF mass spectrum of $\text{Cr}^+(\text{C}_2\text{H}_2)_n$ clusters using low laser power. Metal target was ablated 578.7 $\mu\text{s}$ after nozzle opened ( $t_0$ ) and accelerating plates were pulsed 1.12 ms after $t_0$ . Background pressure was 50 PSI (helium) and 1.5 PSI acetylene (3%). Pressure of the source chamber was $5.3 \times 10^{-5}$ Torr. ....	236

- Figure 91: TOF mass spectrum of  $\text{Cr}^+(\text{C}_2\text{H}_2)_n$  clusters at early arrival times ( $<20 \mu\text{s}$ ). Chromium isotopes are responsible for the observed multiplets. Also, chromium isotope complexes,  $^y\text{Cr}^+(\text{C}_2\text{H}_2)_n$ , coincides with  $\text{C}_2\text{H}_x(\text{C}_2\text{H}_2)_n$  (where  $x = 0$  and 2) fragments. .... 237
- Figure 92: Reflectron Time of Flight (RTOF) mass spectrum of  $\text{Mn}^+(\text{C}_2\text{H}_2)_n$  clusters. Notice the enhanced intensity for the  $n = 5$  peak. .... 238
- Figure 93: Time of Flight (TOF) mass spectrum of  $\text{Fe}^+(\text{C}_2\text{H}_2)_n$  clusters at early arrival times (low mass range). .... 239
- Figure 94: Time of Flight (TOF) mass spectrum and intensity plot (inset) of  $\text{Co}^+(\text{C}_2\text{H}_2)_n$  clusters. Here, the Nd: YAG laser was timed to fire  $578.7 \mu\text{s}$  after the nozzle opened ( $t_0$ ). The acceleration plates were pulsed  $1.08 \text{ ms}$  after  $t_0$ . Pressure of the first chamber was  $3.1 \times 10^{-5}$  Torr. .... 240
- Figure 95: TOF mass spectrum of  $\text{Pd}^+(\text{C}_2\text{H}_2)_n$  clusters. Multiplets are as a result of the extensive isotopic matrix for palladium. Also coincident with the palladium isotopes are fragments of the form  $(\text{C}_2\text{H}_2)_n^+$  and  $\text{C}_2\text{H}(\text{C}_2\text{H}_2)_{n-1}^+$ . .... 241
- Figure 96: TOF mass spectrum of  $\text{Au}^+(\text{CO})_n$  clusters. The helium stagnation pressure was 48 PSI and the CO pressure was 10 PSI. .... 242
- Figure 97: Time of Flight (TOF) mass spectrum of  $\text{Cu}^+(\text{CH}_3\text{OH})_n$  clusters. Here, the Nd: YAG laser was timed to fire  $564 \mu\text{s}$  after the nozzle opened ( $t_0$ ). The acceleration plates were pulsed  $1.04 \text{ ms}$  after  $t_0$ . Pressure of the first chamber was  $1.7 \times 10^{-5}$  Torr. Helium stagnation pressure was 11 PSI and methanol temperature was  $27^\circ \text{C}$ . .... 243
- Figure 98: TOF mass spectrum of photoionized benzene/water clusters. Helium pressure was 70 PSI and the water and benzene temperatures were  $-78.5^\circ \text{C}$  and  $27^\circ \text{C}$  respectively. .... 244

- Figure 99: TOF mass spectrum of photoionized benzene/water clusters. Helium pressure was 20 PSI and the water and benzene temperature was 27° C. Benzene and water are mixed in the bubbler. .... 245
- Figure 100: TOF mass spectrum of photoionized benzene/water clusters. Helium pressure was 70 PSI and the water and benzene temperature was 27° C. Benzene and water are mixed in the bubbler. .... 246
- Figure 101: Electron Impact (EI) ionized mass spectrum of acetylene/methylacetylene clusters. Helium stagnation pressure was 60 PSI and electron energy was 74 eV. .... 247
- Figure 102: Time of Flight (TOF) mass spectrum of negative Au/styrene/water clusters. Here, the Nd: YAG laser was timed to fire 500  $\mu s$  after the nozzle opened ( $t_0$ ). The acceleration plates were pulsed 920  $\mu s$  after  $t_0$ . Pressure of the first chamber was  $1.1 \times 10^{-5}$  Torr. Helium stagnation pressure was 30 PSI and the styrene and water temperature was 27° C. .... 248

## Abstract

### STRUCTURES AND REACTIVITIES OF IONIZED AND METAL CATION- CONTAINING ACETYLENE CLUSTERS

By Paul O. Momoh, Ph.D

A Dissertation submitted in partial fulfillment of the requirements for the degree of Doctor of Philosophy at Virginia Commonwealth University.

Virginia Commonwealth University, 2007

Major Director: M. Samy El-Shall  
Professor, Department of Chemistry

In this dissertation, the ion mobility technique is used to determine the structures of small acetylene cluster ions,  $(\text{C}_2\text{H}_2)_{1-3}^+$ , mass-selected from the largest ever reported ionized acetylene clusters. The technique is also used to characterize the reaction of acetylene clusters with water in an effort to elucidate thermochemistry and kinetics of some interesting ion-molecule reactions suspected to occur in interstellar clouds and other interplanetary bodies.

A combination of ion mobility measurements, collision induced dissociation (CID), and theoretical calculations are used to provide the most conclusive evidence for the



frequently hypothesized trimerization of ionized acetylene to form the benzene ion. The results also provide evidence for the isomerization of the acetylene dimer ion,  $(\text{C}_2\text{H}_2)_2^+$ , to form the cyclobutadiene and vinylacetylene ions.

Investigation of the reactions of acetylene radical ions  $(\text{C}_2\text{H}_2^{\bullet+})$  with water reveals competing kinetics for two primary,  $\text{C}_2\text{H}_4\text{O}^{\bullet+}$  and  $\text{C}_2\text{H}_3\text{O}^+$ , and a secondary,  $\text{H}^+(\text{H}_2\text{O})_n$ , product with an overall reaction rate coefficient of  $2.0 \times 10^{-11} \text{ cm}^3\text{s}^{-1}$ . By comparing experimentally observed reactions to theoretically (G3MP2) predicted thermochemistry, the  $\text{C}_2\text{H}_4\text{O}^{\bullet+}$  ion is suggested to be the ethenolium ion (vinyl alcohol ion,  $\text{CH}_2\text{CHOH}^{\bullet+}$ ) and the  $\text{C}_2\text{H}_3\text{O}^+$  ion is suggested as either the 1-hydroxy-ethenylum ( $\text{CH}_2\text{COH}^+$ ) or cyclic 2H-oxirenum (*c*- $\text{CH}_2\text{CHO}^+$ ) ion. Investigation of the temperature dependence of the equilibrium constant for the association reaction  $(\text{C}_2\text{H}_2)_3^+ + (\text{H}_2\text{O})_{n-1} \rightleftharpoons (\text{C}_2\text{H}_2)_3^{\bullet+}(\text{H}_2\text{O})_n$  using the van't Hoff plot revealed binding energies and reaction entropies identical to those recently published for the benzene<sup>+</sup>/water system thus providing even more evidence for the formation of benzene ions from ionized acetylene clusters.

We also provide a density functional (UB3LYP/Wachters+f) investigation of  $\text{Fe}^+$ ,  $\text{Co}^+$ , and  $\text{Ni}^+(\text{C}_2\text{H}_2)_n$  clusters (where  $n = 1-3$ ) to supplement mass spectrometric analysis of the acetylene-solvated cations. For the  $\text{Co}^+(\text{C}_2\text{H}_2)_n$  clusters, the mass spectrum revealed an intriguing behavior of oscillating magic numbers which we suspect to be the consequence of a  $\text{Co}^+$ -mediated polymerization reaction to form covalent  $\text{Co}^+\text{C}_n\text{H}_n$  complexes. The UB3LYP/Wachters+f predicted barrier and exothermicity for the initial step of the proposed trimerization reaction are 25.4 and 101.4 kcal/mol respectively. Our results

suggest the efficiency of this reaction is facilitated by cooperative interactions and favorable orientations of acetylenes in the cluster.

## CHAPTER 1      Introduction

The recent discovery of benzene in the carbon-rich proto-planetary nebula, CRL 618,<sup>1</sup> has prompted enhanced interest in the chemistry of interstellar clouds, aging stars, and other interplanetary bodies. The discovery of benzene in this nebula is important not only because benzene may prove to be the first step in the formation of the pervasive polycyclic aromatic nitrogen hydrocarbons (PAHs and PANHs) believed by astrochemists to be the source of unidentified infrared bands<sup>2,3</sup> but also because its ring structure represents a precursor for functionalization in a majority of biologically significant and prebiotic molecules. For the former reason, some have dubbed benzene the “*missing link*”.<sup>1,4-7</sup> Rich concentrations of acetylene and methane have been discovered in aging and evolved stars as well. In fact, over 125 organic molecules have been discovered in interstellar clouds and medium, solar nebulae, and in envelopes expelled by evolved stars.<sup>1,4-14</sup> Ambient conditions of these aging stars such as high velocity winds, high temperatures, dust particles, and ionizing ultraviolet radiations create conditions amenable to termolecular collision and surface interactions for benzene formation from acetylene.<sup>1,5</sup>

More common in interplanetary media than acetylene and aromatic hydrocarbons is water. It is known to exist in diffuse and dense interstellar clouds,<sup>12</sup> oxygen-rich nebulae, and remarkably, the carbon-rich proto-planetary nebulae (CRL 618, +IRC 10°216)<sup>5</sup> where it is also subject to powerful ionizing radiation. As a result, the reaction of water and acetylene is of fundamental interest.

PAH formation is terrestrial as well and acetylene is known to be an integral part of polymerization reactions that form PAHs and soot in combustion gases.<sup>15-17</sup> PAHs are considered mutagenic and a biological pathway linking it to human lung cancer has been established.<sup>18,19</sup> Soot, a much larger PAH is considered an environmental pollutant. Acetylene and its analog, diacetylene, are also utilized in the production of conjugated polymers (CPs) with the potential of industrial application as sensitive sensors.<sup>20-22</sup> A mixture of acetylene and vapor metal catalyst at high temperatures is also used in the efficient production of carbon nanotubes (CNTs).<sup>23</sup> Consequently, an understanding of acetylenes' ion-molecule reactions and polymerization processes is of environmental and economic importance.

Numerous efforts have been made to investigate the polymerization of ionized acetylene,<sup>1,4-7</sup> particularly in the search for benzene ions in small acetylene clusters.<sup>24-27</sup> Early experiments found the fragment ions observed from photoionization of the acetylene trimer to be identical to those obtained from benzene ion fragmentation. This observation is complicated by the fact that the same fragment pattern was observed in other stable  $C_6H_6^+$  isomers such as 2,4-hexadiyne, 1,3-hexadiyne, and 1,5-hexadiyne,<sup>24</sup> thus rendering dissociation experiments inadequate for the unambiguous elucidation of the  $(C_2H_2)_3^+$  ion identity. In addition, photoelectron-photoion coincidence experiments and *ab initio* calculations showed that ionized acetylene trimers and tetramers rearrange to produce stable covalent core ions ( $C_4H_4^+$  and  $C_6H_6^+$ , respectively), and the  $C_6H_6^+$  ion was suggested to be the benzvalene ion.<sup>26</sup> Electron impact (EI) ionization of acetylene clusters  $(C_2H_2)_n^+$  showed magic numbers for the  $n = 3$  and 14 peaks. These magic numbers were speculated

in a previous report to be the benzene ( $\text{C}_6\text{H}_6^+$ ) and  $\text{C}_{28}\text{H}_{28}^+$  molecular ions, respectively.<sup>27</sup> However, none of the speculated structures in all previous experiments on ionized acetylene clusters have been verified.

As mentioned above, the ion-molecule chemistry of acetylene and water is of interest as it can lead to more complex molecules. For example, the ion-molecule reaction of  $\text{C}_2\text{H}_2^+$  and  $\text{H}_2\text{O}$  may produce the  $\text{C}_2\text{H}_4\text{O}^+$  ion, isomers of which have been observed in interstellar clouds ( $\text{HCOCH}_3$ , *c*- $\text{C}_2\text{H}_4\text{O}$ ,<sup>28</sup> and  $\text{CH}_2\text{CHOH}$ <sup>29</sup>) Also, the reaction of  $\text{H}_3\text{O}^+$  with  $\text{C}_2\text{H}_2$  forms  $\text{H}_2\text{C}=\text{CHOH}^+$  and possibly  $\text{CH}_3\text{CHOH}^+$  ions.<sup>30</sup> In-depth theoretical<sup>31-35</sup> and experimental<sup>36-41</sup> studies addressed the bare acetylene ion ( $\text{C}_2\text{H}_2^+$ ) and neutral acetylene/water clusters.<sup>24,42-44</sup> However, reactions of the acetylene radical ion with water have not yet been studied.

In the present work, we use a combination of mass-selected ion mobility, collision induced dissociation (CID), thermochemical measurements, and theoretical calculations to provide the most conclusive evidence to date for the formation of benzene ions from the largest ever reported, ionized acetylene clusters. Evidence is also provided for the formation of, at least, the cyclobutadiene and vinylacetylene ions in the ionized acetylene clusters. The ion-mobility technique is also used to obtain the rate constant for the  $\text{C}_2\text{H}_2^{\bullet+}/\text{H}_2\text{O}$  ion-molecule reaction. A comprehensive density functional (DFT) survey of probable  $\text{C}_6\text{H}_6^+$  and  $\text{C}_4\text{H}_4^+$  isomers as well as an *ab initio* assessment of structures and thermochemistry of select  $\text{C}_4\text{H}_4^+(\text{H}_2\text{O})_{1-2}$  complexes and ions with the compositions,  $\text{C}_2\text{H}_3\text{O}^+$ ,  $\text{C}_2\text{H}_4\text{O}^{\bullet+}$ ,  $\text{C}_2\text{H}_3\text{O}^+(\text{H}_2\text{O})$ , and  $\text{C}_2\text{H}_4\text{O}^{\bullet+}(\text{H}_2\text{O})$  will be presented.

The study of these systems in gas-phase molecular cluster ions is ideal because size effect and the complexities of intermolecular interactions can be systematically defined. In addition, cluster packing permits unique cooperative effects analogous to three body interactions that are generally not efficient under low pressure conditions.<sup>45-49</sup> The ion-mobility technique provides an accurate measure of a molecules mobility based on its drift through an inert (or slowly reacting) buffer gas under low field conditions.<sup>50,51,52</sup> This technique represent a preferable investigative tool for the unambiguous elucidation of the  $(\text{C}_2\text{H}_2)_3^+$  and  $(\text{C}_2\text{H}_2)_2^+$  identities since it measures mobility which is a function of average collision cross section and therefore of molecular structure. Structural analysis using ion-mobility measurements involves a comparison of the measured collision cross section to the calculated average collision cross section for candidate geometries selected from those predicted theoretically.

The majority of olefinic and acetylenic polymerization processes are catalytic, most often involving a heterogeneous catalyst. The study of the analogous processes in the gas phase and within clusters is important not only for probing the mechanisms of such catalytic processes, but also for the design of new catalysts with tailored reactivity and selectivity. The interaction of transition metal cations with acetylenic and olefinic molecules has been an area of considerable interest due to the facile tendency of these cations to mediate isomerization reactions via C-C and C-H bond activation as described by the Dewar-Chatt-Duncanson (DCD)  $\pi$ -bonding model.<sup>53,54</sup> In this model, C-C and C-H bond activation results from donation of ligand  $\sigma$ -electron density to the empty  $d$ -orbital of

the transition metal and a corresponding back-donation of metal electron density to the  $\pi^*$ -orbital of the ligand.

Though numerous theoretical and experimental inquiries have been made into the interactions and reactions of transition metals and acetylene,  $M^+/C_2H_2$ , these studies have mainly concentrated on the monomer adduct,  $M^+C_2H_2$ .<sup>55-58</sup> Other studies have been devoted to the  $Fe^+$ -mediated cyclotrimerization of acetylene to form benzene.<sup>59-62</sup> Not much has been done by way of a direct comparison of the structures, packing characteristics, vibrational frequencies, and suspected intracluster reactivity of larger clusters,  $M^+(C_2H_2)_n$  (where  $n \geq 2$ ).<sup>63,64</sup> We present here mass spectrometric and density functional results for the interaction and reactivity of acetylene clusters with iron, cobalt, and nickel monocations. We discuss and compare the structures, binding energies, relative energies, and C-H stretch frequencies of these complexes,  $Fe^+/Co^+/Ni^+(C_2H_2)_n$ . We also discuss the DFT predicted intermediate structure and calculated reaction thermochemistry for the  $Co^+$ -mediated cyclotrimerization reaction of acetylene to form benzene suspected to be the cause of an intriguing magic number behavior in our cobalt<sup>+</sup>/acetylene mass spectra.

## CHAPTER 2      Experimental Setup

The experiments discussed in this work utilized three different mass spectrometers, the Quadrupole Mass Selected Ion-Mobility Quadrupole Mass Spectrometer (QMS-IM-QMS), Reflectron Time-of-Flight (RTOF) mass spectrometer, and Quadrupole Time-of-Flight (QTOF) mass spectrometer. All systems were built in-house and are described below. Since acetylene clusters form the majority of this work, all descriptions will relate to their formation and ionization but the processes described may apply to other systems.

### 2.1      Ion Generation

In all experiments described, ions were generated by one of the following techniques: Laser Vaporization Ionization (LVI) and Electron Impact (EI) Ionization.

#### 2.1.1      Laser Vaporization Ionization (LVI)

For the  $M^+(C_2H_2)_n$  experiments, transition metal cations ( $M^+$ ) were generated by laser vaporization/ionization (LVI). LVI is used in a wide variety of applications. For example, it is used in generation of metal cations (as used here),<sup>65-70</sup> in ion-induced nucleation,<sup>71</sup> in gas phase polymerization initiation reactions,<sup>72,73,74</sup> in the production of ionized atomic clusters, and in the synthesis of nanoparticles.<sup>75</sup> In this work, the second harmonic (532 nm) of an Nd:YAG laser (Surelite SSP-I Continuum, 4-6 ns, 10 mJ/pulse, 8-10 Hz) was utilized. Metal cations are generated by focusing the laser beam on a metal



target/rod. The exact mechanism of laser vaporization/ablation is still not well known,<sup>76</sup> however, “photothermal” heating is believed to be the main mechanism for the ablative process.<sup>76</sup> Basically, intense laser light with a short pulse width is focused on a very small spot ( $\approx 0.01 \text{ cm}^2$ ) on the metal target (power density  $\approx 10^7 \text{ W/cm}^2$ ), resulting in a dramatic rise in temperature at the local surface. This rise in temperature is because the energy dissipation time is long compared to the laser pulse width which is on the order of nanoseconds. Consequently, a molten layer is formed and subsequently vaporized. The metal vapor absorbs even more light forming a plasma plume. The absorption of photons by the metal target is dependent on the metal target absorption coefficient, laser wavelength, and laser fluence. The source of ions can be attributed to many processes during laser vaporization.<sup>77</sup> The primary ionization mechanism is by direct ionization of the metal by the laser beam with an estimated surface temperature of 3000-6000 K.<sup>78</sup> Secondary ions in the plume include expelled electrons.

Highly energetic metal cations ( $M^+$ ) are timed to intercept neutral acetylene clusters  $(C_2H_2)_n$  thus forming  $M^+(C_2H_2)_n$  clusters. Stabilization of the ionized clusters is by evaporative loss of acetylene molecules. Timing for LVI is critical as this experiment is pulsed at a rate of 8-10 *Hz*. The laser Q-switch must be triggered so that the metal plume is generated coincidently with cluster beam translation past the metal target.

### 2.1.2 Electron Impact (EI) Ionization

In our laboratory, the Extrel axial beam ionizer (model 04-11) coupled to a quadrupole mass filter is employed for electron impact (EI) ionization. Ionizing electrons are thermionically generated from a tungsten filament and are subsequently accelerated to the ion region/cage where they intercept the neutral cluster beam. Quantum effects between the accelerated electrons and neutral clusters result in electron expulsion from a neutral cluster molecule (ionization).<sup>79</sup> Excess energy deposited in the cluster from the ionization process is dissipated by evaporation of cluster molecules. The ionized clusters are subsequently extracted and focused into the quadrupole mass filter by a series of lenses. The electron energy in normal acetylene experiments varies between 40-80 eV.

## 2.2 Cluster Formation

Cluster formation is essential for all experiments discussed in this work. Clusters are finite aggregates of atoms or molecules bound by van der Waals interaction forces, hydrogen bonds, metallic, and/or covalent bonds. Clusters are formed by condensation of rapidly expanding gases or vapors through a small orifice (nozzle) by a process known as supersonic/adiabatic expansion. To generate acetylene clusters, a 2 % partial ratio of acetylene in an inert carrier gas, He, at a stagnation pressure,  $P_o$ , of  $\sim 3\text{-}6\text{ atm}$ , is expanded into a vacuum,  $P_b$  of approximately  $10^{-5}$  Torr. Upon expansion thermal energy is converted into directed translational energy resulting in cooling<sup>80</sup> and condensation.<sup>81</sup> The cooling process is represented by

$$C_p T_o = C_p T_b + mu^2 / 2 \quad (2.1)$$

where  $C_p$  is the heat capacity of the seed gas or vapor,  $T_o$  is the stagnation temperature,  $T_b$ , the temperature of the expanded gas beam,  $m$  is the mass of the expanding gas, and  $u$ , the velocity of the gas. Since this is an adiabatic process, we see that upon expansion, the beam gets cooler as more thermal energy is converted to kinetic energy. The word supersonic refers to the fact that an adequately large pressure gradient ( $P_o/P_b \geq 2.1$ ) is necessary for the mean velocity of the expanding gas to achieve supersonic speeds (mach  $\geq 1$ ).<sup>82</sup> The supersonic criterion is necessary for cluster formation because at subsonic speeds, collisions rates necessary for clustering are not achieved and also, the nozzle-skimmer distance and geometry becomes a significant issue.<sup>83</sup>

Pulsed supersonic expansion is used in cluster generation.<sup>84,85</sup> This is advantageous for several reasons, with the most important being the ability to achieve necessary vacuum in the chamber with more modest sized pumps than are required for continuous beams. Stagnation requirements necessary for effective clustering differ for different precursors and depend on the polarizability, binding interactions, specific heat ratio, temperature, and the collision cross section of the precursor molecules. Latent heat liberated as a result of cluster condensation is eradicated by collision with inert carrier gas.

### 2.3 QMS-IM-QMS

The Quadrupole Mass Selected Ion-Mobility Quadrupole Mass Spectrometer (QMS-IM-QMS), as shown in Figure 1, consists of three distinct chambers although the second is partitioned into two parts that are pumped separately. The first chamber (source chamber) houses a 250  $\mu\text{m}$  nozzle. This chamber is pumped by a Varian VHS-6 diffusion

pump and backed by an Edwards E2M30 rotary pump. The typical operating pressure of this chamber is  $\sim 10^{-5}$  Torr. The second chamber, pumped by an Edwards Diffstak 160/700 M diffusion pump, houses an axial electron impact (EI) source (Extrel model 041-11, tungsten filament) coupled to a quadrupole ( $3/8'' \times 7.88''$ , 1-4000 amu) mass filter. The operational pressure for this chamber is  $\leq 10^{-6}$  Torr. The third chamber houses the drift cell and numerous steering (Einzel) lenses. This chamber is pumped by an Edwards Diffstak 250/2000P diffusion pump [3000 L/s in  $H_2$ ] which is backed by an Edwards E2M40 rotary pump and maintained at pressures  $\leq 10^{-4}$  Torr. The fourth chamber houses a second quadrupole mass filter with an off axis Channeltron electron multiplier detector. This chamber is pumped by an Edwards Diffstak 160/700 M diffusion pump [1300 L/s ( $H_2$ )]. Operational pressure for this chamber is  $\leq 6 \times 10^{-7}$  Torr. A single mechanical pump (Edwards E2M40) is used to back both diffusion pumps for chambers two and four.

The neutral acetylene cluster beam is generated by pulsed supersonic expansion (discussed above) and subsequently collimated by a 3 mm conical skimmer as it enters the second chamber where ionization by EI takes place. Typical electron energies range from 40-80 eV. The ionized clusters are focused into the quadrupole mass filter by a set of six lenses. The quadrupole is powered by a QC-150, 300 Watt, and 880 kHz oscillator. The ionizer and quadrupole are controlled by the Merlin mainframe system supplied by Extrel. The quadrupole shroud is floated at  $\pm 100$  V to accelerate or decelerate ions traveling through the poles for better quadrupole performance. For example, highly energetic cations from LVI can be slowed down by changing the float voltage. The quadrupole can be operated in a *RF-only* mode or a *RF-DC (mass selection)* mode. In the latter mode, a

specific  $m/z$  ratio of interest is selected to filter through the quad poles while all other masses are eliminated. On the other hand, in the *RF-only* mode, a wide range of masses above a certain  $m/z$  filter through the quadrupole. The mass selection mode is preferred as it provides confidence in ion identity. The drawback with use of this mode is that ion count is typically lower than with the *RF-only* mode. In cases where a usable ion count cannot be obtained with the *RF-DC* mode, the *RF-only* mode is used. Ions exiting the mass filter are directed into the third chamber where they are guided by a set of three einzel lenses into the drift cell entrance. Two steering lenses mounted right after the einzel lenses are used to steer the ions into the mobility cell. Each steering lens is made up of two semi-circular nickel pieces with one half of each connected directly to the third set of Einzel lenses. The other semi-circular half of each steering lens is connected to an independent voltage supply biased to the third set of einzel lens as well. Adjustment of the voltage supplies above or below the voltage of the third set of einzel lenses can be used to steer the ions vertically or horizontally into drift cell, thus improving signal. The vertical steering lens also acts a gate to chop the ion beam into 10-50  $\mu s$  widths and serve as zero time,  $t_o$ . Gating is achieved by connection of the vertical lens voltage supplies to a pulse generator (DEI, PVX-4140). The gate is open when the second half of the lens is connected to the third set of Einzel lens as described above (i.e. -240 V and -240 V). The gate is closed when an equal but oppositely charged voltage is applied to one half of the semi-circular lens, thus creating a deflecting field for the incoming ions (i.e. -240 V and +240 V).

The mobility cell was modified during the course of this work. Descriptions of both the old and new cells are given here. The old cell (8.13 cm ID  $\times$  8.89 cm length), shown in

Figure 2, consists of three copper rings separated externally by two ceramic rings. The entrance and exit orifice (1 mm) are bored into copper plates isolated from the cell by Teflon gaskets. Field evenness is achieved in the drift cell by the use of 5 M $\Omega$  resistors between the entrance plate, cell rings and exit plate. Voltage supply for the ionizer lenses, entrance and exit plates, as well as all sets of einzel lenses was provided by an ABB Extrel power supply (150-QC). Inert or reacting gas is supplied to the cell through a stainless steel tube (with ceramic breakers for insulation), with flow rates controlled by two mass flow controllers (MKS 1479A) capable of maintaining cell pressure accuracy of  $\pm 1$  mTorr. Cell pressure is monitored by a capacitance manometer (MKS Baratron type 626). The maximum attainable cell pressure is limited by the pumping speed of the diffusion pump and the diameter of the drift cell entrance and exit orifice. For example, maximum operational pressure for 1 mm orifice plates is  $\sim 3.5$  Torr and  $\sim 10$  Torr for 0.5 mm orifice plates. The cell is heated by three heating cartridges (Watlow 100W/120V) inserted into each cell ring. Though the heaters are capable of attaining higher temperatures, maximum operational temperature of the drift cell is  $\sim 250^\circ\text{C}$ , just below the melting point of Teflon. Cooling of the drift cell is by liquid nitrogen flowed through copper tubing wrapped around the cell. Flexible stainless steel (SS) tubing with ceramic breakers (to isolate the cell from its surroundings) is used to introduce liquid nitrogen to the copper tubes. The lowest attainable temperature is  $-195^\circ\text{C}$ , the temperature of liquid nitrogen. The temperature of the old cell was monitored by seven K-type thermocouples (Omega CO1),

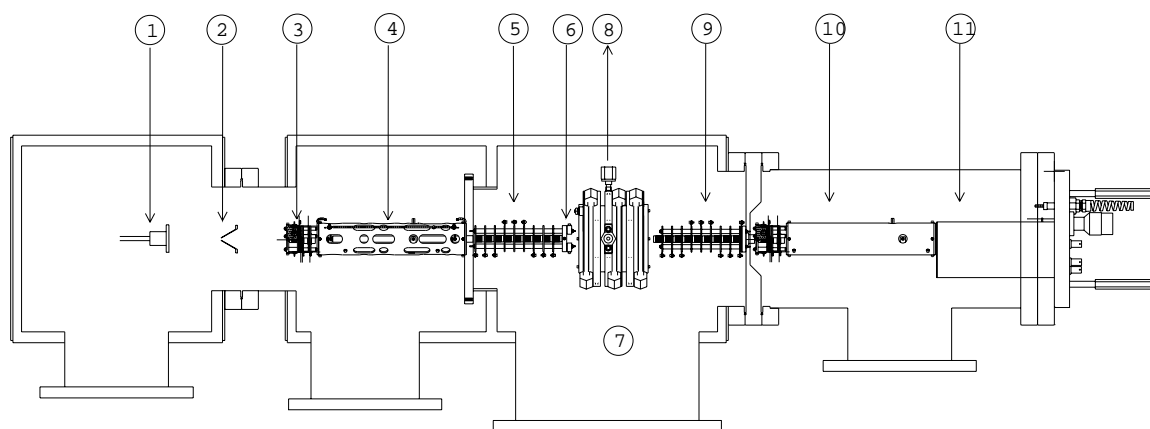


Figure 1: The experiment setup for mass-selected ion mobility spectrometer. (1) pulsed nozzle (2) 5 mm skimmer (3) electron-impact ionizer (4) quadrupole mass filter (5) ions transport lenses (Einzel Lenses 1, 2 and 3) (6) steering lens/ion gate (7) drift cell (8) to manometer (9) ions transport lenses (Einzel Lenses 4, 5 and 6) (10) quadrupole mass filter (11) electron multiplier (detector).

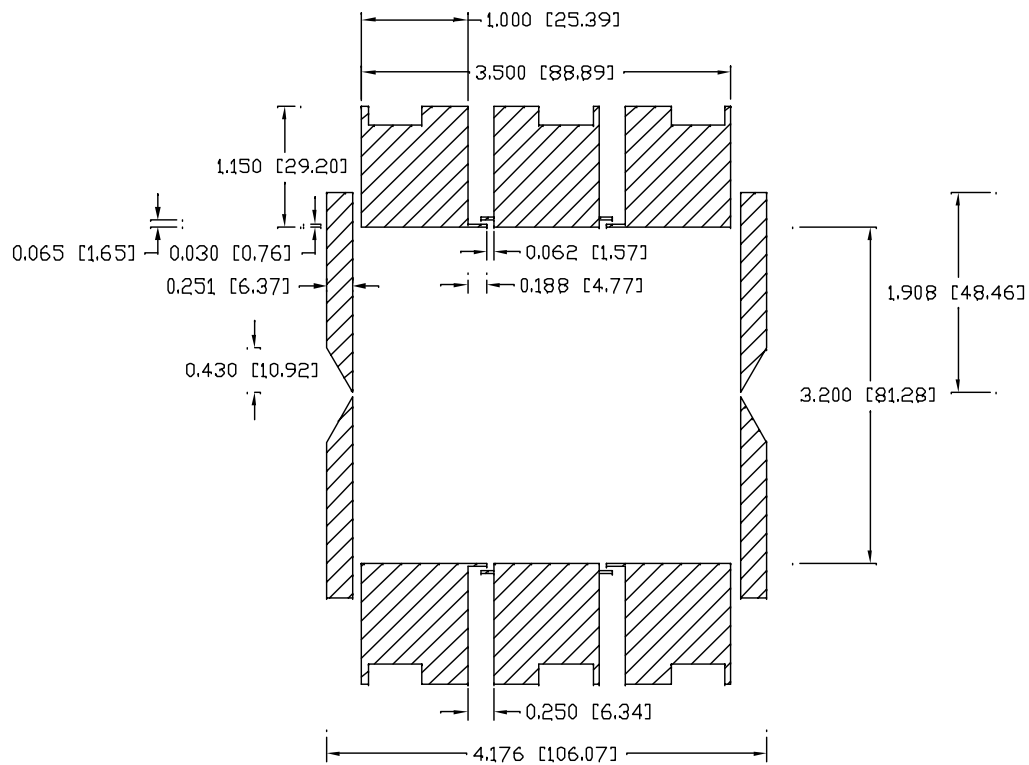


Figure 2: Technical drawing of the drift cell. Dimension in inches [mm].



with two on each ring and one on the exit plate. Heating of the drift cell is controlled by three controllers (Omega type CN3251,  $\pm 1^\circ\text{C}$ ). Cooling is controlled by three Omega type CNi3233 temperature controllers coupled to three On/Off solenoid valves.

The structure of the new mobility cell (Figure 3) differs considerably from that described above but first we mention components of the third chamber that remain the same post-modification. Pumping for third chamber remains the same, all einzel lenses before and after the mobility cell remain the same. Cooling is by liquid nitrogen through stainless steel tubing with ceramic breakers. Buffer/reactant gas is introduced similarly. Voltage supply for the entrance, exit plates, and einzel lenses are the same. Temperature monitoring and control instruments remain the same.

The new drift cell, designed by Dr. Paul Kemper,<sup>86</sup> consists of two major pieces, the *reaction cell body* ( $3.50'' \times 3.50'' \times 2.14''$ ) and the *cell endcap* ( $3.50'' \times 3.50'' \times 0.40''$ ). Both pieces are made from oxygen free high conductivity (Alloy 10100 OFHC) copper. The cylindrical drift cell ( $1.84''$  length  $\times$   $2.0''$  D) is machined into the rectangular reaction cell body. The diameter of the last  $0.28''$  of the drift cell is increased by another  $0.35''$  ( $2.35''$ ) to accommodate a ceramic ring ( $2.34''$  OD,  $1.97''$  ID, and  $0.40''$  width) which separates the reaction cell-body from the endcap. The entrance plate (SS), with a  $0.254$  mm orifice is held in place inside the cell by a copper retainer ( $1.40''$  OD,  $0.60''$  ID, and  $0.064''$  width). Two entrance lenses ( $2.00''$  OD, one of which is a taper lens), separated by ceramic spacers, are mounted on the exterior entrance of the cell-body which is also tapered at an angle of  $45^\circ$ . Both lenses use separate voltage supplies. The exit orifice plate, its retainer, and five drift rings (SS,  $1.40''$  OD,  $0.60''$  ID,  $0.128''$  width) are mounted on the interior of

the endcap by six ceramic rods as shown in Figure 4. Another taper lens (exit lens) mounts on the exterior of the endcap. The exit lens has a separate voltage supply and is insulated from the endcap by ceramic spacers. The assembled drift cell consists of the ring structure (mounted on the endcap) inserted into the cavity of the cell body.

In addition to the considerable differences between the old and new drift cells described above, another significant difference lies in the tubing for liquid nitrogen circulation around the cell. In the old cell, liquid nitrogen flowed through a copper tube wound around the cell. For the new cell, several 0.58" diameter pores were drilled into each cell piece (reaction cell-body and endcap). These pores serve as inlet and outlet tubes for liquid nitrogen flow. In addition, four 0.3" diameter holes are drilled in both sides of the cell-body and two in the endcap to house ceramic rods for the heater circuit.

Unlike the cartridge heaters employed in the old cell, heating of the new cell was accomplished by resistant heaters made from tantalum wires (0.010 cm D) passed through ten four-hole ceramic tubing inserted in the drilled holes described above. All insulating parts were made from ceramic, thus overcoming the temperature limitation (Teflon melting point) inherent in the previous cell. The maximum operational temperature is approximately 450-500°C. Heating is controlled by the same Omega controllers used in the old cell but with drastically reduced voltage than was used for the cartridge heaters (120 VAC). This is due to the lower effective resistance of the heaters ( $\sim 3 \Omega$  compared to  $\sim 146 \Omega$  for the old cartridge heaters). The same controller is used to manage liquid nitrogen flow (Omega type CNi3233).

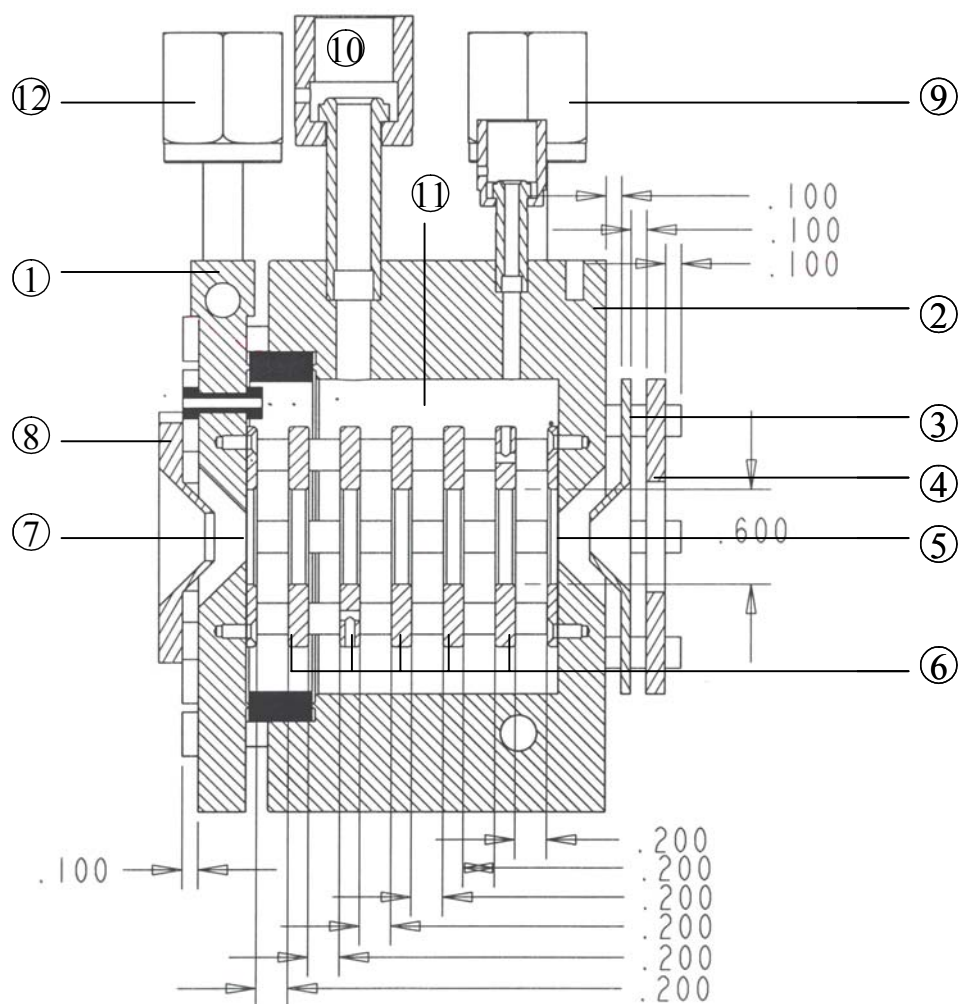


Figure 3: Side view drawing of new drift cell. (1) Endcap (copper) (2) Reaction cell body (copper) (3) Tapered entrance lens (4) Entrance lens (5) Entrance orifice (0.25 mm) (6) Drift rings (7) Exit orifice (8) Tapered exit lens (9) Cell body liquid nitrogen inlet (10) Baratron connector (11) Drift cell (12) Endcap liquid nitrogen inlet. Dimensions in inches.

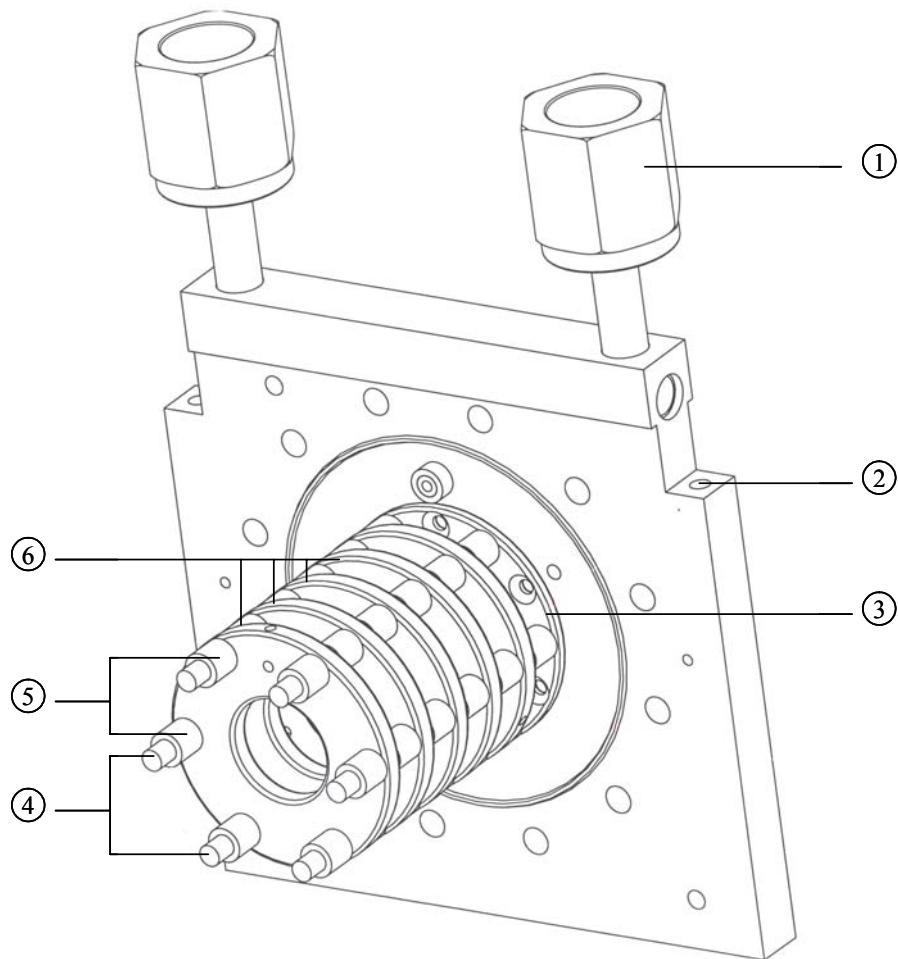


Figure 4: Diagram of endcap assembly. (1) Cooling connection (2) Heater cavity (3) Orifice retainer (4) Ceramic rods (5) Ceramic spacers (6) Drift rings (5 pieces)

Ions exiting the cell are directed by another three sets of einzel lenses into the second quadrupole mass filter with a Channeltron electron multiplier detector. The ionizer for this quad is usually turned off. This quadrupole can be operated in the single ion mode, where the intensity of a single ion of interest is monitored or the scan mode, in which case a scan of all ions exiting the drift cell is performed. Arrival time distributions (ATD), critical to almost all experiments performed with this instrument, are obtained using a multichannel scalar detector with  $2\ \mu\text{s}$  resolution. The arrival times represent the ion drift times from the ion-gate to the detector. Shown in Figure 5 is a schematic of the QMS-IM-QMS system. Figure 6 shows the timing sequence for this experiment.

### 2.3.2 Ion Energy and Injection Energy

The translational energy of ions produced in the electron impact source is well defined. Ion energy is defined as the voltage of the cage where the ions are “born”, the ion region.<sup>79</sup> With this definition, the ion energy is more or less independent of the ionizing electron energy or the potential of the extracting lenses. Since the quadrupole housing is floated (floating voltage) on the ionizer potential, the effective ion energy is the sum of the ion region voltage and the floating voltage. Floating the quad housing is particularly advantageous in experiments where highly energetic preformed ions, such as those generated by laser vaporization of a metal target, are investigated. It helps the quadrupole “manage” the ion energies. Highly energetic ions spend too little time between the quad poles and as a result are poorly resolved. This problem is also addressed by a pole bias, which is voltage applied to the z-axis of the quadrupole. Pole bias reduces ion energy

“seen” by the quadrupole, making the ions manageable by the filter, thus increasing resolution. Ion energy of about 12 eV is recommended for adequate resolution. As an example, the energy of an ion born in the ion region with a 45 V potential, a floating voltage of 40 V, and pole bias of 74 V is 85 eV (i.e.  $45 + 40$ ). The ion energy seen by the filter is 11 eV, because  $(45 + 40) - 74 = 11$  eV. Ions exit the mass filter with the same energy they possessed before entering the mass filter, so for the example above, the energy of the ions exiting the quad is 85 eV.

Another energy consideration is the injection energy, the energy of ions entering the drift cell. The injection energy is the difference between the ion energy and the cell entrance voltage. Using the example above, the injection energy of ions entering a cell with entrance voltage of 70 V is 15 eV (i.e.  $85 - 70$ ). Injection energy consideration is very important. Very small injection energies will result in no signal since the ions are unable to penetrate the barrier created by inert gas exiting the entrance orifice. On the other hand, two major complications arise with excessive injection energies. The first is the ions travel too far into the cell before losing their kinetic energies thus distorting mobility and other drift cell measurements. Ideally, the kinetic energies should be lost immediately before or at the cell entrance. The second complication is that of ion fragmentation. Ions dissociate into fragments at high injection energies resulting in weaker signal intensities and/or occurrence of secondary reactions involving fragment ions and reactant vapor in the cell, complicating or distorting kinetic and thermochemical measurements. Secondary reactions could also be the result of excited state reactions of the parent ions. Typical injection energies range from 10-20 eV. In cases where the mean energy of the ions is unknown

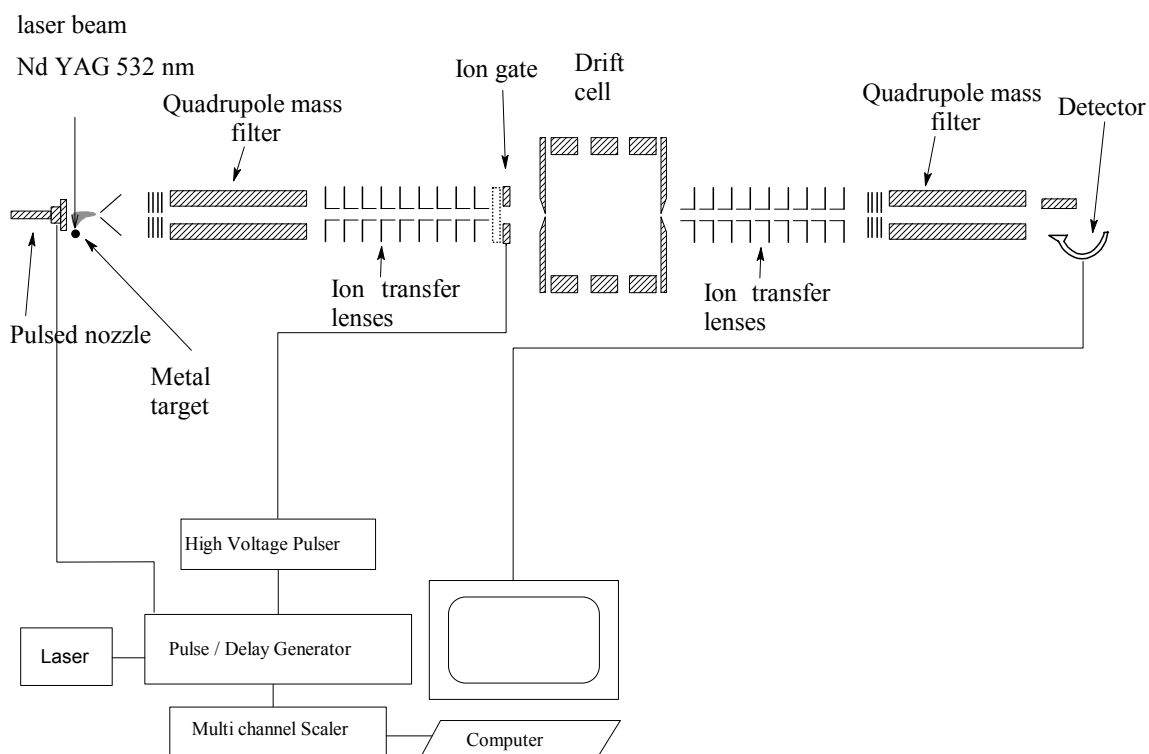


Figure 5: Schematic diagram for the wiring of QMS-IM-QMS for laser vaporization/ionization setup.

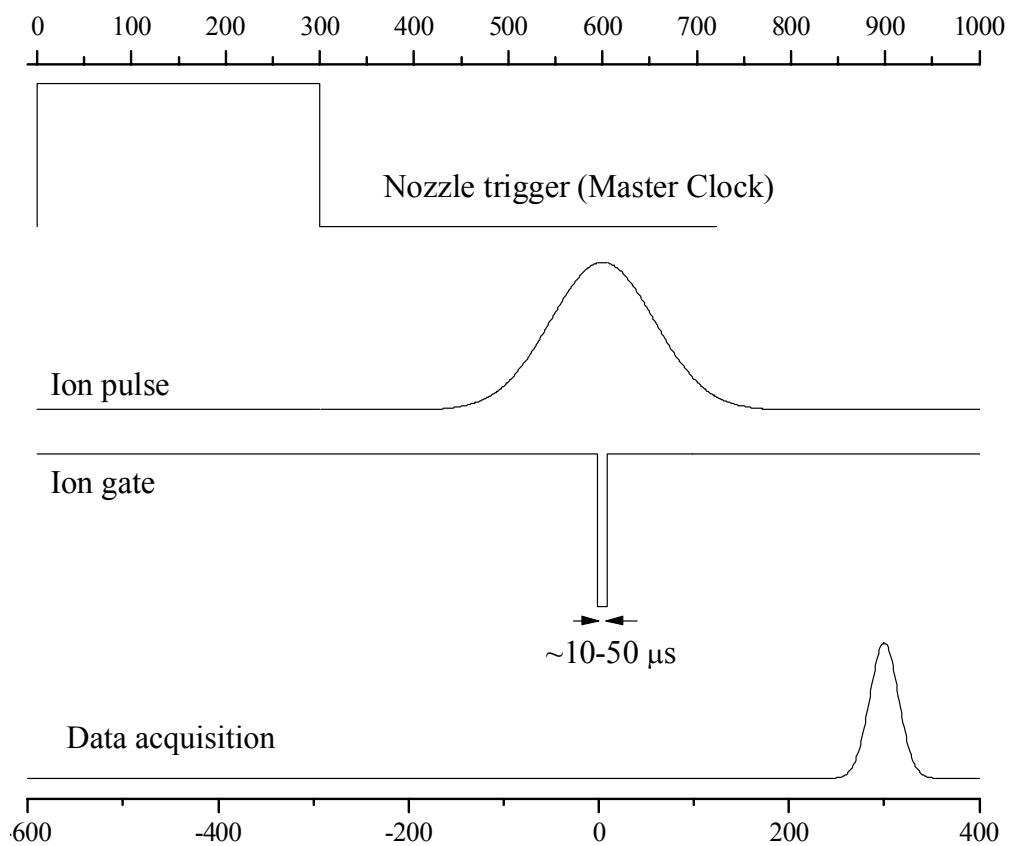


Figure 6: Timing sequence for electron impact ionization experiment.



such as in LVI preformed ions, the pole bias voltage or injection energy can be used to approximate the ion energy. This involves increasing either voltage to a point where the signal just disappears, thus approximating the ion energy.

Ions exiting the drift cell are said to be “reborn”, with their energies approximately that of the cell exit voltage. For good resolution, the ion energy seen by the second filter should be 3-10 eV, so the pole bias voltage of the second mass filter should be adjusted accordingly. The exiting ion energy consideration also means all guide lenses between the cell and quadrupole filter should be adjusted accordingly when the drift cell exit voltage is changed (in mobility and kinetic measurements). The post cell guide lenses include: einzel lenses 4, 5, 6, the ion region for second ionizer, all six ionizer lenses, and the pole bias. All six ionizer lenses for the second quad are biased to the ion region for simplification.

## **2.4 Reflectron Time-of-Flight Mass Spectrometer (RTOF-MS)**

The TOF-MS system is represented in Figure 7. It consist of two differentially pumped chambers: the source chamber, where neutral clusters and cations are produced and the TOF chamber which contains the acceleration plates, flight tube, ion mirror, and detector. The source chamber, pumped by a Varian VHS-6 diffusion pump [3000 L/s (He)], houses a 250  $\mu\text{m}$  conical nozzle (General valve, series 9) for cluster production and a metal target for cation generation (by LVI). The metal target is placed 0.5-1.5 cm from the nozzle face and displaced 0.5-1.2 cm from the beam axis. The typical operating pressure of the source chamber is  $\sim 10^{-5}$  Torr. The source and TOF chambers are separated

by a 3 mm conical skimmer placed at a distance of about 4-7 cm coaxial to the nozzle. The TOF chamber is pumped by a Varian VHS-4 diffusion pump [1500 L/s (He)] and with typical operating pressures  $\leq 6 \times 10^{-6}$  Torr. Both diffusion pumps are backed by two Welch Duo-Seal mechanical pumps. Foreline pressures are maintained below  $3.0 \times 10^{-2}$  Torr at all times. The TOF chamber was modified during the course of this experiment. The old setup consisted of a two stage Wiley-McLaren<sup>87,88</sup> type orthogonal acceleration source and the modified setup consists of a two stage orthogonal acceleration source with de Heer 2<sup>nd</sup> order space focus and a single stage ion mirror. Both setups are discussed below.

The pre-modified TOF setup, shown in Figure 7, consisted of three acceleration plates (repeller, accelerator, and ground plates; 1.3 cm apart), deflector plates, a 1 m Time-of-Flight tube, and a Chevron style microchannel plate (MCP) detector. The voltage gradient between the repeller and accelerator plates was accomplished by a voltage divider with an 80% ratio. The TOF plates are pulsed (10-20  $\mu$ s) using a DEI GRX-3.0K-H pulse generator. The signal from the MCP detector is digitized and stored using a Lecroy (9350A, 500MHz, dual channel) oscilloscope. The deflector plates (5 cm  $\times$  5 cm, SS) are used to correct ion trajectory in the flight tube. Typical resolution for this setup is approximately 200 amu.

The modified setup (Figure 8), designed by Dr. Robert Haufler,<sup>89</sup> offers the added advantages of positive and negative ion detection, better resolution ( $> 3000$  amu in principle), superior ion transmission, and compatibility with future upgrades and experiments: ion-gate, photoelectron spectroscopy time of flight (PES-TOF), photoionization, and photofragmentation experiments. As shown in Figure 8,

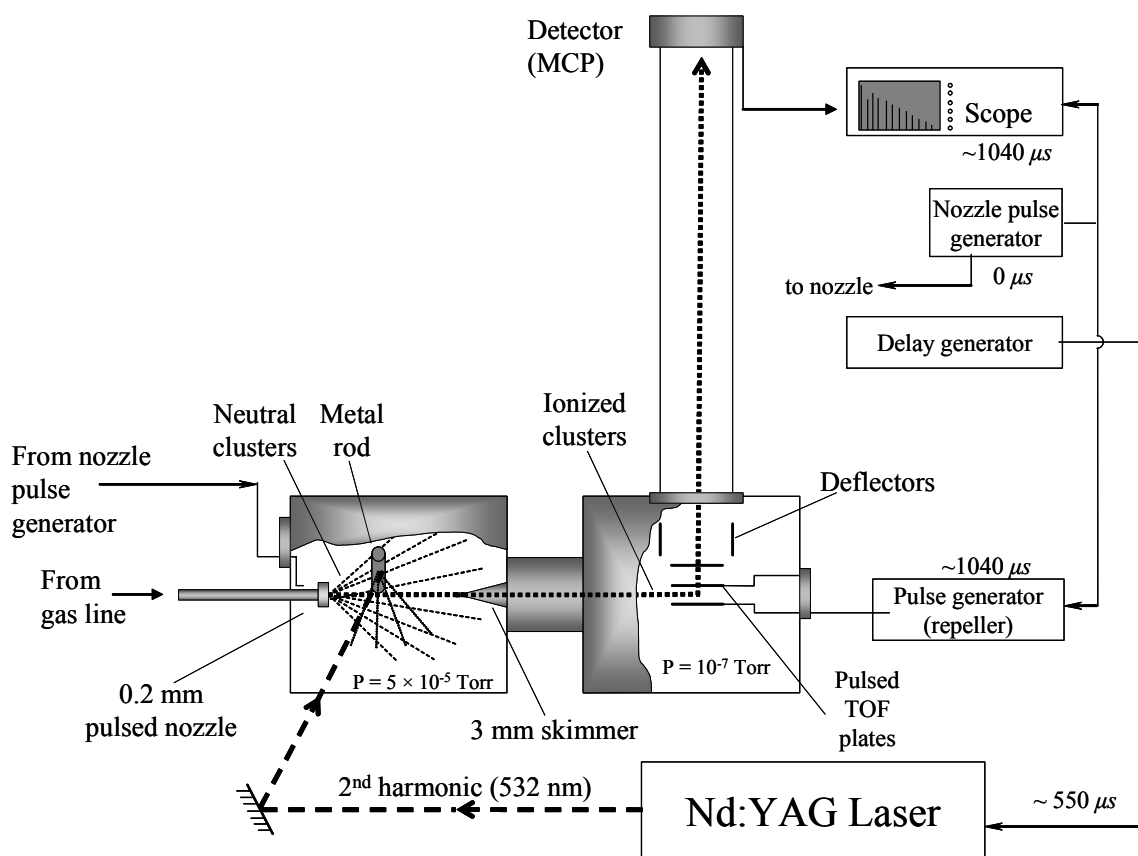


Figure 7: Pre-modified time-of-flight (TOF) mass spectrometer

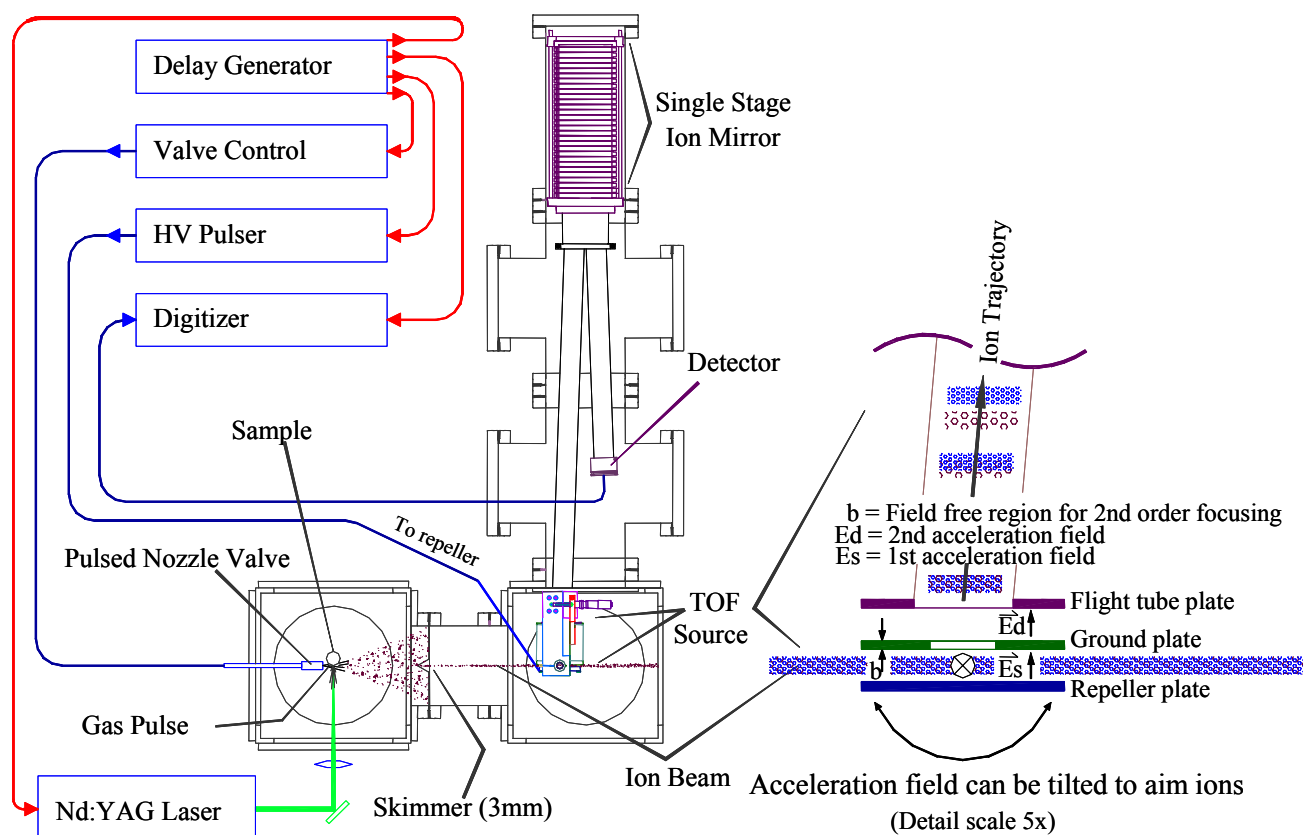


Figure 8: Modified reflectron time-of-flight (RTOF) mass spectrometer

modifications include installation of a gridded one stage ion mirror, a highly symmetric 2<sup>nd</sup> order space focus acceleration source with tilting capability (micrometer head adjuster), and two stainless steel (SS) ion guide tubes (4.1 cm OD  $\times$  0.6 m and 0.4 m length) in the TOF housing. One of the guide tubes directs the “flying” ions into the ion mirror and the other guides the ions out of the mirror to the detector. Here the guide tubes take the place of the ground plate in the old setup making the modified setup also a dual stage apparatus. Second order space focusing is accomplished using an acceleration plate with a field free sub-stage (“b” on Figure 8; 0.32 cm). Although the guide tubes have a voltage (negative for positive ions), the ions experience a field-free flight through them. In the modified setup, the middle plate, which serves the role analogous to that of the accelerator plate (pre-modified setup), is grounded. So sequentially from the bottom, we have the repeller, accelerator (2<sup>nd</sup> order space; grounded), and the guide tube. The separation between the acceleration plates is 1.27 cm. Separate voltage supplies feed the repeller plate and guide tube, thus eliminating the need for a voltage divider. The detector (Burle Long-Life<sup>™</sup> MCP, 40:1,  $>10^7$  gain, Chevron style, 400 M $\Omega$ ) voltage is floated on the guide tube voltage. For example, a voltage readout of -1.5 kV and -2.1 kV for the guide tube and detector respectively is actually, -1.5 kV for the guide tube and -3.6 kV for the detector; of course the detector only sees -2.1 kV. This float capability is accomplished using a custom-made Portware<sup>®</sup> voltage supply (Model 5RFTD3-C,  $\pm 5$  kV,  $\pm 3$  kV float, dual polarity). The guide tubes are perforated with many holes (0.74 cm D) for efficient pumping. The detector is clamped to the end of the guide tube and insulated from the chamber by ceramic spacers. An insulating cap (3.5" D, also drilled with holes) is mounted around the guide

tube entrance to prevent the tube field from interfering with the acceleration fields. Both guide tubes are supported just below the ion mirror entrance by a mirror shield. The reflectron structure consists of 30 rings (Figure 9E) mounted on a 6" stainless steel conflat flange. The rings are separated by sapphire bearings (0.32 cm OD) (Figure 9F) and insulated from the flight tube by two delrin rings (4.7" OD) mounted above and below the mirror structure. The first ring is gridded with fine Ni mesh (Buckbee Mears Cortland, 70 lines per inch (LPI), 88-89% transmittance) for entrance field evenness. This same mesh was used for the accelerator plate. Rigidity of the reflectron structure is accomplished by four 0.25" D rods mounted through the delrin rings on the conflat flange (Figure 9E). The ion mirror rings were interconnected with a chain of 20 M $\Omega$  resistors to maintain desired potential throughout the mirror. The rings were constructed with lips to maximize field evenness. The guide tube is designed to accommodate an ion or mass gate at the first ion space focus point and the detector is installed to coincide with second focus point. Another major difference between the old and new setups is how ion trajectories are corrected for. As mentioned above, the old setup corrects for ion trajectory by the use of deflector plates with a separate voltage supply. For the modified setup, this correction is accomplished by a manipulator flange coupled to the tilting source (acceleration plates structure) as shown in Figure 9 (1, 2, 4, and 9). By changing the orientation of the plates from the horizontal plane, the size of ions reaching the detector can be controlled.

Neutral acetylene clusters,  $(C_2H_2)_n$ , generated at the nozzle interact with cations,  $M^+$ , generated by LVI thus forming a charged cluster beam,  $M^+(C_2H_2)_n$  which is subsequently collimated by the skimmer. In the TOF chamber, the ions are accelerated by a

set of plates through the ion mirror to the microchannel plates for detection. To investigate oppositely charged ions, one only has to change the polarity of the repeller voltage supply, the guide tube and detector voltage supplies (note: this polarity is negative to investigate positive ions and positive to investigate negative ions), and ion mirror voltage supply. The repeller plate is pulsed using the same pulse generator described above. Figure 10 displays the superb resolution attainable using the modified setup. For a comparison to the mass spectrum obtained using the pre-modified instrument, see Figure 49.

Control of the time sequence is essential for this experiment. As represented in Figure 11, a typical sequence begins by opening of the nozzle ( $t_o$ ) which results in the generation of neutral acetylene clusters,  $(C_2H_2)_n$ . After a certain delay ( $\sim 490\text{-}550\ \mu\text{s}$ ), the laser Q-switch is triggered to initiate lasing (lasing delay  $\sim 150\text{-}300\ \mu\text{s}$ ), resulting in vaporized metal cations ( $M^+$ ), anions ( $M^-$ ), electrons, and neutral particles. The cations/anions/electrons subsequently interact with the neutral cluster beam forming charged clusters,  $M^{+/-}(C_2H_2)_n$ . The charged clusters are collimated by a conical skimmer as they enter the detection chamber. Approximately  $1.04\ \text{ms}$  after  $t_o$ , the pulse generator is triggered to supply voltage ( $10\text{-}50\ \mu\text{s}$  pulses) to the repeller plate. Signal intensity is maximized by timing the laser delay so that the cations interaction with maximum cluster intensity and timing the pulse-generator to pulse the repeller plate at appropriate delay times. The delay generator utilized here is a BNC, model 555 generator. Data acquisition is accomplished by the same instrumentation as in the pre-modified system.

## 2.5 Static Time-of-Flight Quadrupole Mass Spectrometer (STOF-QMS)

As shown in Figure 12 the STOF-QMS system consists of three chambers; the source chamber, the TOF chamber, and quadrupole chamber. The source chamber, pumped by a Varian VHS-6 diffusion pump (3000L/s in He), houses a 250- $\mu\text{m}$  diameter nozzle for cluster generation.<sup>85,90</sup> The neutral cluster beam from expansion is subsequently collimated by a 3-mm conical skimmer for ionization and detection. As shown in Figure 12 this setup is composed of two different ionization and detection sources: photoionization coupled to Time-of-Flight detection (two-stage MCP detector) and electron impact (EI) ionization coupled to a quadrupole mass filter (EMT detector). The second chamber, also pumped by a Varian VHS-6 diffusion pump, houses a Wiley-McLauren-type<sup>87,88</sup> acceleration source, a 1.1 m flight tube, and deflector plates to correct for cluster velocity components perpendicular to the flight tube axis. Photoionization is accomplished using the 193 nm (ArF) output wavelength of a Lambda Physik Excimer laser (COMPex-102, multigas, 200 mJ/pulse, 4 W, 25 ns, 157-351 nm). Unlike the RTOF setup, the accelerator and repeller plates are not pulsed. This is because, unlike the RTOF experiment, the ions are generated inside the accelerating field. The MCP signal current is subsequently amplified (Signal Recovery, Model 5185) and digitized with a Lecroy (9450, 350 MHz, dual channel) oscilloscope. The operating pressure for the source and TOF chambers are  $\approx 10^{-5}$  and  $< 10^{-6}$  Torr respectively. The timing for this experiment is simple; the nozzle opening represents  $t_0$  and the laser fires after a delay. The delay/pulse generator used here is a Stanford Research Systems Inc. pulse generator (model DG535, four channels). The timing sequence for this experiment is shown in Figure 13.



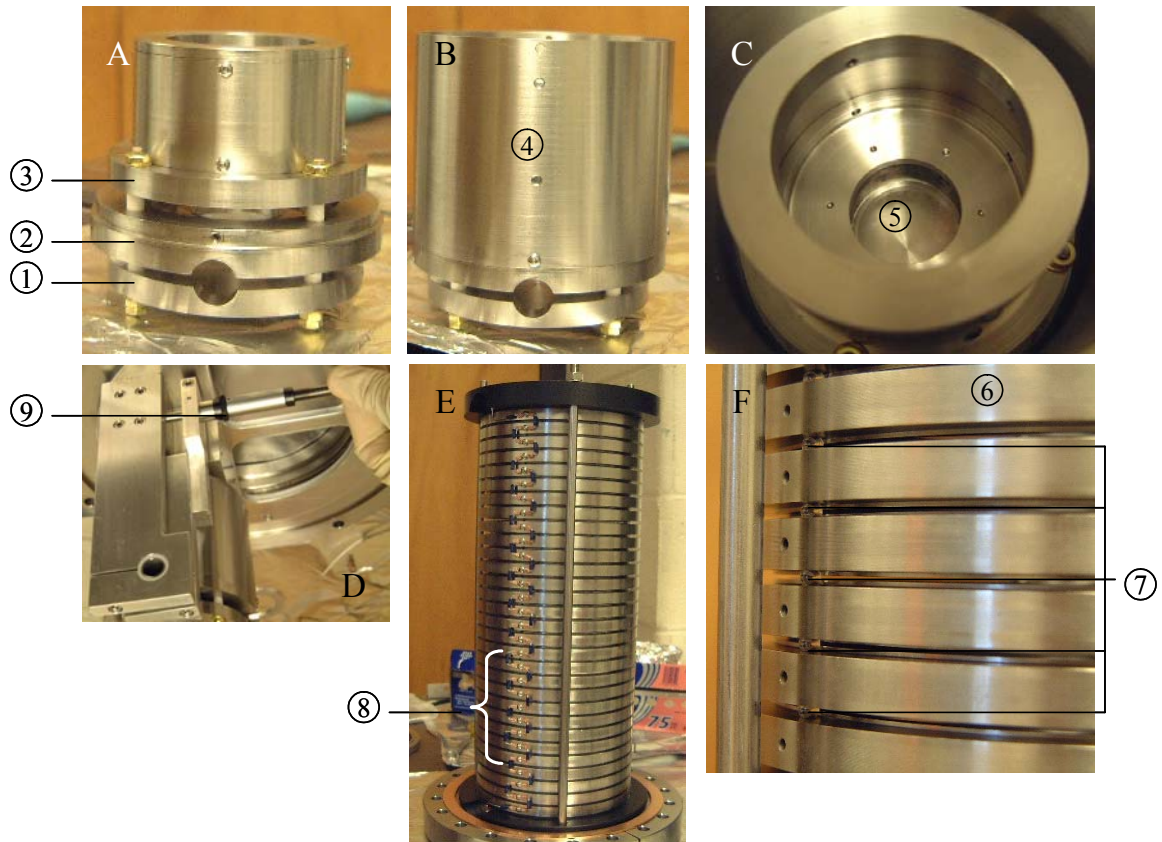


Figure 9: Pictures of the RTOF acceleration source (A – D) and ion mirror structure (E and F). (1) Repeller plate (2) Ground plate (3) Flight tube plate (4) Field shield (5) Nickel mesh on the ground plate (6) Ion mirror ring (7) Sapphire bearings (8) Chain of 20 MΩ resistors (9) Manipulator screw for tilting acceleration source (note the source is upside down here).

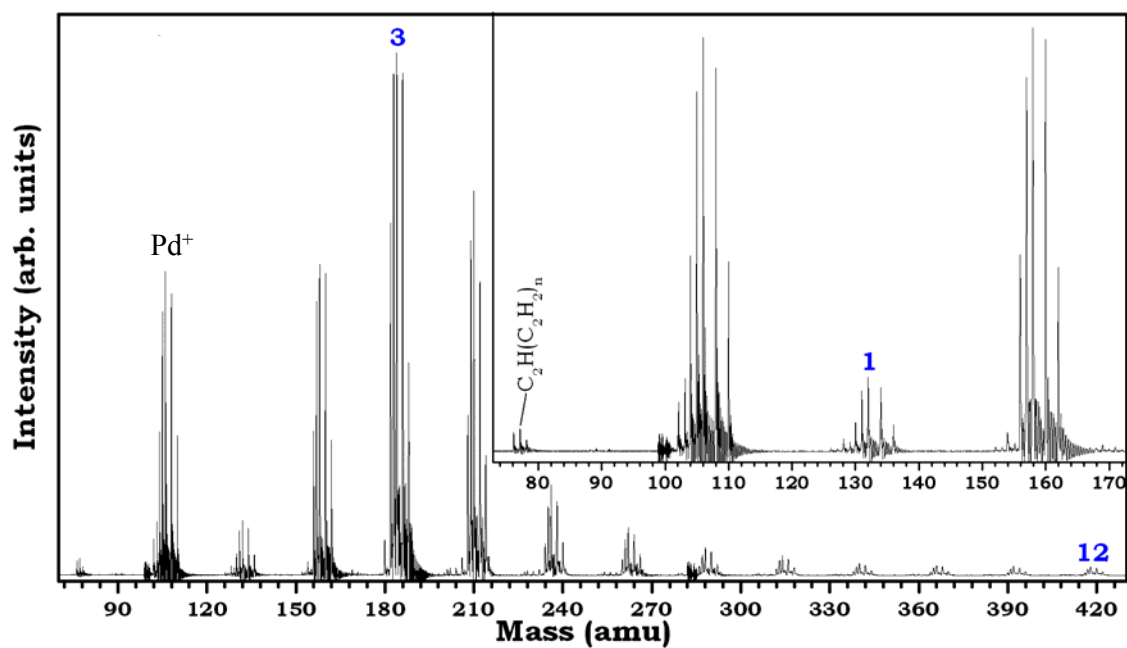


Figure 10: RTOF mass spectrum for  $Pd^+(C_2H_2)_n$  clusters. Multiplets are the result of palladium's extensive isotopic matrix. Resolution = 1600 amu. See Figure 49 for comparison to spectrum obtained using the pre-modified instrument.

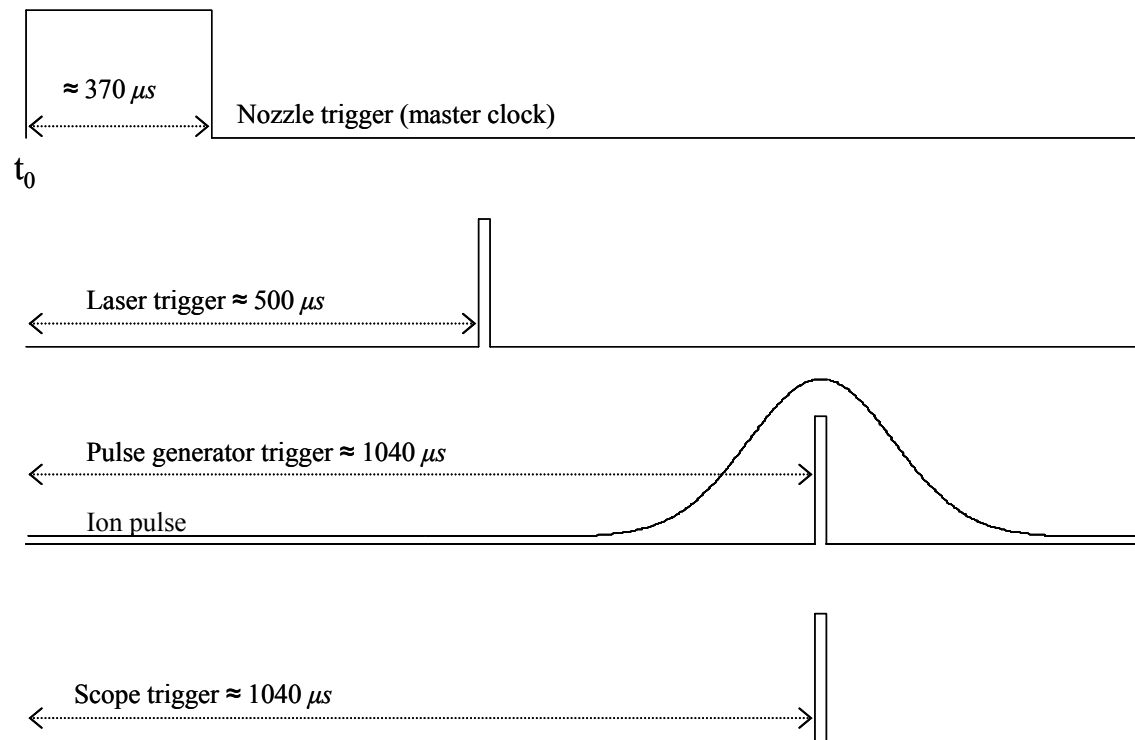


Figure 11: Timing sequence for LVI-TOF experiment.

Two types of acetylene experiments were performed with this instrument. In the first, heterogeneous clusters of the form,  $(\text{C}_6\text{H}_6)_n(\text{C}_2\text{H}_2)_n$  were generated with the benzene molecule acting as a chromophore (since acetylene does not absorb at 193 nm, the wavelength of our laser). In the second type of experiment, homogeneous acetylene clusters were generated and allowed to travel as neutral clusters to the electron impact (EI) source for ionization and detection (Extrel 5221, 880 kHz, 300 W, 4000 amu, 9.5 mm). The quadrupole chamber is pumped by a turbo pump (Pfeiffer Vacuum, TMU 521, 500 L/s in He) and maintained at  $< 8.0 \times 10^{-7}$  Torr during normal operation. In cases where ion signal is low, the output signal from the EMT is boxcar integrated (Princeton Applied Research, model 166) and the resulting AC signal is converted to DC with the aid of a homemade lock-in amplifier. The boxcar is also triggered by the Stanford delay generator.

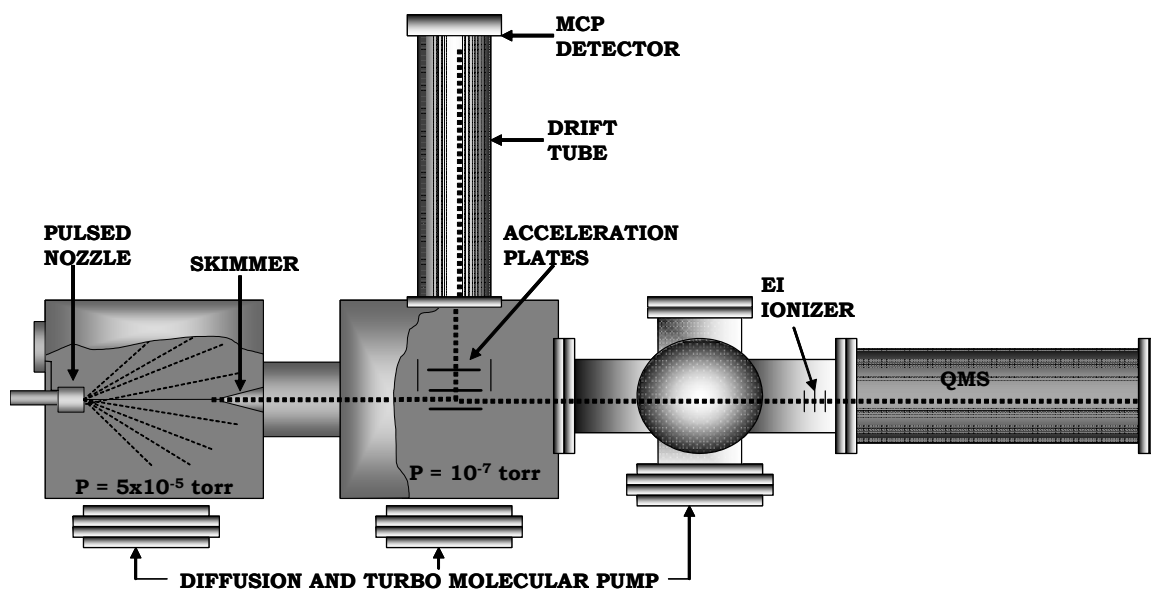


Figure 12: Setup for the modified time of flight/quadrupole mass spectrometer. Dashed lines show trajectory of clusters.

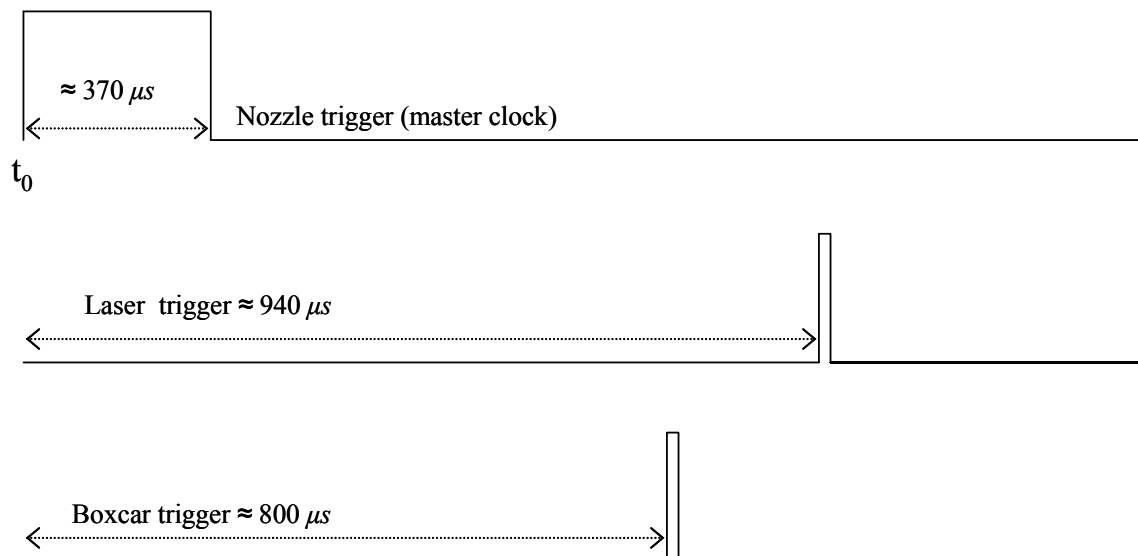


Figure 13: Timing sequence for TOF/QMS experiment.

## CHAPTER 3 Experimental Techniques

### 3.1 Mobility Measurements

Mobility is simply the measurement of ion drift time through an inert buffer gas (He, N<sub>2</sub>, Ar, etc.) under the influence of a low electric field. Mobility is dependent on the average collision cross section ( $\Omega$ ) of the drifting ions, which in turn, is a function of the ion structure. This technique enhances results from dissociation experiment because ions with similar masses and fragmentation products but with sufficiently different structures, hence different collision cross sections, will have different drift times. In this work, the drift cell is filled with buffer gas and a packet of ions (10-50  $\mu$ s pulses) with kinetic energies high enough to penetrate the barrier created by the exiting buffer gas (He), are injected into the cell. The ions are decelerated and thermalized by collisions with the exiting buffer gas before entering the cell. In the cell, two opposing forces act on the ions. A decelerating force, collision with buffer gas, acts to slow the ions down and an accelerating force, the low cell field, acts to accelerate the ions. Mobility,  $K$ , is defined as<sup>52</sup>

$$K = v_d / E \quad (3.1)$$

where  $E$  is the drift field ( $E = V/z$ ,  $V$  is the drift voltage and  $z$ , the length of the cell (cm) and  $v_d$  is the drift velocity ( $v_d = z/t_d$ ,  $t_d$  is the drift time in s). In order to effectively compare mobilities measurements at different cell conditions or different instruments,  $K$  is normalized to standard conditions (STP) and referred to as reduced mobility,  $K_o$ . The reduced mobility is represented below.

$$K_o = K \left( \frac{273.15}{T} \right) \left( \frac{P}{760} \right) \quad (3.2)$$

Here,  $T$  is the buffer gas temperature (K), and  $P$  is the buffer gas pressure (Torr).

Combination of equations (3.1) and (3.2), substituting for  $E$  gives

$$t_d = \left( \frac{z^2 \times 273.15}{T \times 760 \times K_o} \right) \left( \frac{P}{V} \right) + t_o \quad (3.3)$$

where  $t_o$  is the effective time spent outside the drift cell. It is apparent from (3.3) that a plot of the drift time ( $t_d$ ) versus  $P/V$  will give a straight line with slope

$$m = \left( \frac{z^2 \times 273.15}{T \times 760 \times K_o} \right) \quad (3.3b)$$

corresponding to the reduced mobility ( $K_o$ ) and intercept corresponding to  $t_o$ . In practice, a packet of the mass selected ion of interest is injected into the drift cell and the arrival time distribution (ATD) is collected at varying cell voltages,  $V$ , (with  $T$  and  $P$  held constant). The drift time ( $t_d$ ) is taken to be the peak maximum assuming a Gaussian-type distribution. The maximum intensity is located by fitting the ATD to a Gaussian equation or smoothing the ATD and determining the maximum. A small distortion of the ATD by the exit orifice is corrected for by

$$t_d = t_{obs} + 4D/v_d^2 \quad (3.4)$$

where  $t_{obs}$  is the observed time at peak maximum and  $D$  is the diffusion coefficient.<sup>51</sup>  $D$  is related to  $K$  at low drift field condition by the Einstein equation

$$D = D_L = D_T = K \frac{k_B T}{e} \quad (3.5)$$



where  $D_L$  and  $D_T$  are the longitudinal and transverse diffusion coefficients respectively,  $k_B$ , the Boltzmann constant, and  $e$ , the electron charge. Figure 14 shows a sample ATD for mass selected  $C_2H_2^+$  ions at various cell voltages and similar ion-count duration. Notice the distinctive distribution spread as cell voltage decreases. This is due to the increased effect of longitudinal diffusion, the consequence of increased ion dwell time in drift cell. Transverse diffusion results in loss of ion intensity. The inset in Figure 15 represents a typical plot of  $t_d$  versus  $P/V$ . The solid line represents the least square fitting to the data points. The assumptions made in this experiment are as follows,<sup>91</sup>

- (i) Measured mobility,  $K$ , is independent of drift field
- (ii) Ion drift time,  $t_d$ , is represented by maximum peak intensity of a Gaussian-type distribution
- (iii) The injected ions do not penetrate significantly into the drift cell before thermalization and loss of excessive kinetic energy occur.

The first assumption can be satisfied by calculating the effective temperature of drifting ions,<sup>52,92</sup> defined as

$$T_{eff} = T_g + \frac{M_b v_d^2}{3k_B} \quad (3.6)$$

where  $T_g$  is the buffer gas temperature,  $M_b$ , the buffer gas mass, and  $v_d$ , the drift voltage. At low field conditions, defined as  $E/N \leq 6 Td$  (where  $E$  is the drift field,  $N$  is the buffer gas number density, and  $Td = \text{Townsend} = 10^{-17} \text{ cm}^2\text{V}$ ),<sup>52</sup> and for mobility of  $18 \text{ cm}^2\text{V}^{-1}\text{s}^{-1}$  at 298 K, the effective temperature is only about 9 % higher than the thermodynamic

temperature. This percentage is even lower at lower drift field conditions. This equates to a  $\leq 2\%$  effect on measured mobility,  $K_o$ .<sup>93</sup>

The second assumption is satisfied by comparison of the arrival time distribution to that predicted by the transport theory for single ionic species under similar physical conditions. In an ideal experiment, the experimental ATD must match that predicted by transport theory (Figure 15). For a finite pulse of ions with the same mass and structure drifting through a cylindrical cell, the flux of ions,  $\phi(t)$ , traveling through an orifice of area  $a$ , is given by

$$\phi(t) = \frac{sa e^{-\alpha t}}{4\sqrt{\pi D_L t}} \left( v_d + \frac{z}{t} \right) \left( 1 - \exp\left(-\frac{r}{4D_T t}\right) \right) \exp\left(-\frac{(z - v_d t)^2}{4D_L t}\right) \quad (3.7)$$

where  $r$  and  $s$  represent the radius and surface density of a thin disk of injected ions respectively with the latter used as a scaling factor and  $\alpha$  is the reaction frequency set equal to zero for the inert buffer gas. For the third assumption, one only needs to calculate penetration of the ions into the drift cell. The energy after  $n$  collisions (hard sphere) with He is given by<sup>51</sup>

$$E_f = E_i M^n \quad (3.8)$$

$$M = \frac{M_i^2 + M_b^2}{(M_i + M_b)^2} \quad (3.9)$$

where  $E_i$  is the initial energy (injection energy),  $M$ , the reduced mass as defined by (3.9),  $M_i$  is the mass of injected ion, and  $M_b$ , the mass of the buffer gas. Assuming a collision rate coefficient of  $10^{-9} \text{ cm}^3 \text{ s}^{-1}$  and injection energy of 13 eV, the number of collisions required to thermalize (i.e.  $E_f = k_B T$ ) the injected ions is approximately 24. With a buffer gas

pressure of 3.5 Torr at room temperature (298 K), the time required for thermalization, according to (3.10) is  $\approx 0.2 \mu s$ .

$$t = n/N \cdot k \quad (3.10)$$

( $n \approx 24$  Collisions,  $k = 10^{-9} \text{ cm}^3 \text{ s}^{-1}$ , and  $N$ , buffer gas number density  $\approx 10^{17} \text{ n/cm}^3$ ). The distance traveled by the ions before being thermalized is given by

$$d = \int_0^t v_d + v_i M \frac{n \cdot k \cdot T}{2} dt \quad (3.11)$$

where  $v_d$  is the drift velocity,  $v_i$  is the initial velocity, and  $M$ , the reduce mass according to (3.9). This distance was determined to be  $< 2\%$  of the total cell length.<sup>93</sup>

### 3.2 Structure Determination

Structure determination is accomplished by comparison of the measured reduced mobility,  $K_0$ , to that obtained from the trajectory method calculations on predicted geometries. The equation relating the collision integral,  $\Omega^{(1,1)}$ , (hence structure) and  $K_0$  is<sup>94</sup>

$$K_0 = \frac{3qe}{16N_0} \left( \frac{2\pi}{k_B T_{eff}} \right)^{\frac{1}{2}} \left( \frac{M_i + M_b}{M_i M_b} \right)^{\frac{1}{2}} \frac{1}{\Omega_{avg}^{(1,1)}} \quad (3.12)$$

where  $qe$  is the ion charge,  $N$ , the number density of the buffer gas,  $T_{eff}$ , the effective temperature defined by  $T_{BG} + m_B v_D^2 / 3k_B$ , where  $v_D$  is the drift velocity,  $T_{BG}$  is the buffer

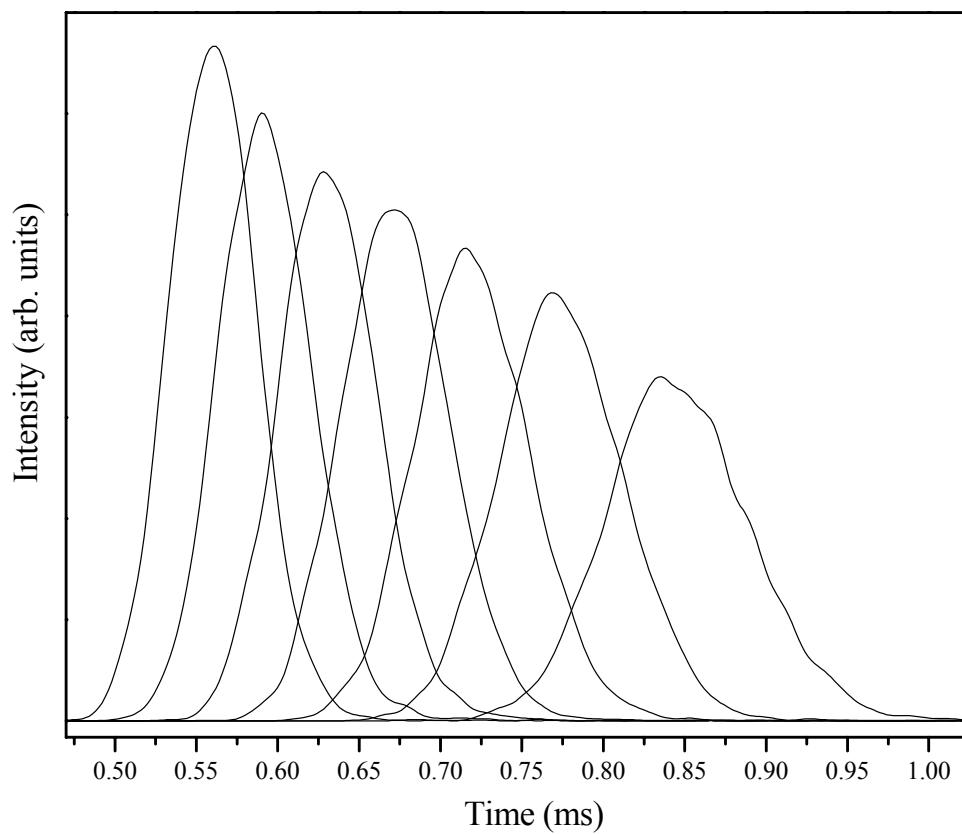


Figure 14: The arrival time distributions (ATDs) of injecting  $20\ \mu\text{s}$   $\text{C}_2\text{H}_2^+$  ion pulse into drift cell filled with 2.1 Torr He at decreasing cell voltages of 2V steps. The earlier ATD corresponds to a drift voltage of 34 V while the later ATD corresponds to a drift voltage of 22 V.

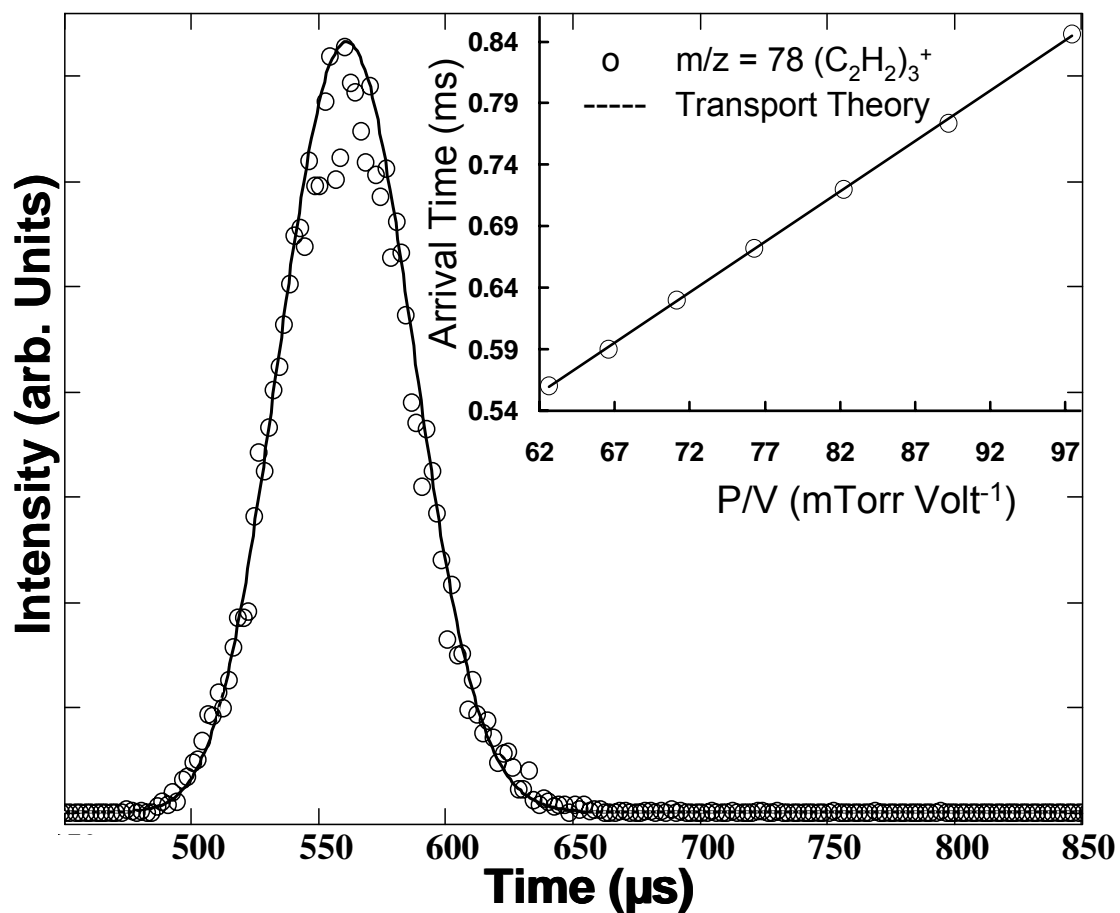


Figure 15: Comparison of measured ATD of the acetylene trimer cation  $(\text{C}_2\text{H}_2)_3^+$  with that predicted by the transport theory equation. The inset shows the linear plot of  $t_d$  vs  $P/V$  used in calculating the reduced mobility.

gas temperature (the second term accounts for temperature perturbation due to the drift field),  $M_i$  and  $M_b$  are the masses of the ion and buffer gas respectively, and  $\Omega_{avg}^{(1,1)}$  is the orientationally averaged collision integral, the average of  $\Omega^{(1,1)}$  over all possible collision orientations. The superscript, (1,1), refers to the pair-wise collision assumption used in the collision cross sectional calculation. The averaged collision cross section can be obtained by three methods which differ in the most part by the interaction potentials utilized in their computation. The first of these methods is called the hard sphere approximation.<sup>77</sup> As the name suggest, a hard sphere potential is assumed for the interaction between an atomic or molecular ion and the buffer gas. Here, a molecule oriented randomly in space is enclosed in a square plane of area  $A$ . A hard sphere radius is drawn around each atom of the molecule and random points are selected within the plane. If a selected point falls within the radius defined by the sum of the atom and He hard sphere radius, a collision is assumed. The product of the ratio of “hits” to number of tries and area,  $A$ , represents the cross section of a particular orientation. The process is repeated for different orientations. An average collision cross section over all orientations is then obtained. The second approach is similar to the first but differs in the method of hard sphere determination. This method utilizes a temperature-dependent collision radius ( $R_{coll}$ ) obtained from a compilation of collision integrals for atom-atom collision using a 12-6-4 potential.<sup>95</sup> This potential has the form

$$U(r) = \frac{n\varepsilon}{n(3 + \gamma) - 12(1 + \gamma)} \left[ \frac{12}{n} (1 + \gamma) \left( \frac{r_m}{r} \right)^n - 4\gamma \left( \frac{r_m}{r} \right)^6 - 3(1 - \gamma) \left( \frac{r_m}{r} \right)^4 \right] \quad (3.13)$$

where  $\varepsilon$  is the potential depth,  $r_m$ , the distance at the potential minimum,  $n$  is an exponent for short range interaction behavior (repulsion) and equal to 12 for this method, and  $\gamma$  is a dimensionless parameter defining the relative strengths of the  $r^{-6}$  and  $r^{-4}$  terms. The last term ( $r^{-4}$  term),  $U_4(r)$ , represents attractive charge ( $q$ ) and ion-induced dipole interaction between the ion and buffer gas. This term is given by

$$U_4(r) = -\frac{q^2 \alpha}{2R^4} \quad (3.14)$$

where  $\alpha$  is the polarizability of the gas. Expressed as a sum of Lennard-Jones (LJ) potential and ion-induced dipole interaction, (3.13) becomes

$$U(r) = \varepsilon_{LJ} \left[ \left( \frac{r_{LJ}}{r} \right)^{12} - 2 \left( \frac{r_{LJ}}{r} \right)^6 \right] - \frac{q^2 \alpha}{2r^4} \quad (3.15)$$

here,  $\varepsilon_{LJ}$  and  $r_{LJ}$  are Lennard-Jones parameters, corresponding to well depth and position respectively,  $\alpha$  is the polarizability of the neutral gas.  $\gamma$ ,  $r_m$ , and  $\varepsilon$  (3.13) can thus be obtained by fitting  $q$ ,  $\varepsilon_{LJ}$  and  $r_{LJ}$  (3.14) into (3.13). For a given set of  $\gamma$ ,  $r_m$ , and  $\varepsilon$  parameters at a particular temperature,  $T$ , the momentum-transfer collision integral,  $\Omega^{(1,1)}$ , can be obtained from a table. From  $\Omega^{(1,1)}$ ,  $R_{coll}$  can be obtained using the relationship

$$R_{coll} = \left( \frac{\Omega^{(1,1)}}{\pi} \right)^{\frac{1}{2}} \quad (3.16)$$

The projection approximation gives better results than the hard sphere method due to the inclusion of long-range potential effects. The sigma program, written by the Bowers group,<sup>77,95,96</sup> uses both methods described above. The third method is called the trajectory method.<sup>94</sup> In this method the collision integral,  $\Omega^{(1,1)}$  is related to the angle defining pre-

and post-impact trajectories of ion and buffer gas molecules (scattering angle). It is the average over the impact parameter and relative velocity. The average collision integral,  $\Omega_{avg}^{(1,1)}$ , is the average over all collision geometries. The same potential (3.13) as that used in the projection approximation is used for the trajectory method. A program, Mobcal, written by Jarrold *et al.*<sup>94,97,98</sup> is used here. This method is computationally expensive but gives more reliable results when compared to experiment. This method was utilized for all studies in this work.

### 3.3 Kinetic Measurements

Kinetics is the study of reaction rates and the corresponding dependence on time, concentration, temperature, and reactant surface area and morphology. For an irreversible second-order reaction such as



the reaction rate is given by

$$rate = -\frac{d[A^+]}{dt} = k_2[A^+][B] \quad (3.18)$$

where  $-\frac{d[A^+]}{dt}$  is the rate of disappearance of  $A^+$ ,  $k_2$  is the second-order rate constant, and  $[A^+]$  and  $[B]$  are the concentrations of  $A^+$  and B respectively. With the concentration of reactant in the cell,  $[B]$ , much greater than the injected ion,  $[A]$ , the reaction can be considered pseudo-first order and the integrated rate law can be written in the form

$$-\ln \frac{[A^+]}{[A^+]_0} = k_2[B]t \quad (3.19)$$



where  $[A^+]_0$  is the initial concentration of  $A^+$ , and  $t$  is the reaction time. Typically, the concentration of  $B$  (reacting gas/vapor) is much more than that of  $A^+$  and as a result, the reaction can be treated as a pseudo-first order reaction and the rate constant of this reaction,  $k_l$ , is determined from the plot of

$$-\ln \frac{[A^+]}{[A^+]_0} \quad (3.20)$$

as a function of residence time in the cell,  $t_d$ . Since the concentration of  $B$  is known,  $k_2$  can be calculated. In this experiment, the reactant ion is injected into the drift cell containing the neutral vapor,  $B$ , and He. As the reactant ion drifts through the cell, it reacts with the neutral vapor to give products. The initial concentration of the reactant ion,  $[A^+]_0$ , is the sum of both reactant and product ions,  $[A^+] + [B^+]$  and the reaction time is the ion residence time in the cell.<sup>99,100</sup> The arrival time obtained in this experiment represents the time the ions spend inside and outside the cell. To obtain the true residence time, the intercept ( $t_o$ ) from a mobility measurement (Equation 3.3) on  $A^+$  is subtracted from the arrival time, resulting in  $t_d$ . Equation (3.19) can thus be written as,

$$-\ln \frac{[A^+]}{[A^+] + [B^+]} = k_1 t_d \quad (3.21)$$

where  $k_l$  is the first order rate constant. To obtain  $t_d$  for the plot described in (3.21), the cell voltage is varied. This varies the resident time of the reactant ion and consequently the relative concentrations of  $A^+$  and  $B^+$ . The concentrations of  $A^+$  and  $B^+$  are obtained from the integrated arrival time distribution (ATD) of each species. In a less quantitative technique,  $[A^+]$  and  $[B^+]$  can be obtained from their individual mass spectrum intensity. As

shown in Figure 16, a plot of  $-\ln \frac{[A^+]}{[A^+] + [B^+]}$  versus  $t_d$  gives a straight line with slope equal to  $k_1$ . Knowing  $k_1$ , the second order rate constant,  $k_2$ , can be obtained from the relation

$$k_2 = k_1[B] \quad (3.22)$$

where  $[B]$  is the number density of the neutral reactant gas.

### 3.4 Thermochemical Measurements (van't Hoff Plots)

Information on thermochemical parameters such as  $\Delta H^\circ$  and  $\Delta S^\circ$  for ion-molecule association reactions can be obtained using the drift technique. For a typical association reaction of the form



$\Delta H^\circ$  and  $\Delta S^\circ$  for the addition of neutral  $B$  can be obtained using the van't Hoff equation

$$\ln K = -\frac{\Delta H^\circ}{RT} + \frac{\Delta S^\circ}{R} \quad (3.24)$$

where  $R$  is the gas constant.  $K$ , the equilibrium constant, is calculated from the relation

$$K = \frac{I(A^+ \cdot B_n)}{I(A^+ \cdot B_{n-1})P(B)} \quad (3.25)$$

where  $I$  is the integrated ion intensity of the arrival time distribution (ATD) and  $P(B)$  is the partial pressure of the neutral  $B$  in the drift cell.

For the hypothetical reaction above, the ATD of injected  $A^+$  and association complexes,  $A^+ \cdot (B)_{n-1}$  and  $A^+ \cdot (B)_n$  formed inside the cell, is measured as a function of drift voltage corresponding to different residence (reaction) times. Equilibrium is reached when the ratio

of  $A^+ \cdot (B)_n / A^+ \cdot (B)_{n-1}$  is constant. Another indication of equilibrium is the observation of the same mean arrival time,  $t_d$ , for the injected and association complexes. For Reaction 3.23 above, true equilibrium means a coupling of the association reactant and products  $A^+ \cdot (B)_{n-1}$  and  $A^+ \cdot (B)_n$  respectively, hence the same mean arrival time.<sup>101</sup> Figure 17 shows a typical van't Hoff plot for association reaction 3.23.

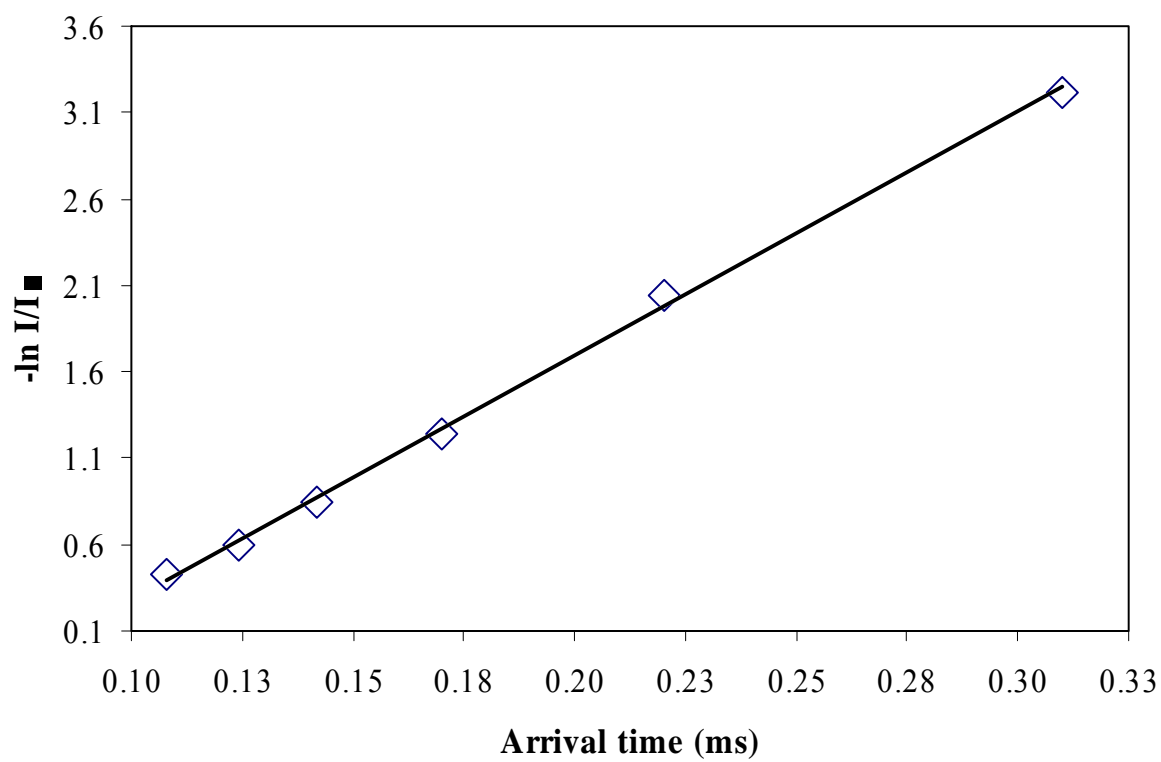


Figure 16: Plot of  $-\ln I/I_0$  vs. arrival time for the reaction of acetylene ions with water at 31°C. The least squares linear fit (solid line) gives a first order rate constant (slope) of  $14.12 \pm 0.04 \text{ s}^{-1}$  and  $R^2 = 0.9984$ .

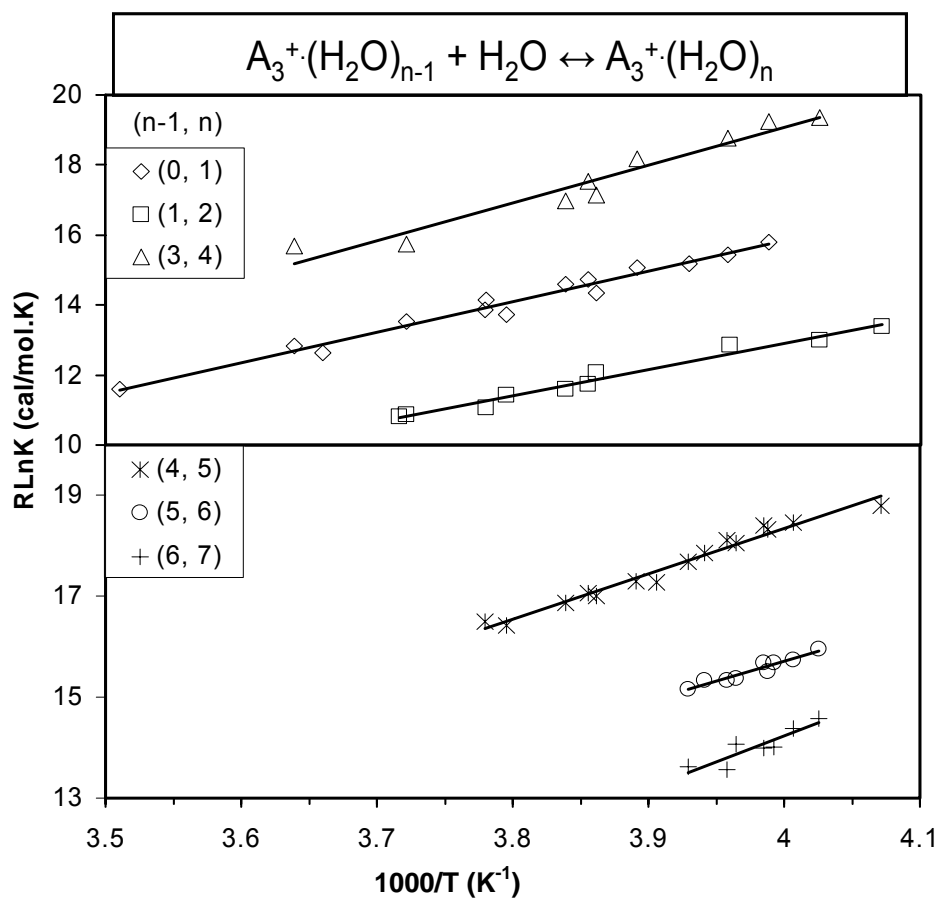


Figure 17: van't Hoff plots for the  $(C_2H_2)_3^+/(H_2O)_n$  association reaction. Here  $A^+ = (C_2H_2)_3^+$  and  $B = H_2O$ .

## CHAPTER 4      Structures of Small Acetylene Cluster Ions $(\text{C}_2\text{H}_2)_n^+$ , where $n = 1-3$

### 4.1      Introduction

The chemistry of acetylene has received considerable attention and continues to be an active area of research.<sup>1,2</sup> This is due not only to the fact that acetylene polymerization produces a variety of industrially and technologically important conducting polymers<sup>20-22</sup> but also to the important roles of acetylene in flames and combustion processes, particularly in the mechanism of soot formation, and in interstellar clouds, principally in the origin of larger hydrocarbon and other complicated molecular species observed in interstellar media.<sup>2</sup> More recently, acetylene in combination with catalyzing transition metals is used in an efficient synthesis of carbon nanotubes (CNTs).<sup>23</sup>

Due to the isomerization tendency of ionized acetylene clusters,  $(\text{C}_2\text{H}_2)_n^+$ , many experimental inquiries have been made with a focus on elucidating the identity of the dimer,  $(\text{C}_2\text{H}_2)_2^+$ , and trimer,  $(\text{C}_2\text{H}_2)_3^+$ , ions.<sup>24,44,102</sup> The daunting task however, is unambiguously deciphering between the numerous isomers that exist for both the  $\text{C}_4\text{H}_4^+$  and  $\text{C}_6\text{H}_6^+$  species, a problem well known for small and medium sized hydrocarbons.<sup>103</sup> For instance, the collision induced dissociation (CID) spectra of an isomer could have an internal energy dependence, rendering dissociation experiments inconclusive for structure identification<sup>104</sup> or different isomers could have similar (CID) spectra, indicative of pre-dissociative collision-induced isomerization.

Consensus on the identity of the  $C_4H_4^+$  ion has significantly strengthened since initial work by Rosenstock *et al.*<sup>105</sup>; which concluded the most probable structure of the  $C_4H_4^+$  ion produced from benzene and pyridine dissociation was of a cyclic rather than linear conformation. Others, using kinetic energy release (KER)<sup>106</sup> and ion-molecule reaction experiments,<sup>102,107</sup> suggested the presence of both cyclic (*c*) and linear (*l*)  $C_4H_4^+$  isomers; one of which was found to be much more reactive towards the neutral acetylene and benzene molecule than the other. The cyclic isomer produced by benzene and pyridine dissociation was concluded to be methylenecyclopropene<sup>102,106</sup> (Figure 18) and using ionization potential arguments, the linear isomer was suggested to be 1-buten-3-yne (vinylacetylene).<sup>102</sup> The same conclusion was reached by Ono and Ng using photoionized acetylene clusters.<sup>44</sup> Ausloos *et al.*<sup>102</sup> provided evidence for the latter (vinylacetylene) as the reactive species as well as showed the ratio of both isomeric populations to be highly dependent on the internal energy of the precursor ion (benzene). Using  $Ar^+$  and  $N_2^+$  (IEs = 15.6 eV) as ionizing agents, Ausloos *et al.* found a >80% production of the reactive  $C_4H_4^+$  ion as opposed to <5% when  $CO^+$  (IE = 14.1 eV) is used as a charge transfer agent. Determination of the  $C_4H_4^+$  fragment structure has been made using various precursor molecules. Some of these precursor molecules include, 1,5-hexadiyne, 2,4-hexadiyne, 1,4-cyclohexadiene, 1,3-cyclohexadiene, 1,3,5-hexatriene, cyclooctatetraene, 2,4,6-cycloheptatriene-1-one, vinylacetylene, butatriene, 6,7-benzo-3-methylenetricyclo[3.2.2.0]nona-6,8-diene, 7,8-benzotricyclo[4.2.2.0]deca-3,7,9-trieneexadiene, 3-butyne-1-ol, 1,4-dibromobut-2-yne, 1,4-benzoquinone, 1,2-benzoquinone, and 3,4-diiodocyclobutene.<sup>108,109</sup> The majority of these molecules have been shown to produce the vinylacetylene and

methylenecyclopropene ions exclusively upon dissociation, with the exception of the latter five (quinones and diiodo/chlorocyclobutenes) which have been shown to dissociate into high relative proportions of the cyclobutadiene ion.<sup>108-110</sup> Using CID and tandem ion cyclotron resonance spectroscopy, Bowers *et al.*<sup>103</sup> convincingly concluded (contradicting Ausloos *et al.*<sup>102</sup>) that the relative isotopic population is more dependent on method of preparation than internal energy of the ions. But, perhaps more interesting, was the conclusion that  $\geq 90\%$  of  $\text{C}_4\text{H}_4^+$  produced from precursor acetylene clusters was cyclic. In the same work, it was also concluded that the *l*- $\text{C}_4\text{H}_4^+$  isomerized to *c*- $\text{C}_4\text{H}_4^+$  according to



at the rate of  $(3 \pm 1.5) \times 10^{-10} \text{ cm}^3 \text{ s}^{-1}$ . Bowers *et al.* suggested the *c*- $\text{C}_4\text{H}_4^+$  isomer from acetylene clusters to be methylenecyclopropene ion. No consideration was made for the cyclobutadiene ion. On the other hand, employing photoionized acetylene trimer clusters and *ab initio* calculations, Baer *et al.*<sup>26</sup> concluded the  $\text{C}_4\text{H}_4^+$  species to be the cyclobutadiene, vinylacetylene, or butatriene ion. Also, in a highly detailed theoretical investigation of the  $\text{C}_4\text{H}_4^+$  potential energy surface (PES), Bally *et al.*<sup>111</sup> concluded that isomerization of the  $(\text{C}_2\text{H}_2)_2^+$  to cyclobutadiene is kinetically more favourable than any of the other  $\text{C}_4\text{H}_4^+$  isomers (Figure 18) due to the absence of H-shifts in its production. In fact, the cyclobutadiene ion is the only  $\text{C}_4\text{H}_4^+$  isomer whose reaction mechanism involves no H-shifts. Therefore, the ion-molecule reaction of acetylene in environments with efficient three-body interactions (i.e., condensed phase or clusters) may be expected to produce a relatively large population of the cyclobutadiene ion.



Condensed-phase experiments confirmed the formation of the cyclobutadiene ion and its derivatives to be efficient. For example, tetramethylcyclobutadiene was observed to efficiently form from the ion-molecule reaction of dimethylacetylene (DMA) and its radical cation<sup>112</sup> and oxidized tetrahedrane is observed to relax to tetra(*t*-butyl)cyclobutadiene.<sup>113</sup> Cooperative interactions in acetylene clusters may also favour formation of the cyclobutadiene ion. A good test of this suggestion will be provided by observation of the primary  $C_4H_4^+$  ions in acetylene clusters. Surprisingly, not a lot of inquiries into  $C_4H_4^+$  ions produced from acetylene clusters have been made.

Here we report the first ion mobility experiments and theoretical studies aimed at elucidating the identity of the acetylene dimer and trimer ions;  $(C_2H_2)_2^+$  and  $(C_2H_2)_3^+$  respectively. Evidence for the likely formation of the cyclobutadiene/1-buten-3-yne radical cation mixture is given. Evidence is also provided for the efficient formation of benzene ions within acetylene clusters. We employ a combination of mass-selected ion mobility, collisional induced dissociation (CID), and theoretical calculations to provide the most conclusive evidence for the formation of cyclobutadiene and benzene ions from the largest ever reported, ionized acetylene clusters. Our approach requires a comparison of the average collision cross section calculated for likely geometries to that measured from experiments. We employed density functional theory (DFT)<sup>114</sup> in the determination of lowest-energy structures of the  $C_4H_4^+$  and  $C_6H_6^+$  potential energy surface (PES).

## 4.2 Experimental Section

Details of the experimental setup, the ion mobility measurement technique, and structure determination were discussed in sections 2.5, 3.1, and 3.2 respectively. Dissociation experiments were performed by one of two techniques: by increasing ion injection energy or by use of very low water vapor pressure ( $\sim 0.018$  Torr) in collision induced dissociation (CID) of injected clusters. Acetylene clusters were generated by supersonic expansion of a 2% acetylene/helium mixture (He  $\sim 4$  atm). The mixture was passed through dry-ice and moisture traps to diminish water vapor and acetone impurities. Acetone is used as a stabilizing agent for pressurized acetylene. Typical ionizer electron-energies ranged from 40-80 eV. The mass spectrum of acetylene clusters was generated using the STOF-QMS system described in section 2.6.

## 4.3 Theoretical Section

Geometries and relative energies for a number of interesting isomers of the empirical formulas  $C_4H_4^+$  and  $C_6H_6^+$  were calculated using the unrestricted Perdew, Burke, and Enzerhof exchange and correlation functional (UPBEPBE) and the augmented correlation-consistent polarized valence double  $\zeta$  basis set (aug-cc-pVDZ) of Dunning *et al.*<sup>115-119</sup> The aug-cc-pVDZ basis is a  $5s2p/3s2p$  set for H, and a  $10s5p2d/4s3p2d$  set for C. Likely geometry candidates for both the dimer and trimer ions were derived by one of two methods, (i) all known  $C_4H_4^+$  and  $C_6H_6^+$  isomers were obtained from scientific databases such as NIST<sup>120</sup> and Sci-Finder<sup>121</sup> (b) an electron was removed from the optimized neutral cluster which was then allowed to relax unconstrained. All geometry optimizations were

followed by vibrational frequency calculations to confirm all minimums on the relevant potential energy surface. All relative energies were zero point energy (ZPE) corrected. No basis set superposition error (BSSE) was performed on the loose complexes. The Gaussian03 suite of programs was utilized here.<sup>122</sup>

#### 4.4 Results and Discussion

Figure 19 displays a typical mass spectrum obtained by 46 eV EI ionization of neutral acetylene clusters formed by supersonic expansion. The distribution of the cluster ions formed reveals some striking features corresponding to the enhanced intensities (magic numbers) for the  $(\text{C}_2\text{H}_2)_n^+$  ions with  $n = 3, 6, 14, 33, 36,$  and  $54-56$ . The strong magic number at  $n = 3$  is consistent with previous work and suggests the formation of a stable  $\text{C}_6\text{H}_6^+$  ion in an exothermic process that can lead to extensive evaporation of neutral acetylene molecules from the cluster.<sup>24-27</sup> Following EI ionization, energy transfer to the low-frequency cluster modes leads to evaporation which is the primary process of excess energy dissipation after covalent reactions. This results in the emergence of enhanced intensities for some cluster ions reflecting structural stability or reduce evaporation (kinetic bottleneck).<sup>45</sup> The depletion of the ion intensity for the  $n = 4$  and  $5$  clusters is a direct manifestation of the exothermic isomerization process coupled with evaporative cooling to produce the  $\text{C}_6\text{H}_6^+$  covalent ion.<sup>26</sup> The other magic numbers such as  $n = 14, 33,$  etc. most likely reflect the solvation of the  $\text{C}_6\text{H}_6^+$  core ion with neutral acetylene molecules where solvent shells are formed with specific numbers of the acetylene molecules. Others have hypothesized the isomerization of the  $(\text{C}_2\text{H}_2)_{14}^+$  cluster to a covalent  $\text{C}_{28}\text{H}_{28}^+$  ion.<sup>27</sup>

#### 4.4.2 Dissociation of the Acetylene Dimer and Trimer Ions

Figure 20 displays the mass spectra of mass-selected  $(\text{C}_2\text{H}_2)_2^+$ ,  $(\text{C}_2\text{H}_2)_3^+$  and  $(\text{C}_2\text{H}_2)_4^+$  ions injected into the drift tube containing 1.5 Torr of He at 300 K using an injection energy of 12 eV (*lab*). Under these conditions, typical cluster ions show extensive fragmentation upon the ion injection process. For example, a benzene dimer cation with a significant binding energy of 18 kcal/mol shows 72% fragmentation to the benzene cation using 12 eV of injection energy.<sup>101,123</sup> In contrast, the  $(\text{C}_2\text{H}_2)_2^+$  and  $(\text{C}_2\text{H}_2)_3^+$  ions show no fragmentations upon their injections using the 12 eV injection energy consistent with the formation of stable  $\text{C}_4\text{H}_4^+$  and  $\text{C}_6\text{H}_6^+$  covalent ions, respectively. However, the  $(\text{C}_2\text{H}_2)_4^+$  cluster shows extensive fragmentation, mainly to the  $(\text{C}_2\text{H}_2)_3^+$  ion.

Given the indications that the  $(\text{C}_2\text{H}_2)_2^+$  and  $(\text{C}_2\text{H}_2)_3^+$  ions are covalent in nature, we investigated their fragmentation using high injection energy (IE) and CID experiments. Figure 21 displays the mass spectra upon injection of mass selected  $(\text{C}_2\text{H}_2)_2^+$  ions into the drift cell containing 0.22 Torr of He using various IEs. The observed fragments using a 53 eV injection energy are  $\text{C}_4\text{H}_4^+$ ,  $\text{C}_4\text{H}_3^+$ ,  $\text{C}_4\text{H}_2^+$ ,  $\text{C}_4\text{H}^+$ ,  $\text{C}_3\text{H}_3^+$ ,  $\text{C}_2\text{H}_5^+$ ,  $\text{C}_2\text{H}_3^+$ ,  $\text{C}_2\text{H}_2^+$ , and  $\text{C}_2\text{H}^+$  corresponding to  $m/z$  values of 52, 51, 50, 49, 39, 29, 27, 26, and 25 respectively. Though the resolution of the dimer mass spectra only permits qualitative conclusions, it is obvious that the observed fragments are in agreement with previous collision activated (CA) spectra of  $\text{C}_4\text{H}_4^+$  radical cation generated from different precursor molecules.<sup>107</sup> The

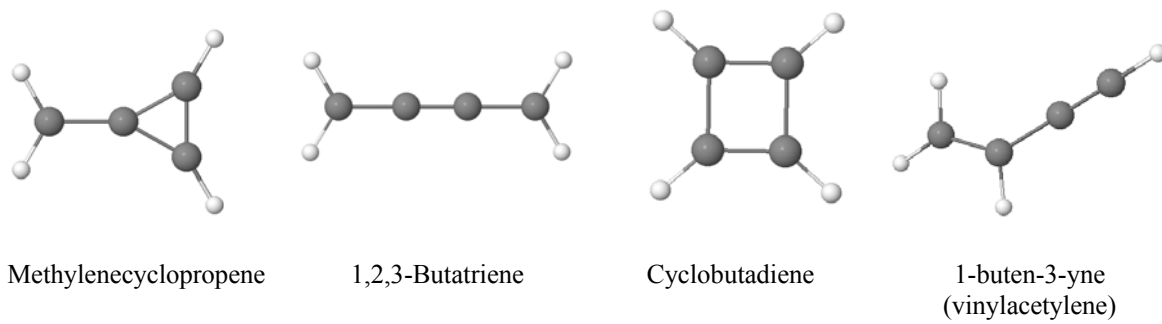


Figure 18: Structures of the experimentally observed  $C_4H_4^+$  isomers

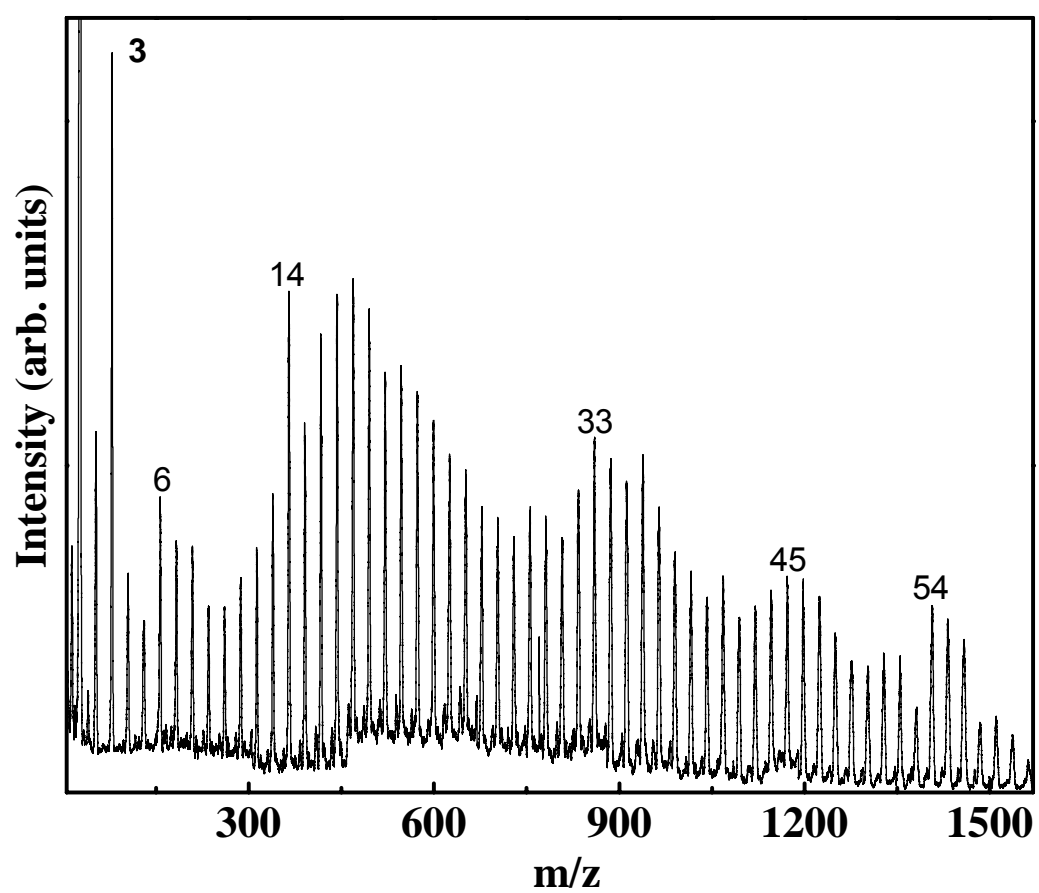


Figure 19: Mass spectrum of EI ionized (46eV) acetylene clusters in a vacuum.

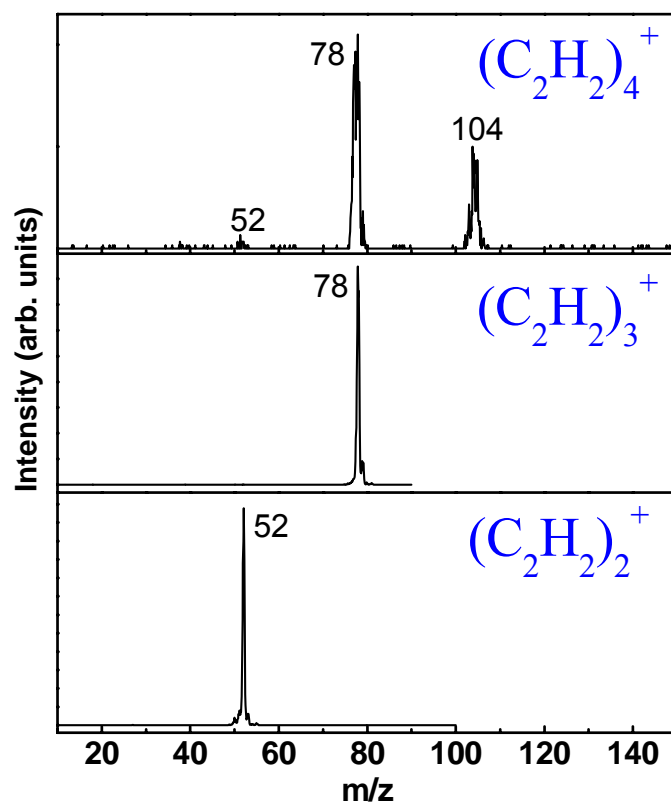


Figure 20: Mass spectrum of mass selected dimer, trimer, and tetramer acetylene clusters injected into the drift cell at 300 K, with injection energy of 12 eV, and cell pressure of 1.5 Torr He.

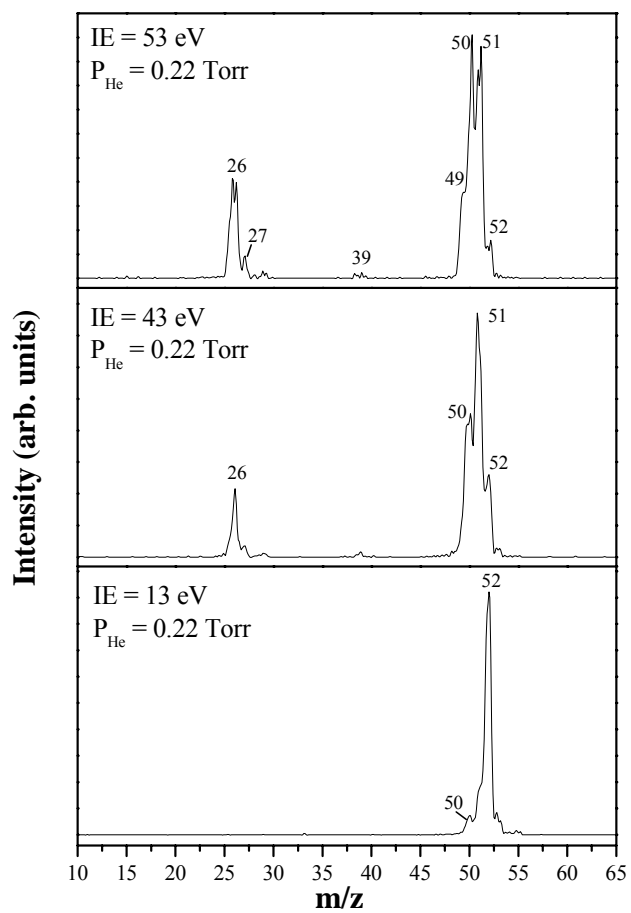


Figure 21: Dissociation pattern resulting from injection of mass selected  $(\text{C}_2\text{H}_2)_2^+$  into the drift cell containing 0.22 Torr of helium at 298 K using different injection energies.



obvious question thus pertains to the true identity of the  $\text{C}_4\text{H}_4^+$  cation generated by ionized acetylene clusters. Figure 22 displays the mass spectra upon injection of mass selected  $(\text{C}_2\text{H}_2)_3^+$  ions into 0.4 Torr He (b and c) as well as CID mass spectra (a) obtained from injection of the trimer ion into 0.018 Torr of water vapor. Using an IE of 62 eV (Figure 22c), the observed fragments from the  $(\text{C}_2\text{H}_2)_3^+$  ion are  $\text{C}_6\text{H}_5^+$ ,  $\text{C}_6\text{H}_4^+$ ,  $\text{C}_4\text{H}_4^+$ ,  $\text{C}_4\text{H}_3^+$ ,  $\text{C}_4\text{H}_2^+$ , and  $\text{C}_3\text{H}_3^+$  corresponding to  $m/z$  of 77, 76, 52, 51, 50, and 39, respectively. The origin of the  $\text{C}_3\text{H}_3^+$  fragment is interesting since, unlike the  $\text{C}_4\text{H}_3^+$  and  $\text{C}_4\text{H}_2^+$  fragments, the  $\text{C}_3\text{H}_3^+$  ion is not produced by any of the known ion-molecule reactions of acetylene.<sup>24,124</sup> All the observed fragment ions from  $(\text{C}_2\text{H}_2)_3^+$  are identical to the major fragment ions resulting from the unimolecular decomposition of the benzene ion.<sup>24</sup> In Figure 23, we compared the mass spectra obtained in Figure 22c to EI ionization (70 eV) mass spectra of benzene reported in the NIST data base.<sup>120</sup> All the observed fragment ions from  $(\text{C}_2\text{H}_2)_3^+$  are identical to the major fragment ions resulting from the EI ionization of the benzene ion, thus providing evidence for the structure of the  $(\text{C}_2\text{H}_2)_3^+$  ion. However, this result does not provide conclusive evidence for the formation of a benzene cation since identical CID spectra do not necessarily mean identical ion structures. In fact, it is well-known that the CID spectra of the benzene cation and its acyclic isomers such as 1,5-hexadiyne, 2,4-hexadiyne, and 1,3-hexadiyne ions are essentially identical.<sup>125,126</sup>

#### 4.4.3 DFT Structures of Neutral Acetylene Dimer and Trimer Clusters

As a prelude to the discussion of predicted dimer and trimer ion geometries, we briefly discuss predicted structures for the neutral dimer and trimer clusters. Shown in

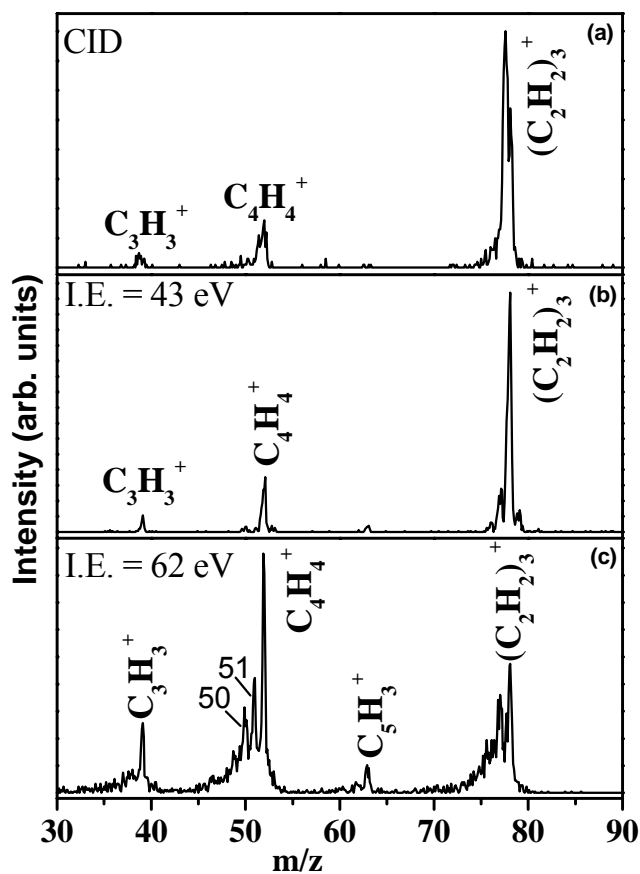


Figure 22: (a) CID spectrum of the mass-selected  $(\text{C}_2\text{H}_2)_3^+$  ions using water vapor at 0.018 Torr as a collision gas. (b) and (c): Mass spectra obtained following the injection of the mass-selected  $(\text{C}_2\text{H}_2)_3^+$  ions into the drift tube containing 0.4 Torr He at 300 K using 43 and 62 eV injection energies. The observed fragments at m/z 77, 63, 52, 51, 50, 39, and 26 correspond to the  $\text{C}_6\text{H}_5^+$ ,  $\text{C}_5\text{H}_3^+$ ,  $\text{C}_4\text{H}_4^+$ ,  $\text{C}_4\text{H}_3^+$ ,  $\text{C}_4\text{H}_2^+$ ,  $\text{C}_3\text{H}_3^+$ , and  $\text{C}_2\text{H}_2^+$  ions are identical to the EI fragmentation of the benzene ion.

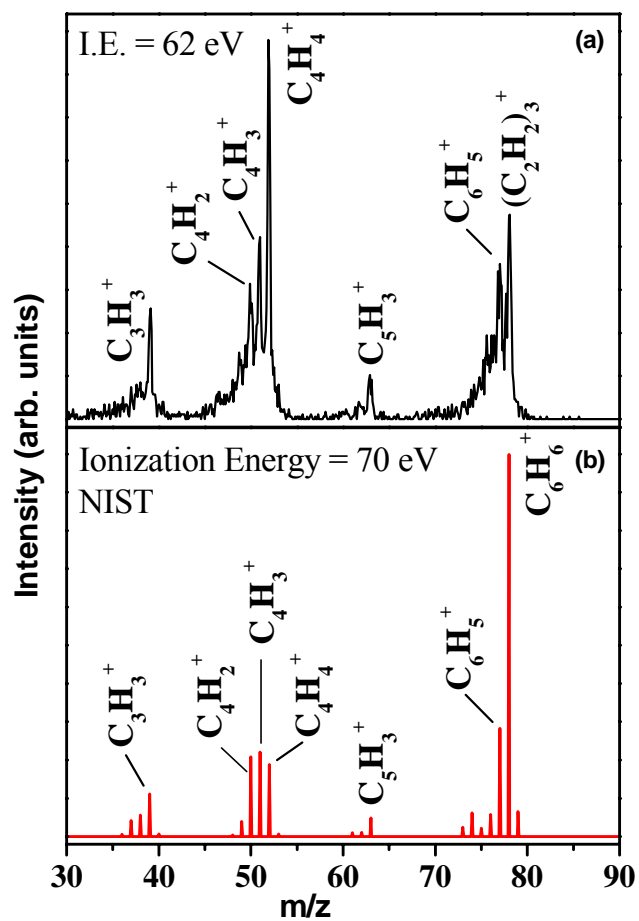


Figure 23: Mass spectra obtained following the injection of mass-selected  $(C_2H_2)_3^+$  ions into the drift cell containing 0.4 Torr He at 300 K using injection energy of 62 eV (*lab*). (b) Electron impact (70 eV) mass of the benzene ion obtained from the NIST database.<sup>120</sup>

Figure 24 are the DFT predicted geometries for the neutral  $(C_2H_2)_2$  and  $(C_2H_2)_3$  clusters. The dimer cluster is predicted to possess a T-shaped structure with  $C_{2v}$  symmetry. The predicted C-C and C-H bond lengths for the neutral dimer cluster are 1.21 Å and 1.07 Å respectively in excellent agreement with previous values of 1.21 Å and 1.07 Å respectively.<sup>111</sup> The neutral trimer is predicted to possess a planar triangular structure with  $C_{3h}$  symmetry in which an H atom from each acetylene moiety interacts with the  $\pi$ -electron density of the neighboring acetylene molecule. C-C and C-H bond lengths for the trimer cluster are 1.19 Å and 1.06 Å respectively, also in excellent agreement with previous values of 1.19 Å and 1.06 Å respectively.<sup>127</sup> Clearly, both cluster conformations favor the weak CH/ $\pi$  interaction with maximization of this interaction in the  $(C_2H_2)_3$  cluster. The slipped conformation (Figure 24c), which maximizes CH/ $\pi$  interaction for the  $(C_2H_2)_2$  cluster is predicted to be a transition state with the imaginary frequency motions/vectors in the direction of reestablishing the T-configuration. Indeed, previous experimental investigation of the neutral dimer cluster concluded the slipped conformation is a transition state for a swift tunneling automerization of the T-structure.<sup>128</sup> ZPE corrected binding energy for the T-structure is 1.7 kcal/mol which is higher than the experimental value of 0.7 kcal/mol.<sup>44</sup> The disagreement in binding energies here is perhaps due to an inadequate description of the  $\pi$ -electron densities and weak H/ $\pi$  interaction of the acetylene moieties by DFT. Previous investigations suggests the acetylene CH/ $\pi$  binding interaction to be predominantly of an acid/base type interaction rather than dispersive interactions due to a lack of dependence of the predicted structure on electron correlation correction and diffuse

functions.<sup>111</sup> The acetylene monomer geometry is also shown with C-C and C-H bond lengths of 1.21 Å and 1.07 Å respectively (Figure 24a).

#### 4.4.4 DFT Structures of the Acetylene Dimer and Trimer Cations

As stated above, initial geometries of the  $C_4H_4^+$  and  $C_6H_6^+$  ions were obtained from a database search. Also, the predicted structures for the neutral dimer and trimer ( $C_4H_4$  and  $C_6H_6$ ) were used as initial structures for the respective ion ( $C_4H_4^+$  and  $C_6H_6^+$  respectively) geometry optimization. Figure 25 and Figure 26 displays the predicted geometries for the dimer and trimer ions respectively. Also included are the predicted relative energies as well as calculated collision integral,  $\Omega$ , for all isomers. The optimized geometry of the monomer cation is similar to that obtained for the neutral with slightly elongated bond lengths. The C-C bond length is 1.25 Å (1.21 Å for the neutral) and the C-H bond length is 1.08 Å (1.07 Å for the neutral).

##### 4.4.4.2 DFT Structures of the Acetylene Dimer Cation

As expected, the most stable  $C_4H_4^+$  isomer is the methylenecyclopropene ion (**MC**,  $C_{2v}$ ). The 1,2,3-butatriene ion (**OB**,  $D_2$ ) is the second most stable with a relative energy of 12.17 kJ/mol. Two conformers, with planar (**CBD**,  $D_{2h}$ ) and rhombic (**CBC**,  $C_{2v}$ ) symmetries are predicted for the cyclobutadiene ion. Their relative energies to **MC** are 25.83 kJ/mol and 27.22 kJ/mol respectively. Next, is the 1-buten-3-yne ion (**VA**), predicted to be 37.82 kJ/mol less stable than **MC**. The sixth most stable  $C_4H_4^+$  isomer is the radical of methyleneallene (**CM**) and it is significantly less stable than those mentioned so far (Figure 25). This structure, as well as structures (**TM**) and (**SB**) are direct products of

relaxation of an optimized neutral dimer from which an electron had been removed. It is interesting to note that **CM** possess the same connectivity as methylenecyclopropene (**MC**) suggesting its involvement in the reaction pathway leading to **MC**. Isomer **SB**, with a relative energy of 222.94 kJ/mol, is analogous to the slipped geometry of the neutral dimer (Figure 24) but in this case, both acetylenes are covalently bound with C-C length of 1.55 Å and distorted CH bonds. Our final  $C_4H_4^+$  isomer is the bicycle-1-but-1,3-ene ion (**BB**) with a relative energy of 246.50 kJ/mol.

Interestingly, all predicted  $C_4H_4^+$  isomers are of a tight, covalent linear/branched type conformation. No ion-molecule complex of the form  $C_2H_2^+ \cdot C_2H_2$  interaction was found using the UPBEPBE/aug-cc-pVDZ method. This observation is not without precedence. Bally *et al.*<sup>111</sup> found B3LYP displayed irregular behavior in loosely bound complexes such as  $C_2H_2^+ \cdot C_2H_2$  where charge and spin localization is required. Other methods utilized, restricted open shell Hartree-Fock (ROHF), configuration interaction with single and double substitutions (CISD),<sup>129</sup> and coupled cluster calculations (CCSD(T)),<sup>111</sup> showed better charge/spin behavior. DFT was concluded to be ineffective at predicting loosely bound complexes but was acceptable for more tightly bound covalent complexes. The previously predicted  $C_2H_2^+ \cdot C_2H_2$  complex was a T-type structure (similar to the neutral) with  $C_{2v}$  symmetry with intermolecular distance of  $\sim 4$  Å.<sup>111</sup>

The relative energies of the  $C_4H_4^+$  isomers as predicted by the method used here, UPBEPBE/aug-cc-pVDZ, is in qualitative agreement with the results from UQCISD/6-31G\* calculations<sup>111</sup> but differ from the UB3LYP/6-31G\* calculation in which the 1-buten-3-yne ion (**VA**) was predicted to be more stable than the cyclobutadiene ion (**CBD**).

#### 4.4.4.3 DFT Structures of the Acetylene Trimer Cation

Figure 26 shows the name, structure, relative energies, and calculated collision cross sections,  $\Omega^{(1,1)}$ , of all optimized  $C_6H_6^+$  isomers. As expected, the benzene ion (**4.8.1**) is predicted to be the most stable  $C_6H_6^+$  isomer. Next was the fulvene ion (**4.8.2**) which is 43.31 kJ/mol less stable than **4.8.1**. Further down is the benzvalene ion (**4.8.6**) with a relative energy of 220.45 kJ/mol. The most stable linear isomer is found to be the 1,5-hexadien-5-yne ion (**4.8.4**). Its relative energy to benzene is 191.02 kJ/mol.  $C_6H_6^+$  isomers, 2,4-hexadiyne (**4.8.8**), 1,3-hexadiyne (**4.8.11**), and 1,5-hexadiyne (**4.8.14**), with dissociation products similar to that of the benzene ion<sup>24</sup> (as discussed above) are found to have relative energies of 230.57 kJ/mol, 311.53 kJ/mol, and 390.95 kJ/mol respectively. The cyclopropanetrismethylene ion (**4.8.10**) is the least stable cyclic ion with a relative energy of 305.63 kJ/mol. The least stable of all the  $C_6H_6^+$  isomers is structure C (**4.8.17**), an ion-molecule complex with a relative energy of 577.22 kJ/mol. As shown in Figure 27, predicted geometries for the  $C_6H_6^+$  ion can be grouped into three categories namely, covalent cyclic, covalent linear and branched, and ion-molecule complexes with a majority of the predicted structures falling under the former two categories.

#### 4.4.5 Mobilities of the Acetylene Dimer and Trimer Cations

To more conclusively determine the structure of the  $(C_2H_2)_2^+$  and  $(C_2H_2)_3^+$  ions, we measured the reduced mobility ( $K_0$ ) of the respective mass-selected ions. Mobility can provide direct structural characterizations of these ions on the basis of their collision integrals which depend on their geometric shapes.<sup>5,6</sup> This is, of course, a better criterion for

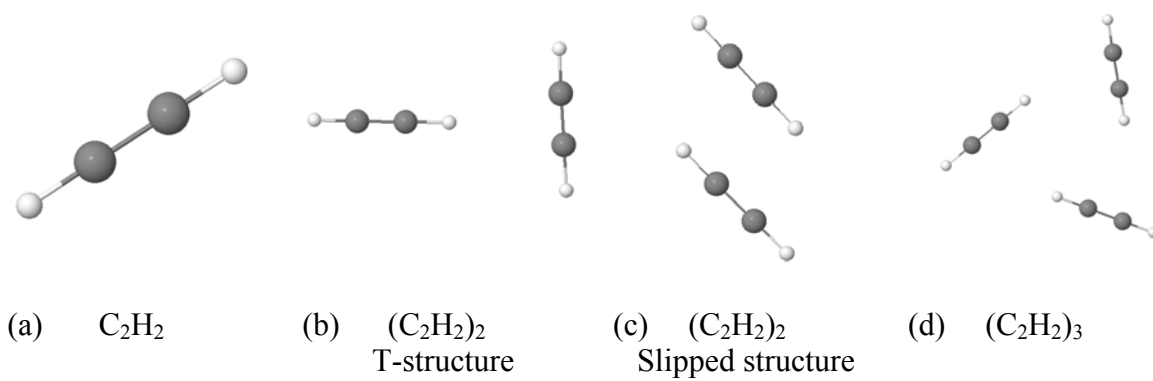


Figure 24: DFT predicted geometries for the neutral  $C_2H_2$ ,  $(C_2H_2)_2$  and  $(C_2H_2)_3$  clusters



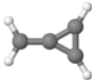
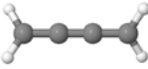
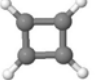
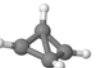
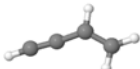
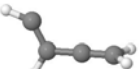
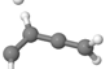
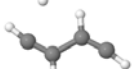
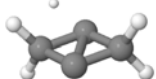
	Name	Optimized Structures	Rel. Energy (kJ/mol)	$\Omega$ ( $\text{\AA}^2$ ) <sub>calculated</sub>
MC	Methylenecyclopropene		0	39.99
OB	1,2,3-butatriene		12.17	41.10
CBD	Cyclobutadiene(D <sub>2</sub> H)		25.83	38.64
CBC	Cyclobutadiene(C <sub>2</sub> V)		27.22	38.45
VA	1-buten-3-yne		37.82	41.08
CM	cisMA		138.08	41.04
TM	transMA (16)		138.56	41.05
SB	Structure B(32)		222.94	41.06
BB	Bicyclo-1-but-1,3-ene		246.50	38.63

Figure 25: Relative total energies (DFT / UPBEPBE/aug-cc-pVDZ relative to the energy of the methylenecyclopropene ion), structures and calculated collision integrals ( $\Omega$ ,  $\text{\AA}^2$ ) of the  $\text{C}_4\text{H}_4^+$  isomers. The collision integrals in helium at 300 K are calculated using the trajectory method.<sup>94</sup>

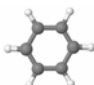
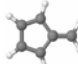
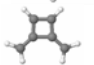
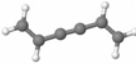
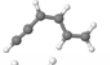
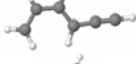
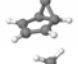
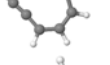
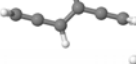
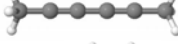
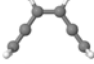

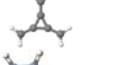

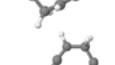
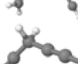
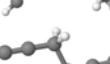
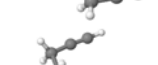
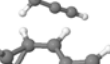
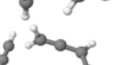
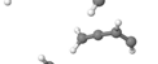

Name	Optimized Structures	Rel. Energy (kJ/mol)	$\Omega(\text{\AA}^2)_{\text{calculated}}$
Benzene		0	46.588
Fulvene		43.31	47.649
3,4-dimethylenecyclobut-1-ene		190.72	49.297
1,5-hexadien-3-yne		191.02	52.41
Z-1,3-hexadien-5-yne		200.26	51.31
1,3-hexadien-5-yne		209.81	51.41
Benzvalene		220.45	46.229
Z,Z-1,3-hexadien-5-yne		222.13	50.33
1,2,4,5-hexatetraene		223.50	52.29
2,4-hexadiyne		230.57	52.704
Z-1,2,4,5-hexatetraene		231.20	51.87
Bicyclo[2.2.0]hexa-2,5-diene		269.41	46.101
Cyclopropanetrismethylene		305.63	51.591
1,3-hexadiyne		311.53	52.87
Hexa-1,2-diene-5-yne		327.05	52.097
Cis-hexa-1,2-dien-5-yne		332.82	51.930
1,4-hexadiyne		347.38	52.822
1,5-hexadiyne		390.95	52.51
Cis-1,5-hexadiyne		403.29	49.55
Structure A		413.04	54.164
Structure B		577.22	62.960
Structure C		577.22	57.319

Figure 26: Relative total energies (DFT / UPBEPBE/aug-cc-pVDZ relative to the energy of the benzene ion), structures and calculated collision integrals ( $\Omega$ ,  $\text{\AA}^2$ ) of the  $\text{C}_6\text{H}_6^+$  isomers. The collision integrals in helium at 300 K are calculated using the trajectory method.<sup>94</sup>

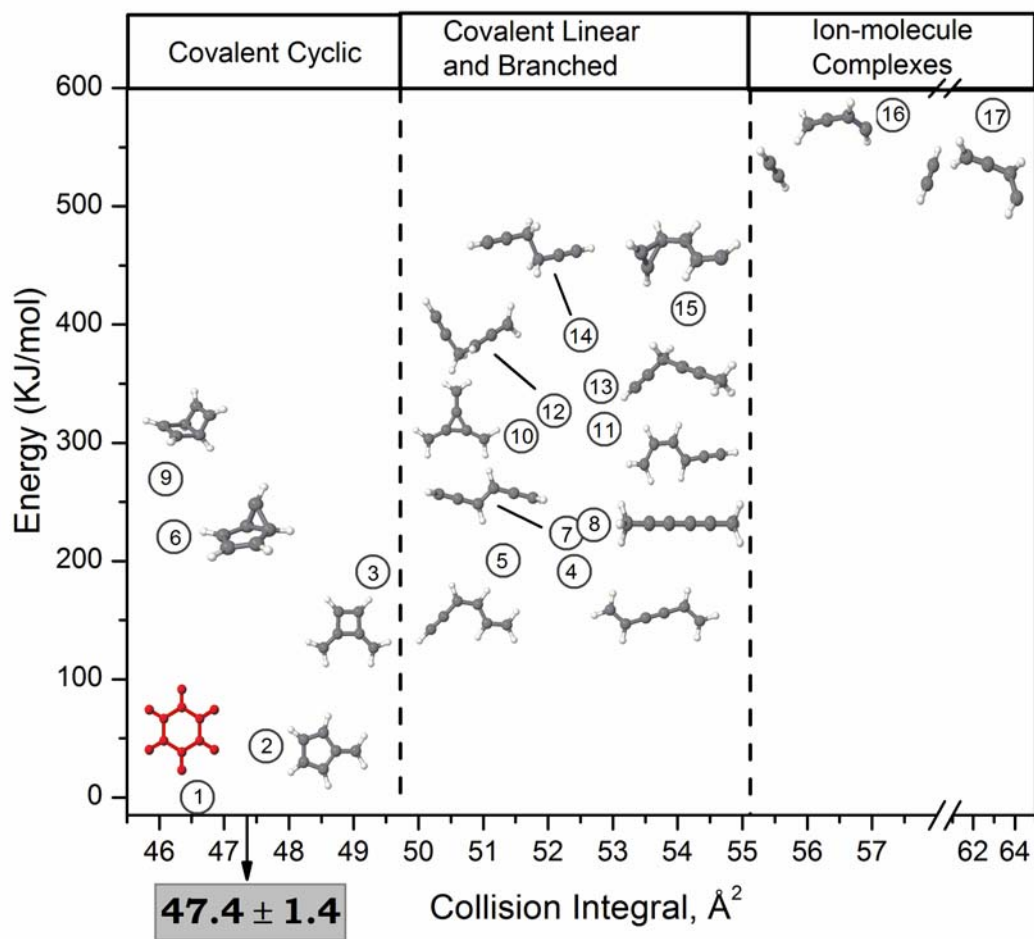


Figure 27: Relative energies and collision integrals of the  $C_6H_6^+$  isomers

judging the structures of ions that have similar CID spectra as is the case for the dimer and trimer cations. Before discussing the mobility results of the  $(\text{C}_2\text{H}_2)_2^+$  and  $(\text{C}_2\text{H}_2)_3^+$  ions, we describe the results for the monomer,  $\text{C}_2\text{H}_2^+$ , ion.

Shown in Figure 28 is a typical (open circles) arrival time distribution (ATD) for mass selected acetylene monomer ions injected into a cell containing helium (2.1 Torr) at 300 K with injection energy of 12 eV (*lab*) and a 50  $\mu\text{s}$  gate pulse. The inset in Figure 28 shows a plot of mean arrival time ( $t_d$ ) versus  $P/V$  used to obtain the reduced mobility of the  $\text{C}_2\text{H}_2^+$  ion. The excellent linear fitting of this plot indicates that our measurements were carried out under low drift field conditions ( $\leq 6$  Td) where ion kinetic energy is principally thermal; a condition necessary for most assumptions made in this experiment.<sup>52</sup> The measured  $\text{C}_2\text{H}_2^+$  reduced mobility,  $K_0$ , at 303 K is  $19.02 \pm 0.3 \text{ cm}^2\text{V}^{-1}\text{s}^{-1}$ . The ATD of injected ions was calculated for finite packet of ions,  $\phi(t)$ , exiting a cylindrical drift tube through an aperture area ( $a$ ) of  $78.5 \mu\text{m}^2$  using the transport equation given in section 3.1 and again here

$$\phi(t) = \frac{sa e^{-\alpha t}}{4\sqrt{\pi D_L t}} \left( v_d + \frac{z}{t} \right) \left( 1 - \exp\left(-\frac{r}{4D_L t}\right) \right) \exp\left(-\frac{(z - v_d t)^2}{4D_L t}\right) \quad (3.7)$$

where  $r$  and  $s$  represent the radius and surface density of a thin disk of injected ions respectively with the latter used as a scaling factor,  $z$  is the length of the drift cell, and  $\alpha$ , the reaction frequency set to zero. As displayed in Figure 28, comparison of both experimental (open circles) and calculated (solid line) ion distribution show an excellent fit indicating (a) only one  $\text{C}_2\text{H}_2^+$  isomer is produced in our cluster beam (b) existence of two or more isomers with similar collision cross sections,  $\Omega$ , or (c) existence of rapidly inter-

converting isomers. For the acetylene monomer ions, the former (a), is the most likely. A good fit also indicates use of reasonable injection energy (IE) as to prevent dissociation within the drift cell and/or extended ion penetration into the cell before thermalization by the buffer gas.

A corresponding average collision cross section,  $\Omega^{(1,1)}$ , of the monomer ( $\text{C}_2\text{H}_2^+$ ) ions with helium buffer gas was calculated according to the kinetic theory equation given in Section 3.2 and again here

$$K = \frac{3qe}{16N} \left( \frac{2\pi}{k_B T_{eff}} \right)^{\frac{1}{2}} \left( \frac{M_i + M_b}{M_i M_b} \right)^{\frac{1}{2}} \frac{1}{\Omega_{avg}^{(1,1)}} \quad (3.12)$$

where  $qe$  is the ion charge,  $N$ , the number density of the buffer gas,  $T_{eff}$ , the effective temperature,  $M_i$  and  $M_b$  are the masses of the ion and buffer gas respectively, and  $\Omega_{avg}^{(1,1)}$  is the orientationally averaged collision integral. The corresponding  $\text{C}_2\text{H}_2^+$  average collision cross section for the measured  $K_0$  of  $19.02 \pm 0.3 \text{ cm}^2\text{V}^{-1}\text{s}^{-1}$  at 303 K is  $30.2 \pm 1.4 \text{ \AA}^2$  which is in excellent agreement with that calculated using the trajectory method,  $30.3 \text{ \AA}^2$ .<sup>94</sup> This indicates the acetylene monomer cation ( $\text{C}_2\text{H}_2^+$ ) possesses a structure similar to that predicted by DFT.

#### 4.4.5.2 Mobility of the Acetylene Dimer Cation

Figure 29 displays typical ATDs of mass selected  $\text{C}_2\text{H}_2^+$ ,  $(\text{C}_2\text{H}_2)_2^+$ , and  $(\text{C}_2\text{H}_2)_3^+$  ions. As shown and discussed below, the ATD of the dimer ion is analyzed in terms of two structural isomers. Shown in Figure 30 is the experimental ATD for the  $(\text{C}_2\text{H}_2)_2^+$  ions injected into the cell at 5.0 Torr He pressure. At first glance, the seemingly unperturbed

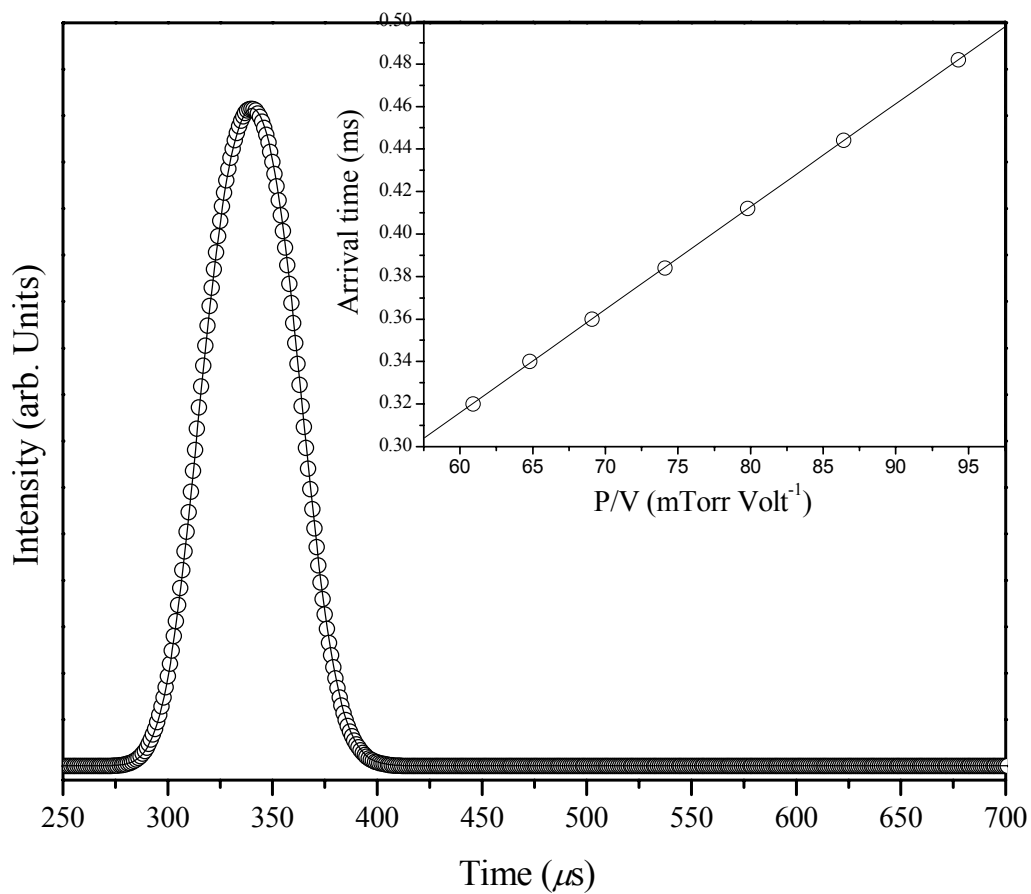


Figure 28: Comparison between the measured ATD of the mass-selected acetylene monomer ion with that predicted by transport theory. The inset shows the linear plot of arrival time ( $t_d$ ) vs.  $P/V$  used to calculate the mobility.

Gaussian distribution suggest the presence of only one  $\text{C}_4\text{H}_4^+$  isomer but as shown in Figure 31, a comparison of the ATD (open circles) to that predicted by transport theory (solid line) show a bad fit. The experimental ATD is considerably broader than that calculated using the transport equation (equation 3.7) suggesting the existence of more than one  $\text{C}_4\text{H}_4^+$  isomer in our beam. The use of very high injection energy may also cause a bad fit due to the possibility of cluster dissociation inside the drift cell. Cluster dissociation is not likely the cause of ATD broadening because (1) dissociation experiments showed no fragmentation (Figure 21) at the injection energy utilized, 12 eV and (2) no obvious tailing was observed for the ATD at long residence times. If dissociation of the dimer cluster occurred in the drift cell, an increase in the ion residence time will result in significant tailing of the ATD. The broadened ATD indicates that the collision cross sections of the  $\text{C}_4\text{H}_4^+$  isomers present are not sufficiently different to resolve their ATDs in our drift cell. Resolution of isomers is governed by the rate of diffusion of the drifting ion-packet.<sup>130</sup> If the difference in mobilities of the isomers is smaller than the diffusion rate of the ion-packet, the isomers will not be resolved. Our drift cell resolution is 20 which means isomers with less than 5% difference in collision cross section cannot be resolved.

Based on previous experiments<sup>26,44,102,103,105-110</sup> and the DFT predicted  $\text{C}_4\text{H}_4^+$  geometries discussed above, four candidate isomers are possible here. As shown in Figure 25, they include methylenecyclopropene (**MC**), 1,2,3-butatriene (**OB**), cyclobutadiene (**CB**), and 1-buten-3-yne (**VA**). Though a combination of more than two of the suspect  $\text{C}_4\text{H}_4^+$  isomers is possible, the majority of previous experiments reported the co-existence of only two isomers. To investigate the identities of  $\text{C}_4\text{H}_4^+$  isomers in our beam, the



calculated structures were used to obtain average collision cross sections (Figure 25) and mobilities using the trajectory calculations.<sup>94</sup> Also, hypothetical relative concentrations of all combinations of isomer pairs were fitted to the experimental ATD using transport theory (equation 3.7). For example, (**MC**) and (**CB**) at different relative concentrations (90:10, 40:60, 75:25 etc) are fitted to the experimental ATD. Of all six  $C_4H_4^+$  isomer combinations, only a mixture of the cyclobutadiene and 1-buten-3-yne (vinylacetylene) ions with a ratio of  $\approx 62:38$  gave a good fit as shown in Figure 32. The variation in ATD with changing cell voltage is shown in Figure 33. This result indicates that the measured reduced mobility,  $K_0$ , using the mean arrival time,  $t_d$ , obtained from the experimental ATD is an average of both the cyclobutadiene and 1-buten-3-yne ion mobilities. Combinations of methylenecyclopropene, the most stable  $C_4H_4^+$  isomer, with the other suspect isomers gave bad fits. Production of the cyclobutadiene ion is the most kinetically favored of all suspect  $C_4H_4^+$  isomers as it is the only isomer that requires no H-shift from its precursor cluster ion,  $C_2H_2^+ \cdot C_2H_2$ .<sup>44,111</sup> The intracuster cyclization to produce the cyclobutadiene ion is suspected to be kinetically driven (within the time frame of this experiment) since the heat produced by dimerization of the loose  $C_2H_2^+ \cdot C_2H_2$  complex is larger than the predicted barrier for production of the methylenecyclopropene ion which is  $\approx 6$  kcal/mol more stable than the cyclobutadiene ion.<sup>44</sup> In addition, Ono and Ng described a van der Waals type well for the loose  $C_2H_2^+ \cdot C_2H_2$  ion;<sup>44</sup> which may favor a cyclobutadiene ion route on the reaction coordinate if excess energy dissipation is efficient. Efficient stabilization of the cyclobutadiene ion by evaporation of acetylene molecules in cluster mimic condensed-phase conditions where the cyclobutadiene ion formation is very

stable.<sup>112,113</sup> The same relative concentration of cyclobutadiene and 1-buten-3-yne ions was observed when higher injection energies (17 eV) were used indicating both ions are generated during the EI ionization process.

$K_0$  of the injected dimer ion was measured many times using a 20  $\mu$ s ion gate width. Figure 34 displays a plot of  $t_d$  versus  $P/V$  used in calculating the reduced mobility. The measurements yield a  $K_0$  value of  $14.2 \pm 0.4 \text{ cm}^2\text{V}^{-1}\text{s}^{-1}$  at 303 K. The uncertainty given here is  $\pm 0.2$  standard deviation in the repeated measurements. This value represents the average mobility for the cyclobutadiene and 1-buten-3-yne ions. The averaged mobility calculated using the trajectory method for a combination of the cyclobutadiene ion ( $14.3 \text{ cm}^2\text{V}^{-1}\text{s}^{-1}$ ) and 1-buten-3-yne ion ( $13.5 \text{ cm}^2\text{V}^{-1}\text{s}^{-1}$ ) at a 62:38 ratio was  $14.0 \text{ cm}^2\text{V}^{-1}\text{s}^{-1}$  which is in excellent agreement with the experimentally measured value. The corresponding experimental collision cross section of  $38.9 \pm 1.4 \text{ \AA}^2$  is also in good agreement with the averaged  $\Omega^{(1,1)}$  value of  $39.6 \text{ \AA}^2$ . A combination of experimental and calculated mobilities thus confirm the identity of the  $\text{C}_4\text{H}_4^+$  isomers produced under our experimental conditions as the cyclobutadiene and 1-buten-3-yne ions. Of course, a combination of more than two  $\text{C}_4\text{H}_4^+$  isomers remains a possibility.

#### 4.4.5.3 Mobility of the Acetylene Trimer Cation

Figure 35 shows a typical ATD peak for mass selected acetylene trimer ions (open circles) fitted with the calculated time distribution (solid line) using the transport equation. The inset shows a typical plot of  $t_d$  versus  $P/V$  used in obtaining the reduced mobility,  $K_0$ . As discussed in the previous sections, the excellent fit between measured and calculated

ion distribution indicates only one  $\text{C}_6\text{H}_6^+$  isomer may be present. Our results indicate that reduced mobility of the  $(\text{C}_2\text{H}_2)_3^+$  ions is  $11.54 \pm 0.3 \text{ cm}^2 \text{ V}^{-1} \text{ s}^{-1}$ , in excellent agreement with the value measured for the benzene cation ( $11.43 \pm 0.4 \text{ cm}^2 \text{ V}^{-1} \text{ s}^{-1}$ ).<sup>123</sup> The corresponding collision integrals at 300 K for the  $(\text{C}_2\text{H}_2)_3^+$  and the benzene ions are  $47.4 \pm 1.4 \text{ \AA}^2$  and  $47.9 \pm 1.4 \text{ \AA}^2$  respectively. For comparison with the linear isomers and other possible structures of the  $\text{C}_6\text{H}_6^+$  ions, collision integrals for candidate geometries of 17  $\text{C}_6\text{H}_6^+$  isomers were calculated using the trajectory method.<sup>94</sup>

Figure 27 displays the collision integrals ( $\Omega$ ) calculated for the  $\text{C}_6\text{H}_6^+$  isomers and their relative total energies to the benzene ion, the most stable  $\text{C}_6\text{H}_6^+$  isomer. As displayed in Figure 27, the  $\text{C}_6\text{H}_6^+$  isomers can be grouped into three distinct categories based on similarities in their collision integrals. These groups are identified as covalent cyclic, covalent linear and branched, and noncovalent ion-molecule isomers. The ions in the second and third groups, including all the acyclic isomers, have collision integrals substantially larger than the measured values for the  $(\text{C}_2\text{H}_2)_3^+$  and benzene cations. In the first group, other cyclic isomers such as fulvene, 3,4-dimethylenecyclobutene, and benzvalene have collision integrals similar to those measured for the  $(\text{C}_2\text{H}_2)_3^+$  and benzene cations within experimental uncertainty. Previous studies have found major differences in the CID spectra of the benzene cation and these cyclic isomers.<sup>131,132</sup> Specifically, the diminished intensity of the  $\text{C}_3\text{H}_3^+$  fragment ion in the CID spectra of the cyclic isomers benzvalene, 3,4-dimethylenecyclobutene, and fulvene provides a distinction from the CID spectrum of the benzene cation.<sup>131</sup> Therefore, among the cyclic isomers which have collision integrals similar to those measured for the  $(\text{C}_2\text{H}_2)_3^+$ , only the benzene cation

exhibits a fragmentation pattern (including the characteristic  $\text{C}_3\text{H}_3^+$  fragment) similar to that measured for the  $(\text{C}_2\text{H}_2)_3^+$  ion. Clearly, the combination of ion mobility and fragmentation data (Figure 23) provides conclusive evidence that the  $(\text{C}_2\text{H}_2)_3^+$  ion formed from the ionization of large neutral acetylene clusters has indeed the structure of the benzene cation. Now if  $(\text{C}_2\text{H}_2)_3^+$  is in fact the benzene ion, then it should react like the benzene ion. A comparison of the reaction of  $(\text{C}_2\text{H}_2)_3^+$  with water to previously published  $\text{C}_6\text{H}_6^+$ /water reactions will be explored in the next chapter.

#### 4.5 Infrared Determination of Cluster Ion Structures

The identities of suspect isomerization products in cluster ions can also be investigated using infrared spectroscopy.<sup>133</sup> Technological advances in the areas of gas-phase infrared spectroscopy,<sup>64,133</sup> computing speeds, as well as *ab initio*/DFT accuracy has allowed scientist to spectroscopically investigate the structures of interesting ions in the gas-phase. In such investigations, the experimentally observed vibrational stretch frequencies of certain functional groups (O-H, C-H, N-H,  $\text{C}\equiv\text{C}$ , etc) are compared to the theoretically predicted vibrational frequencies.<sup>133-137</sup> Common gas-phase IR techniques include resonance enhanced photodissociation<sup>133-135</sup> and argon-tagging, the attachment of a messenger atom/molecule to the cluster ion of interest.<sup>64</sup> The messenger molecule binds very weakly and does not significantly perturb the electronic structure of the cluster ion. Duncan *et al.* was able to determine the structures of  $\text{Ni}^+(\text{C}_2\text{H}_2)_{1-4}$  cluster ions using the latter technique.<sup>64</sup> To date, gas-phase infrared methods represent one of the most desirable ways to obtain structural information of cluster ions.

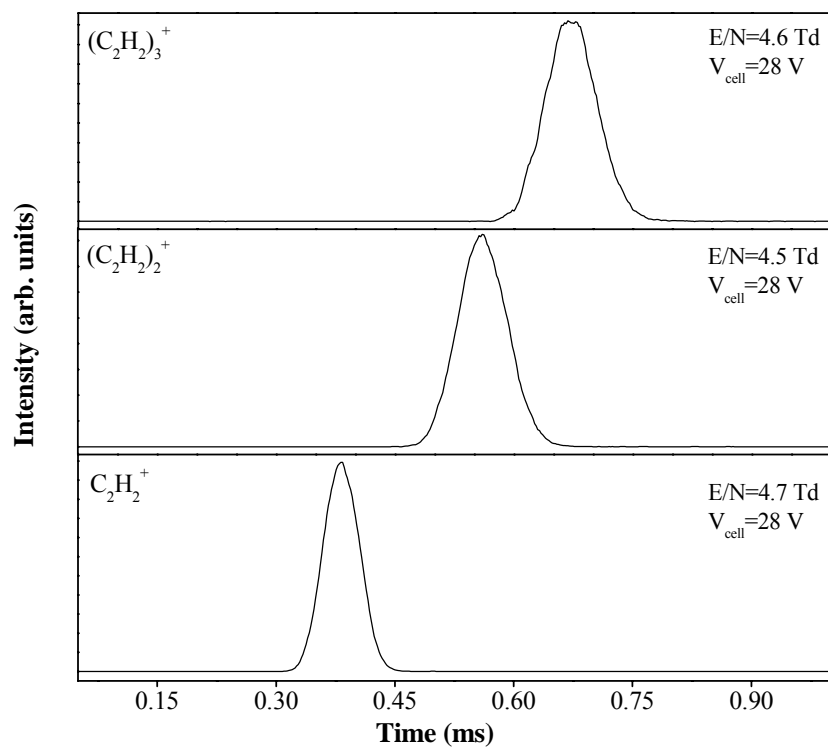


Figure 29: Measured ATDs of  $(\text{C}_2\text{H}_2)_n^+$  with  $n = 1-3$  at 300 K using approximately similar field and collision conditions ( $E/N$ ). The increasing arrival time for  $n = 1-3$  reflects the increase in collision cross section of the injected cluster from the monomer to the trimer.

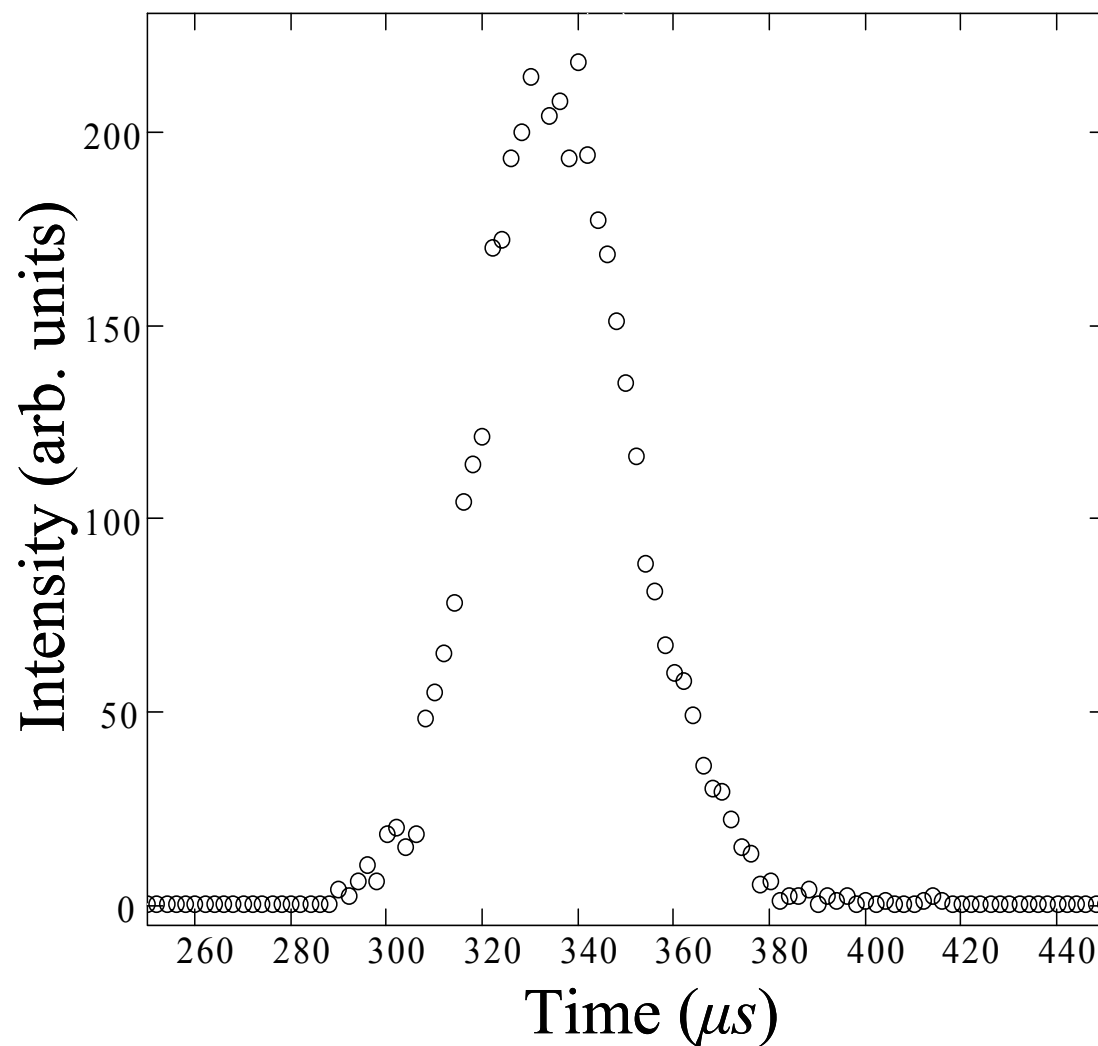


Figure 30: Arrival time distribution of mass-selected acetylene dimer clusters injected into the drift cell with 5.0 Torr helium at 300 K using injection energy of 12 eV.  $E/N = 4.37$  Td.

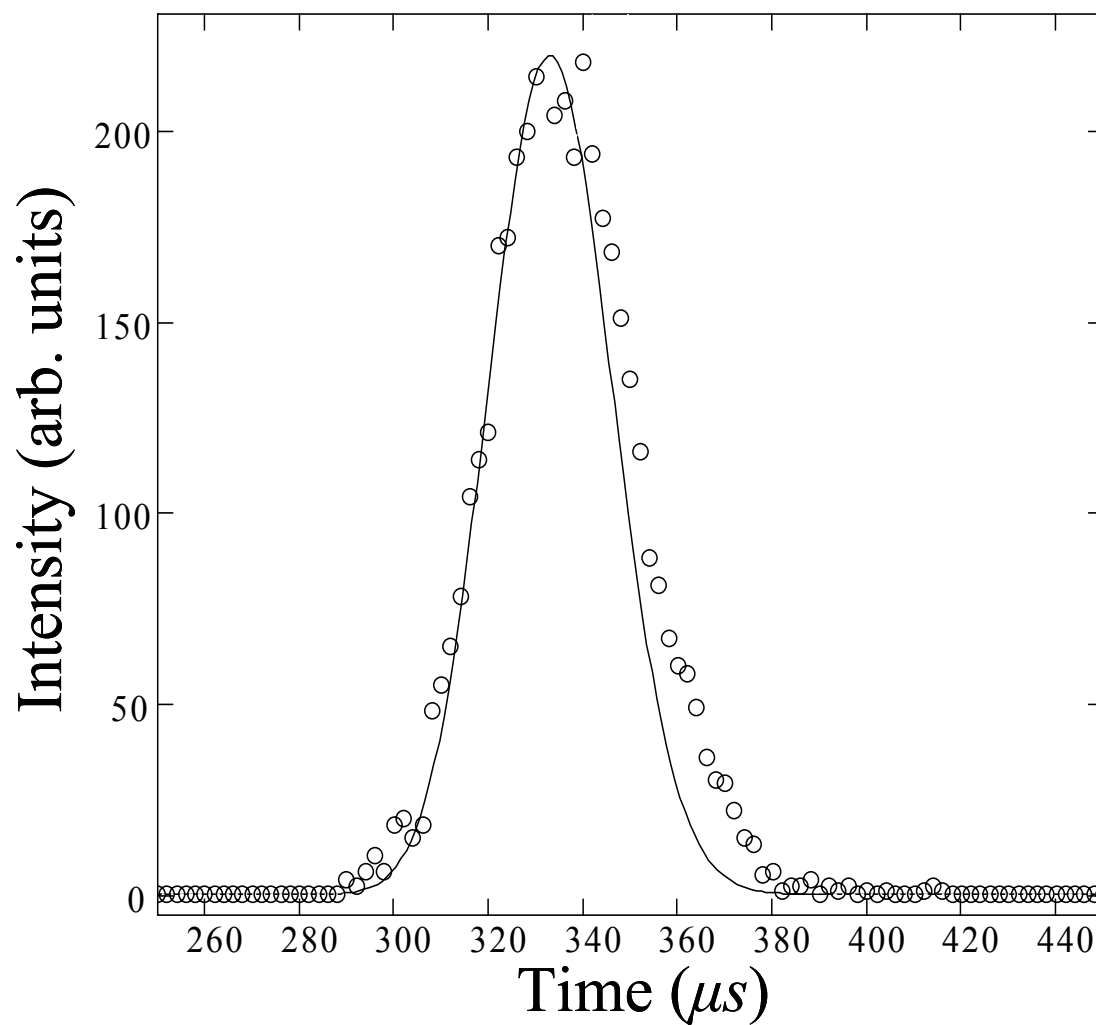


Figure 31: Comparison of experimental arrival time distribution (open circles) of mass-selected acetylene dimer clusters to the distribution predicted by the transport theory equation (solid line). The drift cell temperature and pressure were 300 K and 5.0 Torr (He) respectively and injection energy of 12 eV was utilized.  $E/N = 4.37$  Td.

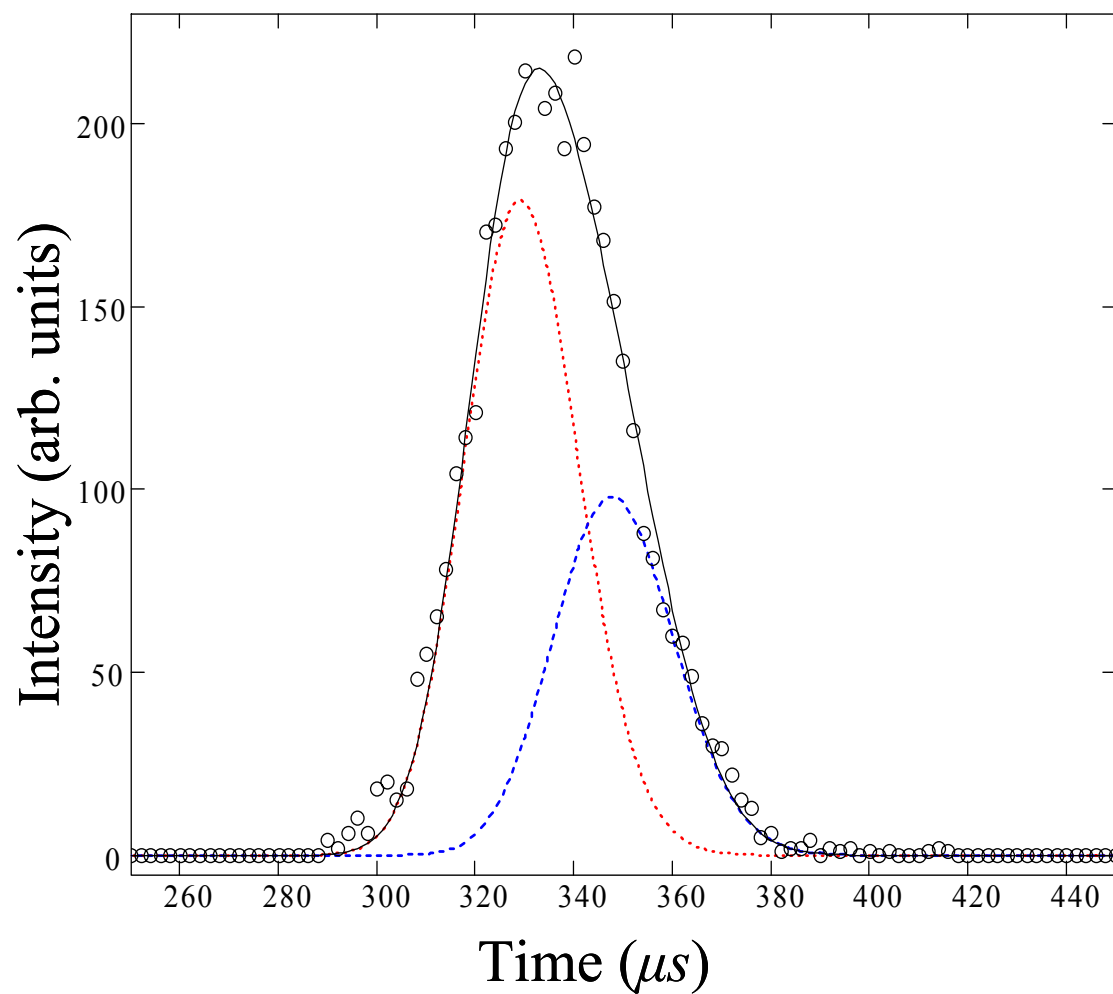


Figure 32: Arrival time distribution of injected acetylene dimer cluster fitted with distribution predicted by transport theory using a combination of two  $\text{C}_4\text{H}_4^+$  isomers, cyclobutadiene (dotted line) and vinylacetylene (dashed line), at a ratio of 62:38 respectively. Experimental condition are the same as given in Figure 29 and Figure 30.



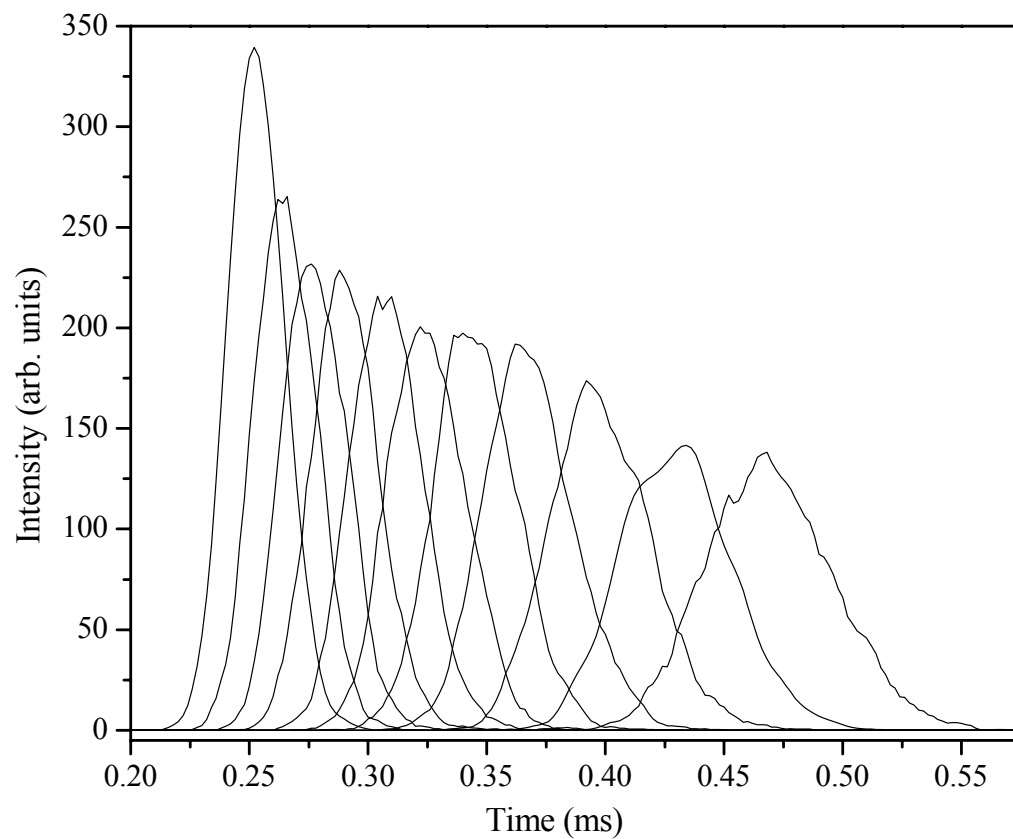


Figure 33: ATDs of the mass selected acetylene dimer ion at different drift voltages (decreasing from left to right) used in obtaining  $t_d$  for the mobility measurements.

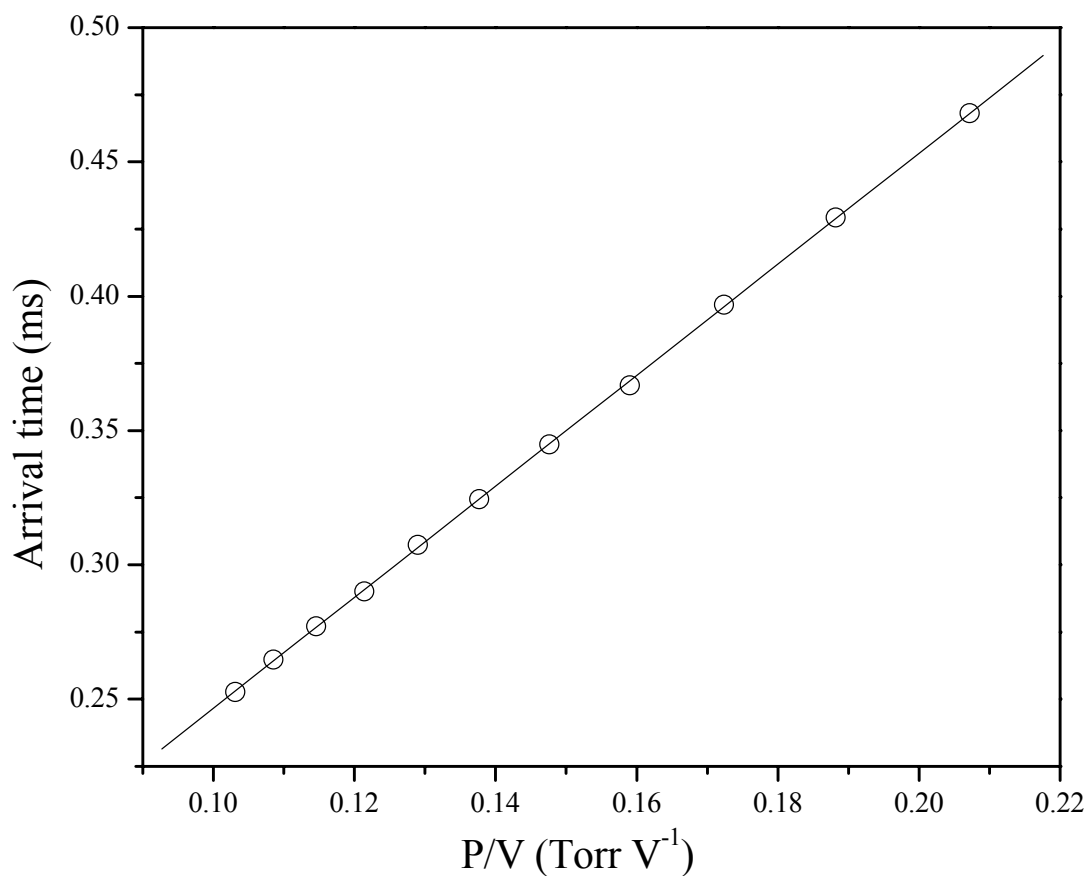


Figure 34: Plot of  $t_d$  versus  $P/V$  (open circles) used in calculating reduced mobility for mass-selected acetylene dimer ions injected into the cell. The solid line represents the linear least square fit of the plot.  $R^2$  and slope values from this fit are 0.9999 and  $2.07 \pm 0.01$  respectively; corresponding to a  $K_0$  value of  $14.2 \text{ cm}^2 \text{ V}^{-1} \text{ s}^{-1}$ . This value represents the averaged mobility of the cyclobutadiene and vinylacetylene ions determined to be present in the molecular beam.

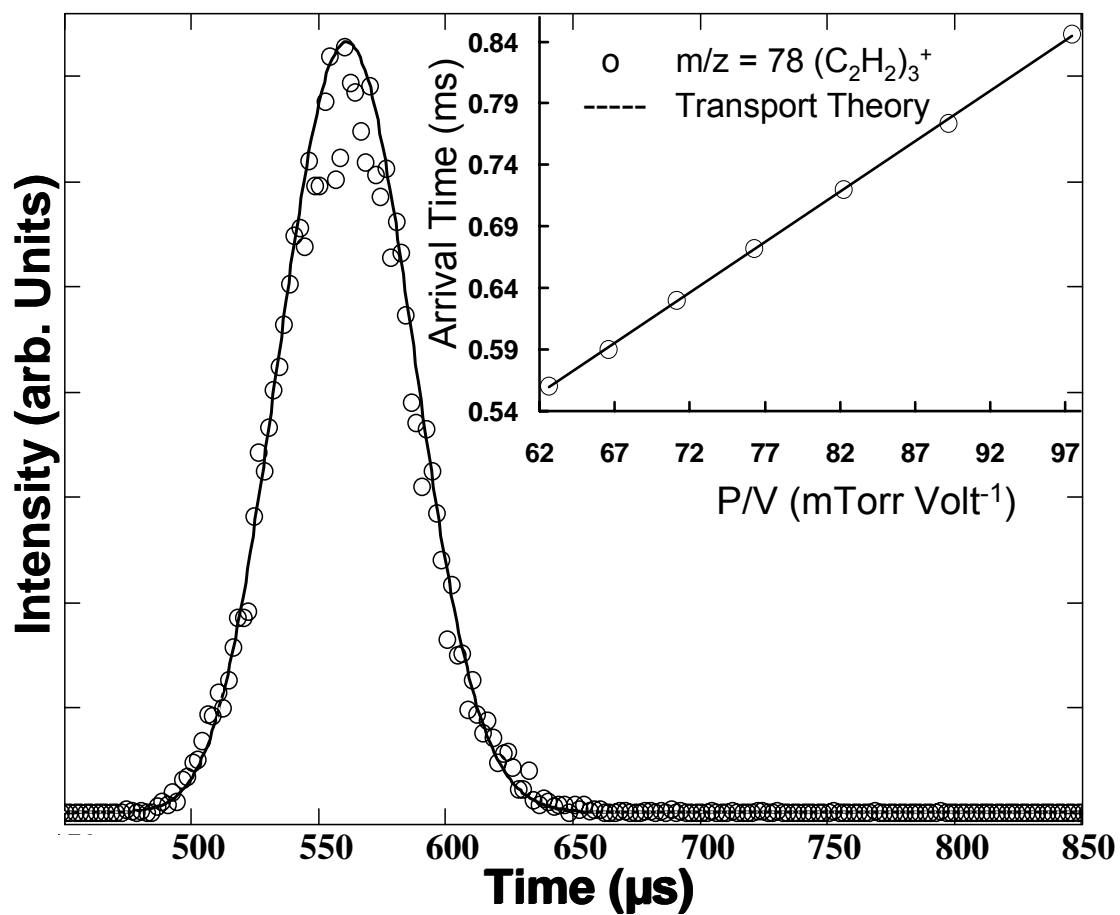


Figure 35: Comparison of the experimental ATD of the acetylene trimer ion  $(\text{C}_2\text{H}_2)_3^+$  with that predicted by the transport theory equation. The inset shows the linear plot of  $t_d$  vs.  $P/V$  used in calculating the reduced mobility.

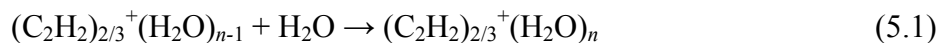
## CHAPTER 5      Reactivity of Small Acetylene Cluster Ions, $(\text{C}_2\text{H}_2)_{1-3}^+$ , with Water

### 5.1      Introduction

Acetylene, the smallest organic molecule that can be polymerized, water, arguably the most biogenic molecule, and benzene, the smallest cyclic aromatic molecule, are all present in interstellar space.<sup>1,4-11</sup> Gases in solar nebulae are subjected to ionizing radiation and unlike interstellar clouds, the relatively high gas densities in parts of the nebula can allow three-body collision processes that form synthetic adducts and clusters.<sup>6</sup> The radiation and the high velocity winds break up the carbonaceous compounds in the dust and trigger new reactions including polymerization of acetylene that can lead to the formation of benzene.<sup>1,5,10</sup>

The polymerization of ionized acetylene into benzene is significant because it may prove to be the first step in the formation of polycyclic aromatic hydrocarbons. Understanding the formation mechanisms of the benzene ions and the chemistry in which ionized acetylene and olefin molecules can cyclize to form ring structures may eventually help us understand the formation processes behind prebiotic molecules.<sup>7</sup> In Chapter 4, we reported evidence for the formation of benzene ions within gas phase ionized acetylene clusters. The results from the mass-selected ion mobility and collisional induced dissociation (CID) experiments coupled with theoretical calculations indicate that benzene ions can be formed following the ionization of neutral acetylene clusters generated by supersonic expansion.

In this chapter, we study the  $(\text{C}_2\text{H}_2)_{1-3}^+(\text{H}_2\text{O})_n$  systems using ion mobility mass spectrometry techniques. A comprehensive *ab initio* survey of ions with the compositions  $\text{C}_2\text{H}_3\text{O}^+$ ,  $\text{C}_2\text{H}_4\text{O}^+$ ,  $\text{C}_2\text{H}_3\text{O}^+(\text{H}_2\text{O})$ ,  $\text{C}_2\text{H}_4\text{O}^+\text{H}_2\text{O}$ ,  $\text{C}_4\text{H}_4^+$ ,  $\text{C}_4\text{H}_4^+\text{H}_2\text{O}$ , and  $\text{C}_4\text{H}_4^+(\text{H}_2\text{O})_2$  will be presented. Also, binding energies and association entropies for the reaction



are measured. Comparison of the stepwise hydration enthalpy and entropy changes of the acetylene trimer ion with the thermochemical data recently reported for the benzene cation<sup>138</sup> provides conclusive evidence for the isomerization of the ionized acetylene clusters to the benzene structure.

## 5.2 Ionic Reactions between $\text{C}_2\text{H}_2^+$ and $\text{H}_2\text{O}$ : The $\text{C}_2\text{H}_3\text{O}^+$ and $\text{C}_2\text{H}_4\text{O}^+$ Ions

### 5.2.1 Experimental and Computational Method

The details of the instrument have been published elsewhere,<sup>101,123</sup> and are discussed in Chapters 2 and 3. Only a brief description is given here. Acetylene ions  $\text{C}_2\text{H}_2^+$  were generated by electron impact ionization of clusters originating from supersonic expansion of an acetylene/helium mixture (2 %). The ions were mass selected by a quadrupole mass filter and transported by a series of lenses into the ion mobility cell, which was filled with pure  $\text{H}_2\text{O}$  or mixtures of  $\text{H}_2\text{O}$  and helium.

Arrival time distributions (ATDs) of the various ions were measured by monitoring the signals corresponding to each ion as a function of time after injection into the cell (residence time). Residence time was varied between 200 and 1000  $\mu\text{s}$  by changing the voltage gradient in the cell. The time-resolved studies determine if products are formed due

to high-energy injection or due to reactions in the cell, and allow the identification of primary and secondary reaction products, and the measurement of rate coefficients.

Pseudo first-order rate constant for the decay of the  $\text{C}_2\text{H}_2^{+\bullet}$  reactant ions were obtained from time-resolved experiments using the relation  $\ln I/\Sigma I = -kt$ . Correspondingly, we obtained  $k_1$  from plots of  $\ln I/\Sigma I$  vs.  $t$ , where  $I$  is the integrated intensity of the product ion peak and  $\Sigma I$  is the sum of intensities of the reactant and all product ion peaks including secondary products, and  $t$  is the mean drift time (taken as the center of the arrival time distribution) of the reactant. Second-order rate coefficients,  $k_2$ , were obtained from  $k_2 = k_1/[N]$  where  $N$  is the number density ( $\text{molecules cm}^{-3}$ ) of the neutral  $\text{H}_2\text{O}$  reactant in the cell.

Geometries and relative energies were calculated using density functional theory (DFT)<sup>114</sup> and the G3(MP2)<sup>139</sup> methods. All DFT calculations were carried out using the unrestricted Perdew, Burke and Enzerhof exchange and correlation functionals (UPBEPBE) and the augmented correlation-consistent polarized valence double zeta basis set (aug-cc-pVDZ) of Dunning *et al.*<sup>115-119</sup> The aug-cc-pVDZ basis is a  $5s2p/3s2p$  set for H, and a  $10s5p2d/4s3p2d$  set for C and O. This results in 87 basis functions for the  $\text{C}_2\text{H}_2\text{O}$  isomers, 96 basis functions for the  $\text{C}_2\text{H}_3\text{O}^+$  isomers, and 105 basis functions for the  $\text{C}_2\text{H}_4\text{O}^{+\bullet}$  isomers. For DFT calculations, all geometries were optimized and then vibrational frequencies were calculated to confirm that the geometries were indeed a minimum on the relevant potential energy surface. DFT relative energy comparisons were not zero point energy corrected. The DFT method was chosen because it is well known to be a computationally efficient way to determine accurate geometries of many systems.

Relative energies were refined using the G3(MP2) procedure. G3(MP2), a composite method for accurate energy predictions, follows HF and MP2 geometry optimizations with a sequence of high level single point energy calculations to improve total energies.<sup>139,140</sup> Average absolute deviation of G3(MP2) enthalpies from experimental values is 0.43 kcal/mol for molecules consisting of C, H, and O atoms only.<sup>140</sup> The G3(MP2) calculations were carried out at the default temperature and pressure of 298K and 1 atm respectively.

In some cases the UPBEPBE/aug-cc-pVDZ calculations and G3(MP2) calculations resulted not only in different relative energies but also in different energy orders for some of the isomers studied. For example, methyloxoniumylidene-methylene (Table 3d) is predicted by G3(MP2) to be 1.34 kcal/mol more stable than 2H-oxirenylium (3c). On the other hand, UPBEPBE/aug-cc-pVTZ predicted 3d to be 10.66 kcal/mol less stable than 3c. In such cases, the correct energetic ordering of the species was determined by calculating the electronic energies using Coupled Clusters with single and double excitations with the aug-cc-pVDZ basis set (CCSD/aug-cc-pVDZ).<sup>141</sup>

In addition, calculations were carried out for two neutral isomers of C<sub>2</sub>H<sub>2</sub>O, ketene and oxirene, in order to estimate the proton affinities (PA) for some of the C<sub>2</sub>H<sub>3</sub>O<sup>+</sup> isomers. Proton affinities of the ketene at both carbons (C<sub>α</sub> and C<sub>β</sub>) and at the oxygen were calculated using G3(MP2) energies, which are corrected for zero point energy, rotational energy and translational energy at 298 K and 1 atm pressure. We also calculated the geometry and energy of the C<sub>2</sub>H<sub>2</sub><sup>+</sup>·H<sub>2</sub>O adduct. The DFT geometries were corrected for basis set superposition error (BSSE) by the counterpoise method of Boys and Bernardi.<sup>119</sup> Finally, to gain further understanding of our experimental results, geometries and binding

energies (BE) were calculated for selected  $\text{C}_2\text{H}_4\text{O}^{+\bullet}\cdot\text{H}_2\text{O}$  and  $\text{C}_2\text{H}_3\text{O}^{+\bullet}\cdot\text{H}_2\text{O}$  ions using the G3(MP2) method. All calculations were performed using the Gaussian 03 suite of programs.<sup>122</sup> For simplicity and readability, predicted geometries will be referred to by their respective table identity. For example, isomer **2a** refers to the ethenolium cation in Table 2. For the  $\text{C}_2\text{H}_3/4\text{O}^{+\bullet}\cdot\text{H}_2\text{O}$  complexes, the same nomenclature applies with inherited identities. For example, **4-2b** represents the optimized complex obtained from the addition of a water molecule to **2b**, the acetaldehyde cation, displayed in Table 4.

## 5.2.2 Results and Discussion

### 5.2.2.1 The $\text{C}_2\text{H}_2^{+\bullet}/\text{H}_2\text{O}$ Reaction System and Proposed Mechanism

The ions observed following the injection of  $\text{C}_2\text{H}_2^{+\bullet}$  ions into  $\text{H}_2\text{O}/\text{He}$  are shown in Figure 36, and the arrival time distributions of the observed ions are given in Figure 37. The main ions are the remaining unreacted  $\text{C}_2\text{H}_2^{+\bullet}$  ions ( $m/z = 26$ ) exiting the cell; the  $\text{C}_2\text{H}_3\text{O}^+$  product ion ( $m/z = 43$ ); the  $\text{C}_2\text{H}_4\text{O}^{+\bullet}$  ion ( $m/z = 44$ ) and its hydrated adducts  $\text{C}_2\text{H}_4\text{O}^{+\bullet}(\text{H}_2\text{O})_n$  ( $n = 1-3$ ;  $m/z = 62, 80, 98$  respectively); and  $(\text{H}_2\text{O})_n\text{H}^+$  water cluster ions. The primary products correspond to reactions (5.2) and (5.3), and the secondary products to their reactions with further  $\text{H}_2\text{O}$  molecules.

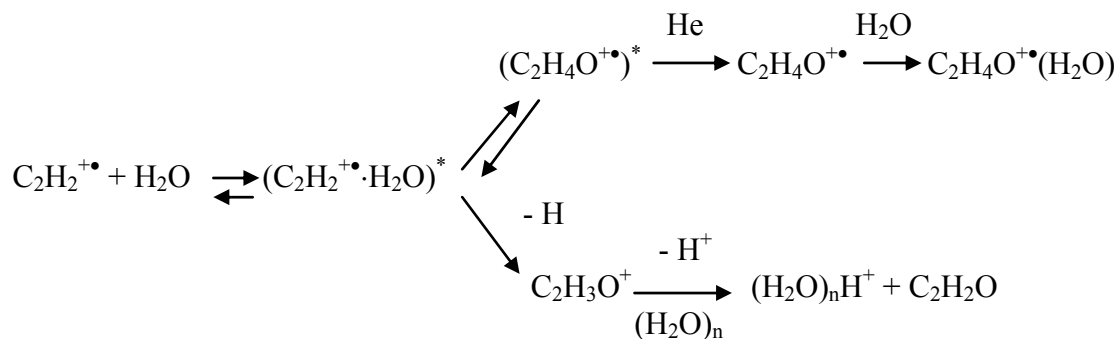


First, we inspect the ATD (Figure 37) of the product ions to establish whether or not the  $\text{C}_2\text{H}_2^{+\bullet}$  ion and its hydrated clusters are in equilibrium. If in equilibrium, the ATD



peaks of the ions should overlap, since equilibrium populations interchange from one form to another and drift coupled together in the cell. However, Figure 37 shows that the ATD peaks of  $\text{C}_2\text{H}_2^{+\bullet}$ , the  $\text{C}_2\text{H}_4\text{O}^{+\bullet}$  complex and its hydrated clusters  $\text{C}_2\text{H}_4\text{O}^{+\bullet}(\text{H}_2\text{O})_n$  do not overlap, indicating that they are not in equilibrium and that at least, the first  $\text{H}_2\text{O}$  molecule adds irreversibly to  $\text{C}_2\text{H}_2^{+\bullet}$  under our experimental conditions. The lack of equilibrium is also shown by the time profiles in Figure 38, where the intensities of the hydrated ions increase with residence (reaction) time and the reactant ion,  $\text{C}_2\text{H}_2^{+\bullet}$ , decreases. The time resolved study in Figure 38, supported by the data in Table 1 show the irreversible decay of the injected  $\text{C}_2\text{H}_2^{+\bullet}$  reactant ion along with a parallel formation of the  $\text{C}_2\text{H}_3\text{O}^+$  and  $\text{C}_2\text{H}_4\text{O}^{+\bullet}$  (and hydrated adduct) ions.

We also observe  $(\text{H}_2\text{O})_n\text{H}^+$  clusters whose time profile can be decomposed into a time-independent component, apparently formed by high-energy collisions upon injection of the  $\text{C}_2\text{H}_2^{+\bullet}$  ion, and a time-dependent component that increases at longer reaction times (Figure 38b). The time-dependent component occurs along with a corresponding decrease in the  $\text{C}_2\text{H}_3\text{O}^+$  ion population, suggesting slow deprotonation of this ion by water to form the  $(\text{H}_2\text{O})_n\text{H}^+$  clusters. Scheme 1 summarizes the indicated reactions.



Scheme 1

Table 1 displays the measured reaction kinetics for reactions 5.2 and 5.3. The main trends observed are:

a. The second-order rate constant for the overall reaction is independent of  $P(\text{H}_2\text{O})$  within the experimental uncertainty ( $\pm 30\%$ ). In other words, the reaction is first order with respect to  $\text{H}_2\text{O}$  as indicated in Scheme 1.

b. The rate coefficient for the overall reaction to form products is on the order of  $2.0 \times 10^{-11} \text{ cm}^3 \text{ s}^{-1}$ ; which is about two orders of magnitude smaller than the collision rate ( $10^{-9} \text{ cm}^3 \text{ s}^{-1}$ ). This suggests back-dissociation of the excited reaction complex  $(\text{C}_2\text{H}_2^{+\bullet} \cdot \text{H}_2\text{O})^*$  as indicated in Scheme 1 at a rate faster by about a factor of 100 than the forward reaction to products.

Comparison of the second order rate coefficient,  $k_2$ , determined from averaging the values in Table 1 ( $2.0 \times 10^{-11} \text{ cm}^3 \text{ s}^{-1}$ ) to that derived from the plot of the pseudo-first order rate constant versus water pressure in the drift cell,  $k_1$  vs.  $P(\text{H}_2\text{O})$ , ( $1.8 \times 10^{-11} \text{ cm}^3 \text{ s}^{-1}$ ) show excellent agreement within the experimental uncertainty. Considering both  $k_2$  values

along with the fact that the overall reactions for production of the  $\text{C}_2\text{H}_3\text{O}^+$  and  $\text{C}_2\text{H}_4\text{O}^{+\bullet}$  ions (reactions 5.2 and 5.3) can be considered parallel to the high-energy collision reaction forming the time-independent  $(\text{H}_2\text{O})_n\text{H}^+$  clusters, the rate constant for the latter reaction under the experimental conditions utilized (injection energy = 12 eV (*lab*), 303 K,  $P(\text{He}) \sim 356$  mTorr) is  $\sim 2.1 \pm 0.6 \times 10^{-12} \text{ cm}^3 \text{ s}^{-1}$ .

c. The reaction efficiency decreases with increasing temperature. This results from the back-dissociation of  $(\text{C}_2\text{H}_2^{+\bullet} \cdot \text{H}_2\text{O})^*$  that becomes faster and competes more efficiently with the forward reaction at higher temperatures.

d. The product ratio  $[\text{C}_2\text{H}_4\text{O}^{+\bullet}]/[\text{C}_2\text{H}_3\text{O}^+]$ , adduct formation vs. H atom loss, increases with third-body pressure,  $P(\text{He})$ , and with decreasing temperature. Figure 38 displays the signal intensities for the unreacted  $\text{C}_2\text{H}_2^{+\bullet}$  and other reaction product ions ( $\text{C}_2\text{H}_4\text{O}^+ + \text{C}_2\text{H}_4\text{O}^+ \cdot (\text{H}_2\text{O})_n$  (adduct),  $\text{C}_2\text{H}_3\text{O}^+$ , and  $\text{H}^+(\text{H}_2\text{O})_n$ ) using two different helium partial pressures in the cell, 332.4 and 1002.0 mTorr for plots (a) and (b) respectively. Water partial pressure,  $P(\text{H}_2\text{O})$ , was constant (19.6 mTorr) in both cases. Inspection of plot (a) reveals the  $\text{C}_2\text{H}_3\text{O}^+$  ion population as greater than that of the  $\text{C}_2\text{H}_4\text{O}^+$  adduct ions. On the other hand, plot (b), with a greater number of third body collisions, shows the  $\text{C}_2\text{H}_4\text{O}^+$  ion population to be greater than that of the  $\text{C}_2\text{H}_3\text{O}^+$  ion population. The average  $[\text{C}_2\text{H}_4\text{O}^{+\bullet}]/[\text{C}_2\text{H}_3\text{O}^+]$  ratio at earlier reaction times was 0.8 and 1.6 for (a) and (b) respectively. This is consistent with the formation of an excited  $(\text{C}_2\text{H}_4\text{O}^{+\bullet})^*$  adduct that can be stabilized collisionally in competition with back-reaction to the  $(\text{C}_2\text{H}_2^{+\bullet} \cdot \text{H}_2\text{O})^*$  excited ion, accounting for the increasing  $[\text{C}_2\text{H}_4\text{O}^{+\bullet}]/[\text{C}_2\text{H}_3\text{O}^+]$  ratio with increasing He third-body

pressure. This back-reaction also increases with increasing temperature, which accounts for the decreasing  $[\text{C}_2\text{H}_4\text{O}^{+\bullet}]/[\text{C}_2\text{H}_3\text{O}^+]$  ratio with increasing temperature.

A mechanism with two consecutive complexes can therefore account for the observed trends. However, the formation of two alternative complexes for the two channels directly by the collision, both of which increasingly back-dissociate with increasing temperature with different temperature coefficients, is also possible.

e. The  $\text{C}_2\text{H}_3\text{O}^+$  product is deprotonated by water to form  $(\text{H}_2\text{O})_n\text{H}^+$  cluster ions. This reaction becomes more pronounced with increasing  $P(\text{H}_2\text{O})$ . In fact, when  $\text{C}_2\text{H}_2^{+\bullet}$  was injected into neat  $\text{H}_2\text{O}$  vapor at  $> 100$  mTorr we did not observe the  $\text{C}_2\text{H}_3\text{O}^+$  ion but only  $(\text{H}_2\text{O})_n\text{H}^+$  cluster ions.

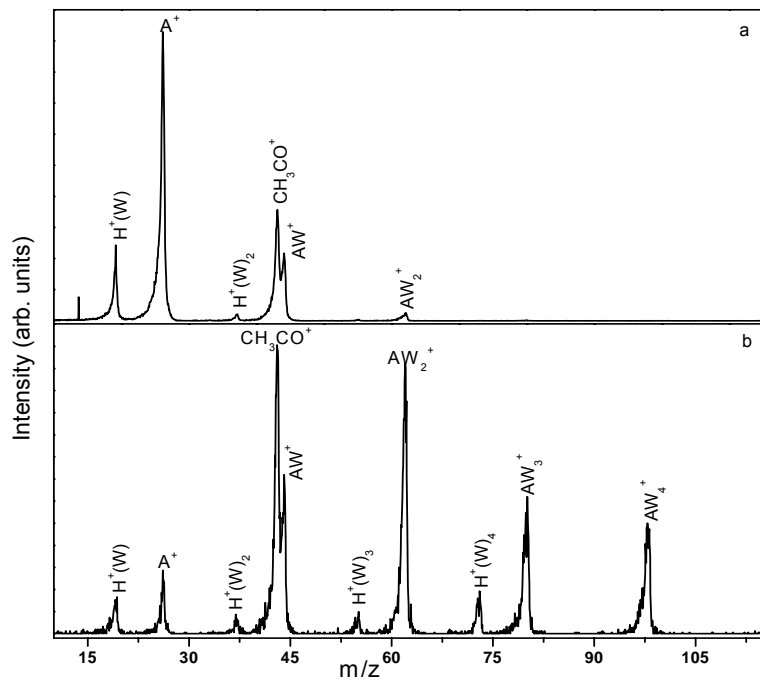


Figure 36: Mass spectrum obtained following the injection of  $C_2H_2^{+\bullet}$  ions into cell containing  $H_2O/He$  at 303 K, cell field 2.81 V/cm,  $P(H_2O) = 20$  mtorr,  $P(He) =$  (top) 358 mtorr and (bottom) 1441 mtorr.

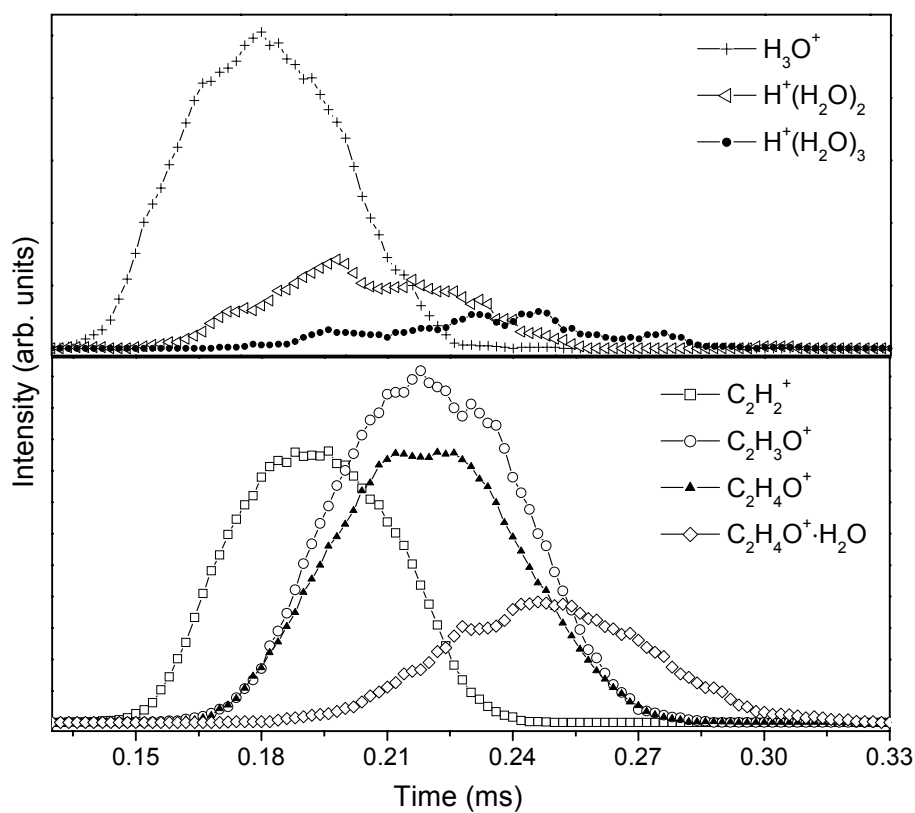


Figure 37: Arrival time distributions (ATDs) of the ions observed following the injection of  $\text{C}_2\text{H}_2^{+\bullet}$  ions into  $\text{H}_2\text{O}/\text{He}$  at 303 K,  $P(\text{H}_2\text{O}) = 20$  mtorr,  $P(\text{He}) = 713$  mtorr, injection energy (lab) = 11.9 eV, cell field = 2.81 V/cm. Overlap in ATD of  $\text{C}_2\text{H}_3\text{O}^+$  and  $\text{C}_2\text{H}_4\text{O}^+$  is as a result of similar drift mobilities.

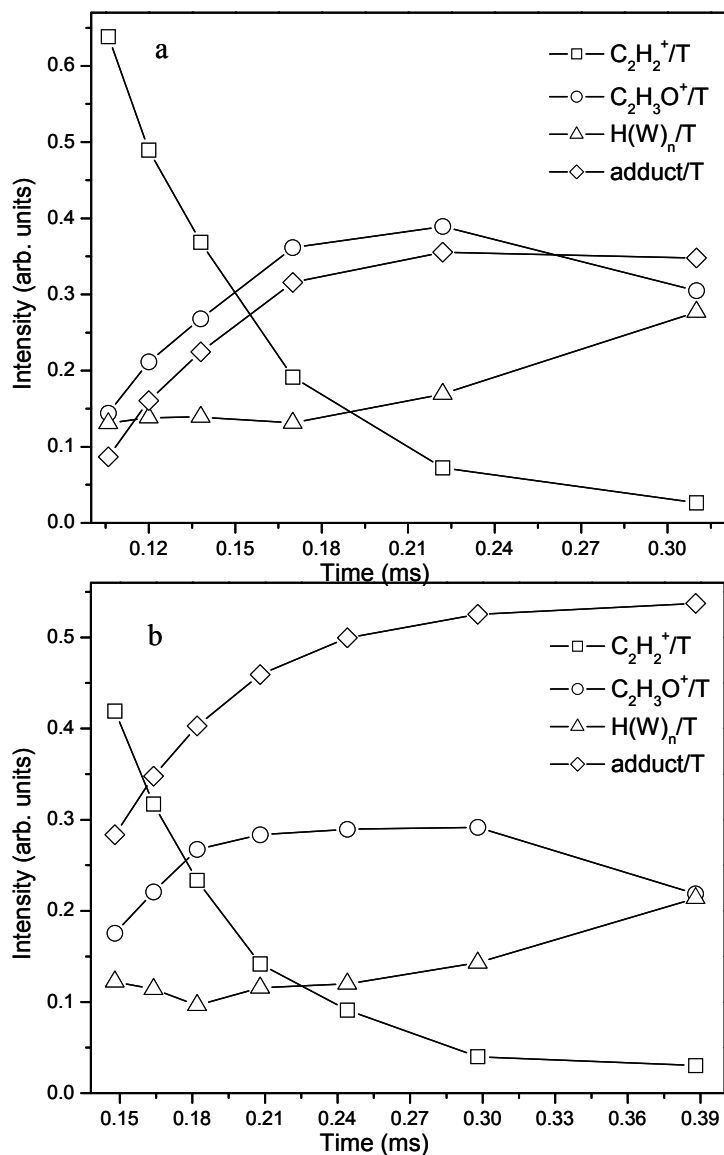


Figure 38: Intensities of ion signals (integrated ATD peaks) as a function of reaction time after injection of  $\text{C}_2\text{H}_2^{+\bullet}$  ions into the mobility cell with  $P(\text{H}_2\text{O}) = 19.6$  mTorr (or  $N[\text{H}_2\text{O}] = 7.19 \times 10^{14}$  molecules/ $\text{cm}^3$ ),  $T = 272$  K, and injection energy = 11.9 eV. Helium partial pressure was (a) 332.4 mTorr ( $N[\text{He}] = 1.22 \times 10^{16}$  molecules/ $\text{cm}^3$ ) and (b) 1002.0 mTorr ( $N[\text{He}] = 3.68 \times 10^{16}$  molecules/ $\text{cm}^3$ ). The time corresponds to the ion mobility time through the cell of the  $\text{C}_2\text{H}_2^{+\bullet}$  (26) ion plus the detection time of the ion after exiting the cell ( $\approx 24.7 \mu\text{s}$ ). In the graphs, "adduct" denotes the combined intensities of the  $\text{C}_2\text{H}_4\text{O}^{+\bullet}(\text{H}_2\text{O})_n$  ( $n = 0 - 4$ ) ions, "H(W) $_n$ " denotes the combined intensities of the  $(\text{H}_2\text{O})_n\text{H}^+$  ( $n = 0 - 4$ ) ions, and "T" denotes sum of intensities for the unreacted  $\text{C}_2\text{H}_2^+$  as well as all other observed products.

Table 1: Pressure and temperature effects on the rate coefficients and product ratios in the  $\text{C}_2\text{H}_2^{+\bullet} + \text{H}_2\text{O}$  system.

T (K)	$P(\text{H}_2\text{O})^a$	$P(\text{He})^a$	$k_f^b$	Product ratio $r = [\text{C}_2\text{H}_4\text{O}^{+\bullet}] / [\text{C}_2\text{H}_3\text{O}^+]^c$	$k^{b,d} (\text{C}_2\text{H}_3\text{O}^+)$	$k^{b,d} (\text{C}_2\text{H}_4\text{O}^{+\bullet})$
Water pressure study						
303	10.0	370	24	0.8	13.2	10.4
303	15.5	362	21	1.0	10.6	10.2
303	21.5	370	20	0.9	10.4	9.6
304	20.6	357	21	0.9	10.9	10.0
303	26.0	349	20	1.0	10.2	9.8
303	35.0	331	19	0.9	10.1	9.1
Helium pressure study @ 244 K						
244	18.6	293	32	0.9	17.3	15.1
244	16.8	751	33	1.6	12.5	20.1
244	16.9	1005	35	2.5	10.1	25.0
Helium pressure study @ 303 K						
303	21.5	370	20	0.9	10.4	9.6
303	20.0	712	23	1.4	9.6	13.6
304	20.6	999	22	1.4	9.1	12.4
303	20.0	1002	24	1.6	9.3	14.4
303	20.0	1441	26	2.2	8.0	17.5
Helium pressure study @ 359 K						
359	22.9	362	13	0.5	8.4	4.4
359	22.3	719	13	0.9	6.8	6.3
359	20.9	999	11	1.0	5.8	5.6
359	20.9	1503	12	0.6	6.1	3.4
Temperature study <sup>e</sup>						
244	18.6	293	32.4	0.9	17.3	15.1
272	19.6	332	26.2	0.8	14.9	11.3
303	21.5	370	20	0.9	10.4	9.6
331	21.9	366	16.0	0.6	10.2	5.8
359	22.9	362	12.8	0.5	8.4	4.4
415	24.5	372	9.2	0.6	5.6	3.6



- a. Units of mTorr.
- b. Rate coefficients for the overall forward reaction  $\text{C}_2\text{H}_2^{+\bullet} + \text{H}_2\text{O} \rightarrow \text{products}$  in units of  $10^{-12} \text{ cm}^3 \text{ s}^{-1}$ . Estimated uncertainty in rate coefficient measurements is usually  $\pm 30\%$ .
- c. Product ion ratio. The hydrated products  $\text{C}_2\text{H}_4\text{O}^{+\bullet}(\text{H}_2\text{O})_n$  are considered secondary products of the primary adduct channels and their intensities are included in the  $\text{C}_2\text{H}_4\text{O}^{+\bullet}$  adduct ion intensities.
- d. Rate coefficients based on product channel ratios. Calculated from the rate coefficients in column 4 and product ion ratios  $r$  in column 5 according to  $k(\text{C}_2\text{H}_3\text{O}^+) = k_f/(1 + r)$  and  $k(\text{C}_2\text{H}_4\text{O}^{+\bullet}) = k_f(r/(1 + r))$ . In units of  $10^{-12} \text{ cm}^3 \text{ s}^{-1}$ .
- e. Experiments using  $\text{C}_2\text{D}_2^{+\bullet}$  ions.
- e. The temperature study was conducted at constant number densities of  $N[\text{H}_2\text{O}] = 6.76(\pm 0.6) \times 10^{14} \text{ molecules/cm}^3$  and  $N[\text{He}] = 1.12(\pm 0.1) \times 10^{16} \text{ molecules/cm}^3$ .

### 5.2.2.2 Thermochemistry and Structure of the $\text{C}_2\text{H}_4\text{O}^{+\bullet}$ Adduct Ion

The association reaction  $\text{C}_2\text{H}_2^{+\bullet} + \text{H}_2\text{O} \rightarrow \text{C}_2\text{H}_4\text{O}^{+\bullet}$  was irreversible under all of our conditions, reaching, for example, a product/reactant ion ratio  $[\text{C}_2\text{H}_4\text{O}^{+\bullet}]/[\text{C}_2\text{H}_2^{+\bullet}] = 16.8$  at the longest reaction time observed at 363 K. If the reaction proceeded further toward equilibrium, the product/reactant ion ratio should increase further. In other words, the observed ratio is the lower limit of the equilibrium product/reactant ion ratio.

From this we can calculate a limit of  $\Delta G^\circ_{(363\text{K})}(\text{association}) = -RT \ln K_{(363\text{K})} < [\text{C}_2\text{H}_4\text{O}^{+\bullet}]/([\text{C}_2\text{H}_2^{+\bullet}]P(\text{H}_2\text{O})) = -RT \ln(16.8/2.8 \times 10^{-5} \text{ (atm)}) = -9.6 \text{ kcal/mol}$ . If the adduct was a hydrogen-bonded cluster we could assume  $\Delta S^\circ(\text{association}) \sim -20 \text{ cal/mol K}$  giving at 363 K the value of  $\Delta H^\circ(\text{association}) = \Delta G^\circ(\text{association}) + T\Delta S^\circ(\text{association}) < -16.9 \text{ kcal/mol}$  as the lower limit if the binding energy. This is somewhat larger than the binding energies for cluster ions with  $\text{CH}^{\delta+}\cdots\text{OH}_2$  binding energies that are usually 10 - 14 kcal/mol.<sup>142</sup>

If the adduct is covalently bonded, we may assume  $\Delta S^\circ \approx -40 \text{ cal/mol K}$ , and using the same limiting  $\Delta G^\circ_{(363\text{K})}(\text{association}) < -9.6 \text{ kcal/mol}$  above would yield  $\Delta H^\circ(\text{association}) < -24.1 \text{ kcal/mol}$ . This is consistent with the association forming covalent  $\text{C}_2\text{H}_4\text{O}^{+\bullet}$  isomers  $\text{CH}_3\text{CHO}^{+\bullet}$ ,  $(\text{H}_2\text{C}=\text{CH}-\text{OH})^{+\bullet}$ , or  $c-(\text{CH}_2=\text{CH}_2-\text{O})^{+\bullet}$  with exothermicities of -64.2 kcal/mol, -74.7 kcal/mol, and -28.3 kcal/mol respectively.<sup>120</sup> Note however that most stable isomers may not be produced if their formation involves a significant energy barrier, such as the hydrogen shifts required to form these isomers. The identity of the product isomer will be further tested below by its observed reactivity.

### 5.2.2.3 Formation and Deprotonation of the $\text{C}_2\text{H}_3\text{O}^+$ Product Ion

The  $\text{C}_2\text{H}_3\text{O}^+$  product ion is formed through hydrogen atom loss from the  $(\text{C}_2\text{H}_2^{+\bullet} + \text{H}_2\text{O})$  reactants. The stable isomers are  $\text{CH}_3\text{CO}^+$ ,  $\text{H}_2\text{C}=\text{C}=\text{OH}^+$  (O-protonated ketene), a linear or cyclic  $\text{CH}_2\text{CHO}^+$  ( $\text{C}_\alpha$ -protonated ketene) and a linear or cyclic  $\text{HCCHOH}^+$  ion.

The G3(MP2) predicted structures for the  $\text{C}_2\text{H}_3\text{O}^+$  ion are presented in Table 3. As for the thermochemistry of reaction 5.2, both experimental ( $\Delta H_r^\circ$ )<sup>43</sup> and theoretical data ( $\Delta E_r$ ) show the formation of isomers **3a** and **3b** (Table 3) from the reactants to be significantly exothermic, while formation of **3c** is less exothermic according to experiments and endothermic according to theory (G3MP2).

Isomer **3c** may be formed most easily by addition of  $\text{H}_2\text{O}$  to  $\text{C}_2\text{H}_2^{+\bullet}$  and  $\text{H}^\bullet$  atom loss from the  $\text{H}_2\text{O}$  moiety. To test this mechanism, we performed an isotope labeling experiment by injecting  $\text{C}_2\text{D}_2^+$  into the cell containing a  $\text{H}_2\text{O}/\text{He}$  mixture. The mass spectra showed the formation of the  $m/z$  45 ( $\text{C}_2\text{D}_2\text{HO}^+$ ) ion where hydrogen loss occurred exclusively from  $\text{H}_2\text{O}$ . This suggests that at least the initial product is an  $\text{HCCHOH}^+$  ion formed by the addition of  $\text{H}_2\text{O}$  with  $\text{H}^\bullet$  loss exclusively from the  $\text{H}_2\text{O}$  moiety without H/D scrambling in the intermediate complex. H/D exchange upon deprotonation of an acetylene carbon still remains a possibility.

While thermochemistry allows the formation of three  $\text{C}_2\text{H}_3\text{O}^+$  isomers, the observed reactivity provides further information. The  $\text{C}_2\text{H}_3\text{O}^+$  ion may be deprotonated slowly by water to form  $(\text{H}_2\text{O})_n\text{H}^+$  clusters. This is noted in Figure 38 where the decrease in  $\text{C}_2\text{H}_3\text{O}^+$  ion population is compensated by a simultaneous increase of the  $(\text{H}_2\text{O})_n\text{H}^+$  clusters at long reaction times. Furthermore, the ATDs in Figure 39 show  $(\text{H}_2\text{O})_3\text{H}^+$

clusters with a tail at long residence times (b) which was not observed for the same species for shorter residence times (a). This is similar to the deprotonation of the hydrocarbon ions,  $c\text{-C}_3\text{H}_3^+$  and  $\text{C}_6\text{H}_6^{+\bullet}$  (benzene cation) by several  $\text{H}_2\text{O}$  molecules to form  $(\text{H}_2\text{O})_n\text{H}^+$  cluster ions, where the ions contain only C-H hydrogens.<sup>138,143</sup> The driving force for this deprotonation reaction is the replacement of the weak  $\text{CH}^{\delta+}\cdots\text{OH}_2$  hydrogen-bonds by the stronger H-bonds in the water clusters. The ATD of Figure 39 suggest an analogous reaction for the cooperative deprotonation of the  $\text{C}_2\text{H}_3\text{O}^+$  ion by 3  $\text{H}_2\text{O}$  molecules forming a  $(\text{H}_2\text{O})_3\text{H}^+$  cluster whose strong hydrogen bond network facilitates the reaction. This analogy suggests that the  $\text{C}_2\text{H}_3\text{O}^+$  ion's neutral precursor ( $\text{CH}_2\text{CO}$ ) is protonated on one of the carbon atoms rather than on the oxygen atom.

However, the  $\text{CH}_3\text{CO}^+$  isomer (**3a**) would react with  $\text{H}_2\text{O}$  to give  $\text{CH}_3\text{COOH}_2^+$  i.e., protonated acetic acid which then forms hydrated  $\text{CH}_3\text{COOH}_2^+(\text{H}_2\text{O})_n$  clusters with further  $\text{H}_2\text{O}$  molecules,<sup>144</sup> which was not observed in our experiments. As for the other isomer, ketene protonated on the oxygen atom,  $\text{H}_2\text{C}=\text{C}=\text{OH}^+$  (**3b**), we note that similar protonated aldehydes and ketones clusters are produced upon reaction with  $\text{H}_2\text{O}$ ; thus forming  $\text{RCOH}^+(\text{H}_2\text{O})_n$  clusters.<sup>145</sup> All of these clusters are stabilized by strong  $\text{OH}^+\cdots\text{O}$  hydrogen bonds between the core ions and the solvent molecules and do not undergo deprotonation. However, the *ab initio* prediction of the precursor  $\text{H}_2\text{C}=\text{C}=\text{O}$  (ketene) proton affinity at the O-site suggest possible proton transfer to water as discussed below.

All in all, the reactivity of the observed  $\text{C}_2\text{H}_3\text{O}^+$  ion gives some indications, but no proof, of its structure. The  $\text{CH}_3\text{CO}^+$  (**3a**) isomer is not indicated as it would associate with  $\text{H}_2\text{O}$  rather than undergoing the observed deprotonation. Based on predicted  $\text{C}_2\text{H}_3\text{O}^+\cdots\text{H}_2\text{O}$

complex geometries and calculated proton affinities below, the thermochemical data and reactivity may be consistent with the **3b** ( $\text{H}_2\text{C}=\text{C}=\text{OH}^+$ ) and possibly with the **3c** ( $c\text{-CHCH}_2\text{O}^+$ ) isomer. Proton affinities ( $\text{PA}_{298\text{K}}$ ) were calculated to be 153.7 kcal/mol and 139.4 kcal/mol for the conjugate bases of **3b** (O protonation) and **3c** respectively, allowing deprotonation by  $\text{H}_2\text{O}$  ( $\text{PA} = 165 \text{ kcal/mol}^{120}$ ). Predicted  $\text{C}_2\text{H}_3\text{O}^+\cdot\text{H}_2\text{O}$  structures show **3b** to undergo an intra-complex H-extraction reaction with water (Table 5-**3b**), and for the fully dissociated species, dissociation to  $\text{H}_3\text{O}^+ + \text{CH}_2\text{CO}$  is also the lower energy path.

#### 5.2.2.4 Interstellar Reaction of the Acetylene-Water System

In astrochemical environments the  $\text{C}_2\text{H}_2^{+\bullet}$  ion will react primarily with  $\text{H}_2$  to give  $\text{C}_2\text{H}_3^+$  ions. This will in turn react with  $\text{H}_2\text{O}$  and most other interstellar or atmospheric molecules by proton transfer. On the other hand, protonated species such as  $\text{H}_3\text{O}^+$  will not protonate acetylene but can form cluster ions and possibly covalent adducts with it. Given the similarity of  $\text{C}_2\text{H}_2$  and  $\text{N}_2$  which are both nonpolar molecules with comparable polarizabilities, the binding energies of  $\text{H}_3\text{O}^+(\text{C}_2\text{H}_2)_n$  should be comparable to  $(\text{H}_3\text{O})^+(\text{N}_2)_n$  which we measured recently as 7.9, 6.9 and 5.4 kcal/mol for adding the first, second and third ligand molecules, respectively.<sup>146</sup>

#### 5.2.2.5 Theoretical Calculations

These calculations concerned the energies and geometries of isomers of the  $\text{C}_2\text{H}_3\text{O}^+$  and  $\text{C}_2\text{H}_4\text{O}^{+\bullet}$  ions and their complexes with a  $\text{H}_2\text{O}$  molecule. The calculations identify low energy isomers that may be the observed species and rule out some other

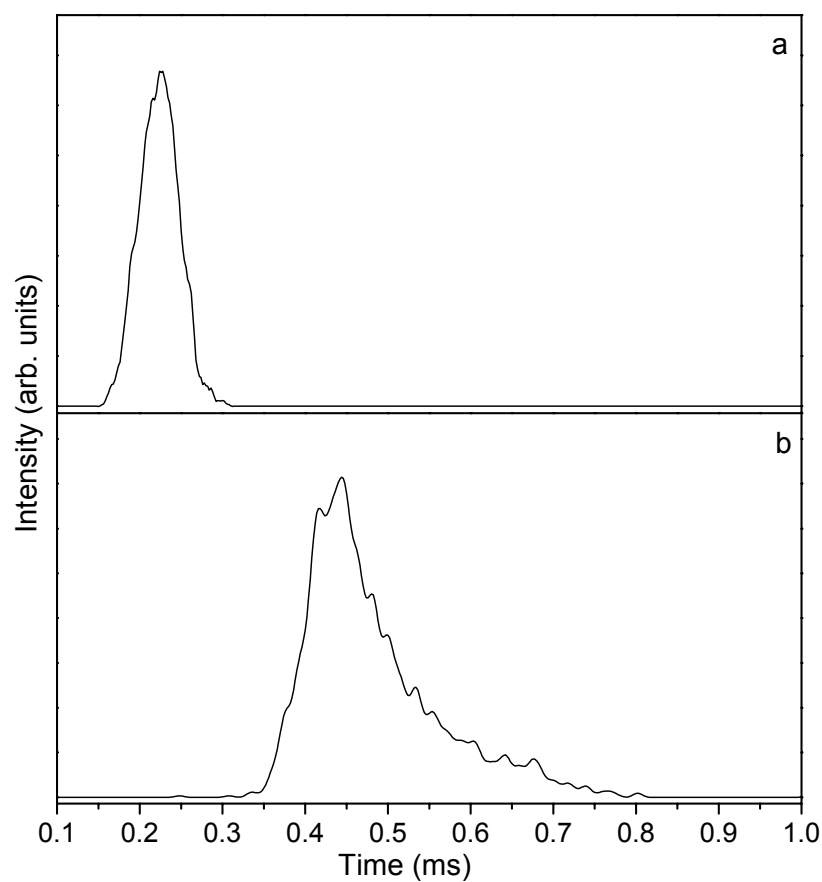


Figure 39: Arrival time distribution (ATD) for the  $\text{H}^+(\text{H}_2\text{O})_3$  cluster produced upon injection of  $\text{C}_2\text{D}_2^{+\bullet}$  ions into cell containing  $\text{H}_2\text{O}/\text{He}$  at 304 K,  $P(\text{H}_2\text{O}) = 20$  mtorr,  $P(\text{He}) = 999$  mtorr, injection energy (lab) = 11.9 eV and cell field of (a) 3.9 V/cm and (b) 1.7 V/cm.

alternatives. Energies of the more highly hydrogenated ions of the formula  $C_2H_5O^+$  that also form in acetylene/water were studied previously.<sup>30</sup>

**$C_2H_4O^{+\bullet}$** . The G3(MP2) and UPBEPBE results (in parentheses) on the  $C_2H_4O^{+\bullet}$  hypersurface are summarized in Table 2. Experimental values, when available, are shown in brackets. As shown in Table 2, the calculated energy of reaction,  $\Delta E_r(298K)$ , for reaction 5.2 below is in excellent agreement with experimentally determined values (where available) thus confirming the G3(MP2) method as satisfactory for this system.

The lowest energy structure is the ethenolium cation  $H_2C=CHOH^{+\bullet}$  (**2a**) (absolute G3(MP2) energy = -153.239 au), followed by the acetaldehyde cation  $CH_3CHO^{+\bullet}$  (**2b**), 13.3 kcal/mol less stable. The cyclic ethylene oxide cation (**2f**) is much higher in energy than **2a** (48.7 kcal/mol). The (methyliumoxy)-methyl ion  $H_2COCH_2^{+\bullet}$  (**2d**) with a relative energy of 26.0 kcal/mol is predicted to be 22.7 kcal/mol more stable than its potential cyclic precursor ion, (**2f**).<sup>147</sup>

Several other species, including 1-hydroxy-1-ethylm-1-yl (**2c**), 16.4 kcal/mol; methyloxoniumylidene-methyl (**2e**), 35.4 kcal/mol; *cis*- $HCCHOH_2^{+\bullet}$  cation (**2g**), 44.4 kcal/mol, and *trans*- $HCCHOH_2$  cation (**2h**), 44.5 kcal/mol are predicted at the G3(MP2) level to be more stable than **2f**, despite structures that suggest substantial instability. The  $CH_2CH_2O^{+\bullet}$  ion converged to **2f** upon optimization. This is in agreement with previous suggestion that  $CH_2CH_2O^{+\bullet}$ , if formed, isomerizes to **2d** via **2f**.<sup>147</sup> Based on theory and experiments, numerous isomerization coordinates have been proposed for this system. For example, Radom *et al.* suggested that  $CH_2CH_2O^{+\bullet}$  isomerizes without a barrier to **2b**.<sup>148</sup>

Based on surface-induced dissociation (SID) experiments, Cooks *et al.* suggested **2d** may subsequently isomerize to **2c** and/or **2e** upon activation.<sup>147</sup> Terlouw *et al.* proposed rearrangement of excited **2f** to **2e**.<sup>149</sup> Clearly, more experiments and calculations will have to be done to elucidate the isomerization coordinates of the  $\text{C}_2\text{H}_4\text{O}^{+\bullet}$  radical ion.

It is interesting to note that at the UPBEPBE/aug-cc-pVDZ level of theory, **2g** and **2h** were less stable than **2f**. The order of relative energies given by the G3(MP2) calculations was confirmed by the results of the CCSD/aug-cc-pVDZ calculations. This result suggests that there may be some problems with the reliability of DFT calculations with this functional for species of this kind.

The  $\text{C}_2\text{H}_2^{+\bullet}\cdot\text{H}_2\text{O}$  complex **2k** was the highest energy species we investigated on the hypersurface; with a relative energy of 58.1 kcal/mol. The corresponding  $\text{HCCH}^{+\bullet}\cdots\text{OH}_2$  hydrogen bond binding energy is predicted to be 17.6 kcal/mol, which is reasonable for a  $\text{CH}^{\delta+}\cdots\text{O}$  type hydrogen bond.<sup>142</sup> However, this complex is predicted as stable only when constrained to a  $C_{2v}$  symmetry. If there is any deviation from this symmetry, G3(MP2) and DFT predicts addition of the water to the acetylene, resulting in the *trans*- $\text{HCCHOH}_2^{+\bullet}$  cation (**2h**). The hydrogen-bonded complex, **2k**, may be an intermediate in the covalent association reaction.

**$\text{C}_2\text{H}_3\text{O}^+$** . Table 3 summarizes the predicted  $\text{C}_2\text{H}_3\text{O}^+$  geometries and thermochemistry. In all, seven stable species are found on the potential hypersurface. The most stable species, is, as expected, 1-oxo-ethylum (**3a**) ( $\text{CH}_3\text{CO}^+$ ) followed by 1-hydroxyethenylum (**3b**), 41.6 kcal/mol higher in energy. The third most stable  $\text{C}_2\text{H}_3\text{O}^+$  isomer is 2H-oxirenylium



(**3c**), with a relative energy of 55.9 kcal/mol. The relative stability of these three ions is predominantly governed by the site of protonation considering the neutral ketene ( $\text{H}_2\text{C}_\beta=\text{C}_\alpha=\text{O}$ ) as a precursor. Using NBO (natural bond orbital) analysis, Terlouw *et al.* suggested preference for protonation at the  $\text{C}_\beta$  site (**3a**) was due to the partial negative charge on this carbon and the occurrence of the largest HOMO orbital coefficient at the  $p$  orbital.<sup>150</sup> Protonation at the  $\text{C}_\alpha$  site, **3c**, is stabilized in part by the partial positive charge on the O atom as a result of the resonance:  $\text{H}_2\text{C}_\beta=\text{C}_\alpha=\text{O} \leftrightarrow \text{H}_2\text{C}_\beta^{\delta-}-\text{C}_\alpha^{\delta+}=\text{O}$ . In addition, electrostatic attraction between the  $\text{C}_\beta^{\delta-}$  and  $\text{O}^{\delta+}$  helps to stabilize **3c** by formation of a C-O bridge. The corresponding proton affinities are discussed in section 5.2.2.6. Two stable structures with COC heavy atom skeletons are also found. They are methyloxoniumylidene-methylene (**3d**) and methylenexoxoniomethylene (**3g**) with relative energies of 54.5 and 106.5 kcal/mol respectively. A cyclic  $\text{CHCHOH}^+$  on (**3e**) and ethynyloxonium ion (**3f**) are also found to be stable with relative energies 82.4 and 82.6 kcal/mol respectively. Previous work by Radom *et al.*<sup>151</sup> at the MP2/6-31G\*\* level also predicted **3e** and **3f** as stable structures with relative energies of 83.7 kcal/mol and 85.3 kcal/mol respectively-in good agreement with our results. The G3(MP2) and UPBEPBE/aug-cc-pVDZ methods differed in their predictions of the relative energies of **3c** and **3d**. G3(MP2) predicted **3d** to be 1.3 kcal/mol more stable than **3c**. On the other hand, UPBEPBE/aug-cc-pVDZ predicted **3c** to be 10.7 kcal/mol more stable than **3d**. The G3(MP2) ordering was confirmed as correct by comparison to the CCSD/aug-cc-pVDZ results. Calculated  $\Delta E_r(298\text{K})$  according to reaction 5.5 reveal the formation of isomers **3c** to **3g** as endothermic while **3a** and **3b** are exothermic. Thermochemical data from the

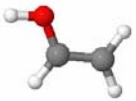
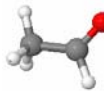

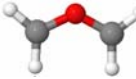
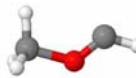
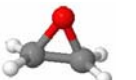
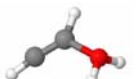
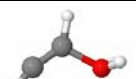


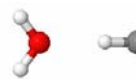
NIST database<sup>120</sup> reveal the heat of formation for **3c** to be moderately exothermic. Predicted thermochemistry for reaction 5.3 will be discussed in the next section. Previous experiments have suggested that **3c** may be a stable/observable  $\text{C}_2\text{H}_3\text{O}^+$  isomer.<sup>152</sup> Optimizations of the acyclic  $\text{CH}_2\text{CHO}^+$  (formylmethyl cation) species converged to **3c** at both levels of theory employed. Previous calculations at the MP3/6-31G(*d,p*) level of theory predicted the formylmethyl cation as stable though 20.6 kcal/mol less stable than **3c**.<sup>151</sup> This suggests that the formylmethyl cation cannot be our experimentally observed isomer. While we tried a substantial number of starting geometries, including all known neutral isomers of  $\text{C}_2\text{H}_3\text{O}$ , at both levels of theory employed, they all relaxed to one of the seven reported isomers.

#### 5.2.2.6 Comparison with Experimental Thermochemistry

The calculated energies of reaction,  $\Delta E_r(298\text{K})$  for reaction 5.2 are compared in Table 2 with the experiment-based enthalpies of reactions ( $\Delta H_r^\circ$ ) that were calculated from data in the NIST database.<sup>120</sup> The  $\Delta E_r(298\text{K})$  for the formation of **2a**, **2b**, and **2f** according to reaction 5.2 are -75.7, -62.4 and -27.1 kcal/mol respectively, in excellent agreement with the experiment-based values of ( $\Delta H_r^\circ$ ) of -75.4, -62.6 and -28.3 kcal/mol, respectively. The predicted  $\Delta E_r(298\text{K})$  for the formation of **3a** and **3c** according to reaction 5.3 are -50.2 kcal/mol and -5.7 kcal/mol respectively; in good agreement with the experiment-based  $\Delta H_r^\circ$  values of -50.2 kcal/mol and -6.2 kcal/mol respectively. The average difference between the predicted and experiment-based reaction energies is  $\sim 0.44$  kcal/mol. Other comparisons of the present computational results and experimental data are possible. We

calculated the proton affinity (PA) of  $\text{CH}_2\text{CHO}^\bullet$  on O to yield  $\text{CH}_2\text{CHOH}^+$  as 185.3 kcal/mol in excellent agreement with the NIST tabulated value of 185 kcal/mol.<sup>120</sup> We also calculated the PA of ketene at the  $\text{C}_\beta$ , O, and  $\text{C}_\alpha$  sites ( $\text{H}_2\text{C}_\beta=\text{C}_\alpha=\text{O}$ ) corresponding to **3a**, **3b**, and **3c** respectively. The G3(MP2) predicted PA of  $\text{C}_\beta$ -ketene, forming **3a**, is 195.2 kcal/mol, which compares very well with the experimental value of 197.3 kcal/mol,<sup>120</sup> and also agrees with the previous G2(MP2) prediction by Wong and Ma of 195.8 kcal/mol.<sup>150</sup> The UPBEPBE/aug-cc-pVDZ proton affinity of  $\text{C}_\beta$ -ketene was 190.3 kcal/mol. Proton affinities of ketene at the O-site (**3b**) and  $\text{C}_\alpha$ -site (**3c**) are calculated to be 153.7 kcal/mol and 139.3 kcal/mol respectively, also in good agreement with previous values.<sup>150</sup> The predicted PA of  $\text{H}_2\text{O}$  is 163.4 kcal/mol in good agreement with the experimental value of 165 kcal/mol.<sup>120</sup> Comparison of the proton affinities of **3b** and **3c** to that of water indicates deprotonation of both these  $\text{C}_2\text{H}_3\text{O}^+$  isomers by  $\text{H}_2\text{O}$  is thermochemically allowed. Certainly, this deprotonation reaction will become more efficient with further addition of water molecules to the  $\text{C}_2\text{H}_3\text{O}^+$  cation. This is in agreement with the experimental observation of  $\text{C}_2\text{H}_3\text{O}^+$  deprotonation by water at long residence times (Figure 38). These examples support the conclusion that G3(MP2) calculations are accurate within  $\pm 1.5$  kcal/mol of experiment-based thermochemistry of the radical ions considered here. Therefore these calculations can help to evaluate conflicting and potentially inaccurate experimental data. For example, the three listed literature values for  $\Delta H_f^\circ$  of ketene,  $\Delta H_f^\circ(\text{H}_2\text{CCO})$ ,<sup>120</sup> are -11.4, -14.78 and -20.85 kcal/mol.<sup>153-155</sup> These values can be combined with  $\text{PA}(\text{H}_2\text{CCO}) = 197.3 \text{ kcal/mol}$ <sup>120</sup> to find  $\Delta H_f^\circ(298\text{K})$  for reaction 5.5 that forms  $\text{CH}_3\text{CO}^+$  **3a**. The theoretical  $\Delta E_r$  for this reaction agrees only with the

Table 2: G3(MP2) and DFT calculated structures and energies of  $C_2H_4O^+$  isomers<sup>a</sup>

Isomer	Structure	Bond Lengths (Å) and Angles (°) <sup>b</sup>	Relative Energy <sup>a,c</sup>	$\Delta E_r(298K)^{c,d,e}$
a Ethenolium		rC-C = 1.41 rC-O = 1.29 CCO = 117.4	<b>0.0<sup>i</sup></b>	<b>-75.73</b> (-84.28) [-75.4]
b Acetaldehyde cation		rC-C = 1.49 rC-O = 1.22 CCO = 123.0	<b>13.34</b> (13.00) [13] <sup>g,h</sup>	<b>-62.39</b> (-73.67) [-62.6]
c 1-hydroxy-1-ethyl-1-yl		rC-C = 1.45 rC-O = 1.25 CCO = 128.5	<b>16.37</b> (16.56)	<b>-59.35</b> (-69.14)
d (Methyliumoxy)-methyl		rC <sub>1</sub> -C = 1.27 rC <sub>2</sub> -O = 1.36 COC = 124.5	<b>26.00</b> (26.40) [22] <sup>g,h</sup>	<b>-49.72</b> (-59.08) [-57.3]
e Methyloxononiumyliden e-methyl		rC <sub>1</sub> -C = 1.54 <sup>f</sup> rC <sub>2</sub> -O = 1.22 COC = 124.5	<b>35.39</b> (40.93) [40] <sup>g,h</sup>	<b>-40.34</b> (-44.67) [-35.3]
f Ethylene oxide cation		rC-C = 1.46 rC-O = 1.49 CCO = 60.7	<b>48.65</b> (45.49) [47] <sup>g,h</sup>	<b>-27.08</b> (-40.77) [-28.3]
g Cis-HCCHOH <sub>2</sub> cation		rC-C = 1.26 rC-O = 1.57 CCO = 120.2	<b>44.36</b> (47.85)	<b>-31.37</b> (-39.07)
h Trans-HCCHOH <sub>2</sub> cation		rC-C = 1.27 rC-O = 1.55 CCO = 116.1	<b>44.46</b> (48.30)	<b>-31.27</b> (-38.44)
i Cyclic CH <sub>2</sub> CHOH cation		rC-C = 1.44 rC-O = 1.56 CCO = 59.1	<b>50.77</b> (51.15)	<b>-24.96</b> (-33.80)
j H <sub>2</sub> CCOH <sub>2</sub> cation		rC-C = 1.28 rC-O = 1.46 CCO = 123.9	<b>49.61</b> (53.10)	<b>-26.12</b> (-32.39)
k C <sub>2</sub> H <sub>2</sub> <sup>+</sup> ·H <sub>2</sub> O <sup>b</sup>		rC-C = 1.26 rC-OH <sub>2</sub> = 2.8	<b>58.09</b> (63.09)	<b>-17.23</b> (-26.13)

- a) Bold numbers were obtained using the G3(MP2) method. Numbers in parentheses were obtained at the UPBEPBE/aug-cc-pVDZ level of theory. Experimental numbers, where available, are shown in brackets. DFT calculations were ZPE and counterpoise corrected.
- b) Bond lengths and angles shown were obtained using the G3(MP2) method.
- c) kcal/mol.
- d) Energy of Reaction 5.4 at 298 K.
- e) Using  $\Delta H_f^\circ(\text{C}_2\text{H}_2^{+\bullet}) = \Delta H_f^\circ(\text{C}_2\text{H}_2) + \text{IE}(\text{C}_2\text{H}_2) = 54.19 + 262.88 = 317.07$  kcal/mol and  $\Delta H_f^\circ(\text{H}_2\text{O}) = -57.80$  kcal/mol from NIST.<sup>120</sup>
- f) C<sub>1</sub> is the methyl carbon.
- g) Experimental heat of formation for **2a** is 184 kcal/mol.<sup>120</sup> Other numbers shown are relative to this value.  $\Delta H_f^\circ$  **2a**, **2b**, and **2f** were obtained from NIST and  $\Delta H_f^\circ$  for **2d** and **2e** were obtained from work of Terlouw *et al.*<sup>149</sup>
- h) Relative energies obtained by the difference in experimental  $\Delta H_f^\circ$ .
- i) Predicted G3(MP2) absolute energy of **2a** is -153.239 au.

Table 3: G3MP2 and DFT results on isomers of  $C_2H_3O^{+a}$ 

Isomer		Structure	Bond Lengths (Å) and Angles (°) <sup>b</sup>	Relative Energy <sup>c,f</sup>	$\Delta E_r(298K)^{c,d,e}$
a	1-oxo-ethylum/Acylum		rC-C = 1.42 rC-O = 1.13 CCO = 180.0	<b>0<sup>g</sup></b>	<b>-50.19</b> (-56.23) [-49.2, <sup>h</sup> -50.2 <sup>i</sup> ]
b	1-hydroxy-ethenylum		rC-C = 1.28 rC-O = 1.23 CCO = 174.5	<b>41.55</b> (37.99)	<b>-8.64</b> (-18.97)
c	2H-oxirenium		rC-C = 1.44 rC <sub>β</sub> -O = 1.64 <sup>j</sup> CC <sub>β</sub> O = 47.4	<b>55.88</b> (52.04) [43]	<b>5.68</b> (-3.98) [-6.2] <sup>k</sup>
d	Methyloxoniumylidene-methylene		rC <sub>1</sub> -O = 1.57 <sup>l</sup> rC <sub>2</sub> -O = 1.17 COC = 180.0	<b>54.54</b> (62.71)	4.35 (5.88)
e	Cyclic CHCHOH/Protonated Oxirene		rC-C = 1.27 rC-O = 1.56 COC = 48.3	<b>82.38</b>	<b>32.18</b>
f	Ethynyloxonium		rC-C = 1.21 rC-O = 1.38 CCO = 177.4	<b>82.55</b>	<b>32.36</b>
g	Methyleneoxonio-methylene		rC <sub>1</sub> -O = 1.29 <sup>m</sup> rC <sub>2</sub> -O = 1.25 COC = 166.6	<b>106.46</b> (102.23)	<b>56.26</b> (44.60)

- a) Bold numbers were obtained using the G3(MP2) method. Numbers in parentheses were obtained at the UPBEPBE/aug-cc-pVDZ level of theory. Experimental numbers, where available, are shown in brackets. DFT calculations were ZPE and counterpoise corrected.
- b) Bond lengths and angles shown were obtained using the G3(MP2) method.
- c) In kcal/mol.
- d) Energy of Reaction 5.5 at 298 K.
- e) Using  $\Delta H_f^\circ$  for  $C_2H_2^{+\bullet} = 317.1$  kcal/mol; for  $H^\bullet = 52.1$  kcal/mol; and for  $H_2O = -57.8$  kcal/mol.<sup>120</sup>
- f) Using  $\Delta H_f^\circ(3a) = 158.5$  kcal/mol and  $\Delta H_f^\circ(3c) = 201$  kcal/mol based on NIST values.<sup>120</sup> Other numbers shown are relative to **3a**.
- g) Predicted G3(MP2) absolute energy of **3a** is -152.698 au.
- h) Obtained using  $\Delta H_f^\circ(CH_3CO^\bullet) = -2.9 \pm 0.7$  kcal/mol and  $IE(CH_3CO^\bullet) = 161.4$  kcal/mol.<sup>120</sup>
- i) Obtained using  $\Delta H_f^\circ(H_2CCO) = -11.4$  kcal/mol and  $PA(H_2CCO) = 197.3$  kcal/mol.<sup>120</sup>
- j) C<sub>β</sub> is the -CH<sub>2</sub> carbon, C<sub>1</sub> is the -CH<sub>2</sub> carbon.
- k) Obtained using  $\Delta H_f^\circ(c-H_2CCHO^+) = 201$  kcal/mol.<sup>120</sup>
- l) C<sub>1</sub> is the methyl carbon.
- m) C<sub>1</sub> is the -CH<sub>2</sub> carbon.

$\Delta H_f^\circ(\text{H}_2\text{CCO}) = -11.4$  kcal/mol while the other experiment-based values of  $\Delta H_f^\circ(\text{H}_2\text{CCO})$  yield  $\Delta E_r$  that differs from theory by several kcal/mol, suggesting the first value is the most accurate. Similarly, for the listed  $\text{IE}(\text{CH}_3\text{CO}^\bullet)$  values of 7.0 and 8.05 eV,<sup>120,156,157</sup> only the former gives  $\Delta H_f^\circ(298\text{K})$  which agrees with theory.

Furthermore, Table 2 and Table 3 also point out the lack of experimental data for several interesting isomers including the relatively low energy  $\text{CH}_3\text{COH}^{+\bullet}$  (**2c**) and  $\text{H}_2\text{CCOH}^+$  (**3b**) ions.

#### 5.2.2.7 Predicted Geometries for the $\text{C}_2\text{H}_n\text{O}^{+\bullet}\cdot\text{H}_2\text{O}$ Complexes ( $n = 3$ and $4$ ).

To gain more insight into subsequent solvation and reactions of the  $\text{C}_2\text{H}_4\text{O}^{+\bullet}$  and  $\text{C}_2\text{H}_3\text{O}^+$  ions, we calculated the geometries and binding energies (BE) for select  $\text{C}_2\text{H}_4\text{O}^{+\bullet}\cdot\text{H}_2\text{O}$  and  $\text{C}_2\text{H}_3\text{O}^+\cdot\text{H}_2\text{O}$  complexes.

**$\text{C}_2\text{H}_4\text{O}^{+\bullet}\cdot\text{H}_2\text{O}$ .** Stable geometries for selected  $\text{C}_2\text{H}_4\text{O}^{+\bullet}\cdot\text{H}_2\text{O}$  complexes are shown in Table 4. Two stable structures (**4-2a1** and **4-2a2**) are found for the hydrated ethenolium (Table 2a) ion. Complex **4-2a1** consists of a water molecule hydrogen bonded (BE = 22.8 kcal/mol) to the OH group of **2a** with  $r\text{OH}\cdots\text{OH}_2$  bond length of 1.60 Å. **4-2a2**, 11.4 kcal/mol less stable than **4-2a1**, consists of the water molecule weakly bound (11.3 kcal/mol) to the  $\text{C}_\alpha$  hydrogen. The  $r\text{C}_\alpha\text{H}\cdots\text{OH}_2$  bond length is 2.13 Å. The large binding energy for **4-2a1** is in agreement with our experimental observation of  $\text{C}_2\text{H}_4\text{O}^{+\bullet}(\text{H}_2\text{O})_n$  clusters with strong binding in the adduct formation. On the other hand, the weak binding interaction of **4-2a2** dismisses it as a possible hydrated species of **2a** as such weakly bound complexes (BE of 11.3 kcal/mol and a typical  $\Delta S^\circ$  association of -20 cal/mol K) would be

small or undetectable under our higher-temperature conditions which was not the case in our experiment. For example, using the calculated binding energy of 11.3 kcal/mol, typical association entropy of -20 cal/mol K, temperature of 415 K, and  $P(\text{H}_2\text{O})$  of  $3.32 \times 10^{-5}$  atm, an adduct/monomer ion ratio,  $I(\text{C}_2\text{H}_4\text{O}^{\bullet+}\cdot\text{H}_2\text{O})/I(\text{C}_2\text{H}_4\text{O}^{\bullet+})$ , of 0.0013 is calculated. The experimental ratio at the same temperature and pressure was 0.5; approximately 385 times larger than the predicted ratio for **4-2a2**. Using the temperature, water pressure, and  $I(\text{C}_2\text{H}_4\text{O}^{\bullet+}\cdot\text{H}_2\text{O})/I(\text{C}_2\text{H}_4\text{O}^{\bullet+})$  ratio above, the limit of  $\Delta G^\circ_{(415\text{K})}(\text{association}) = -RT \ln K_{(415\text{K})} < [\text{C}_2\text{H}_4\text{O}^{\bullet+}\cdot\text{H}_2\text{O}]/([\text{C}_2\text{H}_4\text{O}^{\bullet+}]P(\text{H}_2\text{O})) = -RT \ln(0.2/(0.1 \times 3.32 \times 10^{-5} \text{ (atm)})) = -9.1 \text{ kcal/mol}$ .  $\Delta H^\circ(\text{association}) = \Delta G^\circ(\text{association}) + T\Delta S^\circ(\text{association}) < -17.4 \text{ kcal/mol}$ ; this corresponds to the lower limit if the  $\text{C}_2\text{H}_4\text{O}^{\bullet+}\cdots\text{H}_2\text{O}$  binding energy. The  $r_{\text{O-H}}$  bond length in **4-2a1** (1.05 Å) is elongated compared to that of its unsolvated analog, **2a** (0.99 Å), consistent with H-bonded species. These results are consistent with the usual trends in ionic hydrogen bonds. The  $\text{OH}^+\cdots\text{OH}_2$  bonds such as in **4-2a1** are usually stronger than  $\text{CH}^{\delta+}\cdots\text{OH}_2$  bonds such as in the **4-2a2** complex.<sup>158</sup>

These results are consistent with the usual trends in ionic hydrogen bonds. The  $\text{OH}^+\cdots\text{OH}_2$  bonds such as in **4-2a1** are usually stronger than  $\text{CH}^{\delta+}\cdots\text{OH}_2$  bonds such as in the **4-2a2** complex.<sup>158</sup> Further, the hydrogen bond strength correlates inversely with the proton affinity differences of the clustering components according to  $\Delta H^\circ_D(\text{OH}^+\cdots\text{OH}_2) = 30.4 \pm 0.30 \text{ kcal/mol}$ .<sup>158</sup> In **4-2a1** using  $\text{PA}(\text{CH}_2\text{CHO}) - \text{PA}(\text{H}_2\text{O}) = 20 \text{ kcal/mol}$ ,<sup>120</sup> the correlation yields  $\Delta H^\circ_D(\bullet\text{CH}_2\text{CHOH}^+\cdots\text{OH}_2) = 24.4 \text{ kcal/mol}$  in good agreement with the G3(MP2) value of 22.8 kcal/mol. This shows that the correlation observed in even-electron protonated ions also applies to radical ions, i.e., the presence of an unpaired electron at a



remote site in the ion does not affect the strength of the hydrogen bond. We made similar observations recently concerning the solvation of the pyridine distonic radical cation that will be reported elsewhere.

Our calculations found two interesting structures for the hydrated acetaldehyde cation (**2b**) ion, ( $\text{CH}_3\text{CHO}^+\cdot\text{H}_2\text{O}$ ; **4-2b**), and the hydrated 1-hydroxy-1-ethylion-1-yl (**2c**) ion, ( $\text{CH}_3\text{COH}^+\cdot\text{H}_2\text{O}$ ; **4-2c1**). In both cases, the most stable geometry consist of a complex in which the  $\text{C}_\alpha$  hydrogen and  $r\text{O}$ -hydrogen (**2b** and **2c1** respectively) transfer to the water molecule thus forming a protonated water ion bound to a neutral acetyl radical ( $\text{CH}_3\text{CO}^\bullet\cdots\text{H}^+\text{OH}_2$ ). For **4-2b**, the  $r\text{C}\cdots\text{HOH}_2$  length is 1.74 Å as compared to the **2b**  $r\text{C}_\alpha\text{H}$  bond length of 1.11 Å. OH bond lengths for the  $\text{H}_3\text{O}^+$  ion are 0.99, 0.99, and 1.06 Å (abstracted H). In the case of **4-2c1**,  $r\text{CO}\cdots\text{HOH}_2$  length is 1.41 Å. Inspection of *Mulliken* atomic charges<sup>159</sup> reveals 83% and 93% of total charge densities transfer to the  $\text{H}_3\text{O}^+$  ions for **4-2b** and **4-2c1** respectively. Of course, a more reliable charge density technique will have to be utilized for an unambiguous understanding of charge distribution, since it is well known that *Mulliken* charge distributions overemphasize electron density on heavy atoms when augmented functions are included in the basis set.<sup>160</sup>  $\text{CH}_3\text{CO}^\bullet\cdots\text{H}^+\text{OH}_2$  binding energies for both complexes are strong; with 22.4 and 29.7 kcal/mol for **4-2b** and **4-2c1** respectively. Calculated proton affinities (PA) for the precursor neutral acetyl radical ( $\text{CH}_3\text{CO}^\bullet$ ) at the  $\text{C}_\alpha$  (**2b**) and O (**2c**) sites are 165.6 and 162.6 kcal/mol respectively and the calculated PA for  $\text{H}_2\text{O}$  is 163.4 kcal/mol in good agreement with the experimental value of 165 kcal/mol.<sup>120</sup> These values suggest a very weak thermochemical drive for proton abstraction by a single water molecule in an intermolecular proton transfer-type reaction.

However, the solvation of the  $\text{H}_3\text{O}^+$  ion by the polar and polarizable  $\text{CH}_3\text{CO}^\bullet$  radical should be more efficient than solvation of  $\text{CH}_3\text{CHO}^{\bullet+}$  by the smaller and less polar  $\text{H}_2\text{O}$  ligand, and therefore proton transfer in the complex can be facilitated by the relative solvation energies. Subsequent solvation by more water molecules would form a strong hydrogen bonded  $(\text{H}_2\text{O})_n\text{H}^+$  center and therefore further facilitate proton abstraction.<sup>143</sup> However, our kinetic experiments showed that the  $\text{C}_2\text{H}_4\text{O}^{\bullet+}$  ions did not produce the protonated water clusters  $(\text{H}_2\text{O})_n\text{H}^+$  but rather formed  $\text{C}_2\text{H}_4\text{O}^{\bullet+}(\text{H}_2\text{O})_n$  adducts. This shows that intermolecular proton abstraction reaction does not occur in our system, but does not rule out intra-complex proton transfer.

We also found **4-2c2** as another stable  $\text{CH}_3\text{COH}^{\bullet+}\cdot\text{H}_2\text{O}$  adduct. For this complex, water binds to the  $\text{C}_\alpha$  of  $\text{CH}_3\text{COH}^+$  producing a complex somewhat similar to a protonated acetic acid cation. The calculated  $r\text{C}_\alpha\cdots\text{OH}_2$  binding energy is 14.0 kcal/mol and the  $r\text{C}_\alpha\cdots\text{OH}_2$  bond length is 1.69 Å. **4-2c2** is most likely not our experimentally observed  $\text{C}_2\text{H}_4\text{O}^+\cdot\text{H}_2\text{O}$  adduct due to its small binding energy and lower stability compared to **4-2c1** (16.3 kcal/mol). The next  $\text{C}_2\text{H}_4\text{O}^+\cdot\text{H}_2\text{O}$  species explored is the (methyliumoxy)-methyl (**2d**)/water complex. Two stable complexes are found (**4-2d1** and **4-2d2**) in which the water molecule is weakly bound to the  $\text{C}_2\text{H}_4\text{O}^+$  ion. For **4-2d1**, the water molecule forms a cyclic  $r\text{CH}\cdots\text{O}\cdots\text{HC}r$  hydrogen bond with **2d**. For **4-2d2**, water hydrogen bonds to one of the terminal hydrogens of **2d**. **4-2d1** is 2.6 kcal/mol more stable than **4-2d2**. The binding energies of **4-2d1** and **4-2d2** are calculated to be 12.5 and 9.9 kcal/mol respectively. These complexes would not be observed under high temperature conditions (415 K) for the reason discussed above. The next stable  $\text{C}_2\text{H}_4\text{O}^+\cdot\text{H}_2\text{O}$  complex is **4-2f**. This complex

consists of a water molecule bound to an ethylene oxide cation ( $\text{CH}_2\text{CH}_2\text{O}^+\cdots\text{OH}_2$ ) by strictly electrostatic and van der Waals interactions. The  $r_{\text{O}\cdots\text{OH}_2}$  distance is 1.96 Å and 83 % of charge density resides on the ethylene oxide cation. It is interesting to note that the closest interacting atoms for this complex are the oxygen atoms suggesting a partial positive charge on the ethylene oxide's oxygen as well as orbital interaction preventing the expected  $r_{\text{CH}^{\delta+}\cdots\text{OH}_2}$ -type bonding. The binding energy for this complex is calculated to be 12.0 kcal/mol. This complex is not expected to be the  $\text{C}_2\text{H}_4\text{O}^+$  isomer. The final  $\text{C}_2\text{H}_4\text{O}^+\cdot\text{H}_2\text{O}$  complex in this work is **4-2i** which consists of a cyclic  $\text{CH}_2\text{CHOH}$  (**2i**) hydrogen bonded to a water molecule. The  $r_{\text{OH}\cdots\text{OH}_2}$  hydrogen bond distance is 1.37 Å and binding energy is calculated to be 25.2 kcal/mol. The  $r_{\text{O-H}}$  bond length for the hydrated **2i** is elongated compared to the isolated cation (1.10 Å vs. 0.99 Å) consistent with hydrogen bonded species. Inspection of charge densities showed 88 % of total charge resides on **2i**.

High binding energies for **4-2a1** and **4-2c1** as well as  $\Delta E_r(298\text{K})$  (Table 4) suggest that isomers **2a** and/or **2c** may be the  $\text{C}_2\text{H}_4\text{O}^+$  isomers. The nature of the **4-2b** complex suggest deprotonation to form the neutral acetyl radical ( $\text{CH}_3\text{CO}^\bullet$ ) and  $\text{H}^+(\text{H}_2\text{O})_n$  clusters upon further addition of water molecules. This reaction was not observed in our experiment. Thermochemistry dismisses **2f** as a likely candidate.

**$\text{C}_2\text{H}_3\text{O}^+\cdot\text{H}_2\text{O}$** . Since isomer **3a** is known to form protonated acetic acid and its hydrated clusters upon addition of water,<sup>144,161</sup> we did not attempt any calculation for this species. The most interesting result was seen for the 1-hydroxy-ethenylium (**3b**)/water complex,  $\text{CH}_2\text{COH}^+\cdot\text{H}_2\text{O}$  (**5-3b**). As shown in Table 5, the predicted geometry involves a complex in

which the -OH hydrogen of **3b** migrates to the H<sub>2</sub>O oxygen thus forming a neutral ketene molecule and a protonated water ion, (CH<sub>2</sub>CO...H<sub>3</sub>O<sup>+</sup>). In the input structure, the oxygen of the water molecule was positioned approximately 1.75 Å from **3bs'** OH hydrogen. The optimized CH<sub>2</sub>CO...HOH<sub>2</sub><sup>+</sup> bond length is 1.48 Å as compared to 0.97 Å for the unhydrated ion, **3b**. The OH bond lengths of H<sub>3</sub>O<sup>+</sup> are 0.98, 0.98, and 1.06 Å (abstracted proton). Inspection of the *Mulliken* charge densities revealed a majority (92%) of total charge transfer to the H<sub>3</sub>O<sup>+</sup> ion. The CH<sub>2</sub>CO...H<sub>3</sub>O<sup>+</sup> binding energy (dissociation into CH<sub>2</sub>CO + H<sub>3</sub>O<sup>+</sup>) for **3b** is calculated to be 22.3 kcal/mol. Although intra-complex proton transfer does not necessary lead to intermolecular proton transfer, the latter process was experimentally observed as shown in Figure 38 where, at long residence times, the C<sub>2</sub>H<sub>3</sub>O<sup>+</sup> ion intensity dropped with a corresponding increase in (H<sub>2</sub>O)<sub>*n*</sub>H<sup>+</sup> ion intensity. Comparison of the calculated proton affinities at the O site of neutral ketene, 153.7 kcal/mol with the experiment-based proton affinities for *n* H<sub>2</sub>O molecules (165, 197 and 217 kcal/mol for *n* = 1, 2, and 3 respectively)<sup>120</sup> indicate that proton abstraction reaction from **5-3b** to form protonated water clusters is thermochemically allowed. As noted above, calculated PAs for isomers **3b** and **3c** indicate both isomers can be deprotonated by water, consistent with the observed reactivity. Optimization of the cyclic CH<sub>2</sub>CHO<sup>+</sup>·H<sub>2</sub>O (**3c**) complex resulted in two species **5-3c1** and **5-3c2** with the latter 5.9 kcal/mol more stable than the former. In **5-3c2**, the water molecule is covalently bound to the *r*HC of **3c** with HO...C length of 1.57 Å. In the case of **5-3c1**, the water molecule forms a hydrogen bond with the *r*CH of **3c**. The CH<sub>2</sub>OCH<sup>+</sup>...OH<sub>2</sub> binding energy is calculated to be 14.7 kcal/mol and C<sub>α</sub>H...OH length was 1.74 Å. The **5-3c1** complex was surprising as we expected it to behave like **5-**

**3b** with a deprotonation of the  $C_\alpha$ -hydrogen. As discussed earlier, calculated proton affinities for protonation of different sites ( $C_\alpha$ ,  $C_\beta$ , and O) of a neutral ketene precursor ( $H_2C_\beta=C_\alpha=O$ ) shows the O-site (**3b**) to have a larger PA than the  $C_\alpha$ -site, **3c**; 153.7 kcal/mol versus 139.3 kcal/mol. As a result, the thermodynamic drive for proton abstraction by the water molecule is expected to be more favorable for the  $C_\alpha$ -hydrogen than the O-hydrogen. *Mulliken* charge densities show 95% of total charge resides on the  $c$ - $CH_2CHO^+$  molecule. Apparently, a higher barrier exists for deprotonation of the  $C_\alpha$  hydrogen in this complex as compared to **5-3b** where O-H deprotonation occurs. This is consistent with barriers for C-H deprotonation of the benzene cation.<sup>138</sup>

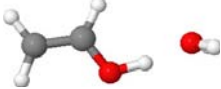
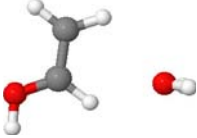
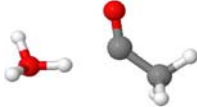
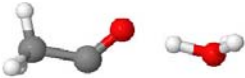
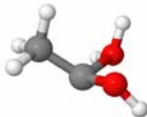
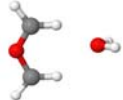
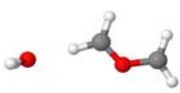
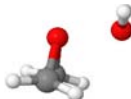
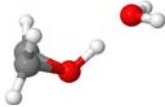
We also investigated the cyclic  $CHCHOH^+$ /water complex, **5-3e**. We chose to investigate this complex due to its structural similarity to the  $c$ - $C_3H_3^+$  ion, recently shown in our lab to undergo deprotonation reaction with water clusters.<sup>143</sup> The  $CHCHOH^+\cdots OH_2$  bond length was 1.37 Å and binding energy was 22.4 kcal/mol and 93% of total charge resided on the  $CHCHOH^+$  ion.

## Conclusion

The acetylene cation  $C_2H_2^{+\bullet}$  reacts with  $H_2O$  vapor by association to produce  $C_2H_4O^{+\bullet}$  and  $C_2H_3O^+$  by  $H^\bullet$  atom loss. As usual in ion-molecule chemistry, the overall rate coefficient increases with decreasing temperature and the adduct/ $H^\bullet$  loss product ratio increases with decreasing temperature and increasing third-body pressure. The association reaction appears irreversible under our conditions and thermochemical estimates suggest that it produces a covalent  $C_2H_4O^{+\bullet}$  adduct. The adduct forms clusters with further  $H_2O$

molecules, and the addition of at least the first H<sub>2</sub>O molecule is irreversible, suggesting strong hydrogen bonding or covalent addition. *ab initio* calculations show the lowest energy C<sub>2</sub>H<sub>4</sub>O<sup>+</sup> isomer to be the ethenolium ion, H<sub>2</sub>CCHOH<sup>+</sup> (**2a**); with an OH<sup>+</sup> group that forms strong hydrogen bonds. Also, H<sub>2</sub>CCHOH<sup>+</sup> may form easily from the reactants by a single H<sup>•</sup> atom shift. These considerations suggest that the observed adduct ion is the H<sub>2</sub>CCHOH<sup>+</sup> isomer (**2a**).

Table 4: G3(MP2) calculations on  $C_2H_4O^{++} \cdot H_2O$  complexes<sup>a</sup>

Isomer $\cdot H_2O$ <sup>b</sup>	Structure	H-bond Lengths ( $\text{\AA}$ ) <sup>g</sup>	Relative Energy	Binding Energies <sup>d</sup>
4-2a1		$rO \cdots OH_2 = 2.59$ $rOH \cdots OH_2 = 1.60$	0 <sup>c</sup>	22.78
4-2a2		$rC_\alpha \cdots OH_2 = 2.91$ $rC_\alpha H \cdots OH_2 = 2.13$	11.44	11.34
4-2b		$rC \cdots HOH_2 = 1.74$	16.16	22.35 <sup>e</sup> (19.96) <sup>f</sup>
4-2c1		$rCO \cdots OH_3 = 2.49$ $rCO \cdots HOH_2 = 1.41$	8.81	29.70 <sup>e</sup> (30.34) <sup>f</sup>
4-2c2		$rC_\alpha O \cdots OH = 1.30$ $rC_\alpha O \cdots OH_2 = 1.69$	25.13	14.02
4-2d1		$rC_1 H \cdots OH_2 = 2.01$ $rC_2 H \cdots OH_2 = 2.27$	36.33	12.45
4-2d2		$rC \cdots OH_2 = 2.95$ $rCH \cdots OH_2 = 1.86$	38.93	9.86
4-2f		$rO \cdots OH_2 = 1.96$	59.43	12.00
4-2i		$rO \cdots OH_2 = 2.47$ $rOH \cdots OH_2 = 1.37$	48.30	25.24

a) All calculations were carried out using the G3(MP2) method.

b) Isomer identity inherited from Table 2.

c) Absolute energy of **4-2a1** is -229.615 au

d) In kcal/mol.

e) Binding for dissociation into  $CH_3CO^\bullet + H^+OH_2$ .

f) Binding for dissociation into corresponding  $C_2H_4O^{++}$  isomer +  $H_2O$ .

g) Bond lengths and angles were obtained at the G3(MP2) level.

Isotopic experiments showed that the  $\text{C}_2\text{H}_3\text{O}^+$  product forms by loss of an  $\text{H}^\bullet$  atom from the  $\text{H}_2\text{O}$  reactant. The lowest energy  $\text{C}_2\text{H}_3\text{O}^+$  product is  $\text{CH}_3\text{CO}^+$  which is inconsistent with the observed reactivity, but  $\text{H}_2\text{COH}^+$  (**3b**) and cyclic  $c\text{-CH}_2\text{CHO}^+$  (**3c**) may be consistent with the thermochemistry and with the observed deprotonation to form  $(\text{H}_2\text{O})_n\text{H}^+$  clusters.

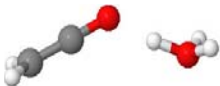
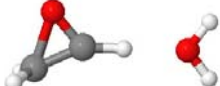
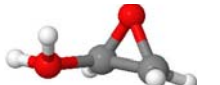

In calculations on the adducts of the  $\text{C}_2\text{H}_4\text{O}^{+\bullet}$  and  $\text{C}_2\text{H}_3\text{O}^+$  with addition of a  $\text{H}_2\text{O}$  molecule, we found in some cases intra-complex proton transfer to form an  $\text{H}_3\text{O}^+$  ion hydrogen bonded to the deprotonated  $\text{C}_2\text{H}_3\text{O}^\bullet$  or  $\text{C}_2\text{H}_2\text{O}$  molecules respectively. With  $\text{C}_2\text{H}_3\text{O}^+$  the intra-cluster proton transfer may be followed by reactions with further  $\text{H}_2\text{O}$  molecules that lead to full deprotonation forming  $(\text{H}_2\text{O})_n\text{H}^+$  cluster ions.

The calculations in this study provide a comprehensive survey of  $\text{C}_2\text{H}_3\text{O}^+$  and  $\text{C}_2\text{H}_4\text{O}^{+\bullet}$  ions and their  $\text{H}_2\text{O}$  adducts. Comparisons with experimental thermochemistry show that the G3(MP2) energies of reaction ( $\Delta E_r$ ) and proton affinities for neutrals and radicals of the present types are accurate within 0.43 kcal/mol or better. These calculations can therefore be used to evaluate conflicting or significantly inaccurate thermochemical data.

The isomers identified by the theoretical calculations may form by ionic reactions in astrochemical environments or as intermediates and products in the dissociation of larger ions. Experiments and theoretical studies of these ions and their neutral counterparts are useful for modeling these environments.



Table 5: G3(MP2) calculations on  $C_2H_3O^+ \cdot H_2O$  complexes <sup>a</sup>

Isomer·H <sub>2</sub> O <sup>b</sup>	Structure	H-bond Lengths (Å)	Relative Energy	Binding Energies <sup>c</sup>
5-3b		$r_{CO \cdots OH_2} = 2.53$ $r_{CO \cdots H^+OH_2} = 1.48$	0 <sup>g</sup>	22.32 <sup>e</sup> (31.90) <sup>f</sup>
5-3c1		$r_{C_\alpha \cdots OH_2} = 2.86^d$ $r_{C_\alpha H \cdots OH_2} = 1.74$	31.38	14.74
5-3c2		$r_{C \cdots OH_2} = 1.57$	25.10	20.65
5-3e		$r_{O \cdots OH_2} = 2.53$ $r_{OH \cdots OH_2} = 1.37$	50.08	22.38

a) All calculations were carried out using the G3(MP2) method.

b) Isomer identity inherited from Table 3.

c) In kcal/mol.

d)  $C_\alpha$  is the  $rCH$  carbon.

e) Binding for dissociation into  $CH_2CO^\bullet + H^+OH_2$ .

f) Binding for dissociation into corresponding  $C_2H_3O^{+\bullet}$  isomer +  $H_2O$ .

g) Absolute energy of **5-3b** is -229.022 au.

### 5.3 Stepwise Hydration of Ionized Acetylene Dimer and Trimer Cations.

#### Experimental and Theoretical section

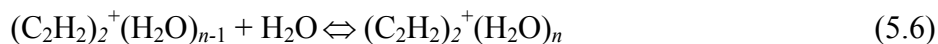
Details of the instrument can be found in Chapters 2 and 3. For the hydration experiments, the  $(\text{C}_2\text{H}_2)_2^+$  and  $(\text{C}_2\text{H}_2)_3^+$  ions are mass-selected from ionized acetylene clusters and injected (10-40  $\mu\text{s}$  pulses) into the drift cell containing water vapor at 0.1 - 0.3 Torr, at controlled temperatures from 240 to 310 K. The thermalized ions travel through the drift cell under a uniform electric field of 1.5 – 3 V/cm. The reaction products are identified by scanning a second quadrupole mass filter located coaxially after the drift cell. The arrival time distributions (ATD) are collected by monitoring the intensity of each ion as a function of time. The ion intensity ratio  $(\text{C}_2\text{H}_2)_m^+(\text{H}_2\text{O})_n / (\text{C}_2\text{H}_2)_m^+(\text{H}_2\text{O})_{n-1}$  (where  $m = 2, 3$  and  $n = 1-7$ ) is measured from the integrated peak areas of the ATDs as a function of decreasing cell drift field corresponding to increasing reaction time, and equilibrium is achieved when a constant ratio is obtained. Equilibrium constants are then calculated from  $K = I[(\text{C}_2\text{H}_2)_m^+(\text{H}_2\text{O})_n] / [I[(\text{C}_2\text{H}_2)_m^+(\text{H}_2\text{O})_{n-1}] P(\text{H}_2\text{O})]$  where  $I$  is the integrated ion intensity taken from the ATD and  $P(\text{H}_2\text{O})$  is the partial pressure of the water vapor in the drift cell. The equilibrium constant measured as a function of temperature yields  $\Delta H^\circ$  and  $\Delta S^\circ$  from the van't Hoff equation  $[\ln K = - \Delta H^\circ/RT + \Delta S^\circ/R]$ . Geometries and single point energies were calculated using the G3MP2 method described earlier.

## 5.4 Results and Discussion

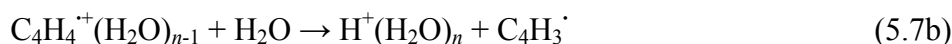
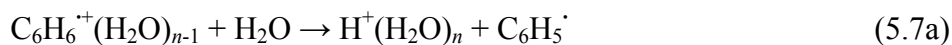
### 5.4.1 Dimer Ion Hydration

Figure 40 shows the observed product distribution upon injection of mass selected  $(\text{C}_2\text{H}_2)_2^+$  into the drift cell containing 0.48 Torr of water vapor at 301 K. At this temperature, the main peaks observed were the dimer and its hydrated adduct ions,  $(\text{C}_2\text{H}_2)_2^+(\text{H}_2\text{O})_{1-5}$ , and protonated water clusters,  $\text{H}^+(\text{H}_2\text{O})_{3-7}$ . The mass spectrum shows a dip in the  $(\text{C}_2\text{H}_2)_2^+(\text{H}_2\text{O})_n$  peak intensity at  $n = 2$ , dividing the spectrum into two groups. This dip was observed at  $n = 3$  for hydrated benzene<sup>138</sup> and acetylene trimer clusters.<sup>162</sup>

Inspection of the arrival time distribution (ATD) for the  $(\text{C}_2\text{H}_2)_2^+(\text{H}_2\text{O})_n$  clusters (Figure 41) reinforces the mass spectra behavior. The ATD peaks are clearly divided into two groups with  $n = 0-1$  making up the first and  $n = 2-5$  for the second group. The ATD behavior suggest each hydrated species is coupled to an association reaction equilibrium as represented in reaction 5.6 but the two groups of ATDs are not in equilibrium with each other. As discussed in section 3.4 of this text, similar ATD indicates the association products are coupled by the equilibrium reaction



An analogous observation was made in hydrated benzene clusters,  $\text{C}_6\text{H}_6^{*+}(\text{H}_2\text{O})_n$ .<sup>138</sup> The separation of the ATDs into groups was ascribed to an association/proton transfer/dissociation (APTD) reaction (reaction 5.7a) which becomes thermoneutral at  $n = 4$ , thus depleting the  $n = 3$  ion population and perturbing the equilibrium. The APTD reaction, represented in reaction 5.7b is suspected here



As expected, the larger ions have longer ATDs due to their relatively larger collision cross sections, hence slower mobilities.

#### 5.4.1.1 Binding Energies and Thermochemistry of the Dimer Ion

Figure 42 shows the van't Hoff plots ( $R \ln K$  vs.  $T$ ) used in obtaining the binding energies and association reaction entropies of reaction 5.6. Table 6 displays the corresponding  $\Delta H_{n-1,n}^{\circ}$  and  $\Delta S_{n-1,n}^{\circ}$  values for  $\text{C}_4\text{H}_4^{++}(\text{H}_2\text{O})_n$  obtained from the measured equilibrium constants,  $K$ , dependence on temperature using the van't Hoff equation,  $\ln K = -\Delta H^{\circ}/RT + \Delta S^{\circ}/R$ . The lower than expected  $-\Delta S_{0,1}^{\circ}$  value (Table 6) may be the result of distortion of the  $n = 1 \rightarrow 2$  equilibrium by the suspect APTD reaction or perhaps, perturbed measurements as a result of the presence of multiple  $\text{C}_4\text{H}_4^{++}$  isomers in the mass selected beam. As discussed in the previous chapter, both the cyclobutadiene and the vinylacetylene isomers (Figure 25) are suspected to be major constituents in our cluster beam. The  $-\Delta S_{1,2}^{\circ}$  and  $-\Delta H_{1,2}^{\circ}$  values could not be measured due to diminished ion count of the  $\text{C}_4\text{H}_4^{++}(\text{H}_2\text{O})_2$  cluster; the result of the suspect APTD reaction, 5.7b. The measured binding energy for the  $\text{C}_4\text{H}_4^{++}\cdot\text{H}_2\text{O}$  cluster,  $9.1 \pm 1$  kcal/mol, is in excellent agreement with the G3(MP2) predicted binding energies for select  $\text{C}_4\text{H}_4^{++}\cdot\text{H}_2\text{O}$  clusters (Table 7). The uncertainty in our binding energy measurements and the relatively similar G3(MP2) predicted binding energies prevented any conclusion about the identity of the  $\text{C}_4\text{H}_4^{++}$  isomers in our cluster beam. Interestingly, the binding energies ( $\Delta H_{n-1,n}^{\circ}$ ) for the

$\text{C}_4\text{H}_4^{++}(\text{H}_2\text{O})_{n-1}\cdots\text{H}_2\text{O}$  ions change very little for  $n = 3-5$  suggesting the availability of several binding sites with similar energies for subsequent water association. The measured  $-\Delta S_{2,3}^\circ$ ,  $-\Delta S_{3,4}^\circ$ , and  $-\Delta S_{4,5}^\circ$  values of 21.3, 22.8, and 25.9 cal mol<sup>-1</sup> K<sup>-1</sup> also suggest formation of adducts with restrained water molecules.<sup>163</sup> These values are in agreement with the model potential/DFT investigation by Hodges and Stone<sup>164</sup> which found the lowest structures of the  $n = 4$  and 5 clusters of  $\text{H}_3\text{O}^+(\text{H}_2\text{O})_n$  to be cyclic. A cyclic structure was also predicted for the  $n = 3$  cluster though 3.9 kcal/mol less stable than the  $\text{H}_3\text{O}^+(\text{H}_2\text{O})_3$  global minimum. Binding for the sixth water molecule ( $\Delta H_{5,6}^\circ$ ) dropped by approximately 3.4 kcal/mol and the  $-\Delta S_{5,6}^\circ$  value (Table 6) dropped suggesting a structure in which the sixth water molecule perhaps hangs loose.

#### 5.4.1.2 Calculated $\text{C}_4\text{H}_4^{++}(\text{H}_2\text{O})_{1-2}$ Structures for Select $\text{C}_4\text{H}_4^{++}$ Isomers

**$\text{C}_4\text{H}_4^{++}\cdot\text{H}_2\text{O}$ :** Shown in Table 7 are the G3(MP2) predicted geometries for the  $\text{C}_4\text{H}_4^{++}\cdot\text{H}_2\text{O}$  complex. The four most stable  $\text{C}_4\text{H}_4^{++}$  isomers (Figure 25), methylenecyclopropene (**MC**); cyclobutadiene (**CB**); 1,2,3-butatriene (**OB**); and 1-buten-3-yne (**VA**), were used as precursors for this investigation. As mentioned previously, the G3(MP2) method is known to accurately predict thermochemistry of C, H, and O containing species ( $\pm 0.43$  kcal/mol from experimental values). It also utilizes less computing resource than the MP or CC methods.<sup>140</sup>

As displayed in Table 7, three structures are predicted for the mono-hydrated methylenecyclopropene (**MCH**) complex. **MCHa** is predicted to be the most stable hydrated methylenecyclopropene complex. It consists of a carbon based  $\text{CH}^{\delta+}\cdots\text{OH}_2$

hydrogen bond (2.0 Å) to one of the methylenecyclopropene hydrogens. *Mulliken* charge analysis<sup>159</sup> show that the charge remain on the methylenecyclopropene radical. The calculated  $\text{CH}^{\delta+}\cdots\text{OH}_2$  binding energy is 11.0 kcal/mol. The other two isomers, **MCHb** and **MCHc**, with respective  $\text{CH}^{\delta+}\cdots\text{OH}_2$  length of 2.8 Å and a bifurcated 2.6 Å and 3.0 Å, are 1.0 kcal/mol and 1.3 kcal/mol less stable than **MCHa** respectively. Two degenerate structures are found for the hydrated cyclobutadiene ion (**CBH**). **CBHa** is found to be only 0.1 kcal/mol more stable than **CBHb**. **CBHa** consists of a bifurcated  $\text{CH}^{\delta+}\cdots\text{OH}_2$  length of 2.6 Å each and **CBHb** consists of a  $\text{CH}^{\delta+}\cdots\text{OH}_2$  length of 2.1 Å. Inspection of *Mulliken* charge densities shows  $\geq 95\%$  of the charge resides on the cyclobutadiene radical in both species. Calculated binding energies are 9.8 kcal/mol and 9.9 kcal/mol for **CBHa** and **CBHb** respectively. These values are in excellent agreement with the measured binding energy of  $9.1 \pm 1$  kcal/mol. As evident in Table 7, no conclusive evidence for isomer identification can be drawn from the calculated binding energies since all values are more or less within the experimental uncertainty. Only one structure was found for the hydrated 1,2,3-butatriene ion (**OBH**) complex. Again, it consists of a  $\text{CH}^{\delta+}\cdots\text{OH}_2$  (2.1 Å) type hydrogen bond. Like the other predicted structures,  $> 95\%$  of total charge resides on the radical ion. Binding energy for this complex is predicted to be 9.9 kcal/mol. Though the predicted binding energy agrees with the measured value, the 1,2,3-butatriene ion is not expected to be a constituent of our cluster beam as discussed in Chapter 4. The final  $\text{C}_4\text{H}_4^{++}\cdot\text{H}_2\text{O}$  complexes investigated was that of the 1-buten-3-yne ion (**VAH**). Four complexes were found for this species. The lowest energy complex (**VAHa**) consists of a  $\text{CH}^{\delta+}\cdots\text{OH}_2$  (1.9 Å) type hydrogen bond. As with the other predicted complexes, greater

than 95% of the charge remains on the 1-buten-3-yne radical. The binding energy in this case is 11.9 kcal/mol, the strongest predicted for all  $\text{C}_4\text{H}_4^{++}\cdot\text{H}_2\text{O}$  ions investigated. Though the 1-buten-3-yne radical ion is expected to be the other  $\text{C}_4\text{H}_4^{++}$  isomer in our beam, the predicted binding energy of 11.9 kcal/mol is larger than the measured binding energy, 9.1 kcal/mol. The skew of the measured binding energy towards lower values suggest that the 1-buten-3-yne radical ion, if present in our molecular beam, is a minor component of the  $\text{C}_4\text{H}_4^{++}$  isomers present. This is in agreement with the mobility results of section 4.4.5.2. The other complexes, **VAHb**, **VAHc**, and **VAHd** are respectively, 0.9 kcal/mol, 1.5 kcal/mol, and 2.5 kcal/mol less stable than **VAHa**.

**$\text{C}_4\text{H}_4^{++}\cdot(\text{H}_2\text{O})_2$ :** The G3(MP2) predicted geometries, relative energies, and binding energies for select  $\text{C}_4\text{H}_4^{++}\cdot(\text{H}_2\text{O})_2$  clusters are displayed in Table 8 **Error! Reference source not found.** The most stable hydrated methylenecyclopropene structure, **MC2Ha**, consists of the addition of another water molecule with carbon based  $\text{CH}^{\delta+}\cdots\text{OH}_2$  hydrogen bonds adjacent to that predicted for the minimum mono-hydrated species, **MCHa** (Table 7). Both  $\text{CH}^{\delta+}\cdots\text{OH}_2$  bond lengths are 1.9 Å; shorter than that of the mono-hydrated analog, **MCHa** (2.6 Å). The predicted **MC2Ha** binding energy is 10.1 kcal/mol and  $\approx 95\%$  of the charge remained on the methylenecyclopropene cation. The other structures, **MC2Hb**, **MC2Hc**, and **MC2Hd** are respectively, 1.04, 1.07, and 1.21 kcal/mol less stable than **MC2Ha**. Two degenerate structures are predicted as most stable for the hydrated cyclobutadiene structure (**CB2Ha** and **CB2Hb**). Essentially, all predicted hydrated cyclobutadiene ions can be considered degenerate Table 8. **CB2Ha** is essentially the addition of another water

molecule with bifurcated  $\text{CH}^{\delta+}\cdots\text{OH}_2$  bonds opposite the mono-hydrated **CBHa** water molecule. The newly formed bifurcated bonds lengths (2.2 and 2.1 Å) are shorter than those of the first water molecule (2.6 Å). For the other hydrated cyclobutadiene isomer, **CB2Hb**, the second water molecule is forms a  $\text{CH}^{\delta+}\cdots\text{OH}_2$  hydrogen bond (2.1 Å) below the center-of-mass plane of the mono-hydrated cation. Again the newly formed  $\text{CH}^{\delta+}\cdots\text{OH}_2$  bond is shorter than that predicted for the mono-hydrated analog. The G3(MP2) predicted binding energy is 9.2 kcal/mol and  $\approx 86\%$  of total charge resides on the cyclobutadiene ion in both cases (**CB2Ha** and **CB2Hb**). The most stable structure for the hydrated 1,2,3-butatriene cluster (**OB2Ha**) is displayed in Table 8. This cation, as was the case for the hydrated cyclobutadiene structures can all be considered degenerate. **OB2Ha** consists of carbon based bifurcated  $\text{CH}^{\delta+}\cdots\text{OH}_2$  hydrogen bonds on the 1,2,3-butatriene cation axis. The  $\text{CH}^{\delta+}\cdots\text{OH}_2$  bond lengths are 1.5 and 1.6 Å, again significantly shorter than that of the mono-hydrated (2.1 Å) ion. The predicted binding energy of **OB2Ha** is 9.2 kcal/mol. For the final hydrated  $\text{C}_4\text{H}_4^{+\cdot}$  isomer investigated (1-buten-3-yne, **VA**), the most stable structure consists of the second water molecule forming a  $\text{CH}^{\delta+}\cdots\text{OH}_2$  hydrogen bond across from the mono-hydrated unit. The predicted binding energy here is 9.6 kcal/mol.

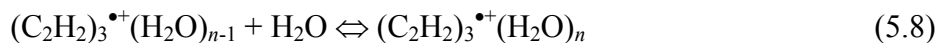
It is interesting to note that in all cases, none of the most stable structures are “externally” solvated.<sup>138</sup> In other words, the most stable structures consists of arrangements in which both water molecules are directly bound to the  $\text{C}_4\text{H}_4^{+\cdot}$  ion rather than to another water molecule. This is a somewhat different result than the ROHF/6-31+G\*\* prediction for hydrated benzene clusters.<sup>138</sup>



### 5.4.2 Trimer Ion Hydration. Further Evidence for the Formation of Benzene Radical Cation

In section 4.4.5.3, ion mobility measurements were used to calculate the reduced mobility ( $K_0$ ) and corresponding collision cross section ( $\Omega$ ) of mass selected acetylene trimer ions. These measurements show that the collision integrals of the  $(C_2H_2)_3^+$  and the benzene ions at 300 K are  $47.4 \pm 1.4 \text{ \AA}^2$  and  $47.9 \pm 1.4 \text{ \AA}^2$ ; respectively. A combination of mobility measurements showing similar  $\Omega$  for the trimer and benzene ions, CID mass spectra with similar fragmentation patterns, and calculated collision integrals,  $\Omega^{(1,1)}$ , for DFT predicted  $C_6H_6^+$  isomers provided evidence that ionized acetylene clusters isomerize efficiently to generate the benzene cation.

If the  $(C_2H_2)_3^+$  ( $A_3$ ) ion from ionized acetylene clusters isomerizes to form benzene ions, then the sequential binding energies of the trimer ion to several water molecules should be similar to the recently measured binding energies for the benzene cation (B)/water (H) association.<sup>138</sup> In order to confirm this, we measured the binding energies of the hydrated trimer ion,  $(C_2H_2)_3^+ \cdot (H_2O)_n$ , where  $n = 1 - 7$ . Figure 43-a displays the mass spectrum obtained following the injection of the  $(C_2H_2)_3^+$  into water vapor in the drift-tube. The hydrated  $(C_2H_2)_3^+$  ions are formed according to the stepwise association reaction (5.8).



For comparison, we also include the mass spectrum of the hydrated benzene cation (Figure 43-b) reported recently.<sup>138</sup> In both cases, two main groups of ions are observed: hydrated ions  $A_3W_n$  or  $BW_n$ , and protonated water clusters,  $W_nH$ . The similarity between the two

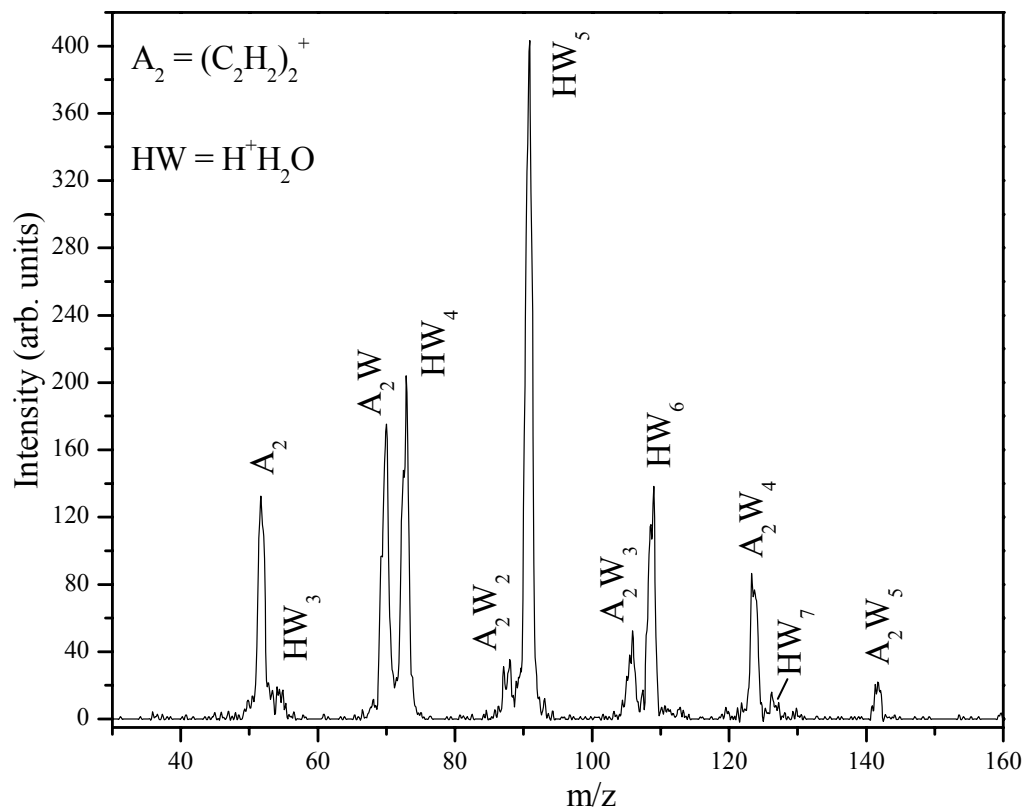


Figure 40: Acetylene dimer ions injected into (504 mTorr at 299 K) pure  $H_2O$  at 15.4 eV injection energy and 24 V drift voltage.

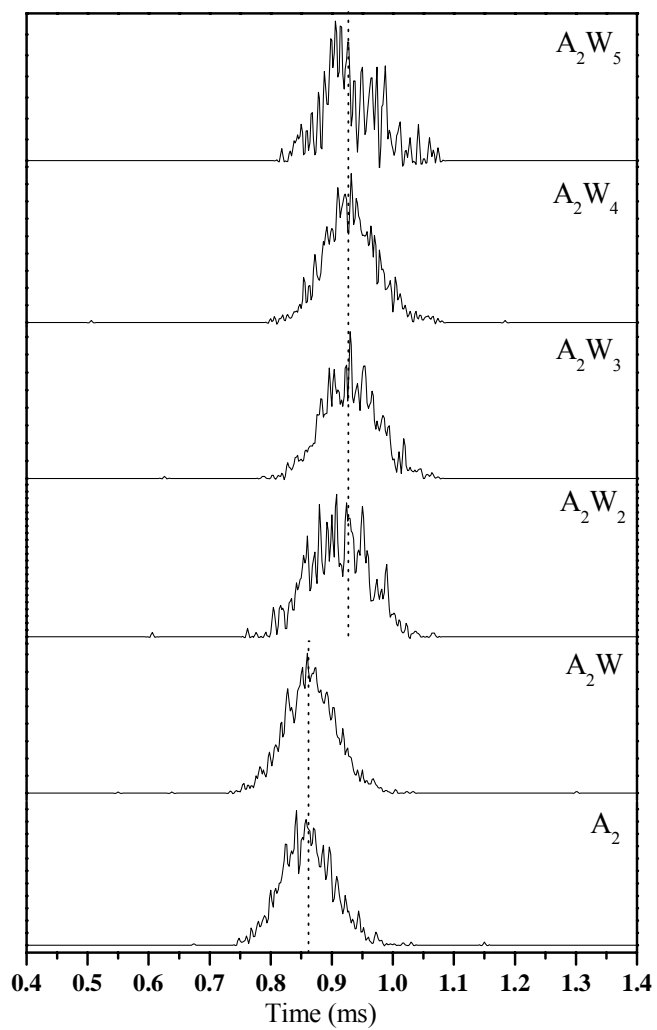


Figure 41: ATDs of  $(C_2H_2)_2^+(H_2O)_n$  clusters obtained by injecting  $(C_2H_2)_2^+$  at 15.4 eV (*lab*) into 526 mTorr of  $H_2O$  vapor and 24 V drift voltage at 307 K.

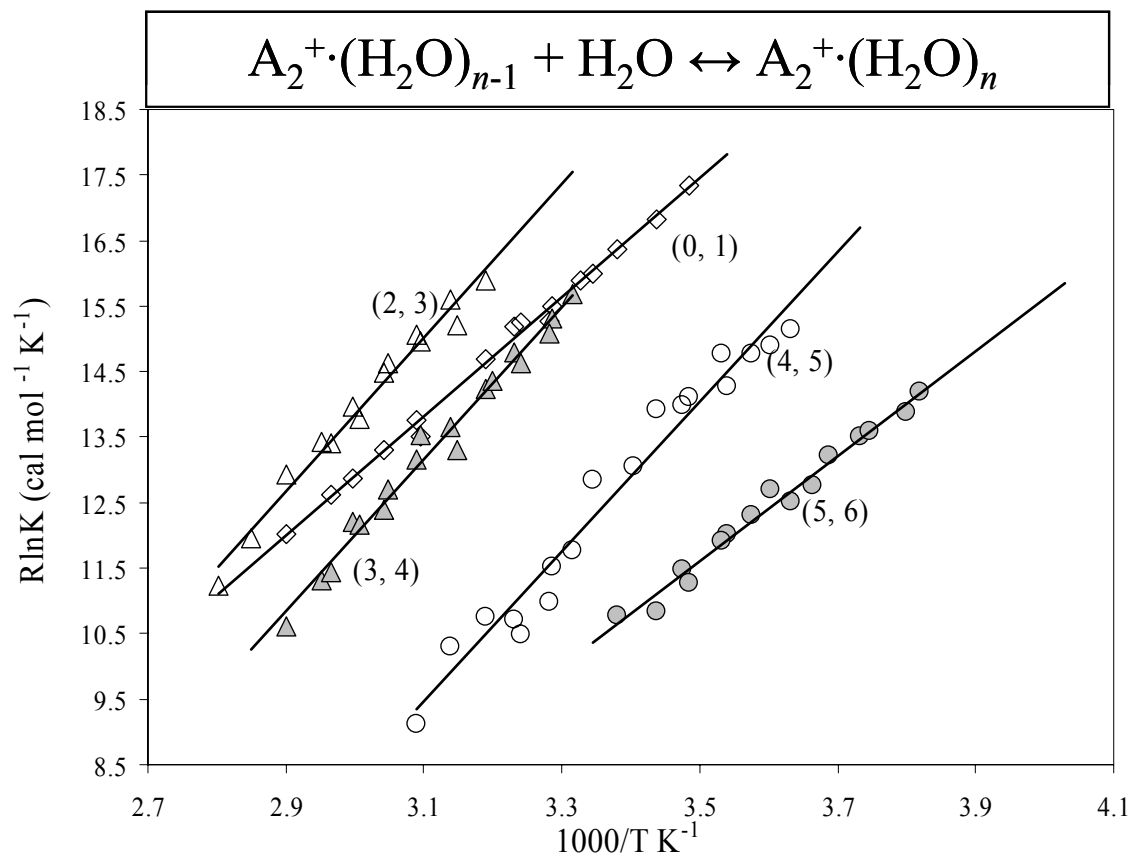


Figure 42: van't Hoff plots of the temperature dependence of the equilibrium constant of the reaction:  $A_2^+(H_2O)_{n-1} + H_2O \leftrightarrow A_2^+(H_2O)_n$ , where  $A_2^+ = (C_2H_2)_2^+$ .

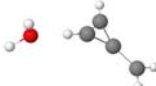




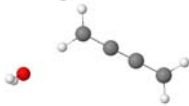




Table 6: Measured thermochemistry ( $\Delta H_{n-1,n}^{\circ}$  and  $\Delta S_{n-1,n}^{\circ}$ ) of clustering reaction 5.6.  
Clustering equilibrium (5.6)<sup>a</sup>

$N$	$\Delta H_{n-1,n}^{\circ}$	$\Delta S_{n-1,n}^{\circ}$
1	-9.1	-14.3
2	-9.2-10.1 <sup>b</sup>	
3	-11.7	-21.3
4	-11.6	-22.8
5	-11.4	-25.9
6	-8.0	-16.4

<sup>a</sup> Units are in kcal/mol; estimated error:  $\Delta H^{\circ} \pm 1$  kcal/mol,  $\Delta S^{\circ} \pm 3$  cal/mol K.

<sup>b</sup> Based on G3(MP2) predicted binding energies.

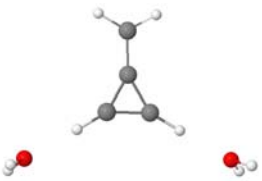
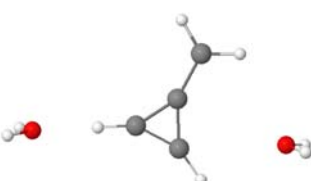
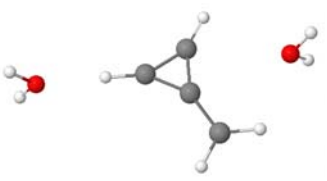
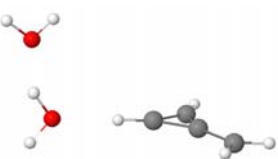

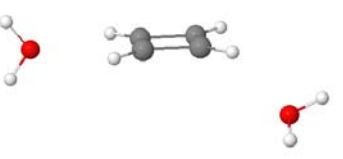
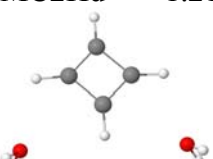
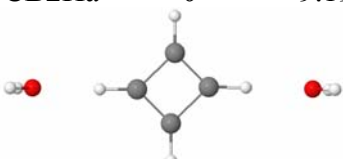
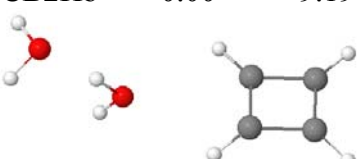
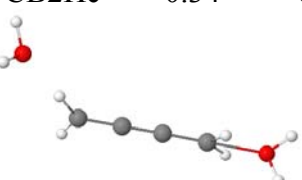
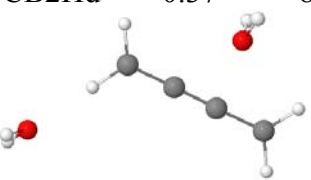
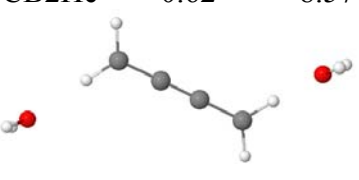
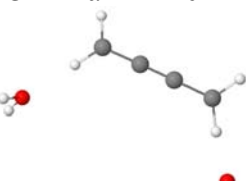
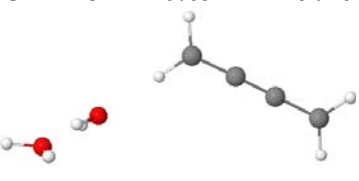
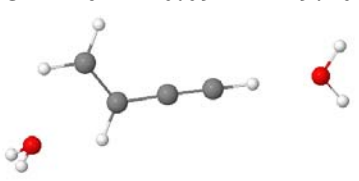
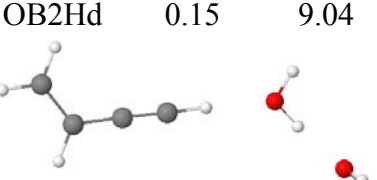
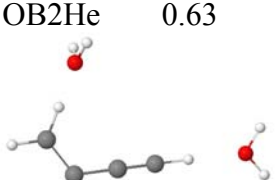
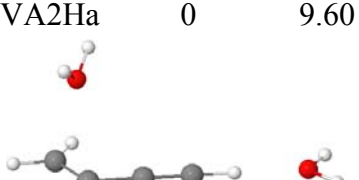
Table 7: Optimized structures of the  $\text{C}_4\text{H}_4^{++}\cdot\text{H}_2\text{O}$  species for select  $\text{C}_4\text{H}_4^{++}$  isomers. Energies are relative to the most stable species for a particular  $\text{C}_4\text{H}_4^{++}$  isomer. Optimization and energies were performed using the G3(MP2) method. Binding energies are for removal of a water molecule,  $\text{C}_4\text{H}_4^{++}\cdots\text{H}_2\text{O}$ .

Name <sup>a</sup>	Optimized Structures	Relative Energies (kcal/mol) <sup>b</sup>	Calculated Binding Energies (kcal/mol) <sup>b</sup>
MCHa		0	11.03
MCHb		0.96	10.07
MCHc		1.26	9.78
CBHa		0	9.89
CBHb		0.14	9.75
OBH		0	9.86
VAHa		0	11.88
VAHb		0.92	10.96
VAHc		1.49	10.39
VAHd		2.53	9.35

<sup>a</sup> Identities are inherited from optimized  $\text{C}_4\text{H}_4^{++}$  ions (Figure 25)

<sup>b</sup> All energies are ZPE corrected

Table 8: G3(MP2) structures of the  $\text{C}_4\text{H}_4^{++}\cdot(\text{H}_2\text{O})_2$  species for select  $\text{C}_4\text{H}_4^{++}$  isomers. Energies are relative to the most stable species for a particular  $\text{C}_4\text{H}_4^{++}$  isomer. Binding energies are for removal of a water molecule,  $\text{C}_4\text{H}_4^{++}\text{H}_2\text{O}\cdots\text{H}_2\text{O}$ .

Name <sup>a</sup>	Relative Energy <sup>b,c</sup>	Binding Energy <sup>b</sup>	Name <sup>a</sup>	Relative Energy <sup>b,c</sup>	Binding Energy <sup>b</sup>	Name <sup>a</sup>	Relative Energy <sup>b,c</sup>	Binding Energy <sup>b</sup>
	0	10.08		1.04	9.03		1.07	9.01
	1.21	8.87		0	9.19		0.00	9.19
	0.34	8.85		0.37	8.82		0.62	8.57
	0	9.19		0.09	9.10		0.09	9.10
	0.15	9.04		0.63	8.56		0	9.60
	0.49	9.11		1.27	8.33		1.27	8.33

<sup>a</sup> Identities are inherited from optimized  $\text{C}_4\text{H}_4^{++}$  ions (Figure 25)

<sup>b</sup> Energies in kcal/mol

<sup>c</sup> All energies are ZPE corrected



mass spectra displayed in Figure 43-a and Figure 43-b is remarkable, and confirms that the  $(\text{C}_2\text{H}_2)_3^+$  ion has the structure of the benzene cation.

The observation of protonated water clusters  $(\text{H}_2\text{O})_n\text{H}^+$  with  $n \geq 4$  is consistent with proton transfer reactions within the  $(\text{C}_2\text{H}_2)_3^+(\text{H}_2\text{O})_n$  clusters with  $n \geq 4$  according to:



We recently observed this reaction for the hydrated benzene cation  $\text{C}_6\text{H}_6^{\bullet+}(\text{H}_2\text{O})_{n-1}$  with  $n \geq 4$ .<sup>138</sup> The reaction is endothermic for  $n < 4$  and becomes thermoneutral at  $n = 4$  since the proton affinity of the water tetramer in the  $\text{C}_6\text{H}_6^{\bullet+}(\text{H}_2\text{O})_4$  cluster is almost similar to that of the phenyl radical  $\text{C}_6\text{H}_5^\bullet$ .<sup>138,163</sup> The observation of the deprotonation reaction (5.9) within the  $(\text{C}_2\text{H}_2)_3^+(\text{H}_2\text{O})_n$  clusters with  $n \geq 4$  confirms that the proton affinity of the radical generated by the deprotonation of the  $(\text{C}_2\text{H}_2)_3^+$  ion is similar to that of the phenyl radical  $\text{C}_6\text{H}_5^\bullet$  (211 kcal/mol).<sup>120</sup>

A good test of equilibrium is the observation of identical ATDs of the reactant and product ions. If the  $(\text{C}_2\text{H}_2)_3^+(\text{H}_2\text{O})_n$  and  $(\text{C}_2\text{H}_2)_3^+(\text{H}_2\text{O})_{n-1}$  ions are in equilibrium, their ATDs must be identical since both species are coupled by equilibrium. The ATDs of the  $(\text{C}_2\text{H}_2)_3^+(\text{H}_2\text{O})_{n-1}$  and  $(\text{C}_2\text{H}_2)_3^+(\text{H}_2\text{O})_n$  ions, displayed in Figure 44, show that the clusters  $(\text{C}_2\text{H}_2)_3^+(\text{H}_2\text{O})_n$  with  $n = 0 - 2$  have equal ATDs and those with  $n = 3 - 7$  have equal but longer arrival times. These ATDs indicate that ions in each group are coupled by equilibria according to the association reaction (5.8), but the two groups are not in equilibrium with each other. We attribute the separation into two groups to the deprotonation side-reaction

(reaction 5.9) that depletes the  $(\text{C}_2\text{H}_2)_3^+(\text{H}_2\text{O})_3$  ion and therefore perturbs the equilibrium between  $(\text{C}_2\text{H}_2)_3^+(\text{H}_2\text{O})_2$  and  $(\text{C}_2\text{H}_2)_3^+(\text{H}_2\text{O})_3$ . For this reason, the  $2 \rightleftharpoons 3$  equilibrium could not be measured. This behavior is similar to that observed for the  $\text{C}_6\text{H}_6^{\bullet+}/\text{water}$  study.<sup>138</sup>

The van't Hoff plots for the stepwise association of reaction (5.8) are presented in Figure 44 and the resulting  $\Delta H_{n-1,n}^\circ$  and  $\Delta S_{n-1,n}^\circ$  are given in Table 9. For comparison, the corresponding thermochemical data for the previously measured  $\text{C}_6\text{H}_6^{\bullet+}(\text{H}_2\text{O})_n$  system<sup>138</sup> are also included.

In both the  $(\text{C}_2\text{H}_2)_3^+(\text{H}_2\text{O})_n$  and the  $(\text{benzene})^+(\text{H}_2\text{O})_n$  clusters, the binding energies change little from  $n-1$ ,  $n = 0,1$  to  $6,7$ , unlike the usual regular decrease with  $n$  for the hydration of other molecular ions.<sup>158</sup> This can be explained by the presence of multiple binding sites with comparable energies for the water molecules to attach to the  $\text{C}_6\text{H}_6^{\bullet+}$  cation. Another interesting result is the remarkable increase in the  $-\Delta S_{6,7}^\circ$  values in both the  $(\text{C}_2\text{H}_2)_3^+(\text{H}_2\text{O})_n$  and the  $(\text{benzene})^+(\text{H}_2\text{O})_n$  clusters which suggests strong orientational restraint of water in these larger clusters.<sup>163</sup> In fact, three-dimensional cage-like structures involving multiple rings sharing edges are the lowest energy conformers of the water heptamer and octamer.<sup>163</sup> The observed large negative entropy of the  $(\text{C}_2\text{H}_2)_3^+(\text{H}_2\text{O})_7$  cluster, similar to the  $(\text{benzene})^+(\text{H}_2\text{O})_7$  cluster, is consistent with the formation of a cage-like structure by 7  $\text{H}_2\text{O}$  molecules around the benzene cation.<sup>163</sup>

From the results shown in Figure 43 and Figure 45 and in Table 9, it is clear that the similarity of the hydration data of the  $(\text{C}_2\text{H}_2)_3^+$  and the benzene ions provides further confirmation that the  $(\text{C}_2\text{H}_2)_3^+$  ion must have the same structure as the benzene cation.

Hartree Fock (ROHF/6-31+G\*\*) predicted geometries for the  $\text{C}_6\text{H}_6^+(\text{H}_2\text{O})_{1-4}$  ions extracted from a previous work<sup>138</sup> are shown in Figure 46.

The polymerization of ionized acetylene clusters to benzene cations is of significant interest in astrochemistry since it explains the origin of benzene and other PAHs in space. We suggest that the  $\text{C}_6\text{H}_6^+$  core ion can activate three acetylene molecules in the cluster to form another benzene cation and a neutral benzene where the new cation can repeat the cycle within the cluster. Eventually, the original ionized acetylene cluster would be converted to a benzene cluster or a mixed benzene-acetylene cluster where neutralization of the cluster will yield complex product molecules. Since cluster formation through termolecular processes is not very likely in the low-density astrochemical environments, these clusters can be stabilized by non-collisional mechanisms involving fast radiative stabilization especially in large complexes with many vibrational degrees of freedom.

### 5.4.3 Conclusions

The  $(\text{C}_2\text{H}_2)_3^+$  ion formed from the ionization of neutral acetylene clusters has unusual stability similar to the benzene cation; its primary fragment ions are similar to those reported from the benzene cation, it has a collision cross section of  $47.4 \text{ \AA}^2$  in helium at 300 K, similar to the value of  $47.9 \text{ \AA}^2$  reported for the benzene cation; it binds several water molecules with binding energies similar to those of the benzene cation with the corresponding number of water molecules; and finally it undergoes dissociative proton transfer reactions in the  $(\text{C}_2\text{H}_2)_3^+(\text{H}_2\text{O})_n$  clusters with  $n \geq 4$ , indicating that the proton affinity of the radical generated by the deprotonation of the  $(\text{C}_2\text{H}_2)_3^+$  ion is similar to that

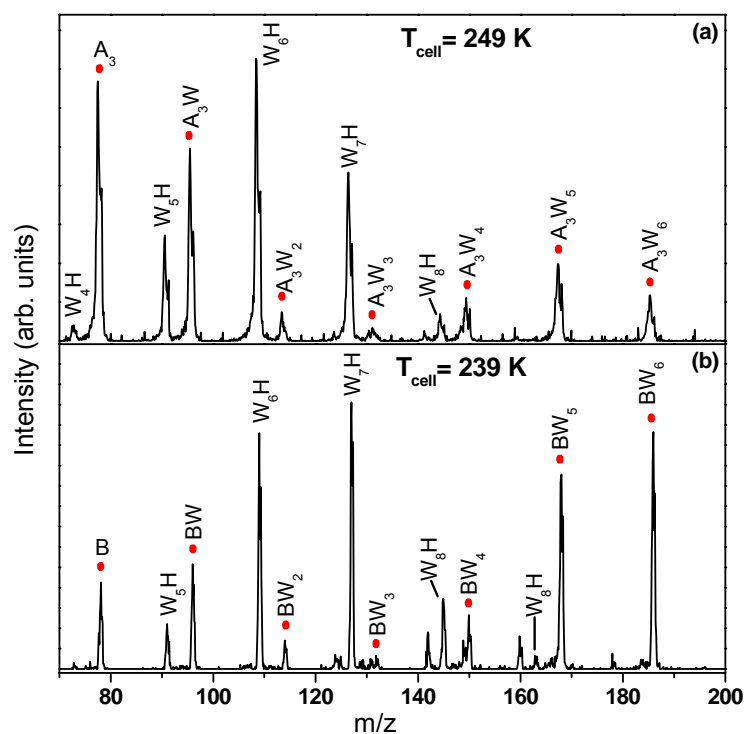


Figure 43: Mass spectrum obtained after injecting  $(\text{C}_2\text{H}_2)_3^+$  into water vapor (0.17 Torr at 249 K) in the drift-tube. Note the formation of hydrated  $(\text{C}_2\text{H}_2)_3^+(\text{H}_2\text{O})_n$  (i.e.  $\text{A}_3\text{W}_n$ ) and the deprotonation products  $\text{H}^+(\text{H}_2\text{O})_n$  (i.e.  $\text{W}_n\text{H}$ ). (b) Mass spectrum obtained after injecting  $\text{C}_6\text{H}_6^+$  into  $\text{H}_2\text{O}$  vapor (0.12 Torr at 239 K) in the drift tube.<sup>138</sup> Note the formation of hydrated  $\text{Bz}^+(\text{H}_2\text{O})_n$  (i.e.  $\text{BW}_n$ ) and the deprotonation products  $\text{H}^+(\text{H}_2\text{O})_n$  (i.e.  $\text{W}_n\text{H}$ ).

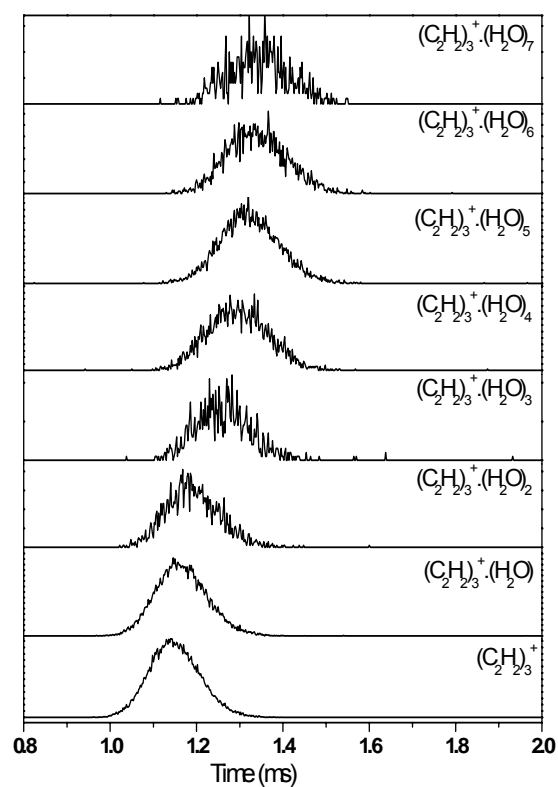


Figure 44: Arrival time distributions (ATDs) of  $(C_2H_2)_3^+(H_2O)_n$  clusters obtained by injecting  $(C_2H_2)_3^+$  at 11.9 eV (lab) into 166 mtorr of  $H_2O$  vapor and 24 V drift voltage at 250 K.

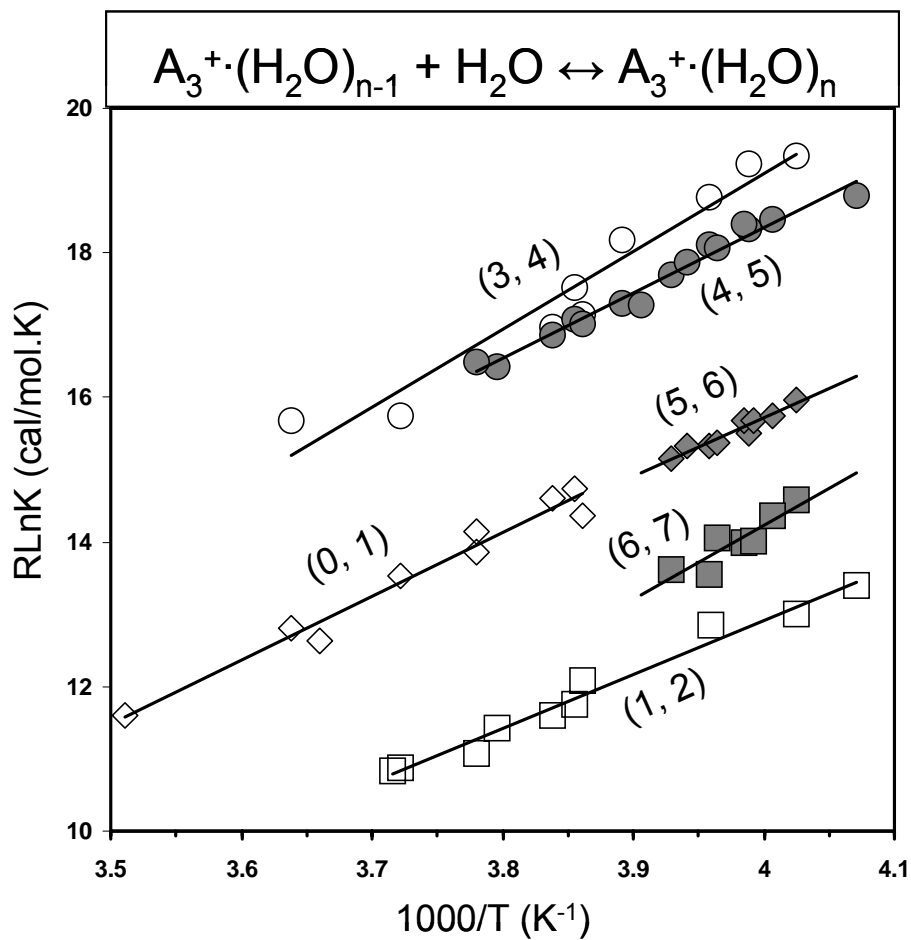


Figure 45: van't Hoff plots of the temperature dependence of the equilibrium constant of the reaction:  $(C_2H_2)_3^{\bullet+}(H_2O)_{n-1} + H_2O \rightleftharpoons (C_2H_2)_3^{\bullet+}(H_2O)_n$ .

Table 9: Measured binding energies and association entropies for the stepwise hydration of the mass selected  $(\text{C}_2\text{H}_2)_3^+$  ion compared to previously published results for the hydration of the  $\text{C}_6\text{H}_6^+$  ion<sup>138</sup>.

$n$	Clustering equilibrium (5.8) with the benzene cation		Clustering equilibrium (5.8) with the $(\text{C}_2\text{H}_2)_3^+$ cation	
	$\Delta H_{n-1,n}^\circ$ <sup>a</sup>	$\Delta S_{n-1,n}^\circ$ <sup>a</sup>	$\Delta H_{n-1,n}^\circ$ <sup>a</sup>	$\Delta S_{n-1,n}^\circ$ <sup>a</sup>
1	9.0	19.5	8.8	19.2
2	8.0	18.9	7.5	17.0
3	b	B	B	B
4	10.3	22.4	10.8	24.1
5	8.6	18.1	9.0	17.8
6	7.8	15.1	8.0	16.2
7	9.8	25.5	10.2	26.6

<sup>a</sup> Units:  $\Delta H_{n-1,n}^\circ$  in kcal/mol,  $\Delta S_{n-1,n}^\circ$  in cal/mol K. Error estimates based on standard deviation of van't Hoff plots,  $\Delta H^\circ \pm 1.0$  kcal/mol,  $\Delta S^\circ \pm 3$  cal/mol K.

<sup>b</sup> Could not be measured due to the very small intensity of the  $n = 3$  ions resulting from the depletion of these ions by the proton transfer reaction (5.9)

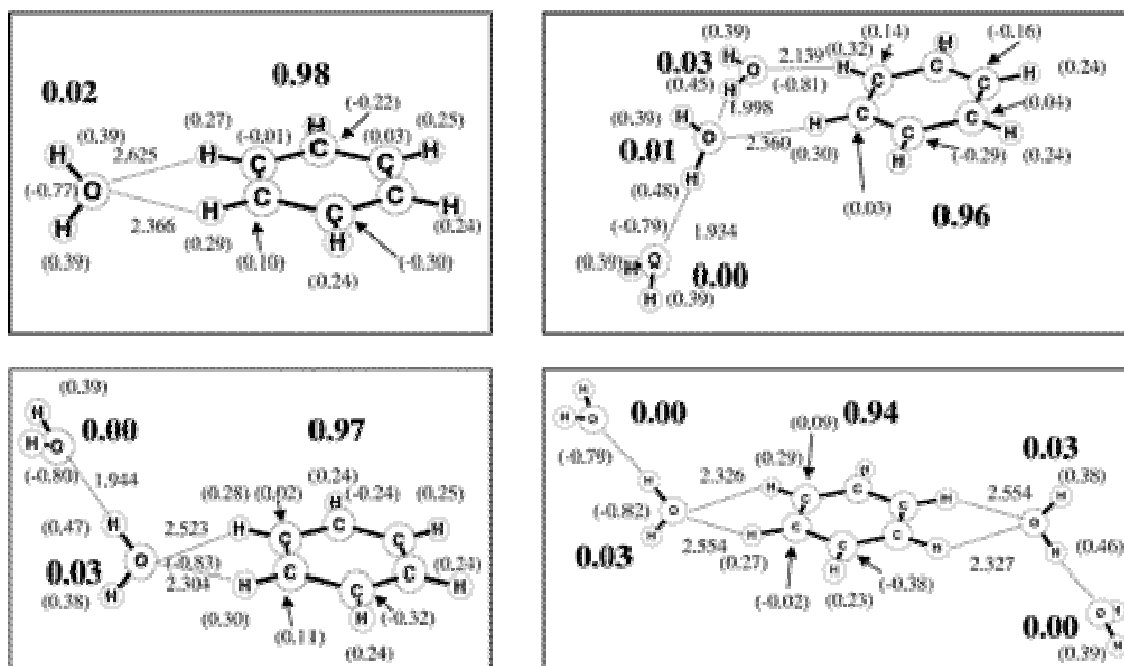


Figure 46: Equilibrium geometries for the  $C_6H_6^+(H_2O)_{1-4}$  clusters at the ROHF/6-31+G\*\* level extracted from previous work.<sup>138</sup> Bond lengths are in angstroms, while the molecular charges are in bold and the atomic charges are in parentheses.



of the phenyl radical  $\text{C}_6\text{H}_5^\bullet$  (211 kcal/mol). A cartoon representation of the overall scheme is given in Figure 47.

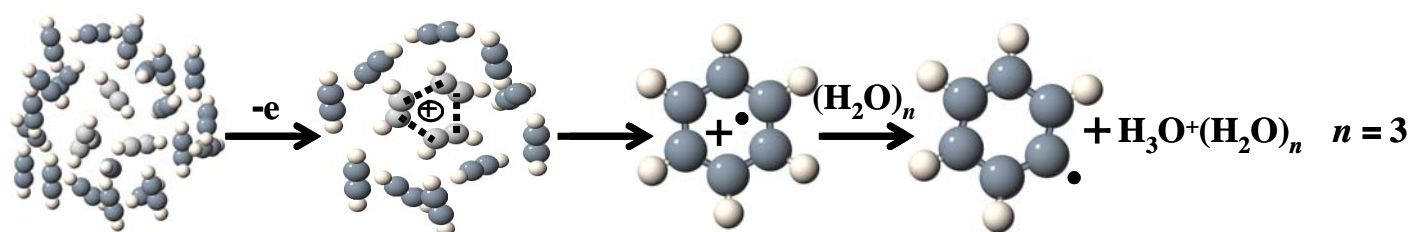


Figure 47: Cartoon representation of the overall trimerization reaction of ionized acetylene clusters and its reaction with water.

## Chapter 6 Interaction of the $\text{Fe}^+$ , $\text{Co}^+$ , and $\text{Ni}^+$ Cations with Acetylene Clusters

### 6.1 Introduction

The majority of olefinic and acetylenic polymerization processes are catalytic, most often involving a heterogeneous catalyst. The study of the analogous processes in the gas phase and within clusters is important for the design of new catalysts with tailored reactivity and selectivity. The interaction of transition metal cations with acetylenic and olefinic molecules has been an area of considerable interest due to the facile tendency of these cations to mediate isomerization of these molecules.<sup>165-167</sup>

Though numerous theoretical and experimental inquiries have been made into the interactions and reactions of transition metals/acetylene clusters,  $\text{M}^+(\text{C}_2\text{H}_2)_n$ , these studies have mainly concentrated on the monomer adduct,  $\text{M}^+\text{C}_2\text{H}_2$ .<sup>55-58</sup> Other studies have been devoted to the  $\text{Fe}^+$ -mediated cyclotrimerization of acetylene to form benzene.<sup>59-62</sup> Not much have been done by way of a direct comparison of the structures, packing characteristics, vibrational frequencies, and suspected intracuster reactivity of larger acetylene clusters with transition metals,  $\text{M}^+(\text{C}_2\text{H}_2)_n$ ;  $n \geq 2$ .<sup>63,64</sup> We present here TOF mass spectrometric and density functional (DFT) results of the interaction and reactivity of acetylene clusters with iron, cobalt, and nickel monocations. We discuss and compare the structures, binding energies, and C-H vibrational frequencies of these complexes,  $\text{Fe}^+/\text{Co}^+/\text{Ni}^+(\text{C}_2\text{H}_2)_n$ . We also discuss the suspect  $\text{Co}^+$ -mediated cyclotrimerization reaction

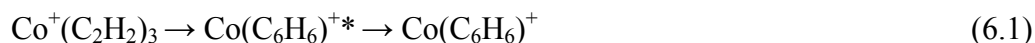
of acetylene to form benzene,  $\text{Co}^+(\text{C}_2\text{H}_2)_3 \rightarrow \text{Co}(\text{C}_6\text{H}_6)^+$ . Predicted intermediate structure and calculated reaction thermochemistry are presented as well.

## 6.2 Experimental and Theoretical Methodology.

The instrument utilized here, reflectron time-of-flight mass spectrometer (RTOF), was discussed in detail in section 2.4 of this text and will briefly be discussed here. Cold acetylene clusters are created by supersonic expansion of a 2-5 % mixture of acetylene (BOC GASES<sup>®</sup>) in helium (ultrahigh purity 6.0, Spectra Gases, 99.99 %, 3-4 atm) carrier gas. The cold clusters subsequently interact with laser (2<sup>nd</sup> harmonic, 532 nm, of a Nd-YAG laser; Continuum-Surelite SSP-I, 8-10 *ns* width) vaporized metal cations (Ni rod, 99.99 % purity; Fe rod, 99.98 % purity; Co rod, 99.9 % purity). Stabilization of the resulting  $\text{M}^+(\text{C}_2\text{H}_2)_n$  clusters is in most part by evaporative loss of acetylene molecules. The ionized clusters are subsequently collimated by a 0.3 mm conical skimmer. In the second chamber, the ionized clusters are accelerated through the drift tube to a microchannel plate (MCP) detector. Timing and data acquisition for this experiment was discussed previously.

The B3LYP hybrid functional<sup>114</sup> of the density functional theory (DFT) was utilized in all calculations here. This functional has been shown to give acceptable results for geometries, binding energies, and vibrational frequencies of transition metal complexes.<sup>55,168</sup> All optimizations employed the 6-31+G(*d,p*) basis set for the C and H atoms and the Wachters+*f* (14*s* 11*p* 6*d* 3*f*)/[8*s* 6*p* 4*d* 1*f*]<sup>169,170</sup> basis set for all transition metal cations. Energies used for calculating binding energies and other thermochemistries

were zero point energy (ZPE) corrected and all C-H stretch frequencies were scaled by 0.96. The geometry of the intermediate,  $\text{Co}(\text{C}_6\text{H}_6)^{+*}$ , shown in reaction (6.1) was predicted using the synchronous transit-guided quasi-Newton (STQN) method of the Gaussian 03 package.<sup>122</sup>



Imaginary frequencies, indicative of local minima (saddle point) or transition states was not observed for the optimized  $\text{M}^+(\text{C}_2\text{H}_2)_n$  and  $\text{MC}_6\text{H}_6^+$  clusters. All transition states are real as they possess only one imaginary frequency.

### 6.3 Results and Discussion

Shown in Figure 48 is the TOF mass spectrum for the  $\text{Fe}^+$ /acetylene clusters (low masses). The major series observed was the  $\text{Fe}^+(\text{C}_2\text{H}_2)_n$  clusters and corresponding isotopic peaks,  $^{54/57/58}\text{Fe}^+(\text{C}_2\text{H}_2)_n$ . The iron dimer cation,  $\text{Fe}_2^+$ , and subsequent solvation peaks,  $\text{Fe}_2^+(\text{C}_2\text{H}_2)_{1-2}$ , were observed as well. Also observed was  $m/z$  ratios of 78, 77, and 76 amu corresponding to fragmentation products  $(\text{C}_2\text{H}_2)_3^+$ ,  $\text{C}_2\text{H}^+(\text{C}_2\text{H}_2)_2$ , and  $\text{C}_2^+(\text{C}_2\text{H}_2)_2$  respectively. These fragment ions are suspected products of the well known  $\text{Fe}^+$ -induced cyclotrimerization reaction of acetylene to form the benzene ion,  $\text{C}_6\text{H}_6^+$ , and its fragment product ions,  $\text{C}_6\text{H}_5^+$  and  $\text{C}_6\text{H}_4^+$ , as previously reported by Schwarz and co-workers.<sup>59,60</sup> The larger homogeneous acetylene cluster,  $(\text{C}_2\text{H}_2)_n^+$ , peaks mainly result from high energy fragmentation of the  $\text{M}^+(\text{C}_2\text{H}_2)_n$  clusters and may also be produced by electron impact (EI) ionization. Here, the ionizing electrons are ejected from the metal target by laser ablation. The mass peak corresponding to  $\text{FeOH}^+(\text{C}_2\text{H}_2)_3$  or  $\text{Fe}^+\text{C}_2\text{H}(\text{C}_2\text{H}_2)_2\text{H}_2\text{O}$ , the result of water

impurity in the stagnation line, was observed as well. Figure 49 displays the mass spectrum for  $\text{Co}^+$ /acetylene clusters ( $< 170$  amu). As was the case for the  $\text{Fe}^+$ /acetylene clusters, the major series observed was the  $\text{Co}^+(\text{C}_2\text{H}_2)_n$  clusters. The dimer cation ( $\text{Co}_2^+$ ) and its solvation product,  $\text{Co}_2^+\text{C}_2\text{H}_2$ , and the hydride cation clusters,  $\text{CoH}^+(\text{C}_2\text{H}_2)_n$  were observed as well. The  $m/z = 78$ ,  $77$ , and  $76$  peaks were also observed and are suspected to also be products of a  $\text{Co}^+$ -mediated trimerization reaction to form the  $\text{C}_6\text{H}_6^+$  ion. The heightened intensity of the  $\text{C}_6\text{H}_6^+$  peak (and fragment peaks  $\text{C}_6\text{H}_5^+$  and  $\text{C}_6\text{H}_4^+$ ) relative to the other  $(\text{C}_2\text{H}_2)_n^+$  and  $\text{C}_2\text{H}(\text{C}_2\text{H}_2)_{n-1}^+$  peaks suggest the former population is fed by more than just the fragmentation reaction channel which is in agreement with a  $\text{Co}^+$ -mediated cyclotrimerization reaction. Dehydrogenation of the  $(\text{C}_2\text{H}_2)_n^+$  clusters may be enhanced by C-H bond activation resulting from donation of acetylene electron density to the  $d$ -orbital of the cobalt cation and a corresponding back-donation of cobalt electron density to the anti-bonding orbital of acetylene (Dewar-Chatt-Duncanson model).<sup>53,54</sup> Clusters corresponding to acetone, a stabilizing agent for pressurized acetylene, were observed in the mass spectrum. The main series for the  $\text{Ni}^+$ /acetylene clusters (not shown) was  $\text{Ni}^+(\text{C}_2\text{H}_2)_n$ . The  $\text{Ni}_2^+(\text{C}_2\text{H}_2)_n$  clusters was observed also.

Shown in Figure 50 is the TOF mass spectrum for the larger  $\text{Fe}^+(\text{C}_2\text{H}_2)_n$  clusters. The inset displays a corresponding intensity plot. Inspection of this spectra showed enhanced intensity for the  $\text{Fe}^+(\text{C}_2\text{H}_2)_2$  cluster. This enhanced intensity suggest stabilization

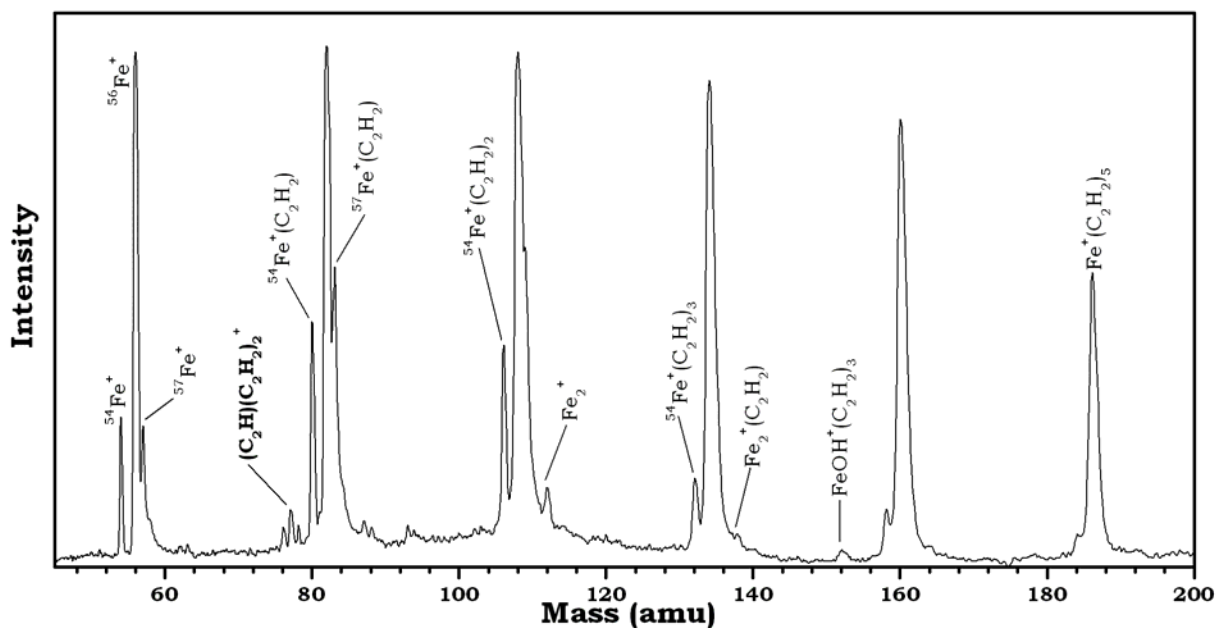


Figure 48: Time of Flight (TOF) mass spectrum of  $\text{Fe}^+(\text{C}_2\text{H}_2)_n$  clusters at early arrival times (low mass range). A 3 % acetylene/helium (60 PSI) was used in cluster generation. Laser intensity at the target surface was  $\sim 10^7 \text{ Wcm}^{-2}$ . Deflector voltages were adjusted to accommodate smaller clusters.

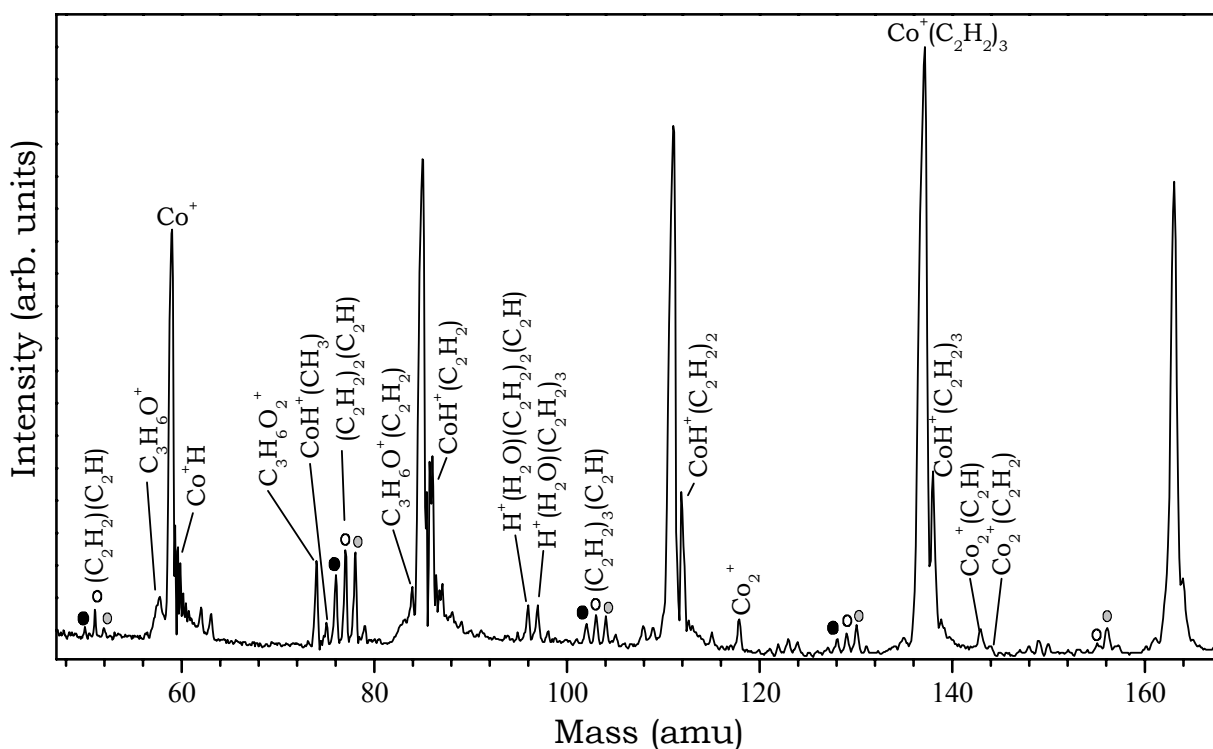


Figure 49: Time of Flight (TOF) mass spectrum for low mass products of  $\text{Co}^+(\text{C}_2\text{H}_2)_n$  clusters. The Nd: YAG laser was timed to fire  $578.7 \mu\text{s}$  after the nozzle opened ( $t_0$ ). The acceleration plates were pulsed  $1.08 \text{ ms}$  after  $t_0$ . Pressure of the first chamber was  $1.3 \times 10^{-4} \text{ Torr}$ . A 3 % acetylene/helium (60 PSI) was used in cluster generation. Laser intensity at the target surface was  $\sim 10^7 \text{ Wcm}^{-2}$ . Deflector voltages were adjusted to accommodate smaller clusters.



of the dimer cluster by a highly symmetric  $\text{Fe}^+$ -bisacetylene arrangement or formation of a stable  $\text{Fe}^+$ -dimer complex,  $\text{Fe}^+\text{C}_4\text{H}_4$ . As will be discussed later, DFT predicted energies suggest the  $\text{Fe}^+$ -bisacetylene geometry to be more stable than the dimerized complex. Further inspection of the mass spectra shows an unusual drop in intensity for the  $\text{Fe}^+(\text{C}_2\text{H}_2)_5$  peak. This behavior suggests only four acetylene molecules are required for geometric closing of the  $\text{Fe}^+$  cation first solvation shell. The diminished intensity of the pentamer peak indicates lowered stability for this cluster suggesting a  $\text{Fe}^+(\text{C}_2\text{H}_2)_{4+1}$  structure. The reduced  $\text{Fe}^+(\text{C}_2\text{H}_2)_5$  cluster population can be visualized as resulting from a geometric structure with a shallow potential energy well. Consequently, a higher proportion of its population will have enough internal energy to surpass the evaporative barrier. It should be mentioned that the  $n = 4$  cluster does not necessarily represent the cations coordination number but rather stability from efficient ligand packing. The  $\text{Fe}^+(\text{C}_2\text{H}_2)_{14}$  cluster was also observed to be a magic number. This magic number, also observed in cobalt and nickel/acetylene clusters, is suspected to be an acetylene polymerization complex of the form,  $\text{Fe}^+\text{C}_{28}\text{H}_{28}$ . Interestingly, the same magic number ( $n = 14$ ) was observed in ionized homogeneous acetylene clusters (Figure 19). Some authors have postulated intracuster isomerization reaction to form a covalent  $\text{C}_{28}\text{H}_{28}^+$  ion.<sup>43</sup>

Figure 51 displays the mass spectrum for larger  $\text{Co}^+(\text{C}_2\text{H}_2)_n$  clusters. Inspection of this spectrum reveals a remarkable and reproducible trend; oscillatory magic numbers for the  $n = 3, 6, 9$ , and  $12$  clusters. We suspect a  $\text{Co}^+$ -mediated multiple intracuster reaction process in which a benzene ring and other covalent  $\text{C}_6\text{H}_6$  products (perhaps multiple cyclic

rings) are formed. Dissipation of excess energy from these reactions is expected to be by evaporative loss of acetylene molecules.

Using FT-ICR mass spectrometry, Schwarz and Wesendrup<sup>60</sup> concluded that the cobalt cation was unreactive in regards to mediation of the acetylene cyclotrimerization reaction. In fact, most late first-row transition metal cations with the exception of iron are not expected to mediate the cyclotrimerization reaction. We therefore suspect this reaction to be the consequence of cooperative ligand arrangement in the acetylene clusters. The cluster environment, much like the condensed phase, increases the rate of certain termolecular processes which may otherwise be inefficient under gas-phase conditions.<sup>45-49</sup> It should be mentioned that at the experimental pressures ( $\ll 5 \times 10^{-5}$  mbar) utilized by Schwarz *et al.*,<sup>60</sup> the probability of orientational collisions amenable to efficient  $\text{Co}^+$ -mediated trimerization reaction kinetics might be too low. Cluster size-specific transition metal-mediated intracluster reactions may also be responsible for the observed magic numbers.<sup>63,171</sup> DFT calculations investigating the  $\text{Co}^+$ -mediated trimerization reaction is discussed below.

Figure 52 displays the mass spectrum of  $\text{Ni}^+(\text{C}_2\text{H}_2)_n$  clusters. Here, the  $n = 4$  peak showed diminished intensity (relative to the trimer peak) suggesting a particularly stable structure for the  $n = 3$  cluster. The enhanced  $n = 3$  cluster is suspected to result from efficient packing of three acetylene molecules around the nickel cation. Using IR dissociation experiments, Duncan and co-workers suggested the Ni/trimer geometry to be analogous to that of the tris(ethylene)platinum complex.<sup>63</sup> The same authors suggested four acetylene molecules are needed to close the  $\text{Ni}^+$  first solvation shell. The latter conclusion

is in agreement with our mass spectrum where an unusually diminished  $\text{Ni}^+(\text{C}_2\text{H}_2)_5$  peak is observed. Figure 52 also shows enhanced intensities for the  $n = 2$  and 14 peaks. Duncan and group suggested the Ni-cyclobutadiene  $\pi$ -complex ( $\text{Ni}^+\text{C}_4\text{H}_4$ ) is formed in larger clusters from a size-specific intracuster reaction.<sup>63</sup>

### 6.3.2 DFT Predicted Structures and Energies of $\text{Fe}^+$ , $\text{Co}^+$ , and $\text{Ni}^+(\text{C}_2\text{H}_2)_n$ clusters

#### $\text{Fe}^+\text{C}_2\text{H}_2$ , $\text{Co}^+\text{C}_2\text{H}_2$ , and $\text{Ni}^+\text{C}_2\text{H}_2$

The DFT predicted global minimum structures for the  $\text{Fe}^+(\text{C}_2\text{H}_2)_n$ ,  $\text{Co}^+(\text{C}_2\text{H}_2)_n$ , and  $\text{Ni}^+(\text{C}_2\text{H}_2)_n$  clusters with  $n = 1, 2$ , and 3 are displayed in Figure 53, Figure 54, and Figure 55 respectively. Spin contamination,  $S^2$ , was high for the  $\text{Fe}^+(\text{C}_2\text{H}_2)_n$  and  $\text{Co}^+(\text{C}_2\text{H}_2)_n$  clusters; 3.75 and 2.00 respectively. High spin contamination is not surprising for these clusters; especially the iron cation in which the ground electronic state of the bare cation,  $^6D\ 3d^6(^5D)4s$ , differs from that in the metal/acetylene complex ( $^4B_2$ ).  $S^2$  for  $\text{Ni}^+(\text{C}_2\text{H}_2)_n$  was 0.75. As shown in Table 10 and Figure 53, C-C bond lengths for the monomer clusters,  $\text{M}^+\text{C}_2\text{H}_2$ , are 1.26 Å, 1.26 Å, and 1.24 Å for iron, nickel, and cobalt respectively. The distance between the metal cation and mid-point of the C=C bond,  $\text{M}^+-\parallel$ , are 1.86 Å, 1.90 Å, and 1.88 Å respectively. These lengths are in good agreement with previously reported B3LYP/6-311+G\*/6-31G\*  $\text{M}^+-\parallel$  values of 1.91 Å, 1.90 Å, and 1.88 Å for iron, cobalt, and nickel respectively.<sup>55</sup> CCH angles are 157.8°, 163.0°, and 165.0° for iron, cobalt, and nickel respectively and followed the expected trend of increasing distortion of the acetylene ligand from linearity from nickel to iron. This trend is the result of increasing cation-acetylene interaction (ligand activation) from nickel to iron.

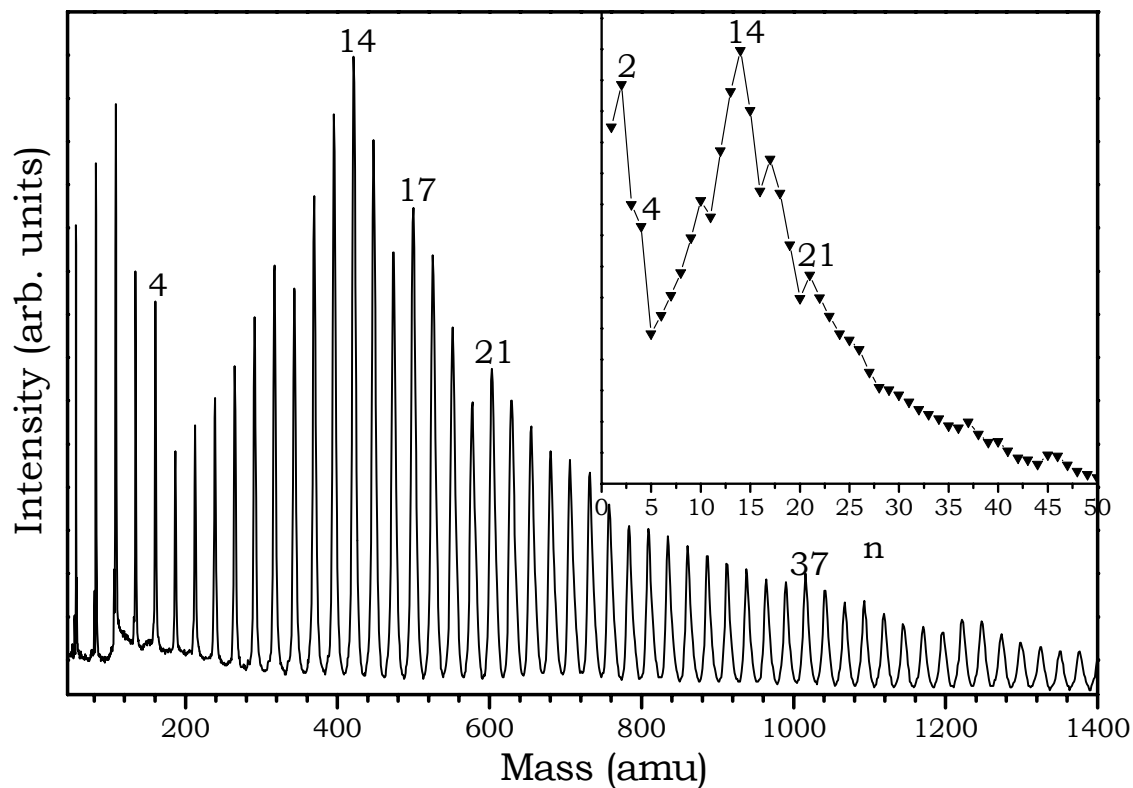


Figure 50: Time of Flight (TOF) mass spectrum and intensity plot (inset) for  $\text{Fe}^+(\text{C}_2\text{H}_2)_n$  clusters. Notice the  $n = 14$  magic number which was observed for all transition metals investigated. A 3% acetylene/helium (60 PSI) was used in cluster generation. Laser intensity at the target surface was  $\approx 10^7 \text{ Wcm}^{-2}$ . Deflector voltages were adjusted to accommodate larger clusters.

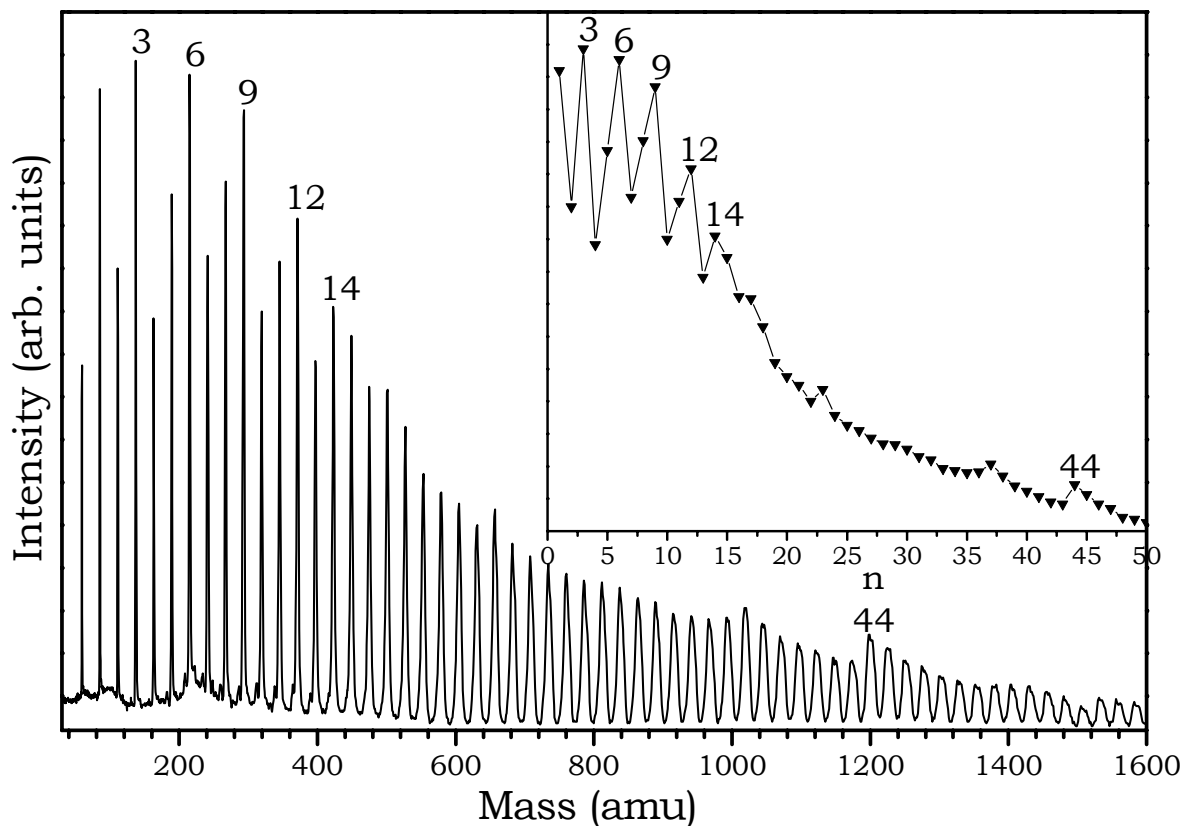


Figure 51: Time of Flight (TOF) mass spectrum and intensity plot (inset) for  $\text{Co}^+(\text{C}_2\text{H}_2)_n$  clusters. Intriguing cyclic magic numbers (3, 6, 9, and 12) suggest a multiple cyclization process mediated by the cobalt cation. A 3% acetylene/helium (60 PSI) was used in cluster generation. Laser intensity at the target surface was  $\approx 10^7 \text{ Wcm}^{-2}$ . Deflector voltages were adjusted to accommodate larger clusters.

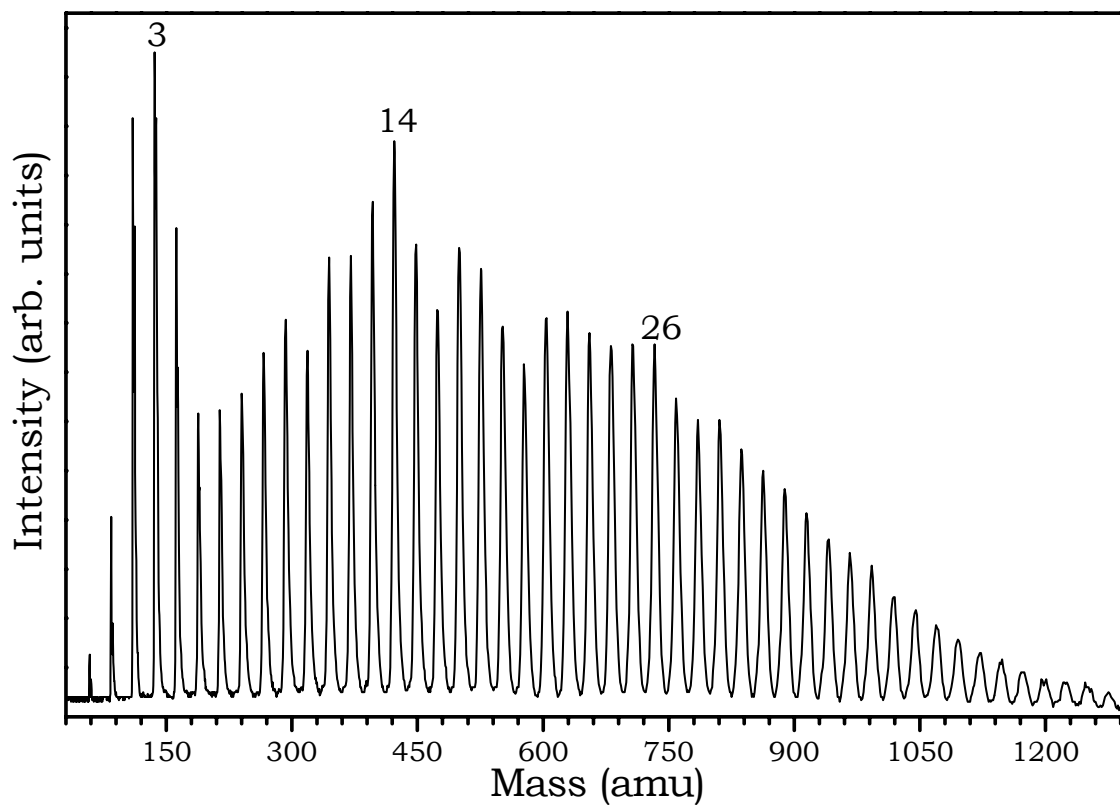


Figure 52: TOF mass spectrum for  $\text{Ni}^+(\text{C}_2\text{H}_2)_n$  clusters. Notice the  $n = 14$  magic number as well as the  $n = 3$  magic number. A 3% acetylene/helium (60 PSI) was used in cluster generation. Laser intensity at the target surface was  $\approx 10^7 \text{ Wcm}^{-2}$ . Deflector voltages were adjusted to accommodate larger clusters.

Activation of the C-C and C-H bonds by the metal cation is indicated by increased bond lengths, red-shifts of vibrational frequencies, and deviation of the CCH bond angles from linearity ( $\angle \text{CCH} = 180^\circ$ ). The symmetry and ground electronic state for all monomer clusters are predicted to be  $C_{2v}$  and  ${}^nB_1$  respectively. C-H stretch frequencies predicted here and in previous theoretical inquiries are also shown in Table 10. The predicted symmetric (S) and asymmetric (A) C-H frequencies for the nickel/acetylene monomer are  $3172 \text{ cm}^{-1}$  and  $3251 \text{ cm}^{-1}$  respectively. These values fall between previously reported values of  $3192 \text{ cm}^{-1}(\text{S})/3273 \text{ cm}^{-1}(\text{A})$  and  $3156 \text{ cm}^{-1}(\text{S})/3204 \text{ cm}^{-1}(\text{A})$ .<sup>55,64</sup>

The only discrepancy between the current work and previous investigations has to do with the  $\text{Fe}^+\text{C}_2\text{H}_2$  ground electronic state.<sup>55,56</sup> The previously predicted  $\text{Fe}^+\text{C}_2\text{H}_2$  ground electronic state was  ${}^4B_2$  and not  ${}^4B_1$  as predicted here. We attribute this discrepancy to the basis set (Wachters+*f* basis set) utilized and DFTs' less than adequate description of spin change in going from the bare  $\text{Fe}^+$  to the complexed  $\text{Fe}^+\text{C}_2\text{H}_2$ . Klippenstein *et al.*, using the B3LYP/6-311+G\* method described a similar problem.<sup>55</sup> For  $\text{Co}^+$  and  $\text{Ni}^+$  complexes where spin is conserved, the results from the Wachters+*f* basis set agree with previous results. It should be pointed out that, calculations by Duncan *et al.* using the B3LYP/6-311+G(3*df*,2*p*) method also arrived at the same ground electronic state ( ${}^4B_1$ ) as we did.<sup>64</sup> Our calculated binding energy,  $D_e[\text{Fe}^+\cdots\text{C}_2\text{H}_2]$ , for the  $\text{Fe}^+\text{C}_2\text{H}_2$  cluster, 46.5 kcal/mol, is approximately 8-10 kcal/mol greater than the experimentally measured value of  $38 \pm 0.5 \text{ kcal/mol}$ <sup>57</sup> and  $36.1 \pm 1.9 \text{ kcal/mol}$ <sup>172</sup> and  $\approx 4 \text{ kcal/mol}$  larger than the previous theoretical<sup>55</sup> value of 42.6 kcal/mol. The discrepancy between experimental and calculated

binding energies for the  $\text{Fe}^+\text{C}_2\text{H}_2$  cluster is attributed DFTs' poor handling of spin change in going from the bare iron cation to the clustered cation.  $D_e[\text{Co}^+\cdots\text{C}_2\text{H}_2]$  and  $D_e[\text{Ni}^+\cdots\text{C}_2\text{H}_2]$  are 45.9 kcal/mol and 47.4 kcal/mol respectively; in excellent agreement with IRMPD values of  $43.0 \pm 1.9$  kcal/mol and  $44.9 \pm 1.9$  kcal/mol respectively<sup>172</sup> and theoretical values of 47.4 kcal/mol and 48.0 kcal/mol respectively.<sup>55</sup>

Table 11 displays the degree of C-H stretch frequency red-shift of the predicted cluster ions,  $\text{M}^+(\text{C}_2\text{H}_2)_{1-3}$ , compared to that predicted for the neutral acetylene molecule,  $3294\text{ cm}^{-1}$  (A) and  $3388\text{ cm}^{-1}$  (S) (B3LYP/6-31+G\*\*<sub>s</sub>; scaled by 0.96). As expected, the magnitude of the C-H stretch frequency red-shift increases from nickel to iron. It should be mentioned that the predicted C-H stretch frequencies for the neutral monomer is in agreement with the experimental value of  $3289\text{ cm}^{-1}$  and  $3374\text{ cm}^{-1}$  for the asymmetric (A) and symmetric (S) stretches respectively.<sup>120</sup>

The insertion product,  $\text{H-M}^+-\text{CCH}$ , and metal-vinylidene,  $\text{M}^+-\text{CCH}_2$ , product were not considered as previous investigations have determined these complexes to be less stable than the  $\pi$ -complex,  $\text{M}^+\text{C}_2\text{H}_2$ , studied here.<sup>58,173,174</sup> Overall agreement between the predictions of the current work and previously reported experimental and theoretical values confirm our theoretical approach as adequate for describing these systems. Charge densities (*Mulliken*)<sup>159</sup> for the  $\text{Fe}^+$ ,  $\text{Co}^+$ , and  $\text{Ni}^+$  cations in the monomer cluster are 81%, 71%, and 71% respectively.



### **$\text{Fe}^+(\text{C}_2\text{H}_2)_2$ , $\text{Co}^+(\text{C}_2\text{H}_2)_2$ , and $\text{Ni}^+(\text{C}_2\text{H}_2)_2$**

As shown in Figure 54, the  $\text{Fe}^+$ ,  $\text{Co}^+$ , and  $\text{Ni}^+$  dimer clusters are predicted to possess the planar bis-acetylene geometry. The  $\text{Fe}^+(\text{C}_2\text{H}_2)_2$  and  $\text{Co}^+(\text{C}_2\text{H}_2)_2$  ions form very symmetric clusters; both possess the  $D_{2h}$  symmetry. The  $\text{Ni}^+(\text{C}_2\text{H}_2)_2$  cluster is predicted to possess a lower symmetry,  $C_{2v}$ . The reduction in symmetry is the result of Jahn-Teller interactions, known to perturb symmetries in  $\text{Ni}^+$  complexes.<sup>64</sup> As shown in Table 12 and Figure 54, the C-C bond length for the  $\text{Fe}^+(\text{C}_2\text{H}_2)_2$  cluster is 1.23 Å; slightly shorter than that predicted for the monomer cluster (1.26 Å). Predicted CCH bond angles ( $\angle \text{CCH}$ ) differ slightly for the  $\text{Fe}^+(\text{C}_2\text{H}_2)_2$  acetylenes, 166.8° and 167.2°. These angles are less distorted from linearity than the monomer cluster (157.8°) indicating weakened  $\text{Fe}^+$ /acetylene interaction in the dimer cluster compared to the monomer. The weaker  $\text{C}_2\text{H}_2 \cdots \text{Fe}^+ \cdots \text{C}_2\text{H}_2$  interaction is due to diffused bonding-orbital interaction between the iron cation and the two acetylene molecules compared to the monomer cluster ion,  $\text{Fe}^+ \cdots \text{C}_2\text{H}_2$ ; or perhaps, mutual destabilizing effect between both acetylene ligands. The distance between the cation and middle of the C=C bond length ( $\|-\text{Fe}^+-\|$ ) is 2.05 Å for both acetylene molecules, much longer than that of the monomer cluster, 1.86 Å. The binding energy for removal of an acetylene molecule from the cluster,  $D_e[\text{Fe}^+\text{C}_2\text{H}_2 \cdots \text{C}_2\text{H}_2]$ , is 33.4 kcal/mol. The  $D_{2h}$  structure predicted here is expected to have four C-H frequencies; two in-phase asymmetric and two out-of-phase symmetric motions. Only the out-of-phase symmetric and in-phase asymmetric stretches are expected to be IR active. Indeed, only two C-H vibrations are predicted for the  $\text{Fe}^+(\text{C}_2\text{H}_2)_2$  ion; 3191  $\text{cm}^{-1}$  (A) and 3269  $\text{cm}^{-1}$  (S). No previously published study of the  $\text{Fe}^+(\text{C}_2\text{H}_2)_2$  ion exist to our knowledge. As discussed

below, there is excellent agreement between the  $D_e[\text{Ni}^+\text{C}_2\text{H}_2\cdots\text{C}_2\text{H}_2]$  predicted here and the previous investigation.<sup>64</sup>

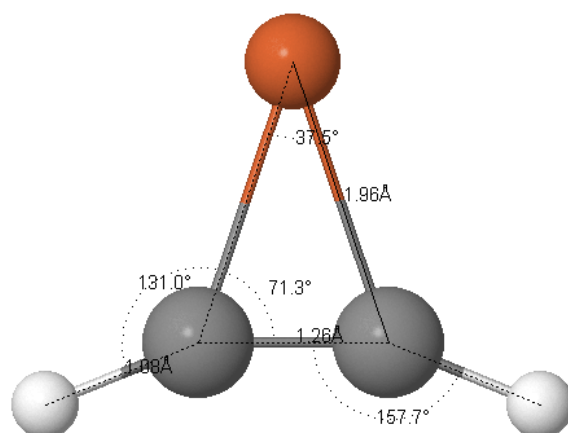
As previously mentioned, the  $\text{Co}^+(\text{C}_2\text{H}_2)_2$  cluster possess a  $D_{2h}$  symmetry with coplanar acetylene molecules. The predicted C=C bond lengths, CCH bond angles, and  $\parallel\text{-Co}^+\text{-}\parallel$  distance are 1.23 Å, 168.6°, and 2.01 Å (for both ligands) respectively. Comparison of these values to those predicted for the monomer cluster (1.25 Å, 163.0°, and 1.90 Å respectively) indicate, as was the case in iron, diffused cation/acetylene interaction for the dimer cluster compared to the monomer cluster. Also, comparison of these values to those predicted for the  $\text{Fe}^+(\text{C}_2\text{H}_2)_2$  ion reveal the expected trend of decreasing cation/acetylene interaction from iron to nickel (Table 11). Predicted stretch frequencies for the  $\text{Co}^+(\text{C}_2\text{H}_2)_2$  cluster are 3198  $\text{cm}^{-1}$  (A) and 3280  $\text{cm}^{-1}$  (S); less red-shifted (compared to the neutral acetylene molecule) than for the  $\text{Fe}^+(\text{C}_2\text{H}_2)_2$  cluster. The calculated binding energy,  $D_e[\text{Co}^+\text{C}_2\text{H}_2\cdots\text{C}_2\text{H}_2]$  is 35.4 kcal/mol. No previous data exist for comparison.

The  $\text{Ni}^+(\text{C}_2\text{H}_2)_2$  cluster was less symmetric ( $C_{2v}$ ) than the  $\text{Fe}^+(\text{C}_2\text{H}_2)_2$  or  $\text{Co}^+(\text{C}_2\text{H}_2)_2$  clusters (Figure 54). The “*puckered*” structure predicted by Duncan *et al.*<sup>64</sup> for this cluster is observed to be a transition state using the wachters+f/6-31+G\*\* basis set. The C-C and  $\parallel\text{-Ni}^+\text{-}\parallel$  bond lengths are 1.23 Å and 1.99 Å respectively, in excellent agreement with previous values of 1.22 Å and 1.99 Å respectively.<sup>64</sup> The predicted  $\angle$  CCH are 168.1° and 169.9° also in agreement with previous values of 169.3° and 170.3°. The angle between two adjacent carbons and the nickel ion,  $\angle \text{CNi}^+\text{C}$ , are 159.3° and 131.6°. Since the  $\text{Ni}^+(\text{C}_2\text{H}_2)_2$  cluster is not as symmetric as the  $\text{Fe}^+/\text{Co}^+(\text{C}_2\text{H}_2)_2$  clusters, all four C-H vibrations are expected to be IR active. The predicted values are, 3200  $\text{cm}^{-1}$  (A)/3201  $\text{cm}^{-1}$

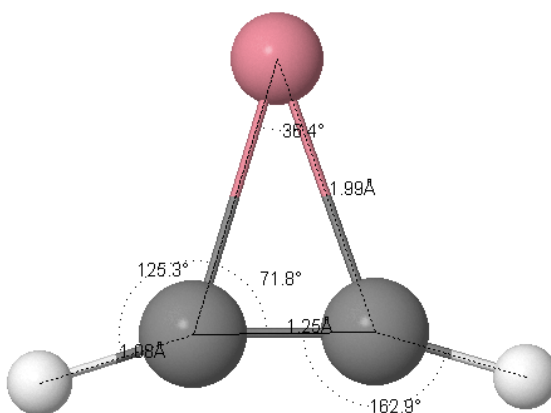
(A) and  $3285\text{ cm}^{-1}$  (S)/ $3290\text{ cm}^{-1}$  (S) which are on the average,  $\approx 13\text{ cm}^{-1}$  higher than the previously reported values.<sup>64</sup> This difference is attributed to the different basis sets employed. C-H frequencies measured by infrared dissociation of argon tagged  $\text{Ni}^+(\text{C}_2\text{H}_2)_2$  clusters were  $3176\text{ cm}^{-1}/3185\text{ cm}^{-1}$  and  $3196\text{ cm}^{-1}/3262\text{ cm}^{-1}$  for the asymmetric and symmetric motions respectively.<sup>64</sup> Though minor perturbations of the C-H vibrations are expected due to the attached Ar molecule, the experimental result suggests a different scaling factor may be appropriate for the B3LYP/Wachters+*f* method. Binding energy,  $D_e[\text{Ni}^+\text{C}_2\text{H}_2\cdots\text{C}_2\text{H}_2]$ , is calculated to be 37.8 kcal/mol in very good agreement with the previous value of 38.4 kcal/mol.<sup>64</sup> No geometry optimization was performed for the metal-butadiene,  $\text{M}^+(c\text{-C}_4\text{H}_4)$  and metallocyclopentadienyl,  $\text{M}^+(n\text{-C}_4\text{H}_4)$ , isomers since previous investigations found these complexes to be less stable than the bis-acetylene structure predicted here.<sup>61,175</sup> We did perform geometry optimizations for the iron and cobalt analogs of the forementioned complexes and in all cases, the  $\text{Fe}/\text{Co}^+(c\text{-C}_4\text{H}_4)$  and  $\text{Fe}/\text{Co}^+(n\text{-C}_4\text{H}_4)$  were predicted to be less stable than the bis-acetylene clusters,  $\text{Fe}/\text{Co}^+(\text{C}_2\text{H}_2)_2$ , discussed above. For example, the  $\text{Co}^+(\text{C}_2\text{H}_2)_2$  cluster is predicted to be 13.3 kcal/mol and 9.3 kcal/mol more stable than the  $\text{Co}^+(c\text{-C}_4\text{H}_4)$  and  $\text{Co}^+(n\text{-C}_4\text{H}_4)$  complexes respectively (Figure 56). Charge densities on the  $\text{Fe}^+$ ,  $\text{Co}^+$ , and  $\text{Ni}^+$  cations in the bis-acetylene clusters are 5%, 14%, and 19% of the total charge respectively. For the  $\text{Co}^+(c\text{-C}_4\text{H}_4)$  and  $\text{Co}^+(n\text{-C}_4\text{H}_4)$  complexes, the cation charges are 53% and 83% of the total charge respectively.

$M^+$ Monomer,  $M^+C_2H_2$ 

Fe



Co



Ni

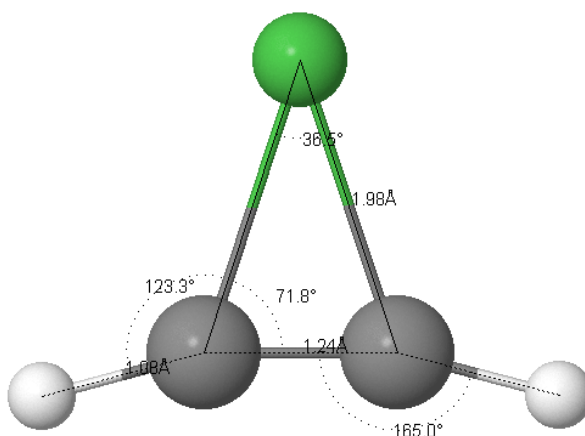


Figure 53: DFT optimized structures for the  $M^+C_2H_2$  cluster ( $M = Fe, Co, Ni$ ). Optimizations were performed with the B3LYP hybrid functional utilizing the Wachters+ $f$  basis set for the transition metals and the 6-31+G\*\* basis set for the C and H atoms.

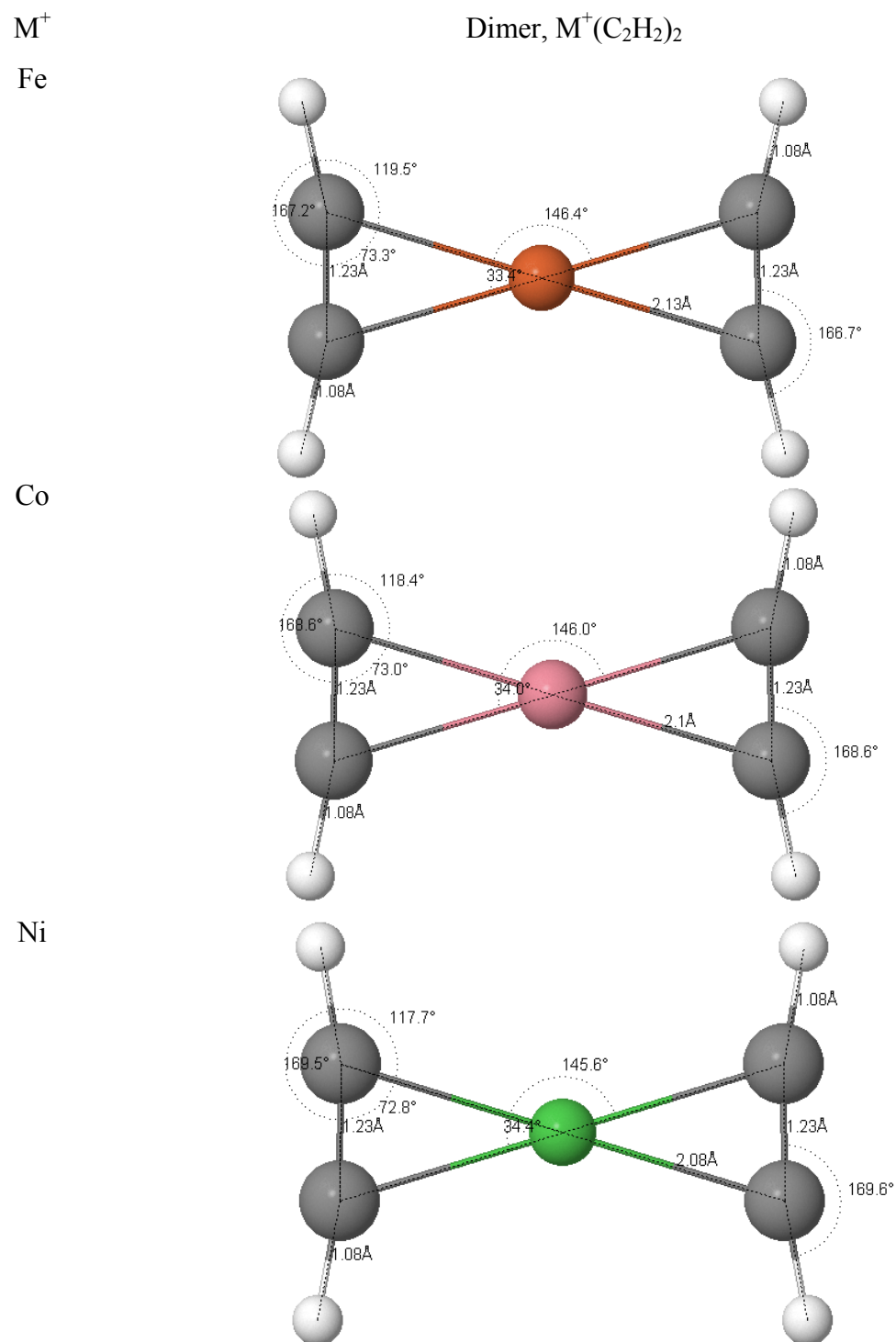
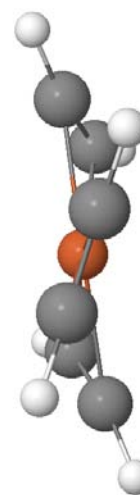
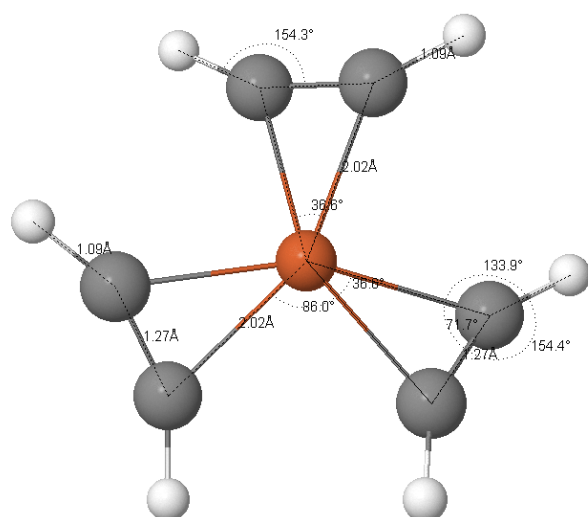


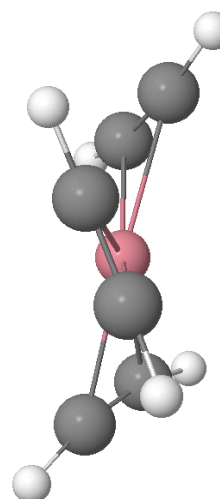
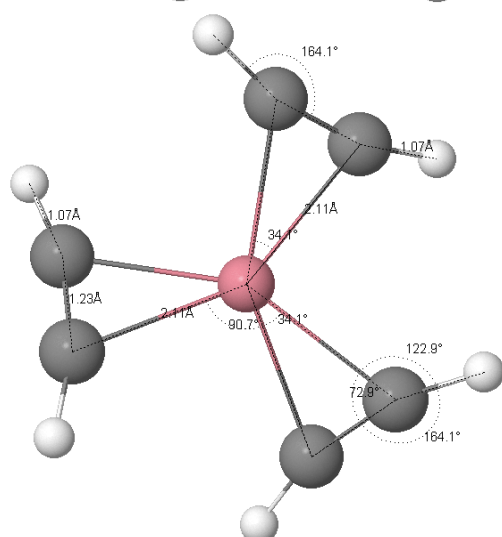
Figure 54: DFT optimized structures for  $M^+(C_2H_2)_2$  clusters ( $M = Fe, Co, Ni$ ). Optimizations were performed with the B3LYP hybrid functional utilizing the Wachters+ $f$  basis set for the transition metal ions and the 6-31+G\*\* basis set for the C and H atoms.

$M^+$ Trimer,  $M^+(C_2H_2)_3$ 

Fe



Co



Ni

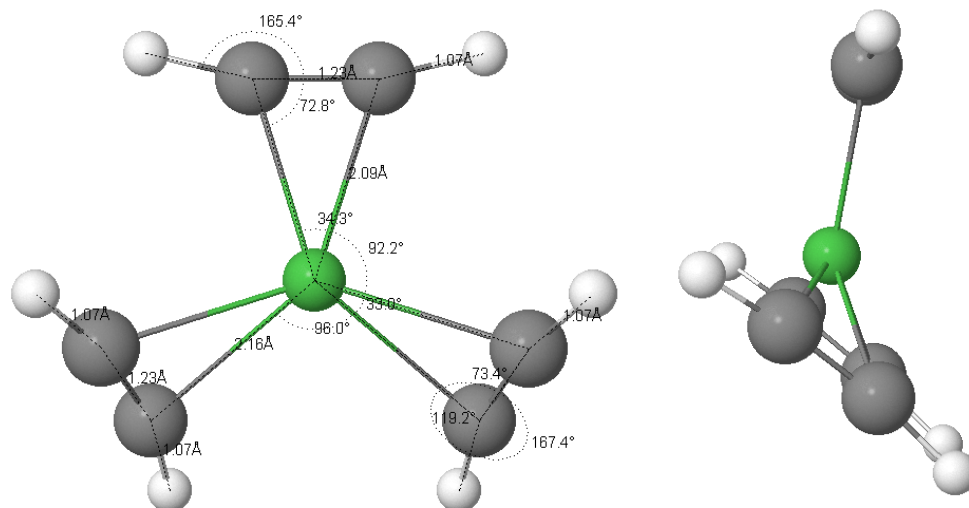


Figure 55: DFT optimized structures for  $M^+(C_2H_2)_3$  clusters ( $M = Fe, Co, Ni$ ). Optimizations were performed with the B3LYP hybrid functional utilizing the Wachters+ $f$  basis set for the transition metal ions and the 6-31+G\*\* basis set for the C and H atoms.

Table 10: Comparison of  $M^+(C_2H_2)$  binding energies, bond lengths and angles, and C-H frequency stretch to those from previous calculations.

$M^+$	State (Symm.)	Binding Energy (kcal/mol)			C-C (Å)		C-H (Å)	$M^+$ -L (Å)		CCH Angle		Frequencies, stretch, (cm <sup>-1</sup> ) <sup>b</sup>		
		a	C	d	a	d	A	A	c	A	d	a	c <sup>c</sup>	d
Fe	$^4B_1 (C_{2v})$	46.5	42.6		1.26		1.08	1.86	1.91	157.7		3144, 3207	3163, 3233	
Co	$^3B_1 (C_{2v})$	45.9	47.4		1.25		1.08	1.90	1.90	163.0		3166, 3241	3174, 3252	
Ni	$^2B_1 (C_{2v})$	47.4	48.0	47.0	1.24	1.23 0.035	1.08	1.88	1.87	165.0	165.8	3172, 3251	3192, 3273	3156, 3204

<sup>a</sup> Current work

<sup>b</sup> Vibrational frequencies were scaled by 0.96.

<sup>c</sup> From results of Klippenstein *et al.*<sup>55</sup>

<sup>d</sup> From results of Duncan *et al.*<sup>64</sup>

<sup>e</sup> Published frequencies were scaled by 0.96 for comparison to this work.



Table 11: UB3LYP/Wachters+*f*/6-31+G\*\* predicted magnitude of C-H stretch frequency red shift compared to that of the neutral acetylene monomer, 3294 cm<sup>-1</sup> (A) and 3388 cm<sup>-1</sup> (S), (B3LYP/6-31+G\*\*). Notice the increasing degree of C-H red shift from Ni<sup>+</sup>(C<sub>2</sub>H<sub>2</sub>)<sub>n</sub> to Fe<sup>+</sup>(C<sub>2</sub>H<sub>2</sub>)<sub>n</sub> clusters. This trend indicates increasing C-H bond activation from the Ni<sup>+</sup>(C<sub>2</sub>H<sub>2</sub>)<sub>n</sub> to Fe<sup>+</sup>(C<sub>2</sub>H<sub>2</sub>)<sub>n</sub> species.

Cluster	Magnitude of C-H red shift compared to the neutral monomer <sup>a,c,d</sup>					
	<i>n</i> = 1		<i>n</i> = 2		<i>n</i> = 3	
	<i>Asymm.</i>	<i>Symm.</i>	<i>Asymm.</i>	<i>Symm.</i>	<i>Asymm.</i>	<i>Symm.</i>
Fe <sup>+</sup> (C <sub>2</sub> H <sub>2</sub> ) <sub>n</sub>	150	181	103	119	90	112
Co <sup>+</sup> (C <sub>2</sub> H <sub>2</sub> ) <sub>n</sub>	128	147	96	108	77 <sup>b</sup>	95 <sup>b</sup>
Ni <sup>+</sup> (C <sub>2</sub> H <sub>2</sub> ) <sub>n</sub>	121	137	93 <sup>b</sup>	103 <sup>b</sup>	63 <sup>b</sup>	76 <sup>b</sup>

<sup>a</sup> All values in cm<sup>-1</sup>.

<sup>b</sup> Only the most intense asymmetric and symmetric C-H stretch vibrations were used in this table.

<sup>c</sup> All values scaled by 0.96.

<sup>d</sup> All values obtained by subtracting the predicted C-H asymmetric (A) and symmetric (S) stretch frequencies from that predicted for the free neutral acetylene molecule, 3294 cm<sup>-1</sup> (A) and 3388 cm<sup>-1</sup> (S).

### **$\text{Fe}^+(\text{C}_2\text{H}_2)_3$ , $\text{Co}^+(\text{C}_2\text{H}_2)_3$ , and $\text{Ni}^+(\text{C}_2\text{H}_2)_3$**

The DFT predicted geometries for the  $\text{Fe}^+(\text{C}_2\text{H}_2)_3$ ,  $\text{Co}^+(\text{C}_2\text{H}_2)_3$ , and  $\text{Ni}^+(\text{C}_2\text{H}_2)_3$  clusters are displayed in Figure 55. Different views are given for each  $\text{M}^+(\text{C}_2\text{H}_2)_3$  cluster to aid visualization. The  $\text{Fe}^+(\text{C}_2\text{H}_2)_3$  cluster possesses a pseudo-cyclic structure with each acetylene molecule distorted from the  $\text{Fe}^+(\text{acetylene})_3$  center-of-mass plane to reduce repulsive interaction between the acetylene ligands. The predicted symmetry for  $\text{Fe}^+(\text{C}_2\text{H}_2)_3$  is  $D_3$ . As was observed for the monomer and dimer clusters, each acetylene molecule is distorted from linearity ( $\angle \text{CCH} = 180^\circ$ ) as a result of interactions between the metal  $d$ -orbitals and acetylene  $\pi^*$  orbitals. This behavior is observed for all clusters investigated, though in varying magnitudes. As shown in Table 13 and Figure 55, C-C bond length for all three acetylene moieties is 1.24 Å, slightly longer than that predicted for the  $\text{Fe}^+(\text{C}_2\text{H}_2)_2$  cluster (1.23 Å). The predicted  $\angle \text{CCH}$  is  $162.1^\circ$  for all acetylene molecules. The  $\text{Fe}^+-\parallel$  length is 2.02 Å indicating, along with the  $\angle \text{CCH}$ , greater  $\text{Fe}^+$ -acetylene interaction for the trimer cluster than in the dimer cluster. The  $D_e[\text{Fe}^+(\text{C}_2\text{H}_2)_2 \cdots \text{C}_2\text{H}_2]$  binding energy is calculated to be 23.5 kcal/mol. Six C-H vibrations are predicted for the  $\text{Fe}^+(\text{C}_2\text{H}_2)_3$  structure. All three asymmetric stretches are degenerate ( $3204 \text{ cm}^{-1}$ ) while two of the symmetric stretches are degenerate ( $3277 \text{ cm}^{-1}$ ); the third symmetric stretch is  $3279 \text{ cm}^{-1}$ . *Mulliken* charge densities<sup>159</sup> showed no charge on the iron cation.

The predicted  $\text{Co}^+(\text{C}_2\text{H}_2)_3$  geometry is quite similar to that predicted for the  $\text{Fe}^+(\text{C}_2\text{H}_2)_3$  cluster though the acetylene molecules are more distorted from the center-of-mass plane than in the  $\text{Fe}^+(\text{C}_2\text{H}_2)_3$  cluster. The  $\text{Co}^+(\text{C}_2\text{H}_2)_3$  geometry is less symmetric ( $C_3$ ) than that of the  $\text{Fe}^+(\text{C}_2\text{H}_2)_3$ . C-C bond length for all three acetylene molecules is 1.23 Å, similar to that predicted for the dimer cluster (1.23 Å) and slightly shorter than that of the  $\text{Fe}^+(\text{C}_2\text{H}_2)_3$  cluster (1.24 Å). All acetylene CCH bond angles ( $\angle \text{CCH}$ ) are  $164.1^\circ$  and the  $\text{Co}^+-\parallel$  length is 2.01 Å. Calculated binding energy for the removal of one acetylene molecule,  $D_e[\text{Co}^+(\text{C}_2\text{H}_2)_2 \cdots \text{C}_2\text{H}_2]$ , is 20.3 kcal/mol. As was the case for the  $\text{Fe}^+(\text{C}_2\text{H}_2)_3$  cluster, six IR active C-H frequencies are predicted; three of which are degenerate asymmetric stretches ( $3217 \text{ cm}^{-1}$ ), another two degenerate symmetric stretches ( $3293 \text{ cm}^{-1}$ ), and the final symmetric stretch,  $3295 \text{ cm}^{-1}$ . *Mulliken* charge densities also showed no charge on the cobalt cation. The behavior of the  $\text{Fe}^+(\text{C}_2\text{H}_2)_3$  and  $\text{Co}^+(\text{C}_2\text{H}_2)_3$  charge densities suggest complexation of these clusters so that a more appropriate representation is  $\text{Fe}(\text{C}_2\text{H}_2)_3^+$  and  $\text{Co}(\text{C}_2\text{H}_2)_3^+$ . The observed charge behavior also suggests these complexes may be precursors for the suspect cyclotrimerization reaction to form  $\text{FeC}_6\text{H}_6^+$  and  $\text{CoC}_6\text{H}_6^+$  complexes. The suspect  $\text{Co}^+$ -mediated cyclotrimerization reaction is explored in the next section. Table 13 also show properties for the STQN (Synchronous Transit-Guided Quasi-Newton method) predicted transition state geometry,  $\text{CoC}_6\text{H}_6^{+*}$  (TS) and predicted  $\text{CoC}_6\text{H}_6^+$  (B) geometry. These geometries will be discussed in the next section as well.

Table 12: Comparison of  $M^+(C_2H_2)_2$  binding energies, bond lengths and angles, and C-H stretch frequency to those from previous calculations.

M <sup>+</sup>	State (Symm.)	Binding Energy (kcal/mol)				C-C (Å)		M <sup>+</sup> -L (Å)		CCH Angle		Frequencies, C-H stretch, (cm <sup>-1</sup> ) <sup>b</sup>	
		A		c		a	C	a	c	a	c	Here	c
		D <sub>e</sub> <sup>d</sup>	BE <sup>e</sup>	D <sub>e</sub> <sup>d</sup>	BE <sup>e</sup>								
Fe	<sup>4</sup> A (D <sub>2h</sub> )	33.4	85.2			1.23		2.05		166.8,166.7, 167.2,167.0		3191, 3269	
Co	<sup>3</sup> A'' (D <sub>2h</sub> )	35.4	83.1			1.23		2.01		168.6		3198, 3280	
Ni	<sup>2</sup> A (C <sub>2v</sub> )	37.8	86.9	38.4	85.5	1.23	1.22	1.99	1.99	168.1, 169.9	170.3, 169.3	3200, 3201, 3285, 3290	3185, 3186, 3275, 3279

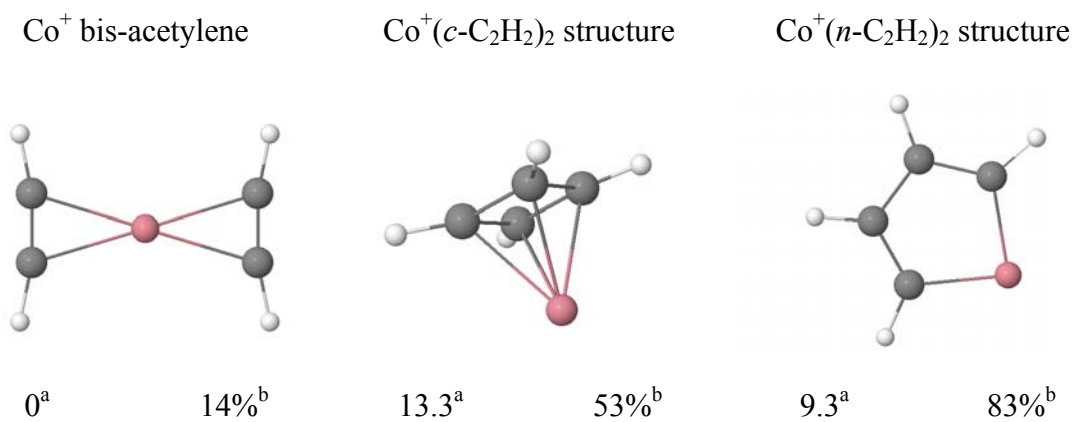
<sup>a</sup> Current work

<sup>b</sup> Vibrational frequencies were scaled by 0.96.

<sup>c</sup> From results of Duncan *et al.*<sup>64</sup>

<sup>d</sup> M<sup>+</sup>(C<sub>2</sub>H<sub>2</sub>)<sub>n</sub> · · · (C<sub>2</sub>H<sub>2</sub>) binding energy.

<sup>e</sup> M<sup>+</sup> · · · (C<sub>2</sub>H<sub>2</sub>)<sub>n</sub> binding energy.



<sup>a</sup> In kcal/mol relative to the most stable isomer.

<sup>b</sup> Charge on cation for respective Co<sup>+</sup>(C<sub>2</sub>H<sub>2</sub>)<sub>2</sub> cluster.

Figure 56: Relative energies of the UB3LYP/Wachter+*f*/6-31+G\*\* predicted isomers of the Co<sup>+</sup>(C<sub>2</sub>H<sub>2</sub>)<sub>2</sub> cluster.

Table 13: Comparison of  $M^+(C_2H_2)_3$  binding energies, bond lengths and angles, and C-H stretch frequency to those from previous calculations. Also included are geometric parameters predicted for  $Co^+(n-C_4H_4) + (C_2H_2)^*$ , intermediate for cyclotrimerization reaction and  $Co(C_6H_6)^+$ .

$M^+$	State (Symm.)	Binding Energy (kcal/mol)		$M^+-L$ (Å)		CCH Angle		Frequencies, C-H stretch, ( $cm^{-1}$ ) <sup>b</sup>	
		a	c	a	C	a	c	a	c
		$D_e$	$D_e$						
Fe	$^4A (D_3)$	23.5 <sup>d</sup>		2.02		162.1		3204, 3277, 3279	
Co <sup>d</sup>	T	$^3A (C_3)$	20.3 <sup>d</sup>		2.01		164.1	3217, 3293, 3295	
	TS	$^3A (C_3)$			1.77, 1.80, 2.10		95.3, 113.1, 132.4, 152.5		
	B	$^3A (C_{6v})$	<b>57.7<sup>g</sup></b>	<b>62.6<sup>f</sup></b>	2.07		120	3085,3092 3092,3100 3100,3105	
Ni	$^2A (C_3)$	13.7 <sup>d</sup> , 100.7 <sup>e</sup>	16.1 <sup>d</sup> , <b>101.6<sup>e</sup></b>	2.07, 2.00	2.091, 2.023	167.4,168.8, 165.4,165.4, 168.8,167.4	169.4,170.2 169.4,170.2 167.7	3226,3228, 3230,3306, 3312,3315	3211,3213, 3214,3300, 3302,3305

<sup>a</sup> Current work

<sup>b</sup> Vibrational frequencies were scaled by 0.96.

<sup>c</sup> Values from previous work.<sup>64</sup>

<sup>d</sup>  $M^+(C_2H_2)_n \cdots (C_2H_2)$  binding energy.

<sup>e</sup>  $M^+ \cdots (C_2H_2)_n$  binding energy.

<sup>d</sup> T =  $Co^+(C_2H_2)_3$ ; TS =  $Co^+(C_6H_6)^*$ , transition state, and B =  $Co(C_6H_6)^+$ .

<sup>f</sup> Values from previous work.<sup>176</sup>

<sup>g</sup>  $Co^+ \cdots (C_6H_6)$  binding energy.

The predicted geometry for the  $\text{Ni}^+(\text{C}_2\text{H}_2)_3$  cluster is markedly different from that of the iron and cobalt trimer clusters. This low symmetry geometry ( $C_s$ ) can be thought of as the addition of one acetylene molecule to the *puckered*  $\text{Ni}^+(\text{C}_2\text{H}_2)_2$  structure with the  $\text{Ni}^+$  elevated from the plane of the dimer structure and the third acetylene over and parallel to the dimer plane (Figure 55). C-C bond angles are  $1.23 \text{ \AA}$ , similar to that predicted for the  $\text{Co}^+(\text{C}_2\text{H}_2)_3$  complexes and the  $\text{Ni}^+(\text{C}_2\text{H}_2)_2$  cluster. CCH angles for both *puckered* acetylene molecules are  $168.8^\circ$  and  $164.4^\circ$  and  $\angle \text{CCH}$  for the third acetylene is  $165.4^\circ$ . The  $\text{Ni}^+-\parallel$  length for both *puckered* acetylenes is  $2.07 \text{ \AA}$  and  $2.00 \text{ \AA}$  for the third acetylene. 14% of the total charge remained on the nickel cation. Predicted C-H vibrations are,  $3226 \text{ cm}^{-1}$  (A),  $3228 \text{ cm}^{-1}$  (A),  $3230 \text{ cm}^{-1}$  (A),  $3306 \text{ cm}^{-1}$  (S),  $3312 \text{ cm}^{-1}$  (S), and  $3315 \text{ cm}^{-1}$  (S). The predicted  $D_e[\text{Ni}^+(\text{C}_2\text{H}_2)_2 \cdots \text{C}_2\text{H}_2]$  is  $13.7 \text{ kcal/mol}$  slightly less than that ( $16.1 \text{ kcal/mol}$ )<sup>64</sup> predicted previously.

### 6.3.3 Investigation of Suspect $\text{Co}^+$ -mediated $\text{C}_2\text{H}_2$ Cyclotrimerization Reaction

As shown in Figure 51 and discussed earlier, the cobalt/acetylene mass spectrum showed oscillating magic numbers for the  $n = 3, 6, 9$ , and  $12$  clusters. Suspected here is a  $\text{Co}^+$ -mediated multiple intracluster isomerization reaction to form  $\text{Co}^+$ /benzene clusters,  $\text{Co}(c\text{-C}_6\text{H}_6)_n^+$ ;  $n = 1\text{-}4$ . This reaction is of interest because it will provide further evidence for intracluster reactions enhanced by cooperative interactions of the packed molecules. In order to gain more insight into this reaction, density functional calculations of the suspect reactive pathway (scheme 6.1) for reaction 6.1 were performed. Scheme 6.1 shows possible pathways for reaction 6.1. Some of the questions we ask are: beginning with

cobalt and two acetylenes, is dimerization to the cobalt cyclobutadiene complex,  $\text{Co}(c\text{-C}_4\text{H}_4)^+$ , or the metallacycle product,  $\text{Co}(n\text{-C}_4\text{H}_4)^+$  thermochemically favored or is the bis-acetylene structure,  $\text{Co}^+(\text{C}_2\text{H}_2)_2$ , preferred? What geometry is preferred for the  $\text{Co}^+$ /trimer cluster? Is it the  $\text{Co}^+(\text{C}_2\text{H}_2)_3$  cluster discussed previously or could it be the  $\text{Co}(c\text{-C}_4\text{H}_4)^+(\text{C}_2\text{H}_2)$  or  $\text{Co}(n\text{-C}_4\text{H}_4)^+(\text{C}_2\text{H}_2)$  complex? Does the cyclotrimerization to form benzene proceed in a concerted mechanism or does it involve stable intermediates? If the latter applies, what are the structures of the intermediates? How does the predicted thermochemistry of the cobalt-mediated cyclotrimerization compare to the iron-mediated mechanism published previously?<sup>61</sup>

The predicted geometries for the  $\text{Co}^+(\text{C}_2\text{H}_2)_2$ ,  $\text{Co}(c\text{-C}_4\text{H}_4)^+$ , and  $\text{Co}(n\text{-C}_4\text{H}_4)^+$  clusters are displayed in Figure 56 along with their relative energies and *Mulliken* charges of the transition metal cations. The  $\text{Co}^+(\text{C}_2\text{H}_2)_2$  cluster is predicted to be 13.3 kcal/mol and 9.3 kcal/mol more stable than the  $\text{Co}(c\text{-C}_4\text{H}_4)^+$  and  $\text{Co}(n\text{-C}_4\text{H}_4)^+$  complexes respectively. This behavior suggest destabilization of the  $\text{Co}^+(\text{C}_2\text{H}_2)_2$  cluster upon C-C bond formation. This behavior was also predicted for the  $\text{Fe}^+(\text{C}_2\text{H}_2)_2$  and  $\text{Ni}^+(\text{C}_2\text{H}_2)_2$  cluster.<sup>61</sup>

It should be mentioned that spin conservation<sup>177</sup> was assumed for all calculations current work. The ground state is known to possess a triplet spin for the  $\text{Co}^+$ /acetylene monomer.<sup>56</sup> This ground state spin is expected to remain unchanged for the subsequent additions of acetylene molecules. In addition, comparison of the predicted singlet and quintet geometry energies of the  $\text{Co}^+(\text{C}_2\text{H}_2)$ ,  $\text{Co}^+(\text{C}_2\text{H}_2)_2$ ,  $\text{Co}^+(\text{C}_2\text{H}_2)_3$ , and  $\text{CoC}_6\text{H}_6^+$  ions to the triplet geometry energies showed the triplet spin as more stable in all cases. For example, the triplet  $\text{CoC}_6\text{H}_6^+$  ion is 33.5 kcal/mol and 41.1 kcal/mol more stable than the

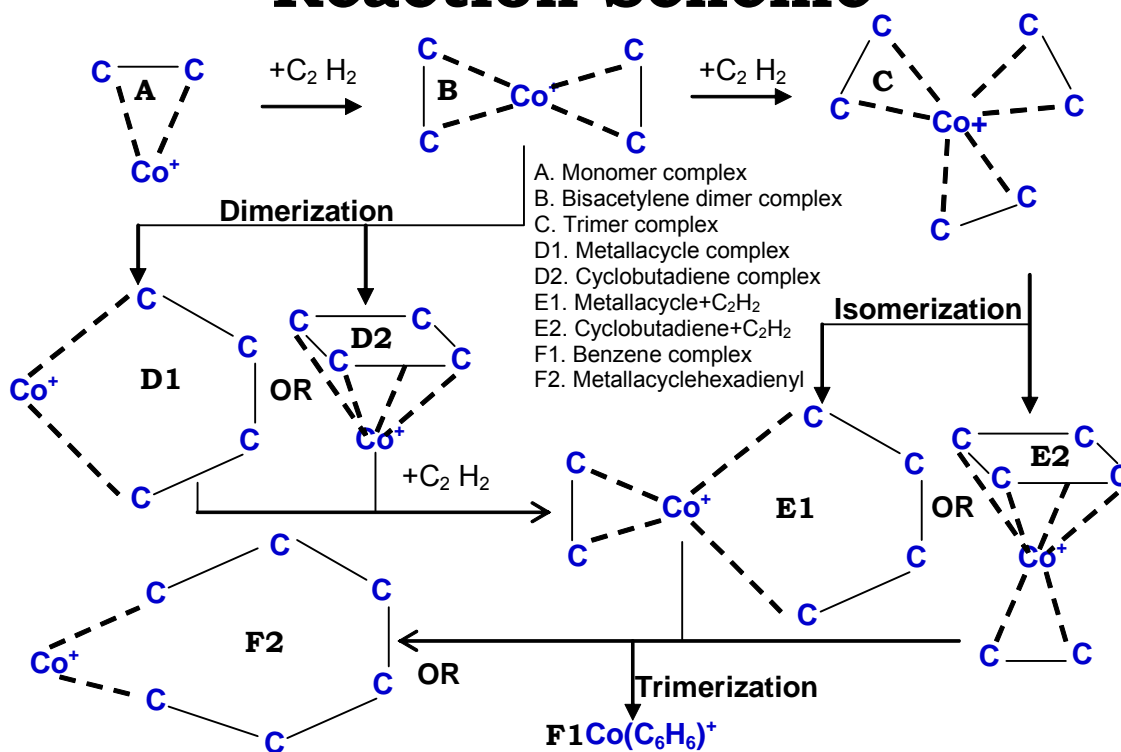


quintet and singlet spins respectively (Figure 59). Similarly, the triplet  $\text{Co}^+(\text{C}_2\text{H}_2)_3$  cluster is 30.7 kcal/mol and 41.1 kcal/mol more stable than the singlet and quintet spins respectively. The  $\text{Co}(n\text{-C}_4\text{H}_4)^+(\text{C}_2\text{H}_2)$  complex is predicted to be transition state and is discussed below. All attempts to optimize the  $\text{Co}(c\text{-C}_4\text{H}_4)^+(\text{C}_2\text{H}_2)$  cluster failed.

Figure 57 displays two views and the predicted bond lengths and angles for the  $\text{Co}(\text{C}_6\text{H}_6)^+$  complex. It possesses a  $C_{6v}$  symmetry with C-C bond lengths of 1.42 Å which is considerably longer than that predicted for the  $\text{Co}^+(\text{C}_2\text{H}_2)_3$  cluster (1.23 Å) and similar to that predicted for the neutral benzene molecule (1.40 Å). The  $\text{Co}^+$  cation is 1.67 Å above the  $C_6$  plane of the benzene molecule, markedly different from  $\text{Co}^+(\text{C}_2\text{H}_2)_3$  cluster where the cation resides on the plane created by the center-of-masses of all three acetylene molecules. The calculated binding energy for the cobalt/benzene complex,  $D_e[\text{Co}^+\cdots\text{C}_6\text{H}_6]$ , is 57.7 kcal/mol which is slightly lower than the experimentally determined binding energy of  $61.1 \pm 2.6$  kcal/mol<sup>178</sup> and the previous theoretical value of 62.6 kcal/mol.<sup>179</sup>

Figure 58 shows the predicted geometry for the cyclotrimerization reaction intermediate,  $\text{Co}(\text{C}_6\text{H}_6)^{+*}$ , (reaction 6.1). This geometry consist of a low symmetry ( $C_s$ )  $\text{Co}^+(n\text{-C}_4\text{H}_4)(\text{C}_2\text{H}_2)$  conformation in which two of the acetylene molecules essentially form a metallocyclopentadienyl ring and the third acetylene molecule is opposite and slightly below the plane defined by the metallacycle acetylenes. The  $\text{Co}^+$  is slightly above this plane and possesses 42% of the total charge. An similar structure was predicted to be a very likely intermediate for the  $\text{Fe}^+$ -mediated cyclotrimerization reaction.<sup>61</sup> As shown in Figure 58, , C-C bond lengths for the  $n\text{-C}_4\text{H}_4$  acetylenes are 1.34 Å and 1.54 Å and 1.28 Å for the third acetylene. CCH bond angles are 121.8° and 132.4° for the  $n\text{-C}_4\text{H}_4$  acetylenes

## Reaction Scheme



Scheme 6.1: Possible reaction pathways for the suspect Co<sup>+</sup>-mediated cyclotrimerization reaction

and  $152.5^\circ$  for the third acetylene molecule. The cobalt metallahexadienyl ion,  $\text{Co}^+(n\text{-C}_6\text{H}_6)$ , shown in Scheme 1, optimized to the  $\text{Co}^+\text{C}_6\text{H}_6$  complex. Also all attempts to locate a singlet and quintet intermediate complex were unsuccessful. As shown in Figure 59, ZPE corrected energies predict the transition state,  $\text{Co}^+(n\text{-C}_4\text{H}_4)(\text{C}_2\text{H}_2)$ , to be 25.4 kcal/mol above the trimer cluster. This predicted barrier of 25.4 kcal/mol is similar to that predicted for the analogous iron-mediated cyclotrimerization reaction (26.05 kcal/mol).<sup>61</sup> Internal energy needed to surpass this barrier is likely from the ionization process (LVI). The predicted exothermicity of this reaction ( $-\Delta H^\circ_r$ ) is 101.4 kcal/mol. The predicted barrier along with cooperative interactions known in clusters make this reaction very likely. The STQN method also found a more symmetric ( $C_{3v}$ ) intermediate though it was discovered not to be a true transition complex.

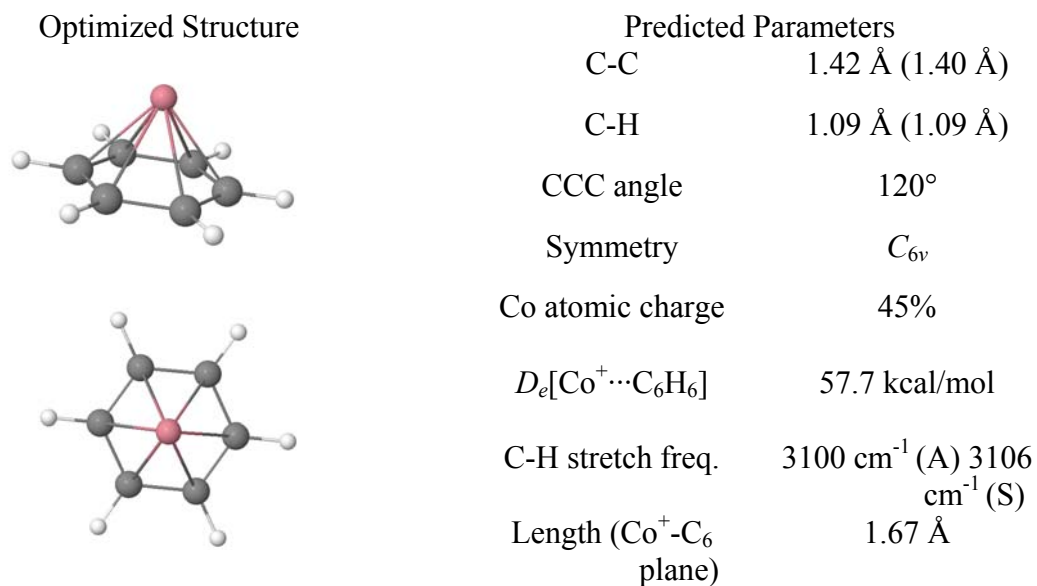


Figure 57: DFT (UB3LYP/Wachters+*f*/6-31+G\*\*) predicted geometry and parameters for the  $\text{Co}(\text{C}_6\text{H}_6)^+$  complex. Two views are presented for clarity. The predicted C-C and C-H bond lengths for the neutral benzene molecule is included in parenthesis.

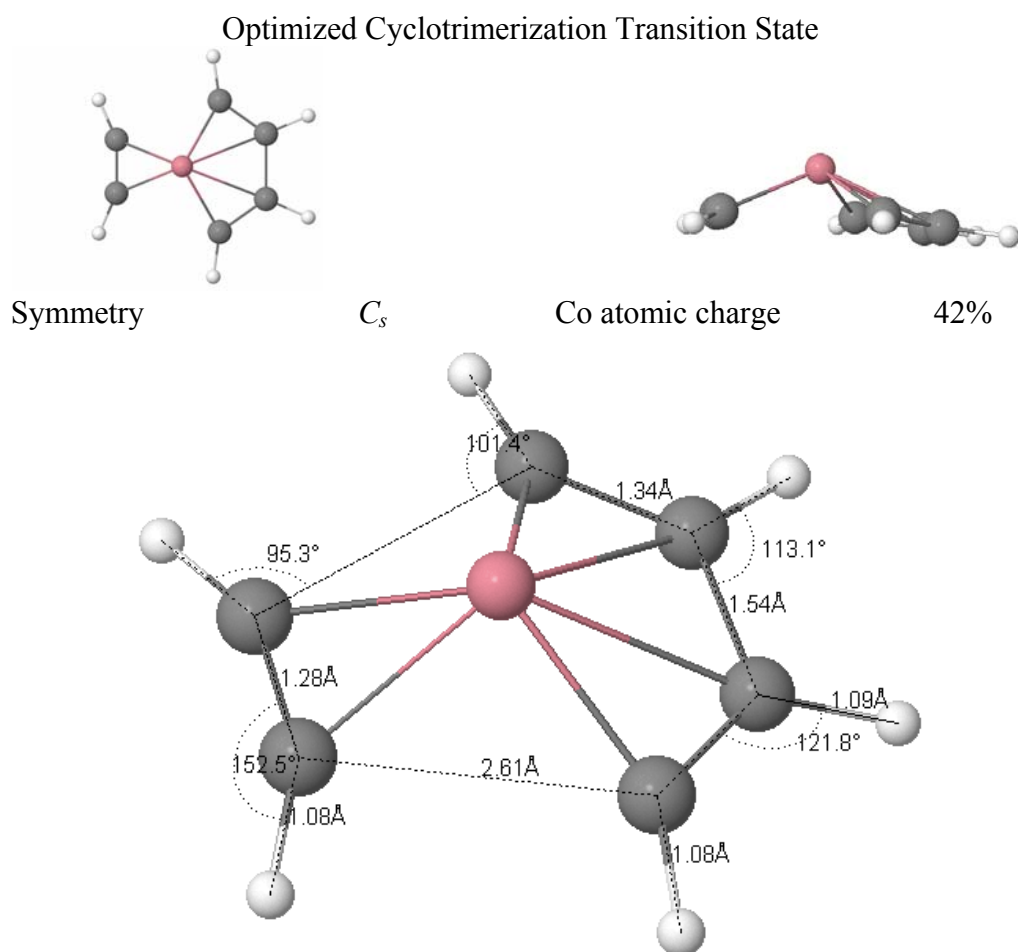


Figure 58: DFT (UB3LYP/Wachters+*f*/6-31+G\*\*) predicted intermediate for  $\text{Co}^+$ -mediated cyclotrimerization of acetylene. The intermediate consist of a  $\text{Co}^+(n\text{-C}_4\text{H}_4) + \text{C}_2\text{H}_2$ -type structure. The lower view is given due to disparity in bond lengths and angles.

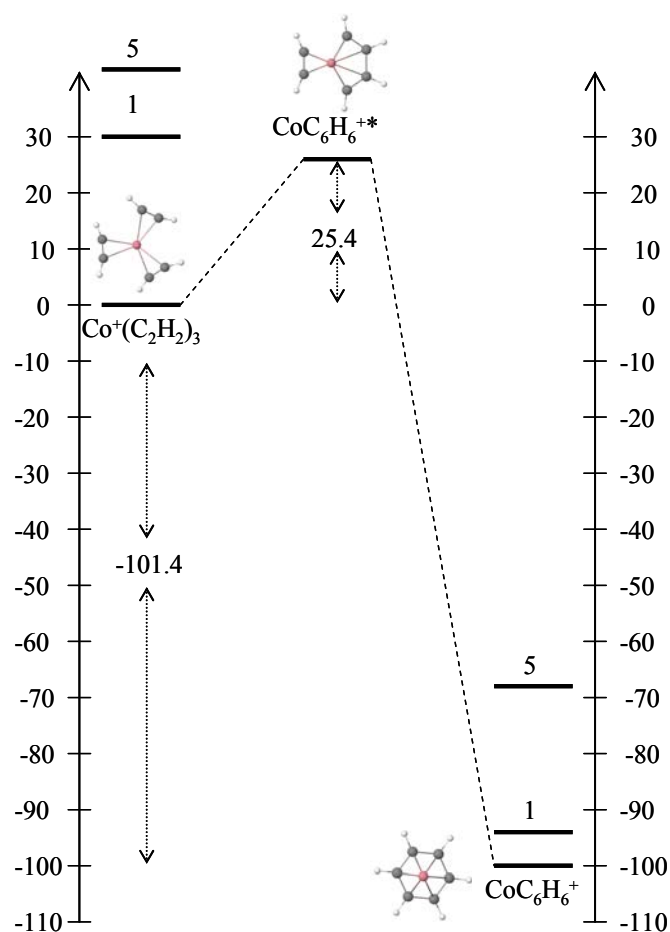


Figure 59: Relative energies (kcal/mol) corrected for ZPE for the Co<sup>+</sup>-mediated cyclotrimerization reaction of acetylene in Co<sup>+</sup>(C<sub>2</sub>H<sub>2</sub>)<sub>n</sub> clusters. Reaction pathway assumes spin conservation. The energy levels with the numbers “1” and “5” represent the singlet and quintet multiplicities respectively. All attempts to optimized the Co<sup>+</sup>(*c*-C<sub>4</sub>H<sub>4</sub>) + C<sub>2</sub>H<sub>2</sub> and Co<sup>+</sup>(*n*-C<sub>6</sub>H<sub>6</sub>) (metallahehexadienyl) species failed.

#### 6.3.4 Conclusion

We have presented geometries, C-H stretch frequencies, and binding energies for ground state  $\text{Fe}^+/\text{Co}^+/\text{Ni}^+(\text{C}_2\text{H}_2)_{1-3}$  clusters. Comparison with available experimental and theoretical data shows good agreement. In order to confirm the feasibility of a proposed  $\text{Co}^+$ -mediated cyclotrimerization reaction (reaction 6.1), DFT investigations of suspect intermediates and the cobalt/benzene ion geometries were made. Our calculated barrier for reaction 6.1 is 25.4 kcal/mol which is similar to the value predicted for the  $\text{Fe}^+$ -mediated reaction.<sup>61</sup> Also, the predicted intermediate geometry,  $\text{Co}^+(n\text{-C}_4\text{H}_4)(\text{C}_2\text{H}_2)$ , is similar to that predicted for the analogous iron-mediated reaction. A conclusion can thus be drawn that, the cobalt cation, under favorable conditions and orientation of the acetylene molecules, as is provided by the cluster environment, is capable of mediating the cyclotrimerization reaction well known for iron.

## Summary and Future Work

As noted in the introductory section and subsequent Chapters of this text, acetylene polymerization reactions are of fundamental interest in the areas of astrochemical,<sup>1,5</sup> industrial, environmental, and biological<sup>18,19</sup> research. Acetylenes' rich pi-electron density enables many polymerization reactions not otherwise observed in smaller hydrocarbon molecules. Some acetylene polymerization products include carbon nanotubes (CNTs),<sup>23</sup> polycyclic aromatic hydrocarbons (PAHs) and soot,<sup>15-17</sup> conjugated polymers.<sup>20-22</sup>

In this work, questions pertaining to the origin and identity of the magic numbers observed in the largest ever reported mass spectrum of EI ionized acetylene clusters were tackled. Some of the observed magic numbers correspond to the  $(C_2H_2)_3^+$ ,  $(C_2H_2)_6^+$ ,  $(C_2H_2)_{14}^+$ ,  $(C_2H_2)_{18}^+$ ,  $(C_2H_2)_{29}^+$ ,  $(C_2H_2)_{33}^+$ ,  $(C_2H_2)_{36}^+$ ,  $(C_2H_2)_{45}^+$ ,  $(C_2H_2)_{46}^+$ , and  $(C_2H_2)_{54}^+$  ion peaks. We suspect these magic numbers may represent covalent polymer ions formed via intracluster polymerization reactions. We systematically began our investigation by looking closely at the smallest acetylene clusters, the  $(C_2H_2)_2^+$  and  $(C_2H_2)_3^+$  ions.

Using a combination of dissociation experiments, ion mobility measurements, thermochemical measurements, and quantum chemical calculations, the dimer cluster ion was determined to be composed of at least the cyclobutadiene and vinylacetylene ions and the trimer ion was unambiguously determined to be the benzene ion. These determinations represent the first leg in a series of inquiries into the identities of suspect acetylene polymerization products in the gas phase. The cyclobutadiene, vinylacetylene, and perhaps,



other unstable dimer product ions are suspected to react with more neutral acetylene molecules to form larger cluster ions. Formation of the benzene ion is suspected to be via the reaction of the vinylacetylene ion with a neutral acetylene molecule. It should be pointed out that the ions observed in our mass spectrum are in fact the stable product ions. Unstable product ions may react with more acetylene molecules and other neutral radicals to form even larger polymer ions, maybe PAHs. These larger covalent ion products may be responsible for the larger magic numbers observed in our mass spectrum. Our future intension is to investigate cluster peaks such as  $(\text{C}_2\text{H}_2)_{14}^+$  which we have observed to consistently appear as a magic number even in transition metal/acetylene experiments. Future work in this area also involves the investigation of heterogeneous acetylene clusters. For example, acetylene/methylacetylene, acetylene/diacetylene, acetylene/benzene, acetylene/naphthalene, acetylene/cyanacetylene, and acetylene/phenylacetylene clusters. Such experiments are expected to provide preliminary insight into the vast array of acetylene polymerization reactions. Mass spectrum of the first of such investigations, acetylene/methylacetylene clusters (not shown), revealed an immense number of product peaks and magic numbers (small and large) not corresponding to the masses of the acetylene, methylacetylene, or their combination thereof. These masses most likely represent covalent product ions generated by intracluster polymerization reactions.

Interesting magic number behavior was also seen for transition metal/acetylene clusters as well. For example, we reported an interesting series of oscillating magic numbers for the  $\text{Co}^+(\text{C}_2\text{H}_2)_n$ , where  $n = 3, 6, 9$ , and  $12$ , system. This behavior is suspected to be the result of  $\text{Co}^+$ -mediated polymerization reactions to form covalent hydrocarbon

complex ions. Results from density functional calculations (DFT) show that the reaction pathway and thermochemistry of the  $\text{Co}^+$ -mediated trimerization reaction mimics that predicted for the  $\text{Fe}^+$ -mediated acetylene trimerization reaction which is well known in gas-phase organometallic chemistry. The calculations suggest, the  $\text{Co}^+(\text{C}_2\text{H}_2)_3$  magic number may in fact be the  $\text{Co}^+\text{C}_6\text{H}_6$  ion complex. Future work in this area includes the experimental investigation of the magic number identities using a combination of dissociation experiments, ion-mobility, and thermochemical measurements.

## List of References

## List of References

- (1) Cernicharo, J.; Heras, A. M.; Tielens, A.; Pardo, J. R.; Herpin, F.; Guelin, M.; Waters, L. *Astrophysical Journal*, **2001**, 546, L123.
- (2) Bregman, J. D.; Rank, D.; Temi, P.; Hudgins, D.; Kay, L. *Astrophysical Journal*, **1993**, 411, 794.
- (3) Hudgins, D.; Bauschlicher, C. W.; Allamandola, L. J. *Astrophysical Journal*, **2005**, 632, 316.
- (4) Brooke, T. Y.; Tokunaga, A. T.; Weaver, H. A.; Crovisier, J.; Bockelee-Morvan, D.; Crisp, D. *Nature*, **1996**, 383, 606.
- (5) Woods, P. M.; Millar, T. J.; Zijlstra, A. A. *Astrophysical Journal*, **2002**, 574, L167.
- (6) Winnewisser, G.; Kramer, C. *Space Science Reviews*, **1999**, 90, 181.
- (7) Ehrenfreund, P.; Irvine, W.; Becker, L.; Blank, J.; Brucato, J. R.; Colangeli, L.; Derenne, S.; Despois, D.; Dutrey, A.; Fraaije, H.; Lazcano, A.; Owen, T.; Robert, F. *Reports on Progress in Physics*, **2002**, 65, 1427.
- (8) Scott, G. B. I.; Fairley, D. A.; Freeman, C. G.; McEwan, M. J.; Adams, N. G.; Babcock, L. M. *Journal of Physical Chemistry A*, **1997**, 101, 4973.
- (9) McEwan, M. J.; Scott, G. B. I.; Adams, N. G.; Babcock, L. M.; Terzieva, R.; Herbst, E. *Astrophysical Journal*, **1999**, 513, 287.
- (10) Woods, P. M.; Millar, T. J.; Herbst, E.; Zijlstra, A. A. *Astronomy & Astrophysics*, **2003**, 402, 189.
- (11) Anicich, V. G.; McEwan, M. J. *Planetary and Space Science*, **1997**, 45, 897.
- (12) Smith, D.; Spaniel, P. *Mass Spectrometry Reviews*, **1995**, 14, 255.
- (13) Williams, D. A.; Herbst, E. *Surface Science*, **2002**, 500, 823.
- (14) Fraser, H. J.; McCoustra, M. R. S.; Williams, D. A. *Astronomy & Geophysics*, **2002**, 43, 10.

- (15) Smyth, K. C.; Lias, S. G.; Ausloos, P. *Combustion Science and Technology*, **1982**, 28, 147.
- (16) Calcote, H. F.; Keil, D. G. *Pure and Applied Chemistry*, **1990**, 62, 815.
- (17) Calcote, H. F.; Olson, D. B.; Keil, D. G. *Energy and Fuels*, **1988**, 2, 494.
- (18) Denissenko, M. F.; Pao, A.; Tang, M. S.; Pfeifer, G. P. *Science*, **1996**, 274, 430.
- (19) Durant, J. L.; Busby, W. F.; Lafleur, A. L.; Penman, B. W.; Crespi, C. L. *Mutation Research-Genetic Toxicology*, **1996**, 371, 123.
- (20) McQuade, D. T.; Pullen, A. E.; Swager, T. M. *Chemical Reviews*, **2000**, 100, 2537.
- (21) Lagow, R. J.; Kampa, J. J.; Wei, H. C.; Battle, S. L.; Genge, J. W.; Laude, D. A.; Harper, C. J.; Bau, R.; Stevens, R. C.; Haw, J. F.; Munson, E. *Science*, **1995**, 267, 362.
- (22) Xu, X. J.; Pacey, P. D. *Physical Chemistry Chemical Physics*, **2005**, 7, 326.
- (23) Du, G. X.; Feng, S. A.; Zhao, J. H.; Song, C.; Bai, S. L.; Zhu, Z. P. *Journal of the American Chemical Society*, **2006**, 128, 15405.
- (24) Ono, Y.; Ng, C. Y. *Journal of the American Chemical Society*, **1982**, 104, 4752.
- (25) Shinohara, H.; Sato, H.; Washida, N. *Journal of Physical Chemistry*, **1990**, 94, 6718.
- (26) Booze, J. A.; Baer, T. *Journal of Chemical Physics*, **1993**, 98, 186.
- (27) Coolbaugh, M. T.; Whitney, S. G.; Vaidyanathan, G.; Garvey, J. F. *Journal of Physical Chemistry*, **1992**, 96, 9139.
- (28) <http://www.cv.nrao.edu/~awootten/allmols.html>.
- (29) Turner, B. E.; Apponi, A. J. *Astrophysical Journal*, **2001**, 561, L207.
- (30) Fairley, D. A.; Scott, G. B. I.; Freeman, C. G.; Maclagan, R.; McEwan, M. J. *Journal of the Chemical Society-Faraday Transactions*, **1996**, 92, 1305.
- (31) Tzeli, D.; Mavridis, A.; Xantheas, S. S. *Journal of Physical Chemistry A*, **2002**, 106, 11327.

- (32) Tzeli, D.; Mavridis, A.; Xantheas, S. S. *Journal of Chemical Physics*, **2000**, *112*, 6178.
- (33) Tzeli, D.; Mavridis, A.; Xantheas, S. S. *Chemical Physics Letters*, **2001**, *340*, 538.
- (34) Dykstra, C. E. *Journal of Physical Chemistry*, **1995**, *99*, 11680.
- (35) VanVoorhis, T.; Dykstra, C. E. *Molecular Physics*, **1996**, *87*, 931.
- (36) Engdahl, A.; Nelander, B. *Chemical Physics Letters*, **1985**, *113*, 49.
- (37) Engdahl, A.; Nelander, B. *Journal of Physical Chemistry*, **1985**, *89*, 2860.
- (38) Engdahl, A.; Nelander, B. *Chemical Physics Letters*, **1983**, *100*, 129.
- (39) Peterson, K. I.; Klemperer, W. *Journal of Chemical Physics*, **1984**, *81*, 3842.
- (40) Silva, S. C.; Devlin, J. P. *Journal of Physical Chemistry*, **1994**, *98*, 10847.
- (41) Block, P. A.; Marshall, M. D.; Pedersen, L. G.; Miller, R. E. *Journal of Chemical Physics*, **1992**, *96*, 7321.
- (42) Anicich, V. G.; Sen, A. D.; Huntress, W. T.; McEwan, M. J. *Journal of Chemical Physics*, **1990**, *93*, 7163.
- (43) Coolbaugh, M. T.; Vaidyanathan, G.; Garvey, J. F. *International Reviews in Physical Chemistry*, **1994**, *13*, 1.
- (44) Ono, Y.; Ng, C. Y. *Journal of Chemical Physics*, **1982**, *77*, 2947.
- (45) Castleman, A. W.; Bowen, K. H. *Journal of Physical Chemistry*, **1996**, *100*, 12911.
- (46) Castleman, A. W.; Wei, S. *Annual Review of Physical Chemistry*, **1994**, *45*, 685.
- (47) Duncan, M. A. *Annual Review of Physical Chemistry*, **1997**, *48*, 69.
- (48) Buck, U. *Journal of Physical Chemistry A*, **2002**, *106*, 10049.
- (49) Armentrout, P. B. *Annual Review of Physical Chemistry*, **2001**, *52*, 423.
- (50) McDaniel, E. W.; Mason, E. A., *The Mobility and Diffusion of Ions in Gases. (Wiley Series in Plasma Physics)*, **1973**,

- (51) Kemper, P. R.; Bowers, M. T. *Journal of the American Society for Mass Spectrometry*, **1990**, *1*, 197.
- (52) Mason, E. A.; McDaniel, E. W., *Transport Properties of Ions in Gases*, John Wiley & Sons: New York, **1988**,
- (53) Chatt, J.; Guy, R. G.; Duncanson, L. A. *Journal of the Chemical Society*, **1961**, 827.
- (54) Chatt, J.; Guy, R. G.; Duncanson, L. A.; Thompson, D. T. *Journal of the Chemical Society*, **1963**, 5170.
- (55) Klippenstein, S. J.; Yang, C. N. *International Journal of Mass Spectrometry*, **2000**, *201*, 253.
- (56) Sodupe, M.; Bauschlicher, C. W. *Journal of Physical Chemistry*, **1991**, *95*, 8640.
- (57) Schroder, D.; Schwarz, H. *Journal of Organometallic Chemistry*, **1995**, *504*, 123.
- (58) Huang, Z. G.; Zeng, A. H.; Dong, J.; Zhou, M. F. *Journal of Physical Chemistry A*, **2003**, *107*, 2329.
- (59) Schroder, D.; Sulzle, D.; Hrusak, J.; Bohme, D. K.; Schwarz, H. *International Journal of Mass Spectrometry and Ion Processes*, **1991**, *110*, 145.
- (60) Wesendrup, R.; Schwarz, H. *Organometallics*, **1997**, *16*, 461.
- (61) Chretien, S.; Salahub, D. R. *Journal of Chemical Physics*, **2003**, *119*, 12291.
- (62) Gevorgyan, V.; Radhakrishnan, U.; Takeda, A.; Rubina, M.; Rubin, M.; Yamamoto, Y. *Journal of Organic Chemistry*, **2001**, *66*, 2835.
- (63) Walters, R. S.; Jaeger, T. D.; Duncan, M. A. *Journal of Physical Chemistry A*, **2002**, *106*, 10482.
- (64) Walters, R. S.; Pillai, E. D.; Schleyer, P. V. R.; Duncan, M. A. *Journal of the American Chemical Society*, **2005**, *127*, 17030.
- (65) Elshall, M. S.; Schriver, K. E.; Whetten, R. L.; Meotner, M. *Journal of Physical Chemistry*, **1989**, *93*, 7969.
- (66) Gibson, J. K. *Journal of Physical Chemistry*, **1994**, *98*, 6063.

- (67) Jones, R. W.; Staley, R. H. *Journal of the American Chemical Society*, **1980**, *102*, 3794.
- (68) Buckner, S. W.; Freiser, B. S. *Journal of the American Chemical Society*, **1987**, *109*, 1247.
- (69) Tonkyn, R.; Weisshaar, J. C. *Journal of the American Chemical Society*, **1986**, *108*, 7128.
- (70) Forbes, R. A.; Lech, L. M.; Freiser, B. S. *International Journal of Mass Spectrometry and Ion Processes*, **1987**, *77*, 107.
- (71) Caldwell, R.; Wright, D.; Elshall, M. S. *Zeitschrift Fur Physik D-Atoms Molecules and Clusters*, **1993**, *26*, S189.
- (72) Pitthawalla, Y. B.; El-Shall, M. S. in *ACS Symp. Ser.* 1998.
- (73) Vann, W.; Elshall, M. S. *Journal of the American Chemical Society*, **1993**, *115*, 4385.
- (74) Daly, G. M.; Elshall, M. S. *Journal of Physical Chemistry*, **1995**, *99*, 5283.
- (75) Yang, Y. L.; Saoud, K. M.; Abdelsayed, V.; Glaspell, G.; Deevi, S.; El-Shall, M. S. *Catalysis Communications*, **2006**, *7*, 281.
- (76) Hercules, D. M.; Day, R. J.; Balasanmugam, K.; Dang, T. A.; Li, C. P. *Analytical Chemistry*, **1982**, *54*, A280.
- (77) Vonhelden, G.; Hsu, M. T.; Gotts, N.; Bowers, M. T. *Journal of Physical Chemistry*, **1993**, *97*, 8182.
- (78) El-Shall, M. S.; Li, S., *Advances in Metal and Semiconductor Clusters*. 1998, *4*,. p. 115.
- (79) *Extrel Application Note RA\_2003B; ABB Automation Inc. Analytical Division - Extrel*.
- (80) Bernstein, E. R.; Editor, *Studies in Physical and Theoretical Chemistry, Vol. 68: Atomic and Molecular Clusters*, **1990**,
- (81) Anderson, J. B.; Wegener, D. P.; Hagena, O. F., *Molecular Beams and Low Density Gas Dynamics*. 1971.



- (82) Anderson, J. B.; Fenn, J. B. *Physics of Fluids*, **1965**, 8, 780.
- (83) Miller, D. L., *Free Jet Sources*. 1990. p. 223.
- (84) El-Shall, M. S.; Daly, G. M.; Wright, D. *Journal of Chemical Physics*, **2002**, 116, 10253.
- (85) Daly, G. M.; Wright, D.; El-Shall, M. S. *Chemical Physics Letters*, **2000**, 331, 47.
- (86) email: kemper@chem.ucsb.edu.
- (87) Wiley, W. C.; McLaren, I. H. *Rev. Sci. Instr.*, **1955**, 26, 1150.
- (88) Wiley, W. C.; McLaren, I. H. *Journal of Mass Spectrometry*, **1997**, 32, 4.
- (89) rehaufler@mac.com
- (90) Germanenko, I. N.; El-Shall, M. S. *Journal of Physical Chemistry A*, **1999**, 103, 5847.
- (91) Vankoppen, P. A. M.; Kemper, P. R.; Bowers, M. T., *Understanding Chemical Reactivity*. 1996, 15, p. 157.
- (92) Kaneko, Y.; Megill, L. R.; Hasted, J. B. *Journal of Chemical Physics*, **1966**, 45, 3741.
- (93) Ibrahim, Y., *Ion Mobility Studies of the Electronic States of Transition Metal Cations and Ion-Molecules Reactions*, in *Chemistry*. 2003, Virginia Commonwealth University. p. 31.
- (94) Mesleh, M. F.; Hunter, J. M.; Shvartsburg, A. A.; Schatz, G. C.; Jarrold, M. F. *Journal of Physical Chemistry*, **1996**, 100, 16082.
- (95) Wyttenbach, T.; vonHelden, G.; Batka, J. J.; Carlat, D.; Bowers, M. T. *Journal of the American Society for Mass Spectrometry*, **1997**, 8, 275.
- (96) [http://bowers.chem.ucsb.edu/theory\\_analysis/cross-sections/sigma.shtml](http://bowers.chem.ucsb.edu/theory_analysis/cross-sections/sigma.shtml).
- (97) Shvartsburg, A. A.; Jarrold, M. F. *Chemical Physics Letters*, **1996**, 261, 86.
- (98) <http://nano.chem.indiana.edu/software.html>.
- (99) Jarrold, M. F. *Journal of Physical Chemistry*, **1995**, 99, 11.

- (100) Jarrold, M. F.; Bower, J. E. *Journal of Chemical Physics*, **1992**, 96, 9180.
- (101) Rusyniak, M.; Ibrahim, Y.; Alsharaeh, E.; Meot-Ner, M.; El-Shall, M. S. *Journal of Physical Chemistry A*, **2003**, 107, 7656.
- (102) Ausloos, P. *Journal of the American Chemical Society*, **1981**, 103, 3931.
- (103) Wagnerredeker, W.; Illies, A. J.; Kemper, P. R.; Bowers, M. T. *Journal of the American Chemical Society*, **1983**, 105, 5719.
- (104) Jarrold, M. F.; Illies, A. J.; Kirchner, N. J.; Bowers, M. T. *Organic Mass Spectrometry*, **1983**, 18, 388.
- (105) Rosenstock, H. M.; McCulloh, K. E.; Lossing, F. P. *International Journal of Mass Spectrometry and Ion Processes*, **1977**, 25, 327.
- (106) Baer, T.; Willett, G. D.; Smith, D.; Phillips, J. S. *Journal of Chemical Physics*, **1979**, 70, 4076.
- (107) Lifshitz, C.; Gibson, D.; Levsen, K.; Dotan, I. *International Journal of Mass Spectrometry and Ion Processes*, **1981**, 40, 157.
- (108) Shay, B. J.; Eberlin, M. N.; Cooks, R. G.; Wesdemiotis, C. *Journal of the American Society for Mass Spectrometry*, **1992**, 3, 518.
- (109) Zhang, M. Y.; Carpenter, B. K.; McLafferty, F. W. *Journal of the American Chemical Society*, **1991**, 113, 9499.
- (110) Bakhtiar, R.; Drader, J. J.; Jacobson, D. B. *Organic Mass Spectrometry*, **1993**, 28, 797.
- (111) Hrouda, V.; Roeselova, M.; Bally, T. *Journal of Physical Chemistry A*, **1997**, 101, 3925.
- (112) Shiotani, M.; Ohta, K.; Nagata, Y.; Sohma, J. *Journal of the American Chemical Society*, **1985**, 107, 2562.
- (113) Bock, H.; Roth, B.; Maier, G. *Chemische Berichte-Recueil*, **1984**, 117, 172.
- (114) Kohn, W.; Sham, L. J. *Physical Review*, **1965**, 140, 1133.
- (115) Perdew, J. P.; Burke, K.; Ernzerhof, M. *Physical Review Letters*, **1997**, 78, 1396.

- (116) Perdew, J. P.; Burke, K.; Ernzerhof, M. *Physical Review Letters*, **1996**, 77, 3865.
- (117) Dunning, T. H. *Journal of Chemical Physics*, **1989**, 90, 1007.
- (118) Kendall, R. A.; Dunning, T. H.; Harrison, R. J. *Journal of Chemical Physics*, **1992**, 96, 6796.
- (119) Boys, S. F.; Bernardi, F. *Molecular Physics*, **1970**, 19, 553.
- (120) NIST Chemistry WebBook, *NIST Standard Reference Database Number 69; National Institute of Standards and Technology: Gaithersburg MD, 20899*  
(<http://webbook.nist.gov>) 2001-2006.
- (121) SciFinder Scholar, <http://www.cas.org/SCIFINDER/SCHOLAR/index.html>.
- (122) Gaussian 03 Revision C.02 Frisch, M. J. T., G. W.; Schlegel, H. B.; Scuseria, G. E.; Robb, M. A.; Cheeseman, J. R.; Montgomery, Jr., J. A.; Vreven, T.; Kudin, K. N.; Burant, J. C.; Millam, J. M.; Iyengar, S. S.; Tomasi, J.; Barone, V.; Mennucci, B.; Cossi, M.; Scalmani, G.; Rega, N.; Petersson, G. A.; Nakatsuji, H.; Hada, M.; Ehara, M.; Toyota, K.; Fukuda, R.; Hasegawa, J.; Ishida, M.; Nakajima, T.; Honda, Y.; Kitao, O.; Nakai, H.; Klene, M.; Li, X.; Knox, J. E.; Hratchian, H. P.; Cross, J. B.; Bakken, V.; Adamo, C.; Jaramillo, J.; Gomperts, R.; Stratmann, R. E.; Yazyev, O.; Austin, A. J.; Cammi, R.; Pomelli, C.; Ochterski, J. W.; Ayala, P. Y.; Morokuma, K.; Voth, G. A.; Salvador, P.; Dannenberg, J. J.; Zakrzewski, V. G.; Dapprich, S.; Daniels, A. D.; Strain, M. C.; Farkas, O.; Malick, D. K.; Rabuck, A. D.; Raghavachari, K.; Foresman, J. B.; Ortiz, J. V.; Cui, Q.; Baboul, A. G.; Clifford, S.; Cioslowski, J.; Stefanov, B. B.; Liu, G.; Liashenko, A.; Piskorz, P.; Komaromi, I.; Martin, R. L.; Fox, D. J.; Keith, T.; Al-Laham, M. A.; Peng, C. Y.; Nanayakkara, A.; Challacombe, M.; Gill, P. M. W.; Johnson, B.; Chen, W.; Wong, M. W.; Gonzalez, C.; and Pople, J. A.; Gaussian, Inc., Wallingford CT, 2004.
- (123) Rusyniak, M. J.; Ibrahim, Y. M.; Wright, D. L.; Khanna, S. N.; El-Shall, M. S. *Journal of the American Chemical Society*, **2003**, 125, 12001.
- (124) Brill, F. W.; Eyler, J. R. *Journal of Physical Chemistry*, **1981**, 85, 1091.
- (125) Cooks, R. G.; Beynon, J. H.; Litton, J. F. *Organic Mass Spectrometry*, **1975**, 10, 503.
- (126) Koppel, C.; Schwarz, H.; Borchers, F.; Levsen, K. *International Journal of Mass Spectrometry and Ion Processes*, **1976**, 21, 15.

- (127) Alberts, I. L.; Rowlands, T. W.; Handy, N. C. *Journal of Chemical Physics*, **1988**, 88, 3811.
- (128) Prichard, D. G.; Nandi, R. N.; Muentner, J. S. *Journal of Chemical Physics*, **1988**, 89, 115.
- (129) Pople, J. A.; Headgordon, M.; Raghavachari, K. *Journal of Chemical Physics*, **1987**, 87, 5968.
- (130) Revercomb, H. E.; Mason, E. A. *Analytical Chemistry*, **1975**, 47, 970.
- (131) Miller, D. L.; Gross, M. L. *Journal of the American Chemical Society*, **1983**, 105, 4239.
- (132) Gross, M. L.; Russell, D. H.; Aerni, R. J.; Bronczyk, S. A. *Journal of the American Chemical Society*, **1977**, 99, 3603.
- (133) Shin, J. W.; Hammer, N. I.; Diken, E. G.; Johnson, M. A.; Walters, R. S.; Jaeger, T. D.; Duncan, M. A.; Christie, R. A.; Jordan, K. D. *Science*, **2004**, 304, 1137.
- (134) Jiang, J. C.; Wang, Y. S.; Chang, H. C.; Lin, S. H.; Lee, Y. T.; Niedner-Schatteburg, G. *Journal of the American Chemical Society*, **2000**, 122, 1398.
- (135) Johnson, M. S.; Kuwata, K. T.; Wong, C. K.; Okumura, M. *Chemical Physics Letters*, **1996**, 260, 551.
- (136) Miyazaki, M.; Fujii, A.; Ebata, T.; Mikami, N. *Science*, **2004**, 304, 1134.
- (137) Okumura, M.; Yeh, L. I.; Myers, J. D.; Lee, Y. T. *Journal of Chemical Physics*, **1986**, 85, 2328.
- (138) Ibrahim, Y. M.; Mautner, M. M. N.; Alshraeh, E. H.; El-Shall, M. S.; Scheiner, S. *Journal of the American Chemical Society*, **2005**, 127, 7053.
- (139) Curtiss, L. A.; Raghavachari, K.; Redfern, P. C.; Rassolov, V.; Pople, J. A. *Journal of Chemical Physics*, **1998**, 109, 7764.
- (140) Curtiss, L. A.; Redfern, P. C.; Raghavachari, K.; Rassolov, V.; Pople, J. A. *Journal of Chemical Physics*, **1999**, 110, 4703.
- (141) Scuseria, G. E.; Janssen, C. L.; Schaefer, H. F. *Journal of Chemical Physics*, **1998**, 89, 7382.

- (142) Meotner, M.; Deakyne, C. A. *Journal of the American Chemical Society*, **1985**, *107*, 469.
- (143) Mabrouki, R.; Ibrahim, Y.; Xie, E. L.; Mautner, M. M. N.; El-Shall, M. S. *Journal of Physical Chemistry A*, **2006**, *110*, 7334.
- (144) Mautner, M. M. N.; Elmore, D. E.; Scheiner, S. *Journal of the American Chemical Society*, **1999**, *121*, 7625.
- (145) Moet-Ner, M. J. *Journal of the American Chemical Society*, **1986**, *106*, 1265.
- (146) Mabourki, R.; Ibrahim, Y.; Xie, E. L.; Mautner, M. M. N.; El-Shall, M. S. *Chemical Physics Letters*, **2006**, *424*, 257.
- (147) Mabud, M. A.; Ast, T.; Verma, S.; Jiang, Y. X.; Cooks, R. G. *Journal of the American Chemical Society*, **1987**, *109*, 7597.
- (148) Nobes, R. H.; Bouma, W. J.; Macleod, J. K.; Radom, L. *Chemical Physics Letters*, **1987**, *135*, 78.
- (149) Buschek, J. M.; Holmes, J. L.; Terlouw, J. K. *Journal of the American Chemical Society*, **1987**, *109*, 7321.
- (150) Ma, N. L.; Wong, M. W. *European Journal of Organic Chemistry*, **2000**, 1411.
- (151) Nobes, R. H.; Bouma, W. J.; Radom, L. *Journal of the American Chemical Society*, **1983**, *105*, 309.
- (152) Terlouw, J. K.; Heerma, W.; Holmes, J. L. *Organic Mass Spectrometry*, **1981**, *16*, 306.
- (153) Nuttall, R. L.; Laufer, A. H.; Kilday, M. V. *Journal of Chemical Thermodynamics*, **1971**, *3*, 167.
- (154) Orlov, V. M.; Krivoruchko, A. A.; Misharev, A. D.; Takhistov, V. V. *Bulletin of the Academy of Sciences of the Ussr Division of Chemical Science*, **1986**, *35*, 2404.
- (155) Rice, F. O.; Greenberg, J. *Journal of the American Chemical Society*, **1934**, *38*, 2268.
- (156) Lias, S. G.; Bartmess, J. E.; Liebman, J. F.; Holmes, J. L.; Levin, R. D.; Mallard, W. G. *Journal of Physical and Chemical Reference Data*, **1988**, *17*, 1.

- (157) Reed, R. I.; Brand, J. C. D. *J. Chem. Soc. Faraday Trans.*, **1958**, 54, 478.
- (158) Meot-Ner, M. *Chemical Reviews*, **2005**, 105, 213.
- (159) Frisch, M. J.; Trucks, G. W., *Gaussian 03 User's Reference*, Carnegie Mellon University, **2003**,
- (160) Guerra, C. F.; Handgraaf, J. W.; Baerends, E. J.; Bickelhaupt, F. M. *Journal of Computational Chemistry*, **2004**, 25, 189.
- (161) Davidson, W. R.; Lau, Y. K.; Kebarle, P. *Canadian Journal of Chemistry-Revue Canadienne De Chimie*, **1978**, 56, 1016.
- (162) Momoh, P. O.; El-Shall, M. S. *Chemical Physics Letters*, **2007**, 436, 25.
- (163) Ludwig, R. *Angewandte Chemie-International Edition*, **2001**, 40, 1809.
- (164) Hodges, P. M.; Stone, A. J. *Journal of Chemical Physics*, **1999**, 110, 6766.
- (165) Shilov, A. E.; Shul'pin, G. B. *Chemical Reviews*, **1997**, 97, 2879.
- (166) Leininger, S.; Olenyuk, B.; Stang, P. J. *Chemical Reviews*, **2000**, 100, 853.
- (167) Eller, K.; Schwarz, H. *Chemical Reviews*, **1991**, 91, 1121.
- (168) Bytheway, I.; Wong, M. W. *Chemical Physics Letters*, **1998**, 282, 219.
- (169) Lebrilla, C. B.; Schulze, C.; Schwarz, H. *Journal of the American Chemical Society*, **1987**, 109, 98.
- (170) Rosi, M.; Bauschlicher, C. W. *Chemical Physics Letters*, **1990**, 166, 189.
- (171) Vankoppen, P. A. M.; Kemper, P. R.; Bushnell, J. E.; Bowers, M. T. *Journal of the American Chemical Society*, **1995**, 117, 2098.
- (172) Surya, P. I.; Ranatunga, D. R. A.; Freiser, B. S. *Journal of the American Chemical Society*, **1997**, 119, 3351.
- (173) Kline, E. S.; Kafafi, Z. H.; Hauge, R. H.; Margrave, J. L. *Journal of the American Chemical Society*, **1985**, 107, 7559.
- (174) Kline, E. S.; Kafafi, Z. H.; Hauge, R. H.; Margrave, J. L. *Journal of the American Chemical Society*, **1987**, 109, 2402.

- (175) Sicilia, E.; Russo, N. *Journal of Molecular Structure-Theochem*, **2004**, 709, 167.
- (176) Bauschlicher, C. W.; Partridge, H.; Langhoff, S. R. *Journal of Physical Chemistry*, **1992**, 96, 3273.
- (177) Armentrout, P. B. *Annual Review of Physical Chemistry*, **1990**, 41, 313.
- (178) Meyer, F.; Khan, F. A.; Armentrout, P. B. *Journal of the American Chemical Society*, **1995**, 117, 9740.
- (179) Bauschlicher, C. W.; Partridge, H.; Langhoff, S. R. *Journal of Physical Chemistry*, **1992**, 96, 2475.

## Appendix

This appendix contains mass spectra from experiments performed by the author of this dissertation, Paul O. Momoh, as well as by Dr. Edreese Alsharaeh. No distinction is made in regards to authorship of each mass spectrum displayed. Work displayed in this section may or may not be related to the general theme of this dissertation.

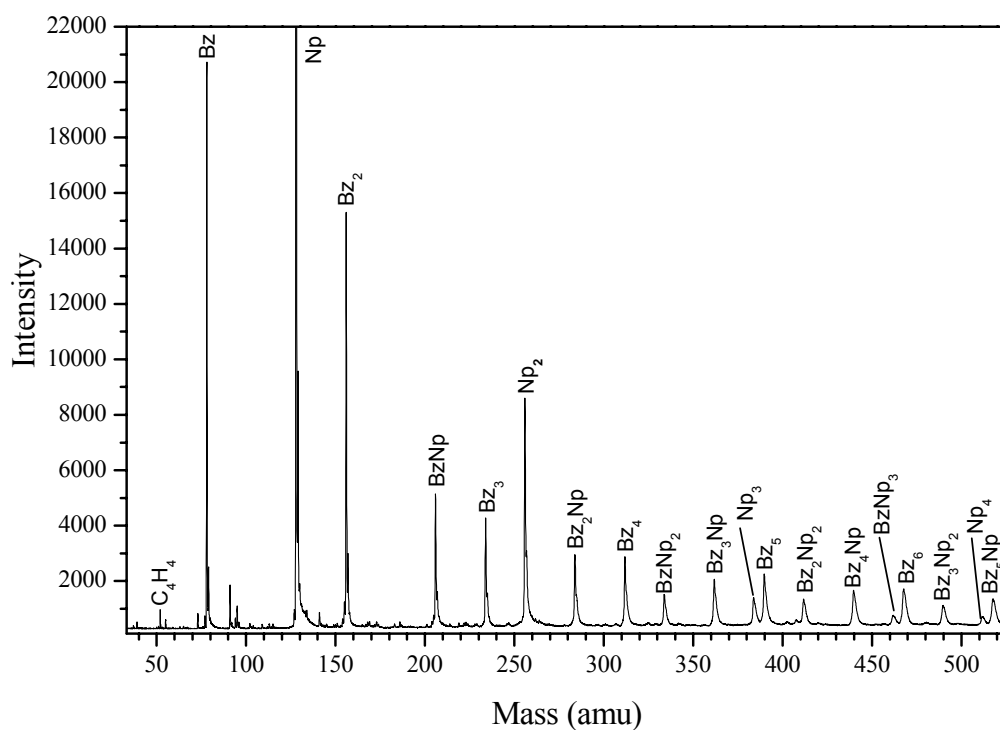


Figure 60: Mass spectrum of photoionized (193 nm) benzene/naphthalene heterogeneous clusters. Benzene and naphthalene were contained in bubblers arranged in series. Helium pressure was 40 PSI and stagnation temperature was 27° C.



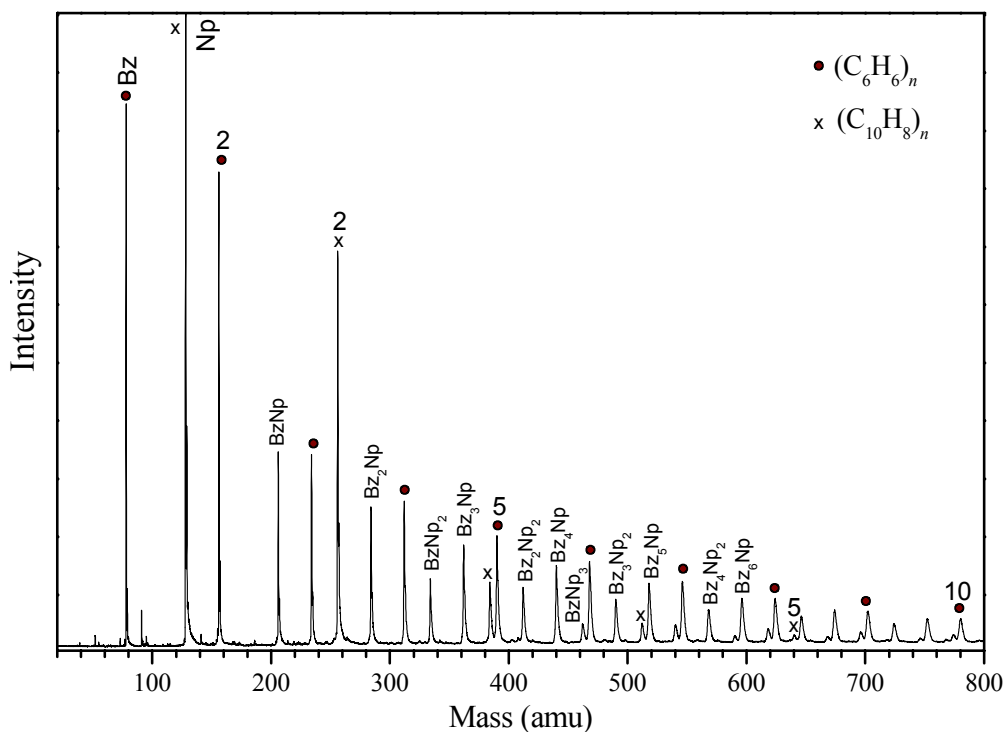


Figure 61: Mass spectrum of photoionized (193 nm) benzene/naphthalene heterogeneous clusters. Benzene and naphthalene were contained in bubblers arranged in series. Helium pressure was 40 PSI and stagnation temperature was 27° C. Raising the naphthalene temperature to increase its partial pressure in the line or cooling the benzene to reduce its relative partial pressure showed no effect on cluster distribution.

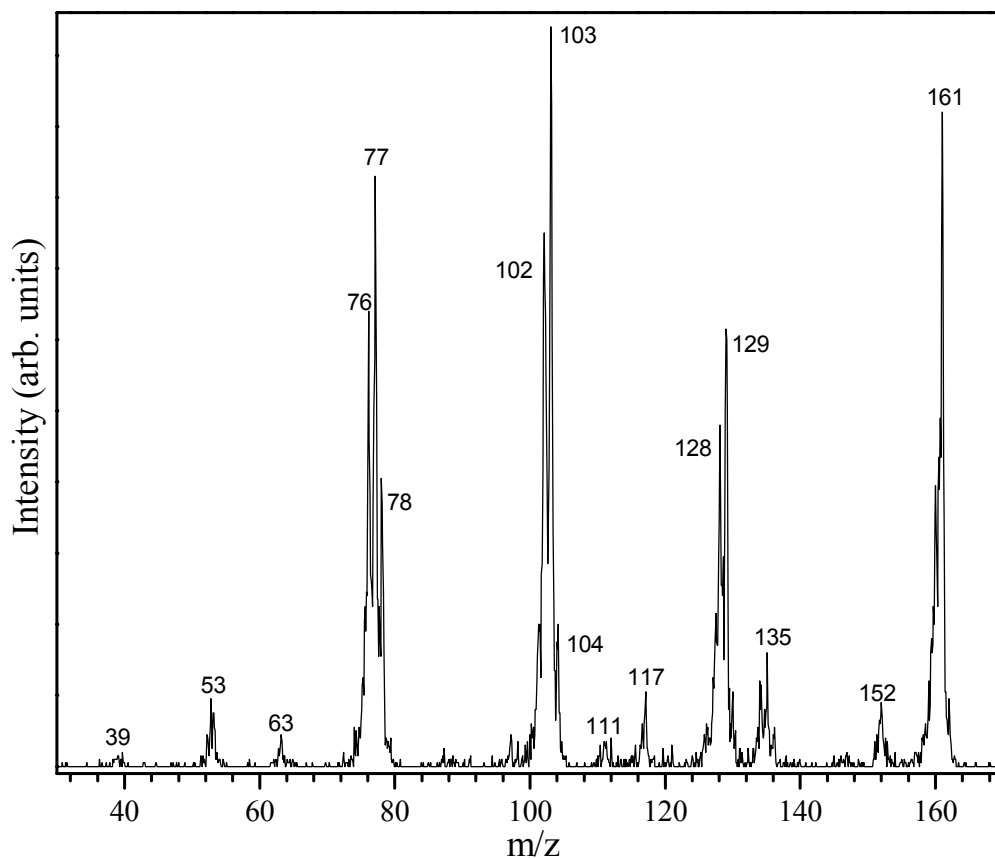


Figure 62: Mass spectrum of mass selected EI ionized acetylene ion,  $C_2H_2^+$ , injected into the cell containing 468 mTorr of  $C_2H_2$  only using an injection energy of 11.9 eV. The temperature of the drift cell was  $31^\circ C$  and the cell voltage was 24 V. Note some of the peaks represent the acetylene/acetone cluster due to the acetone impurity.

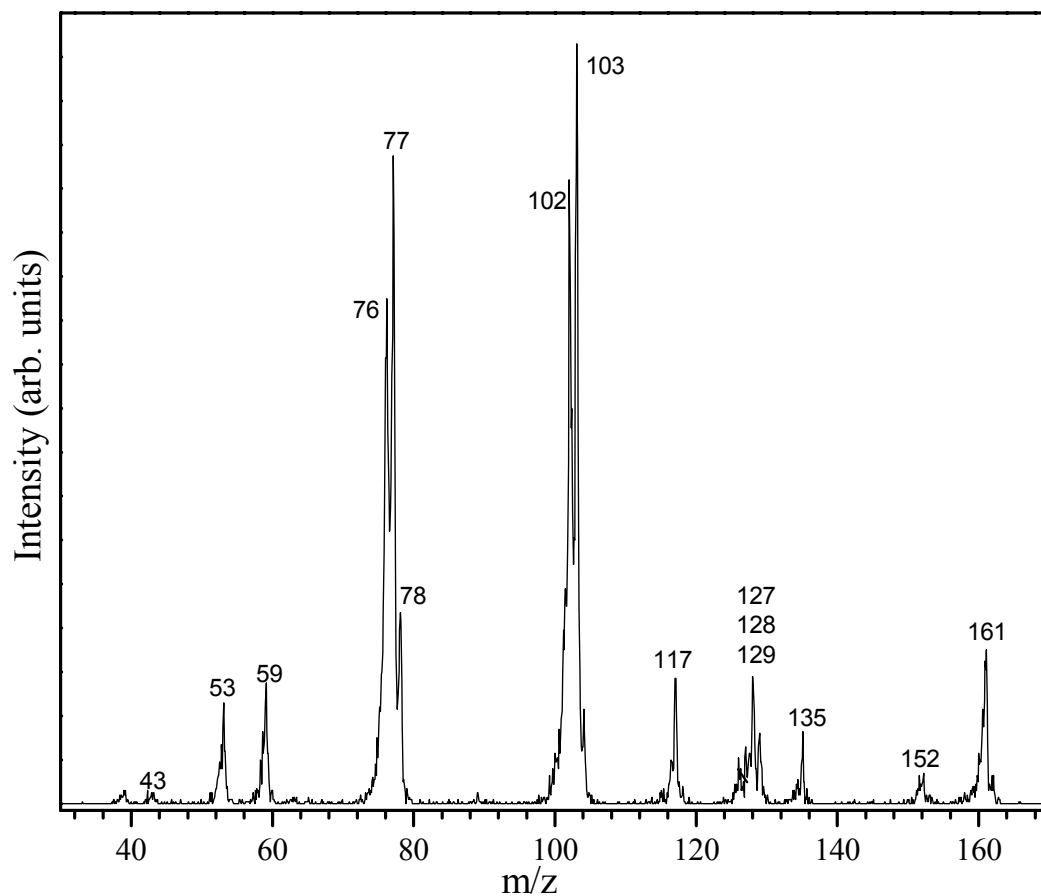


Figure 63: Mass spectrum of mass selected EI ionized acetylene ion,  $C_2H_2^+$ , injected into the cell containing 70 mTorr of  $C_2H_2$  only using an injection energy of 11.9 eV. The temperature of the drift cell was  $31^\circ C$  and the cell voltage was 24 V. Note some of the peaks represent the acetylene/acetone cluster due to the acetone impurity.

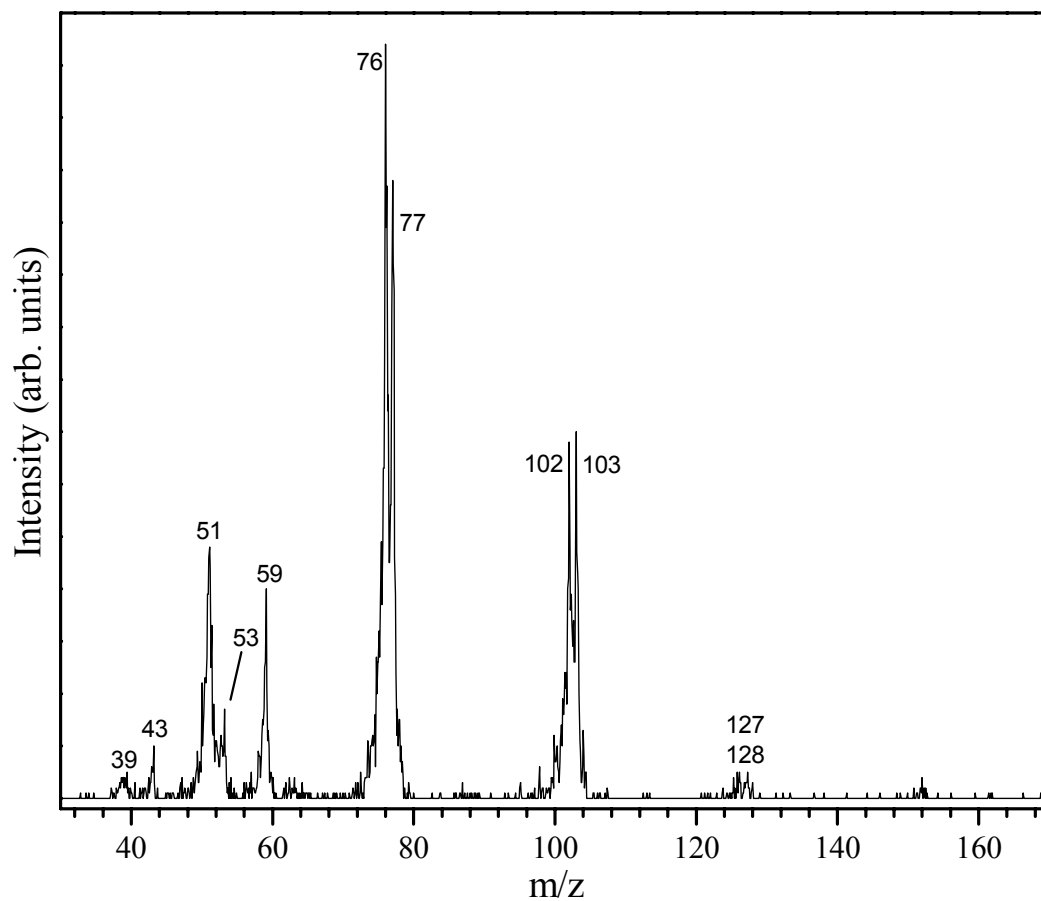


Figure 64: Mass spectrum of mass selected EI ionized acetylene ion,  $\text{C}_2\text{H}_2^+$ , injected into the cell containing 24 mTorr of  $\text{C}_2\text{H}_2$  only using an injection energy of 11.9 eV. The temperature of the drift cell was  $31^\circ\text{C}$  and the cell voltage was 24 V. Note some of the peaks represent the acetylene/acetone cluster due to the acetone impurity.

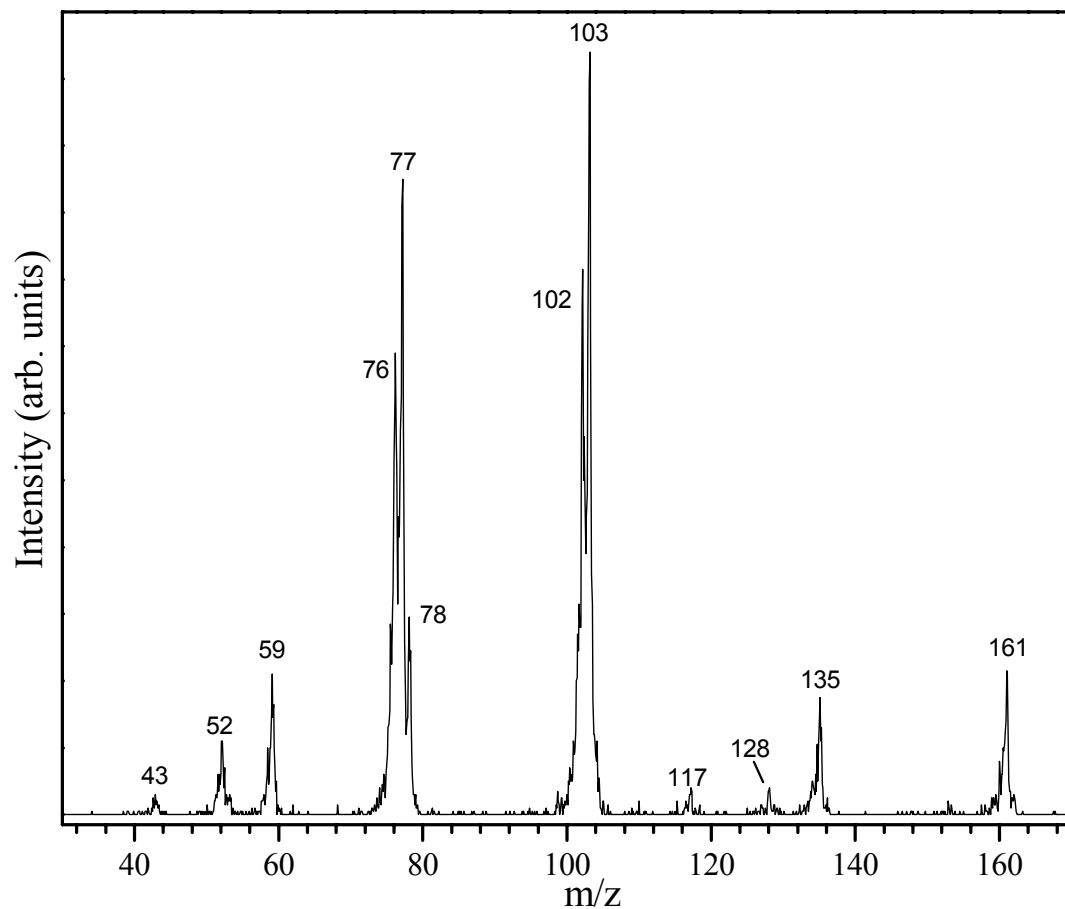


Figure 65: Mass spectrum of mass selected EI ionized acetylene ion,  $\text{C}_2\text{H}_2^+$ , injected into the cell containing 22 mTorr of  $\text{C}_2\text{H}_2$  and 1.206 Torr He using an injection energy of 11.9 eV. The temperature of the drift cell was  $31^\circ\text{C}$  and the cell voltage was 24 V. Note some of the peaks represent the acetylene/acetone cluster due to the acetone impurity.

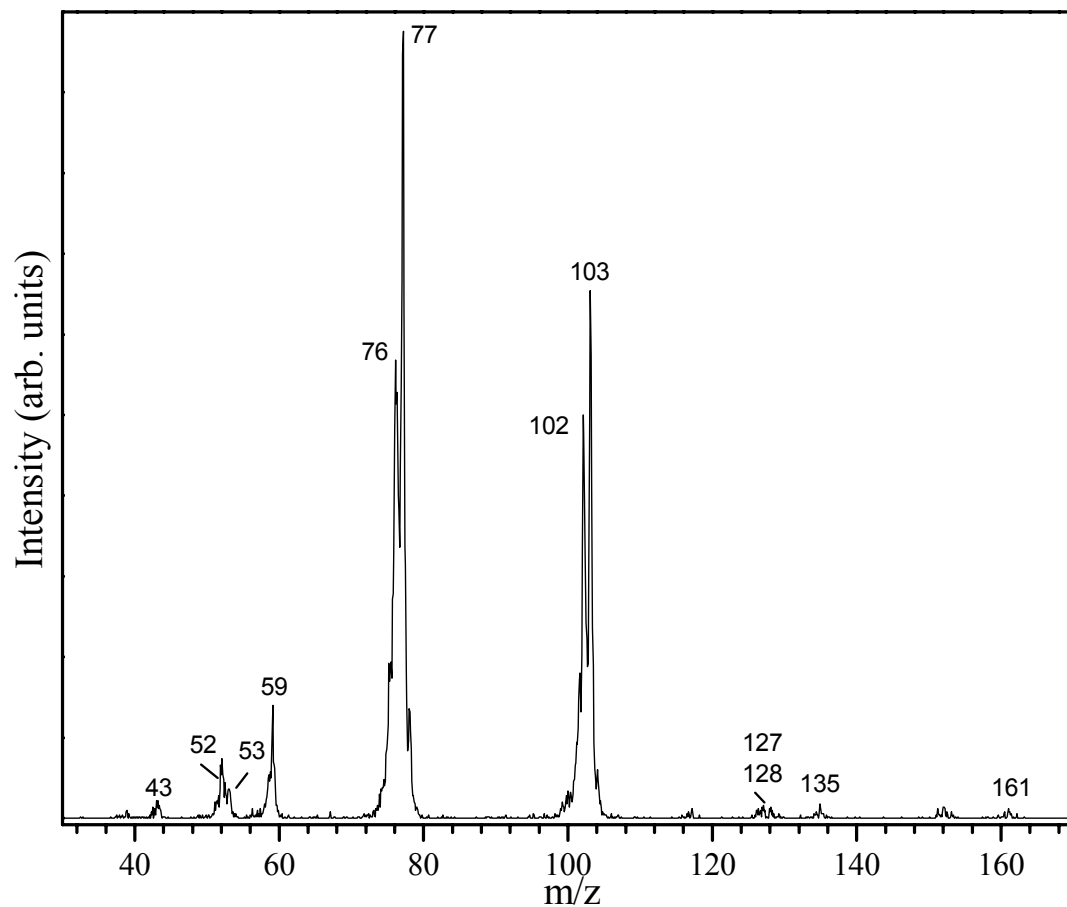


Figure 66: Mass spectrum of mass selected EI ionized acetylene ion,  $\text{C}_2\text{H}_2^+$ , injected into the cell containing 22 mTorr of  $\text{C}_2\text{H}_2$  and 311 mTorr He using an injection energy of 11.9 eV. The temperature of the drift cell was  $31^\circ\text{C}$  and the cell voltage was 24 V. Note some of the peaks represent the acetylene/acetone cluster due to the acetone impurity.

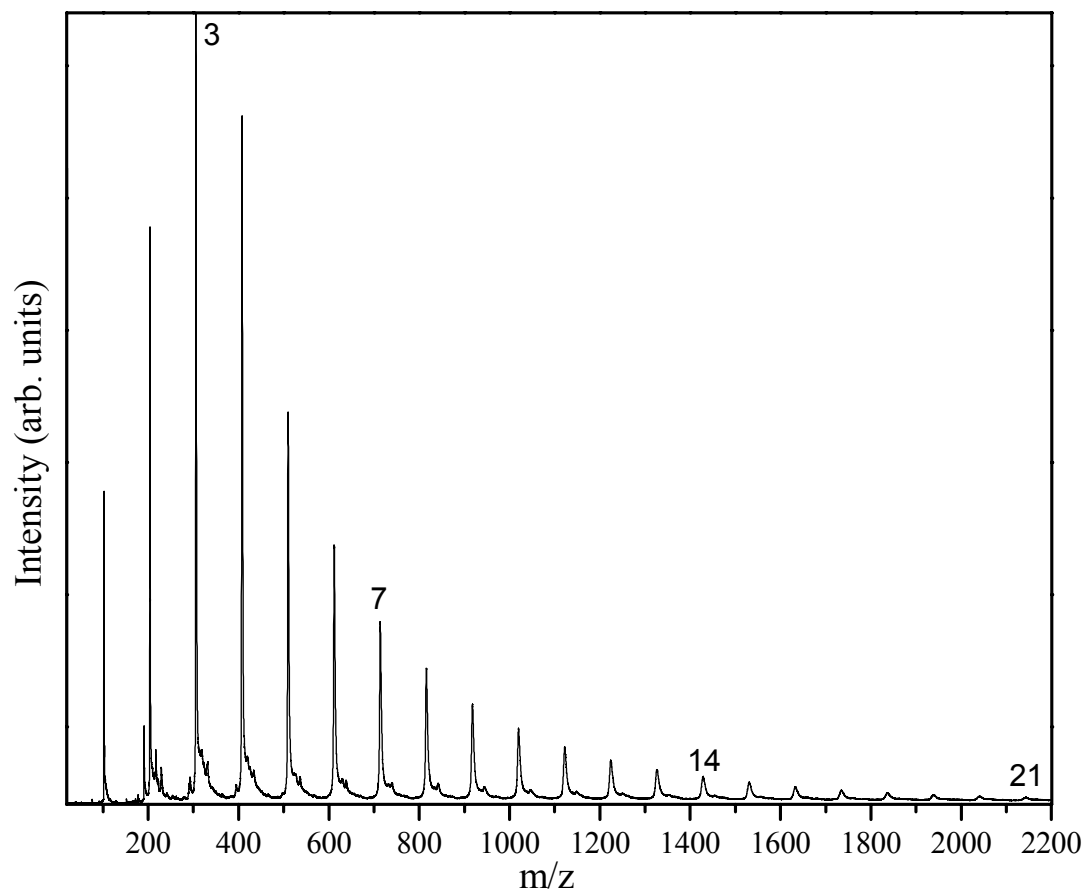


Figure 67: Static TOF mass spectrum of photoionized (193 *nm*)phenylacetylene clusters,  $(\text{C}_8\text{H}_6)_n^+$ . 30 PSI of Argon was passes overed phenylacetylene held at a temperature of 60.1° C.

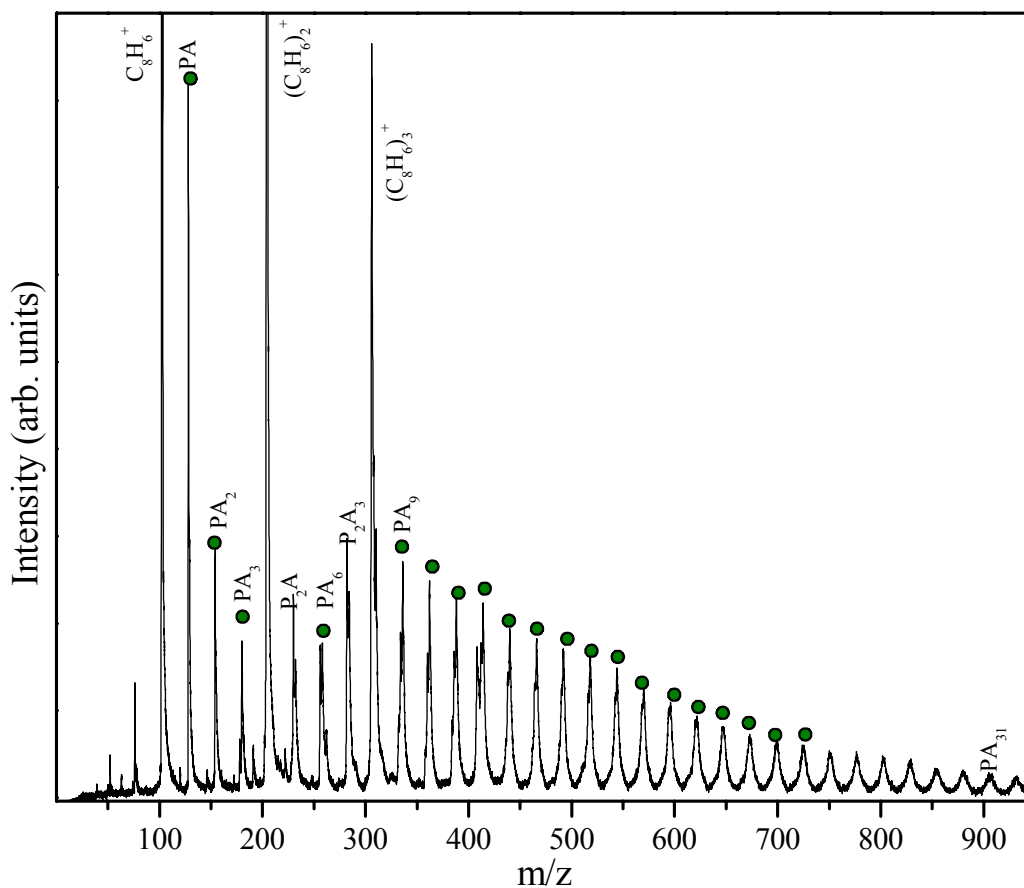


Figure 68: Static TOF mass spectrum of photoionized binary phenylacetylene/acetylene clusters,  $(C_8H_6)_m^+(C_2H_2)_n$ . The major series observed was of the form,  $(C_8H_6)_m^+(C_2H_2)_n$ . Ionization was achieved by photoionization (193 nm) with phenylacetylene acting as a chromophore. 2 PSI of acetylene seeded in helium, 60 PSI, was passed over phenylacetylene held at 0° C to reduce vapor pressure.



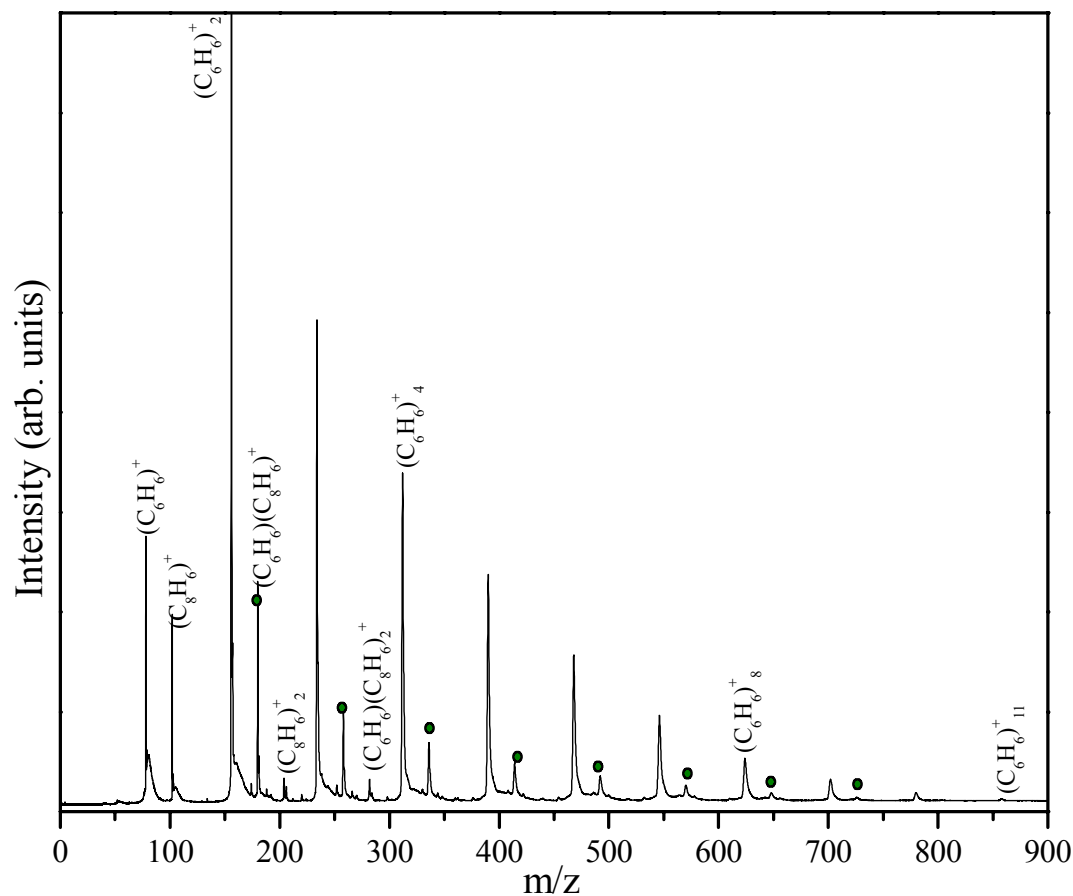


Figure 69: Static TOF mass spectrum of photoionized (193 nm) binary benzene/phenylacetylene clusters,  $(C_6H_6)_m^+(C_8H_6)_n$ . The major series observed was the homogeneous benzene clusters,  $(C_6H_6)_m^+$ . 70 PSI of helium was passed over benzene held at 27° C. Phenylacetylene used was that desorbed in inside surface of line.

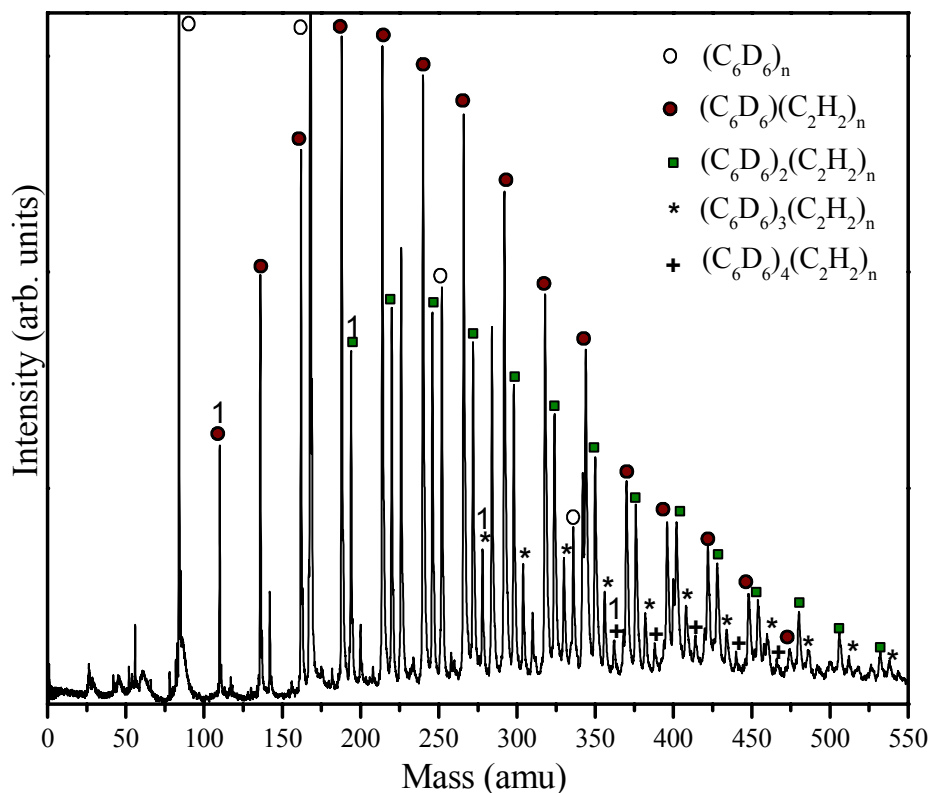


Figure 70: Static TOF mass spectrum of photoionized binary benzene/acetylene clusters,  $(C_6D_6)_m^+(C_2H_2)_n$ . The major series observed was of the form,  $(C_6D_6)_m^+(C_2H_2)_n$  (where  $m=1-4$ ). Most of the unmarked peaks represent reactions of acetone, an impurity in the acetylene tank. Ionization was achieved by photoionization (193 nm) with benzene acting as a chromophore. 5 PSI of acetylene seeded in helium, 60 PSI, was passed over benzene held at  $-78.5^\circ\text{C}$  to reduce vapor pressure, (0.10 mmHg).

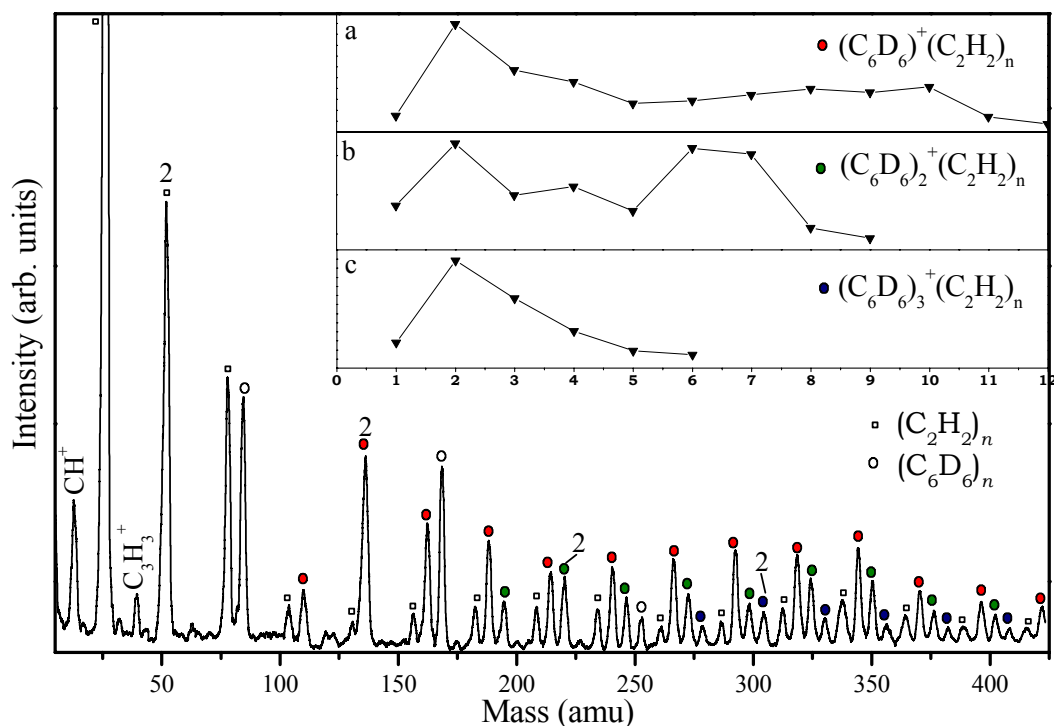


Figure 71: Mass spectrum and intensity plots for electron impact ionized (EI) binary benzene/acetylene clusters of the form,  $(C_6D_6)_m^+(C_2H_2)_n$ . Notice the acetylene cluster series  $(C_2H_2)_n^+$ . In PI (193 nm), the benzene molecules acted as a chromophore because acetylene absorbs at VUV. Charge transfer was undetectably low or absent as benzene has a lower ionization potential (9.24 eV) than acetylene (11.4 eV). On the other hand, in EI ionization, both molecules were ionized and as a result, a substantial proportion of the observed acetylene series is likely the result of EI ionization rather than fragmentation of binary acetylene/benzene clusters. Also interesting was the observation of  $C_3H_3^+$  fragment. Since deuterated benzene was utilized in this experiment, this complex can only be the result of acetylene isomerization reaction.

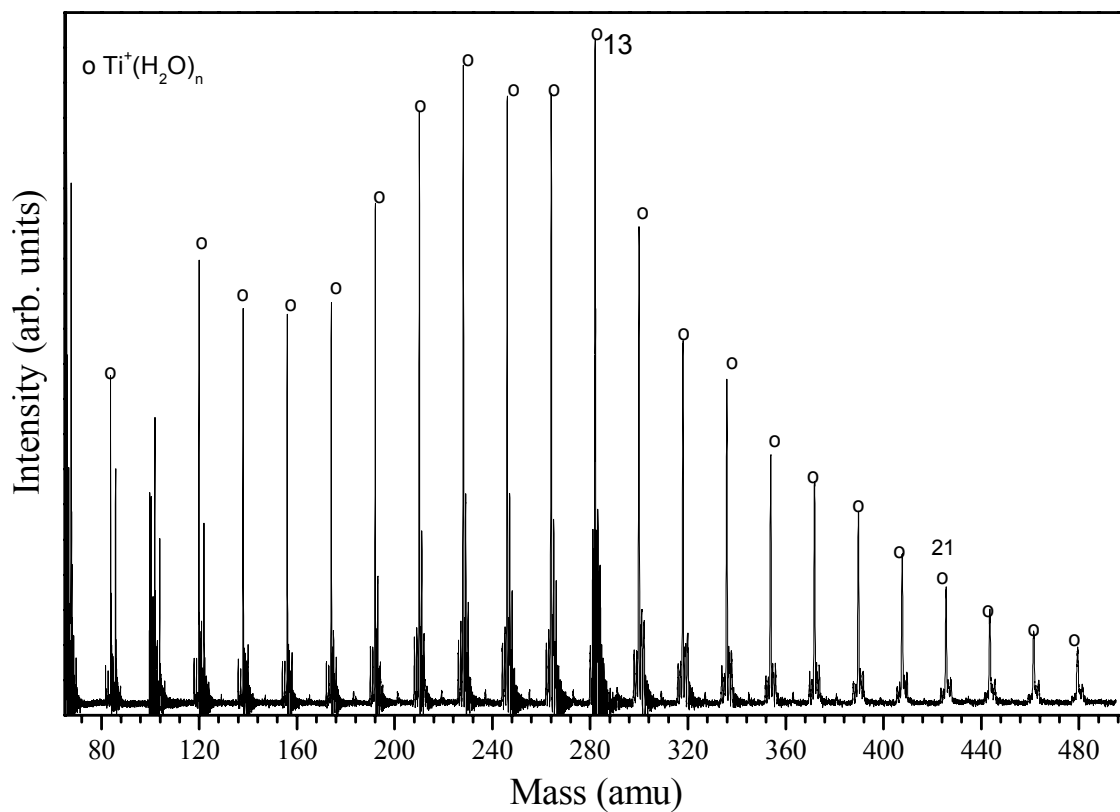


Figure 72: TOF mass spectrum of  $\text{Ti}^+(\text{H}_2\text{O})_n$  clusters using low laser power. The metal target was ablated  $619 \mu\text{s}$  after the nozzle opened ( $t_0$ ) and the accelerating plates were pulsed  $1.12 \text{ ms}$  after  $t_0$ . Stagnation helium pressure was 12 PSI and the water temperature was  $27^\circ \text{C}$ .

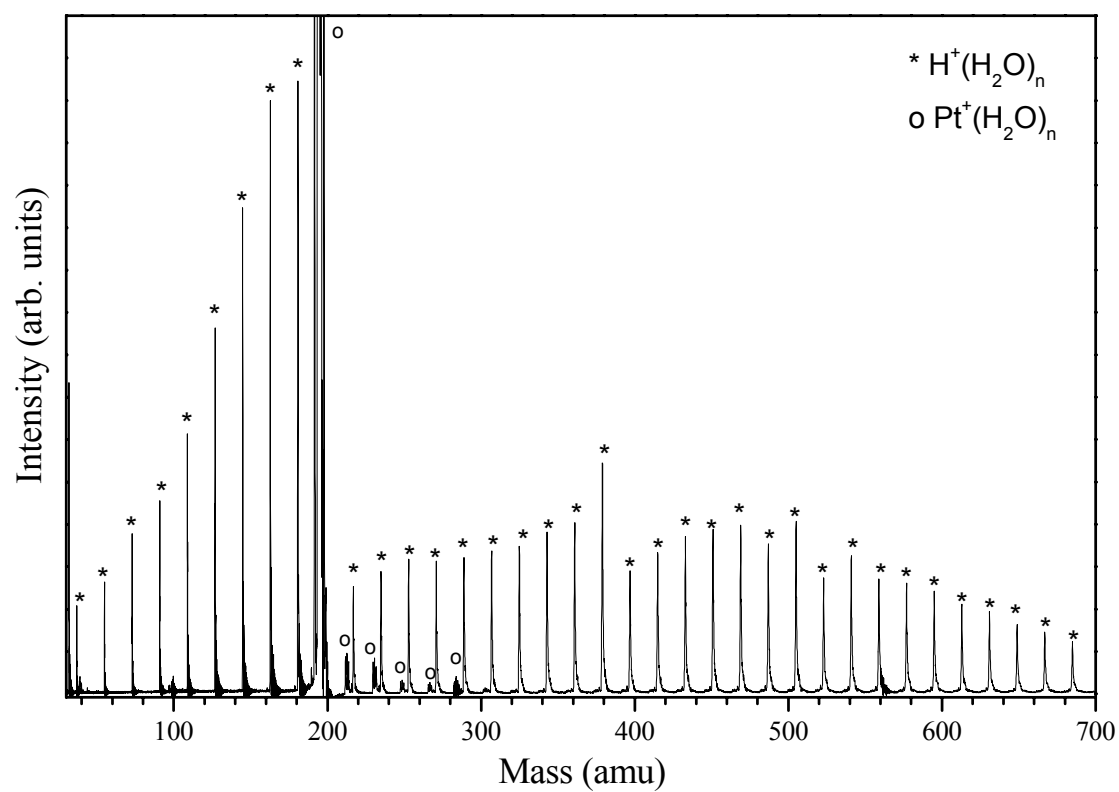


Figure 73: TOF mass spectrum of  $\text{Pt}^+(\text{H}_2\text{O})_n$  clusters. Stagnation helium pressure was 21 PSI and the water temperature was 27° C.

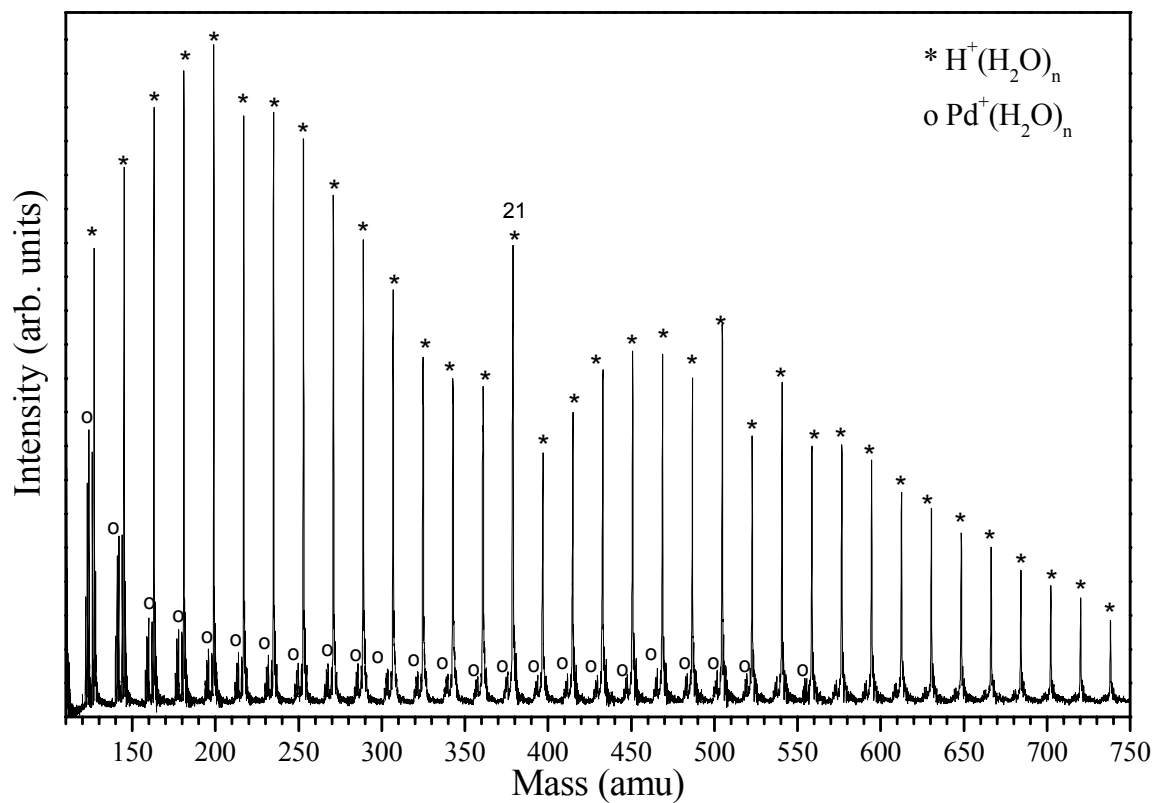


Figure 74: TOF mass spectrum of  $\text{Pd}^+(\text{H}_2\text{O})_n$  clusters. Stagnation helium pressure was 16 PSI and the water temperature was 27° C.

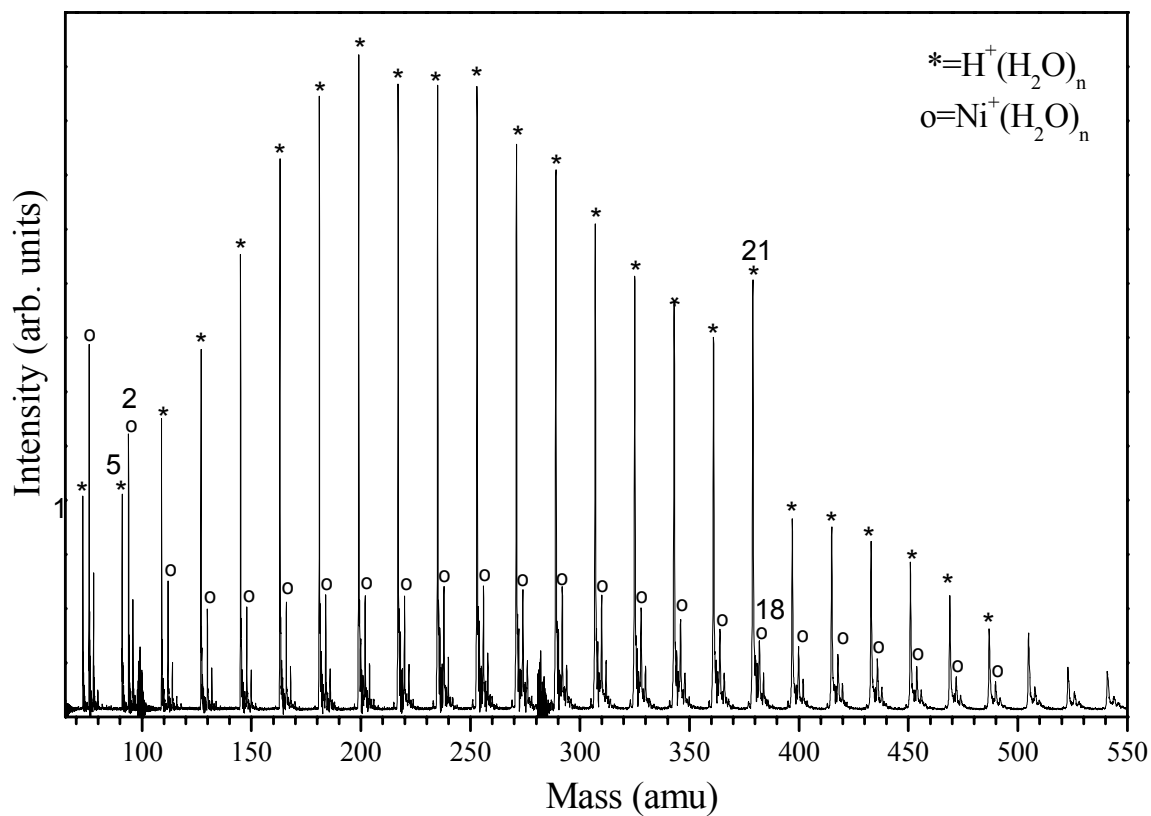


Figure 75: TOF mass spectrum of  $\text{Ni}^+(\text{H}_2\text{O})_n$  clusters. Stagnation helium pressure was 13 PSI and the water temperature was 27° C.

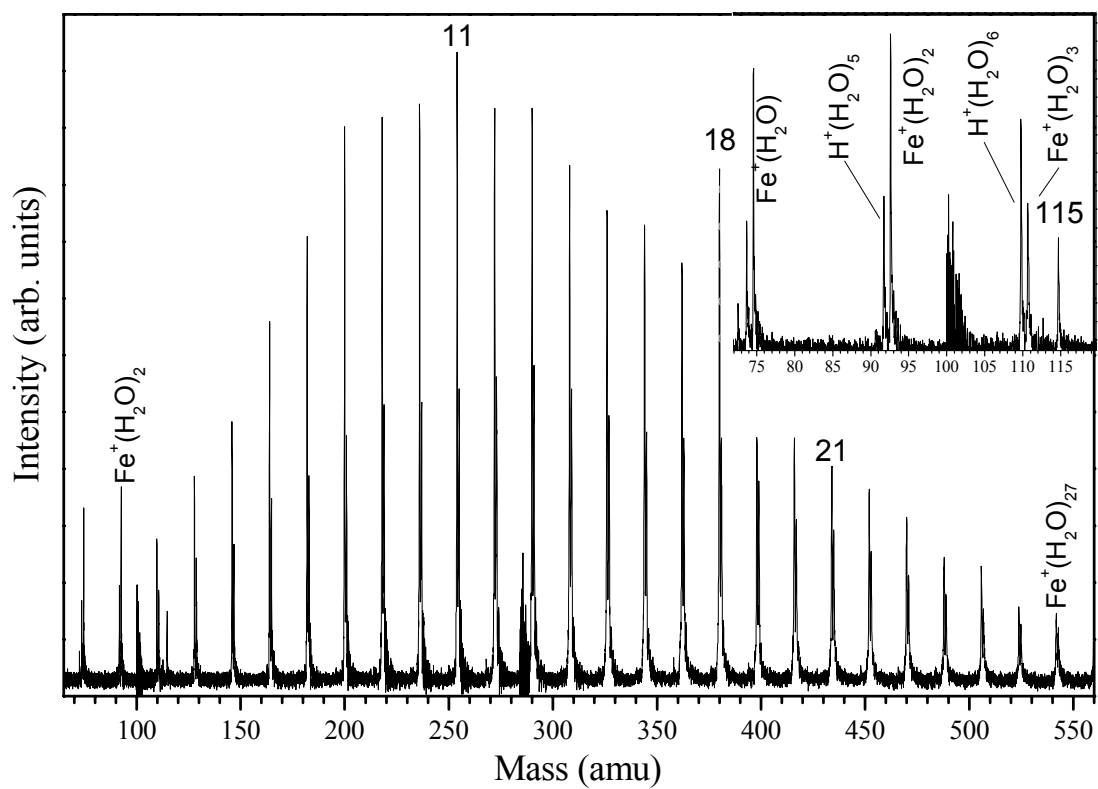


Figure 76: TOF mass spectrum of  $\text{Fe}^+(\text{H}_2\text{O})_n$  clusters. Stagnation helium pressure was 21 PSI and the water temperature was 27° C.



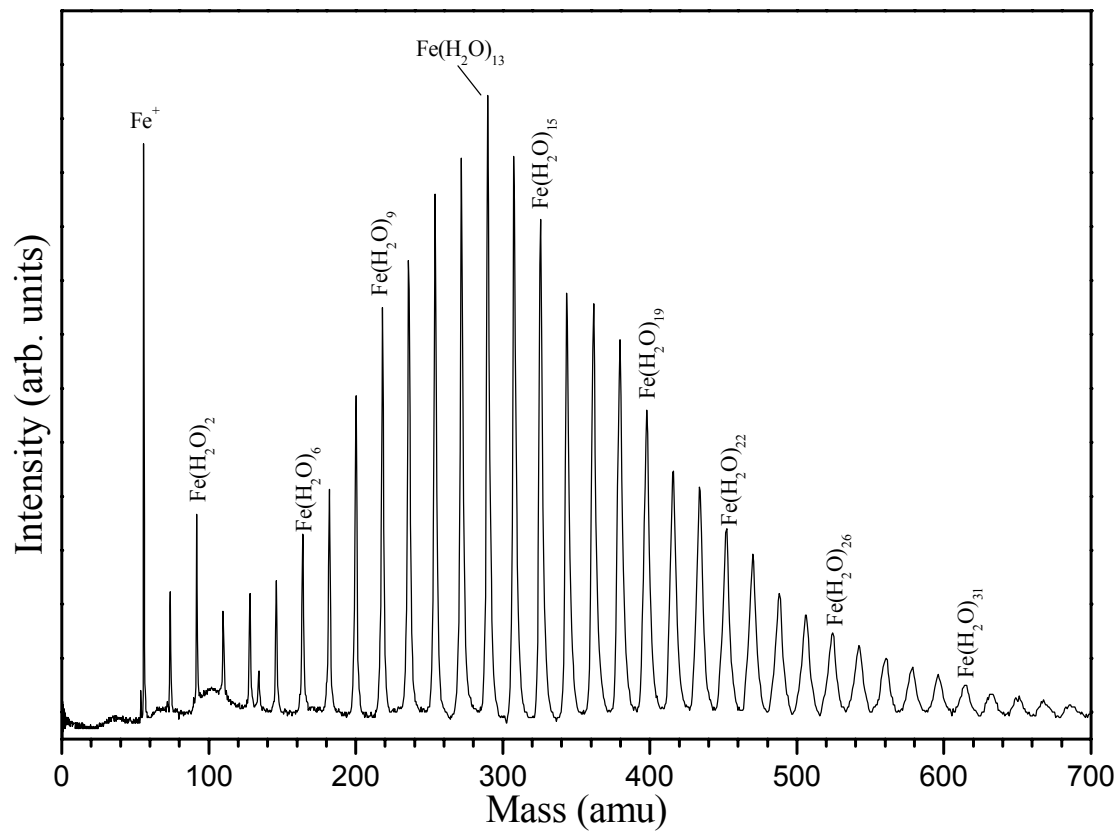


Figure 77: TOF mass spectrum of  $\text{Fe}^+(\text{H}_2\text{O})_n$  clusters. Stagnation helium pressure was 30 PSI and the water temperature was 23° C.

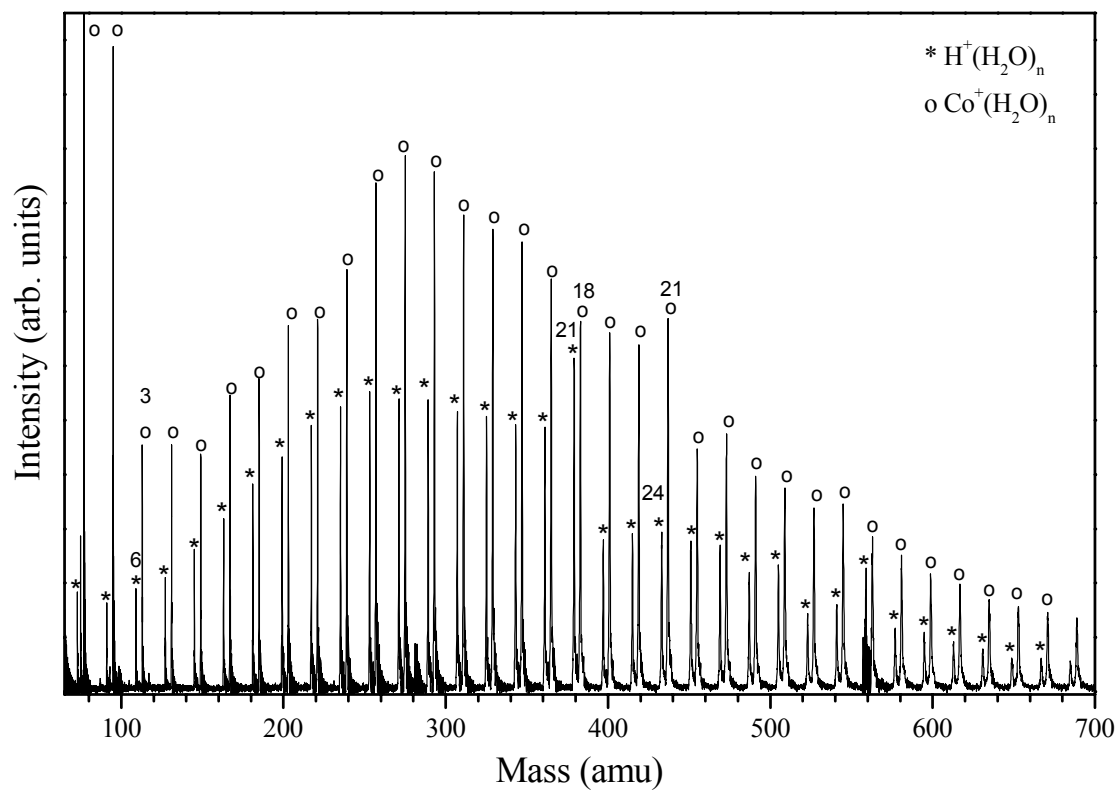


Figure 78: TOF mass spectrum of  $\text{Co}^+(\text{H}_2\text{O})_n$  clusters. Stagnation helium pressure was 16 PSI and the water temperature was  $27^\circ\text{C}$ .

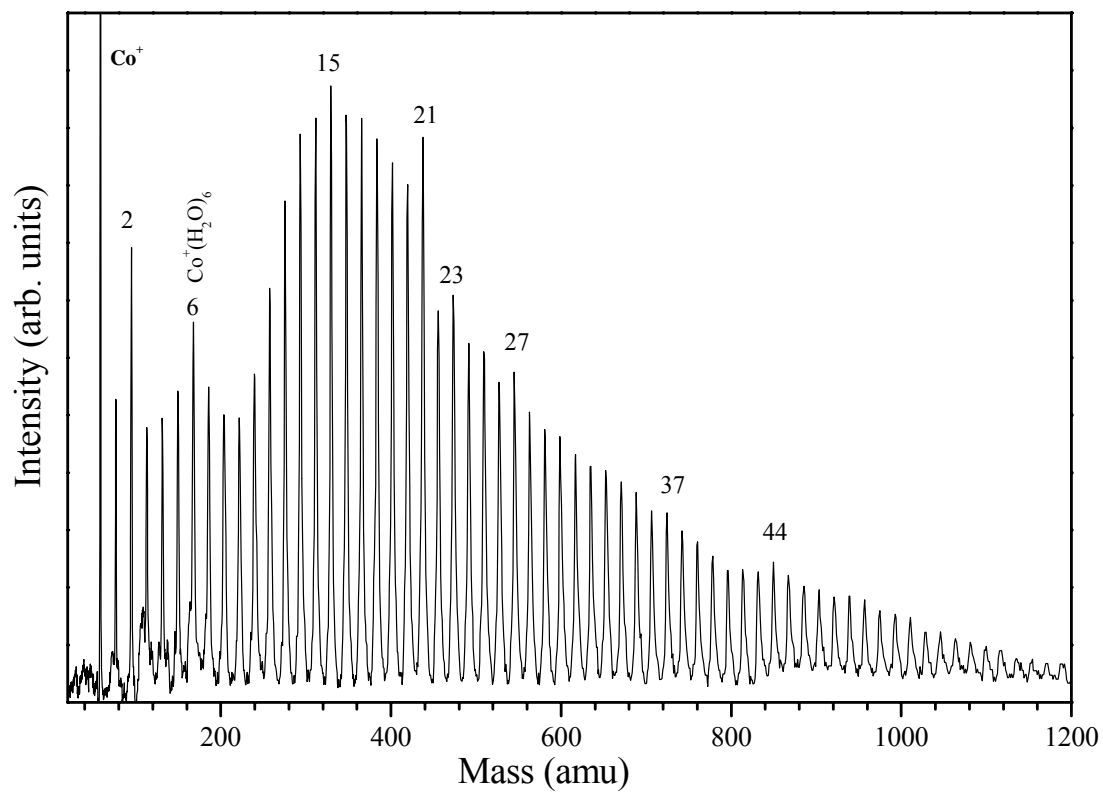


Figure 79: TOF mass spectrum of  $\text{Co}^+(\text{H}_2\text{O})_n$  clusters.

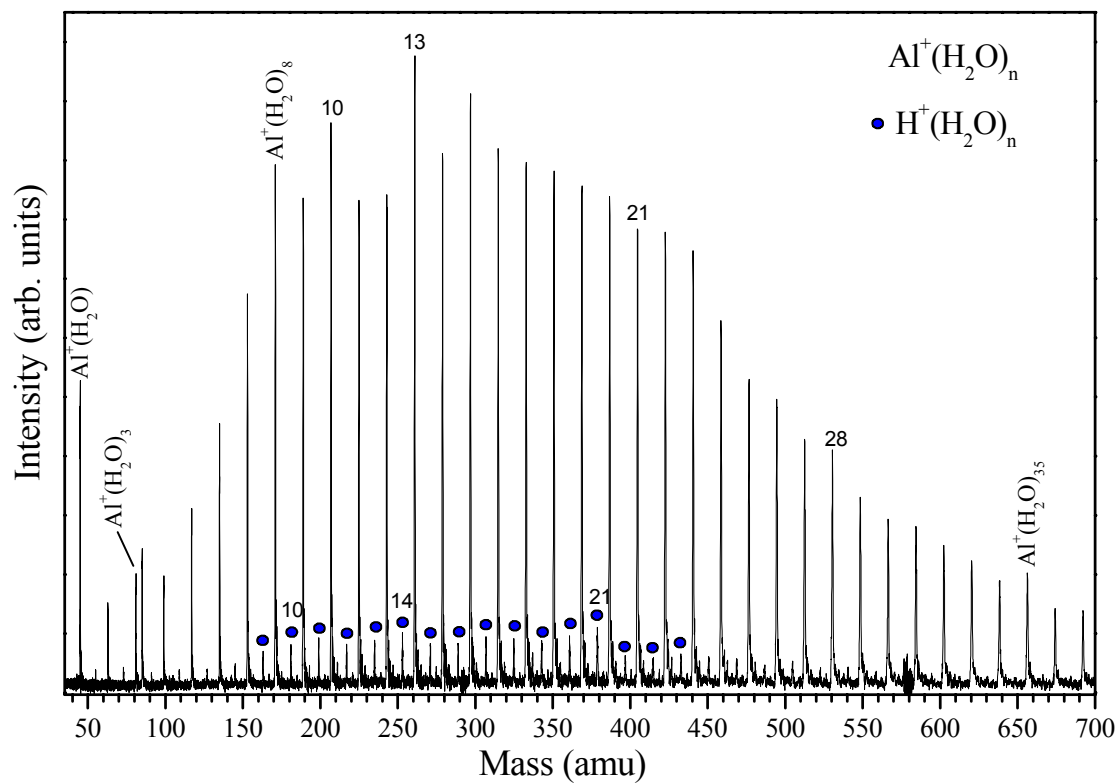


Figure 80: TOF mass spectrum of  $\text{Al}^+(\text{H}_2\text{O})_n$  clusters. Stagnation helium pressure was 20 PSI and the water temperature was 27° C.

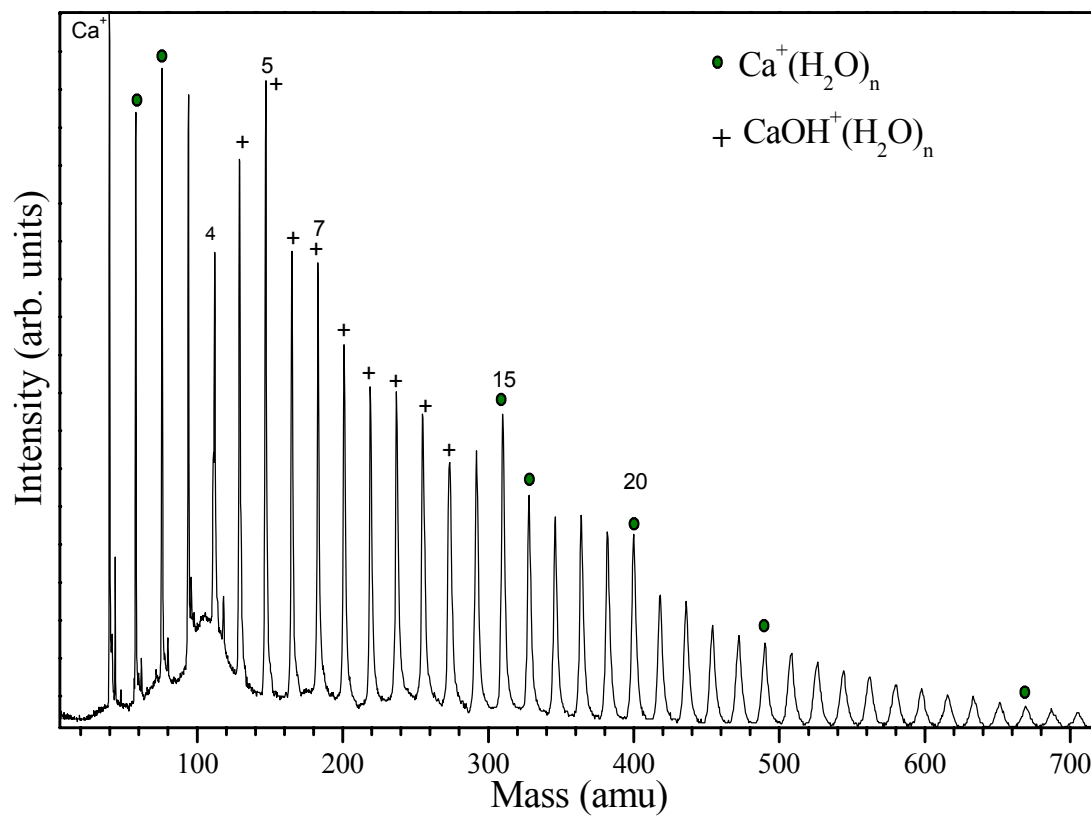


Figure 81: TOF mass spectrum of  $\text{Ca}^+(\text{H}_2\text{O})_n$  clusters.

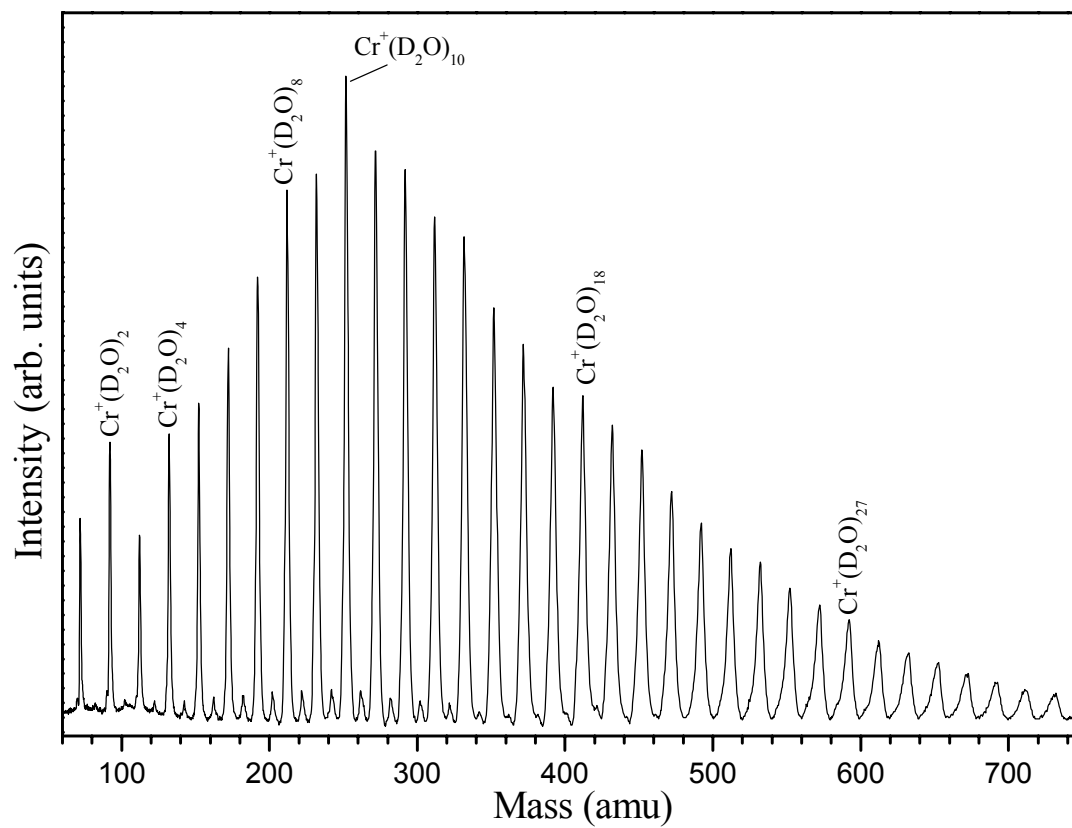


Figure 82: TOF mass spectrum of  $\text{Cr}^+(\text{H}_2\text{O})_n$  clusters. Stagnation helium pressure was 30 PSI and the water temperature was 27° C.

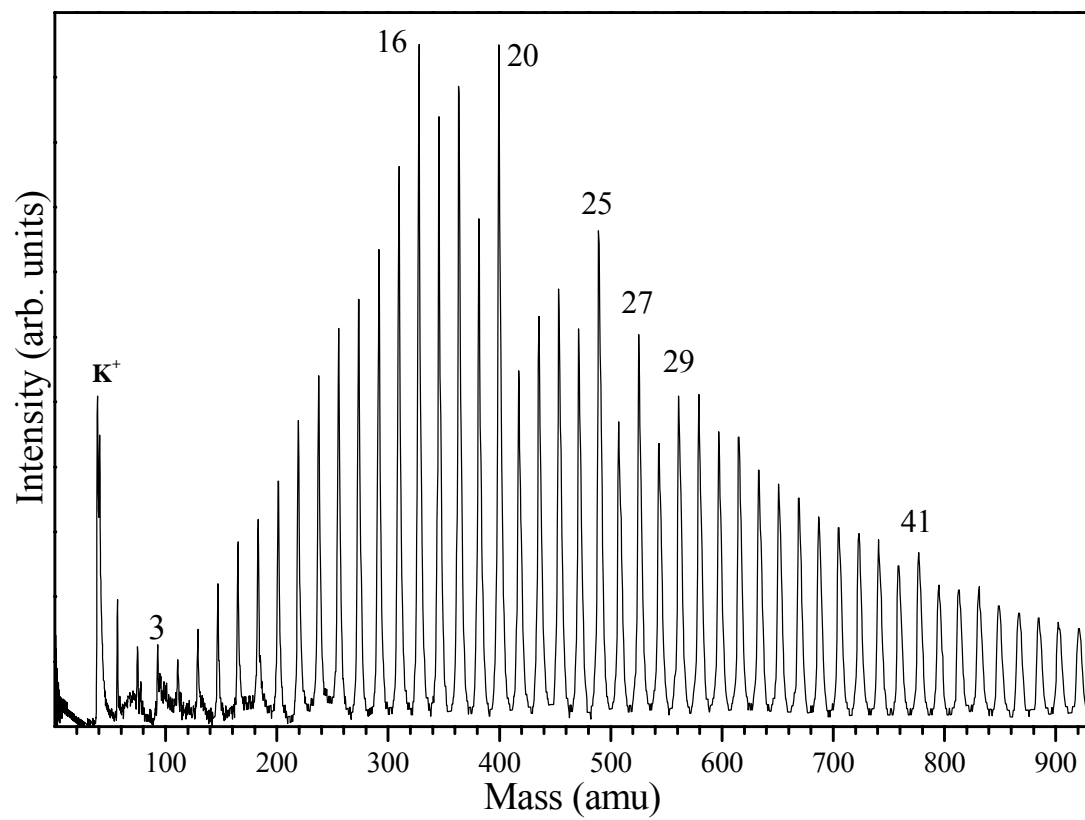


Figure 83: TOF mass spectrum of  $K^+(H_2O)_n$  clusters.

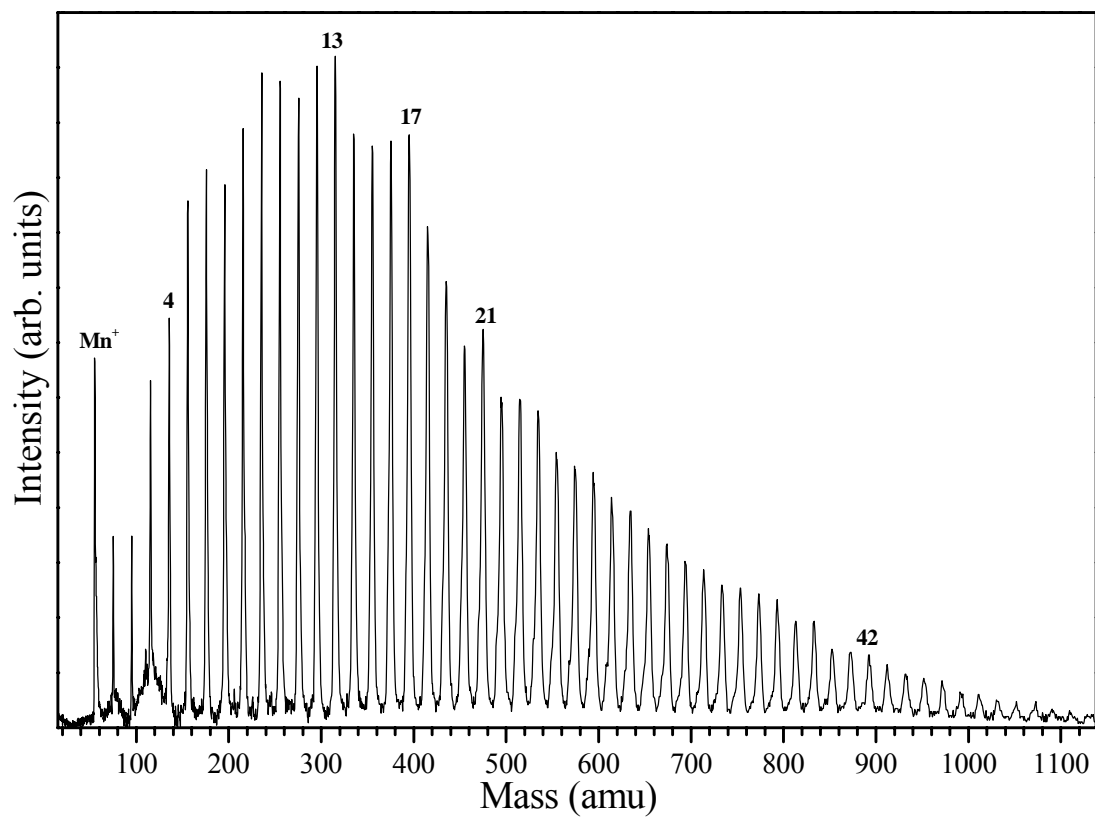


Figure 84: TOF mass spectrum of  $\text{Mn}^+(\text{H}_2\text{O})_n$  clusters.



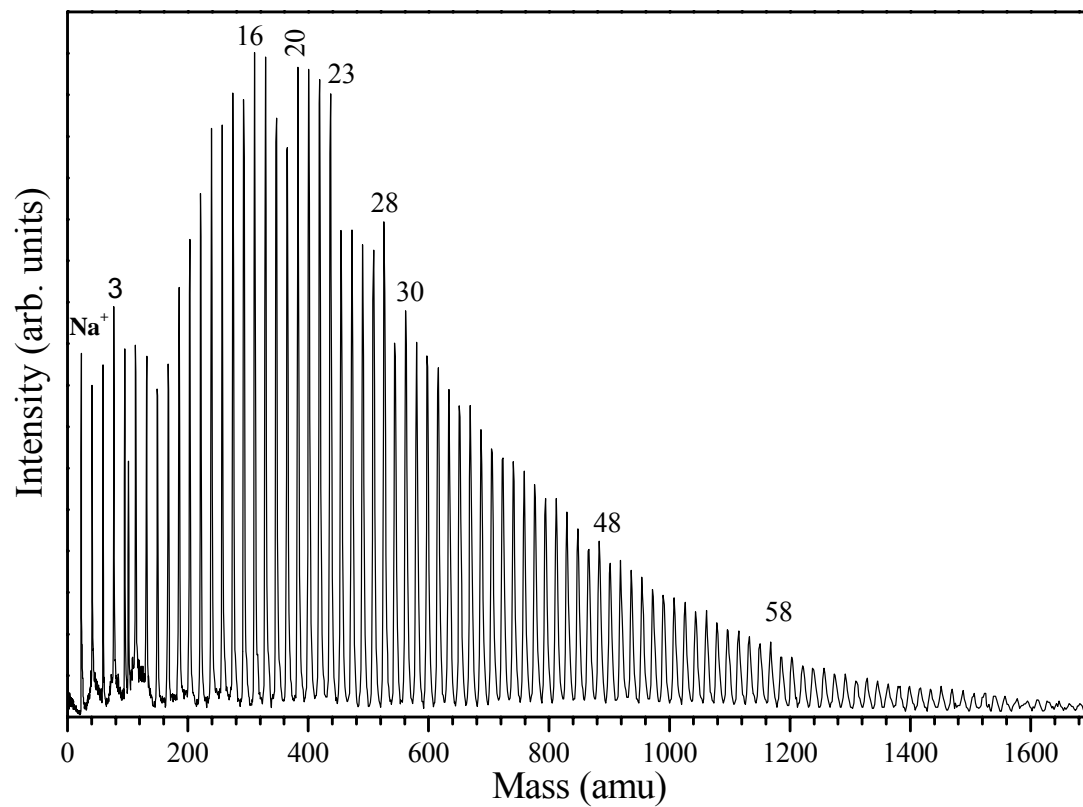


Figure 85: TOF mass spectrum of  $\text{Na}^+(\text{H}_2\text{O})_n$  clusters.

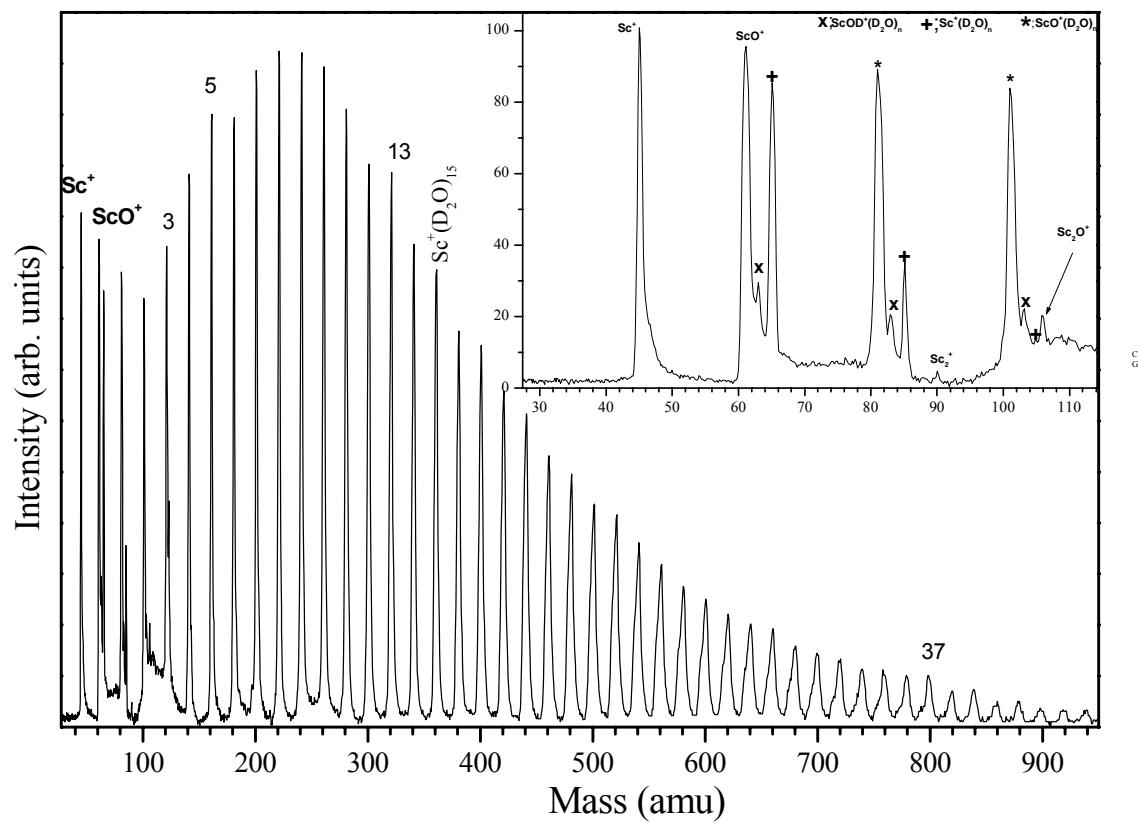


Figure 86: TOF mass spectrum of  $\text{Sc}^+(\text{H}_2\text{O})_n$  clusters.

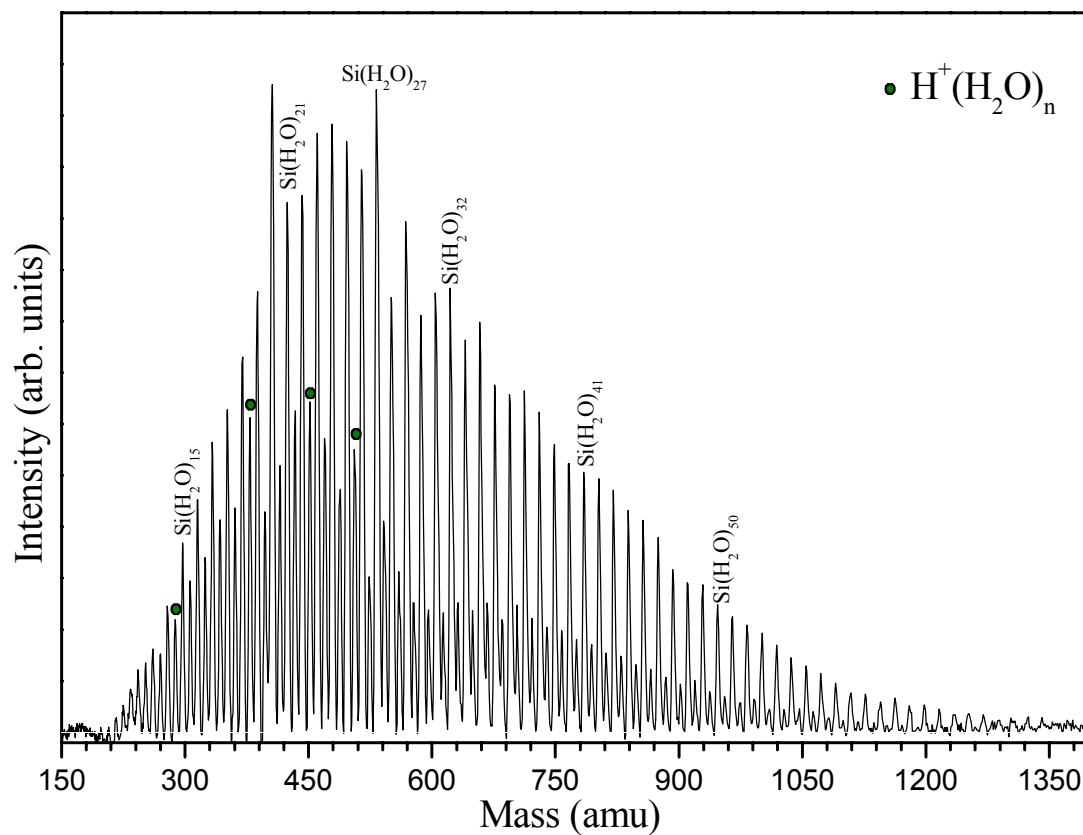


Figure 87: TOF mass spectrum of  $\text{Si}^+(\text{H}_2\text{O})_n$  clusters. Stagnation helium pressure was 30 PSI and the water temperature was  $48^\circ\text{C}$ .

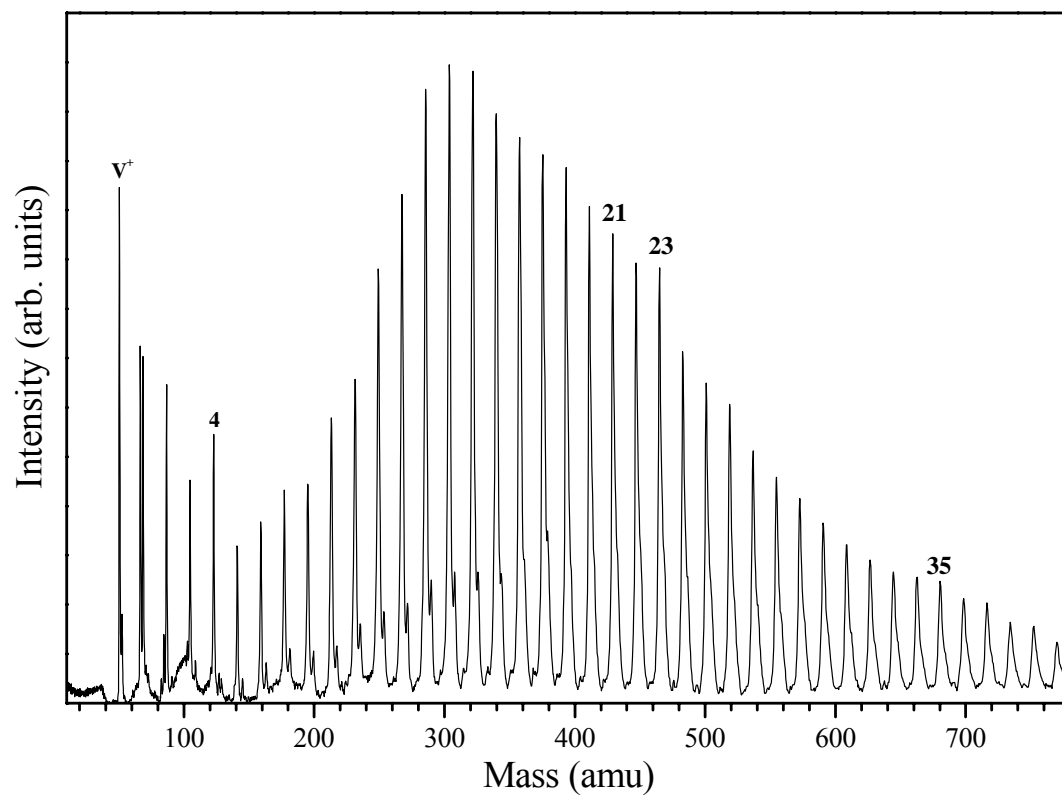


Figure 88: TOF mass spectrum of  $V^+(H_2O)_n$  clusters.

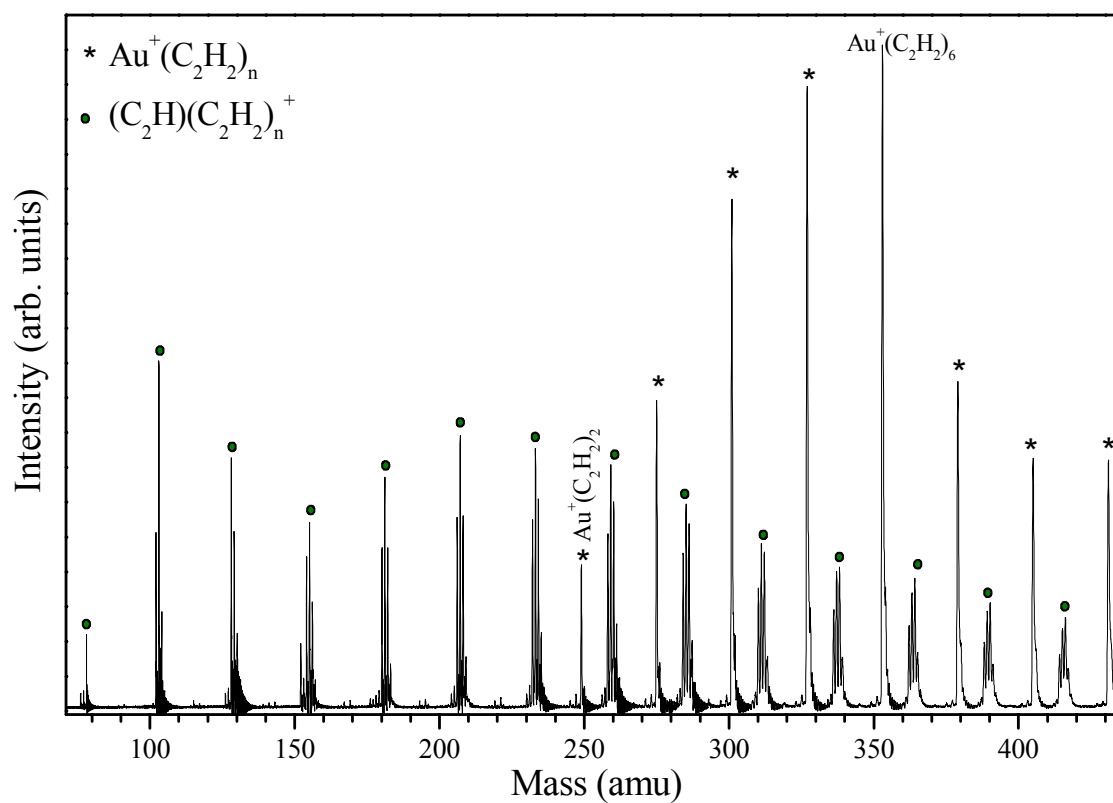


Figure 89: TOF mass spectrum of  $\text{Au}^+(\text{C}_2\text{H}_2)_n$  clusters. Stagnation pressure was 50 PSI (helium) and 1.5 PSI acetylene (3%). Pressure of the source chamber was  $5.3 \times 10^{-5}$  Torr.

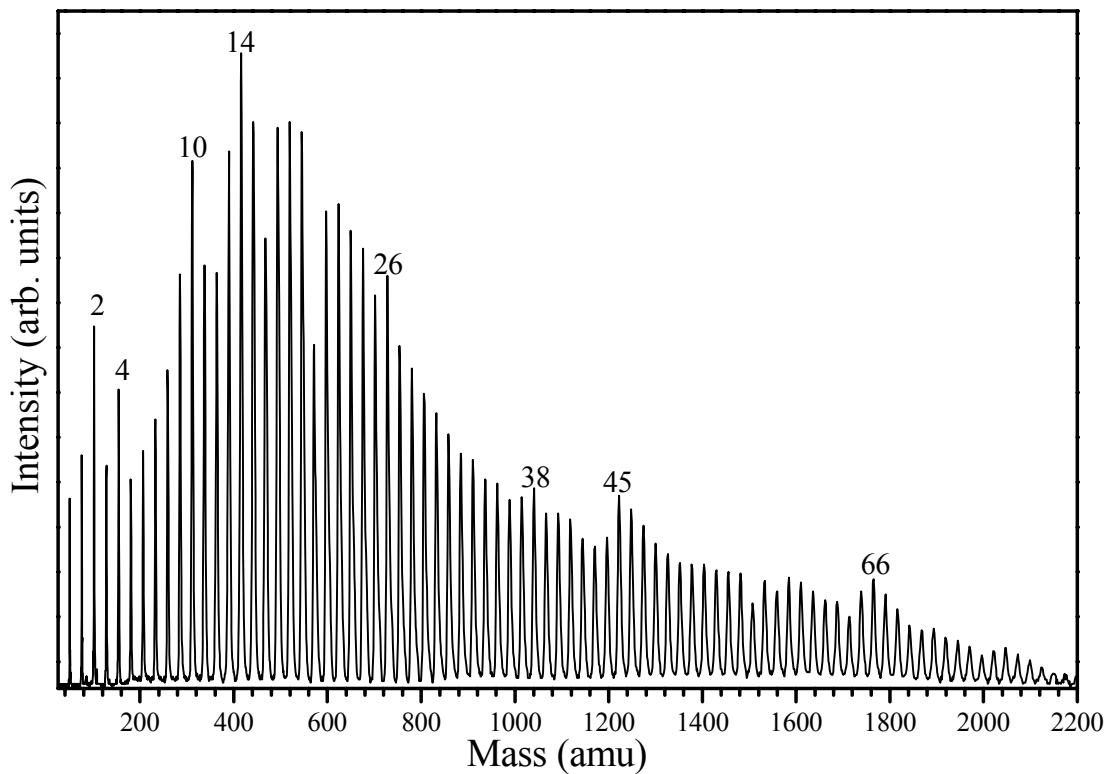


Figure 90: TOF mass spectrum of  $\text{Cr}^+(\text{C}_2\text{H}_2)_n$  clusters using low laser power. Metal target was ablated  $578.7 \mu\text{s}$  after nozzle opened ( $t_0$ ) and accelerating plates were pulsed  $1.12 \text{ ms}$  after  $t_0$ . Background pressure was 50 PSI (helium) and 1.5 PSI acetylene (3%). Pressure of the source chamber was  $5.3 \times 10^{-5}$  Torr.

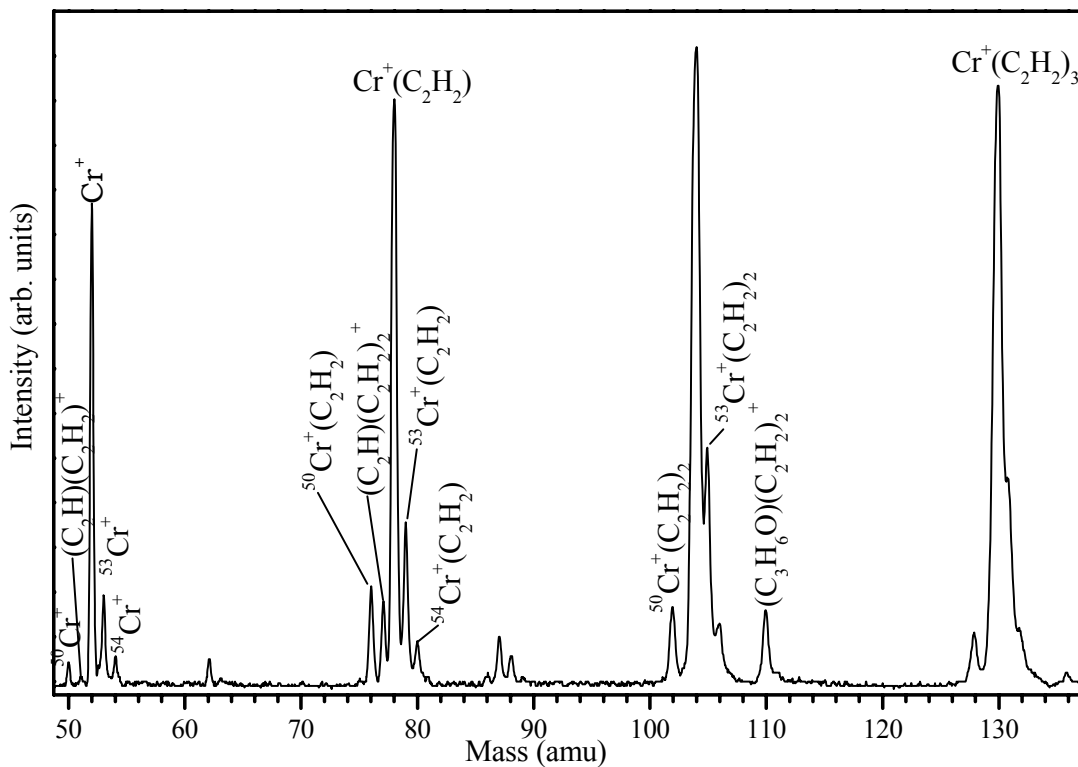


Figure 91: TOF mass spectrum of  $\text{Cr}^+(\text{C}_2\text{H}_2)_n$  clusters at early arrival times ( $<20 \mu\text{s}$ ). Chromium isotopes are responsible for the observed multiplets. Also, chromium isotope complexes,  $^y\text{Cr}^+(\text{C}_2\text{H}_2)_n$ , coincides with  $\text{C}_2\text{H}_x(\text{C}_2\text{H}_2)_n$  (where  $x = 0$  and 2) fragments.

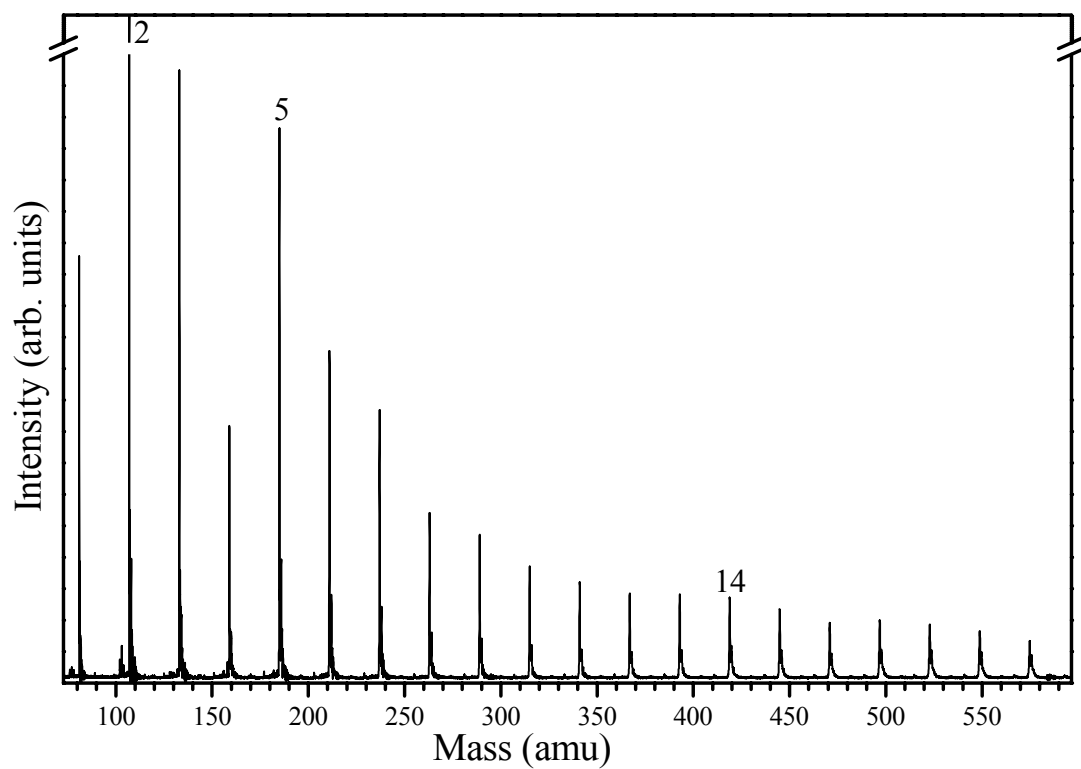


Figure 92: Reflectron Time of Flight (RTOF) mass spectrum of  $Mn^+(C_2H_2)_n$  clusters. Notice the enhanced intensity for the  $n = 5$  peak.



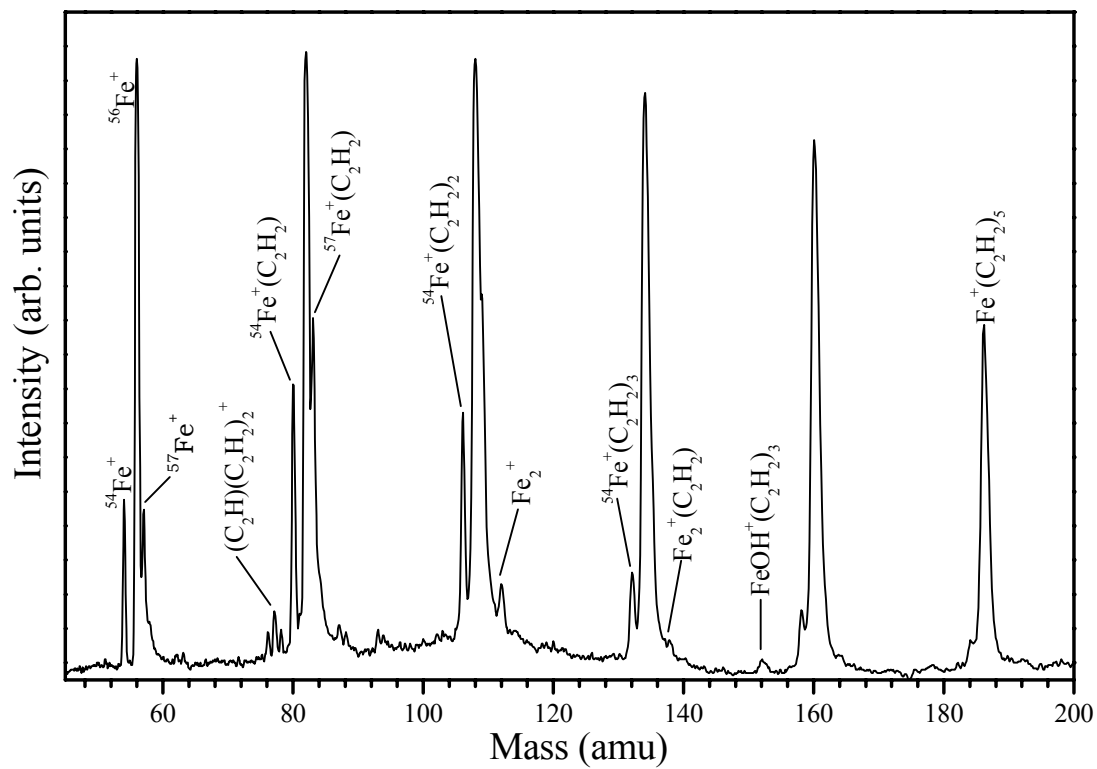


Figure 93: Time of Flight (TOF) mass spectrum of  $\text{Fe}^+(\text{C}_2\text{H}_2)_n$  clusters at early arrival times (low mass range).

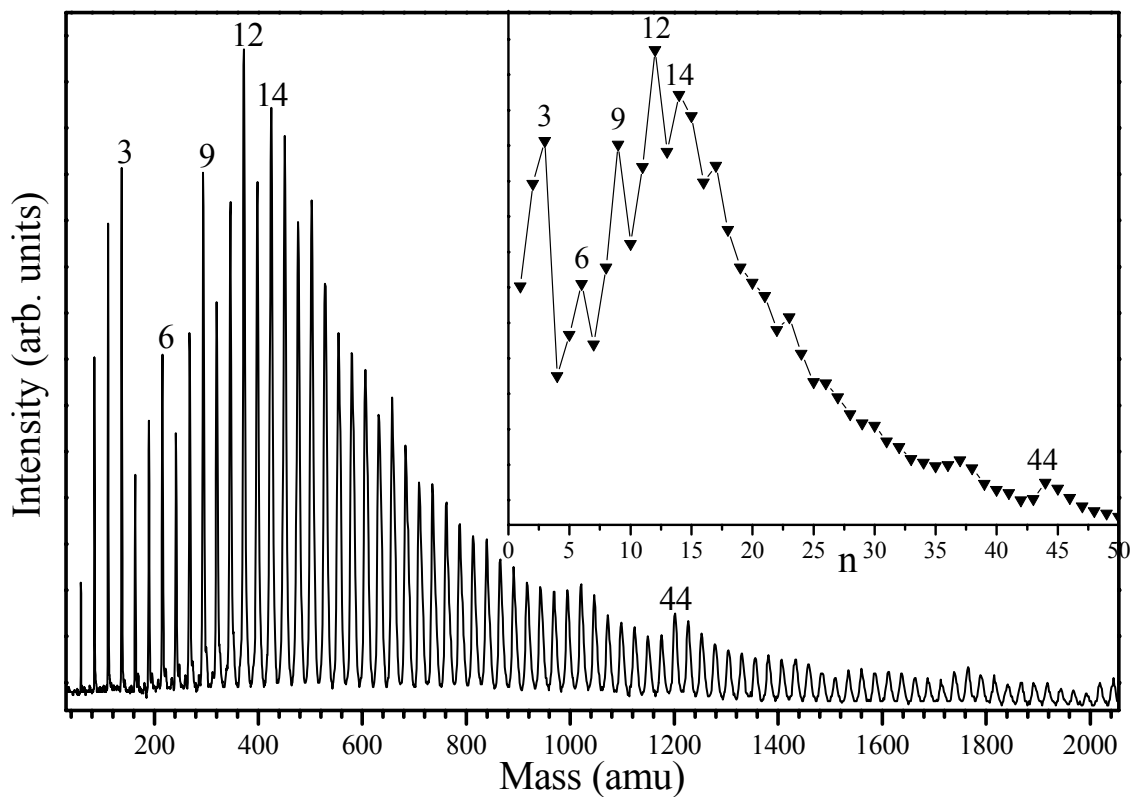


Figure 94: Time of Flight (TOF) mass spectrum and intensity plot (inset) of  $\text{Co}^+(\text{C}_2\text{H}_2)_n$  clusters. Here, the Nd: YAG laser was timed to fire  $578.7 \mu\text{s}$  after the nozzle opened ( $t_0$ ). The acceleration plates were pulsed  $1.08 \text{ ms}$  after  $t_0$ . Pressure of the first chamber was  $3.1 \times 10^{-5} \text{ Torr}$ .

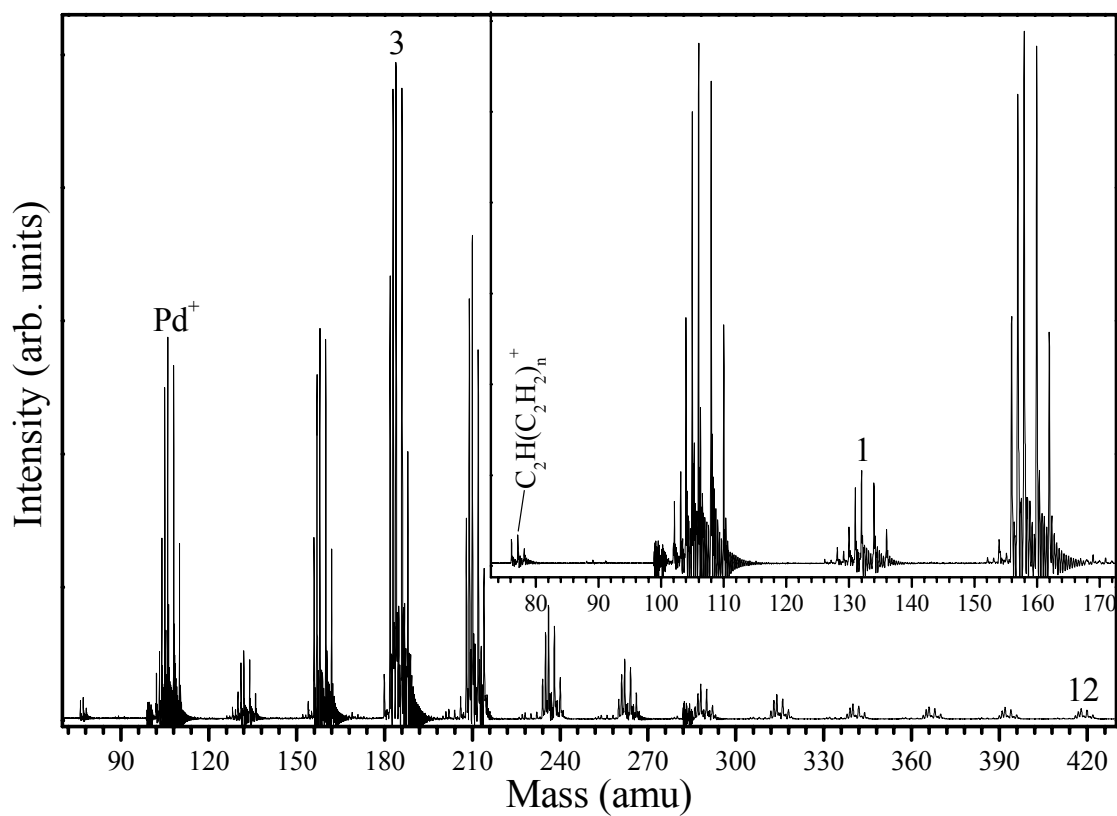


Figure 95: TOF mass spectrum of  $\text{Pd}^+(\text{C}_2\text{H}_2)_n$  clusters. Multiplets are as a result of the extensive isotopic matrix for palladium. Also coincident with the palladium isotopes are fragments of the form  $(\text{C}_2\text{H}_2)_n^+$  and  $\text{C}_2\text{H}(\text{C}_2\text{H}_2)_{n-1}^+$ .

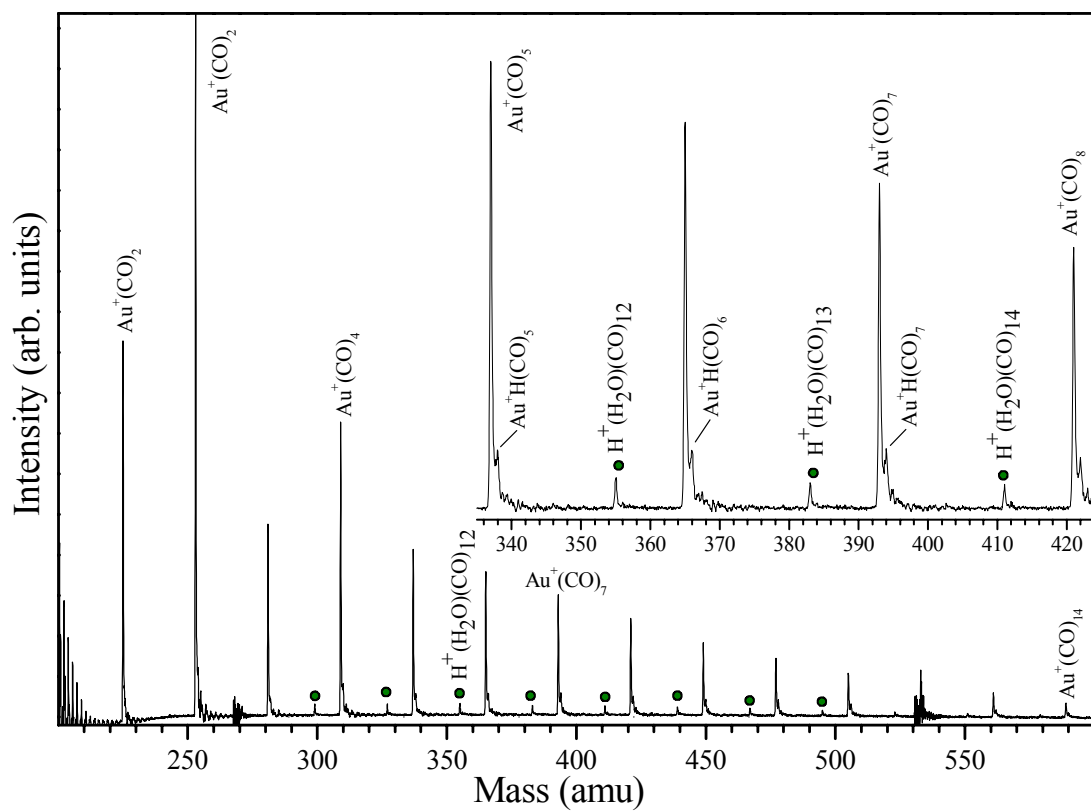


Figure 96: TOF mass spectrum of  $\text{Au}^+(\text{CO})_n$  clusters. The helium stagnation pressure was 48 PSI and the CO pressure was 10 PSI.

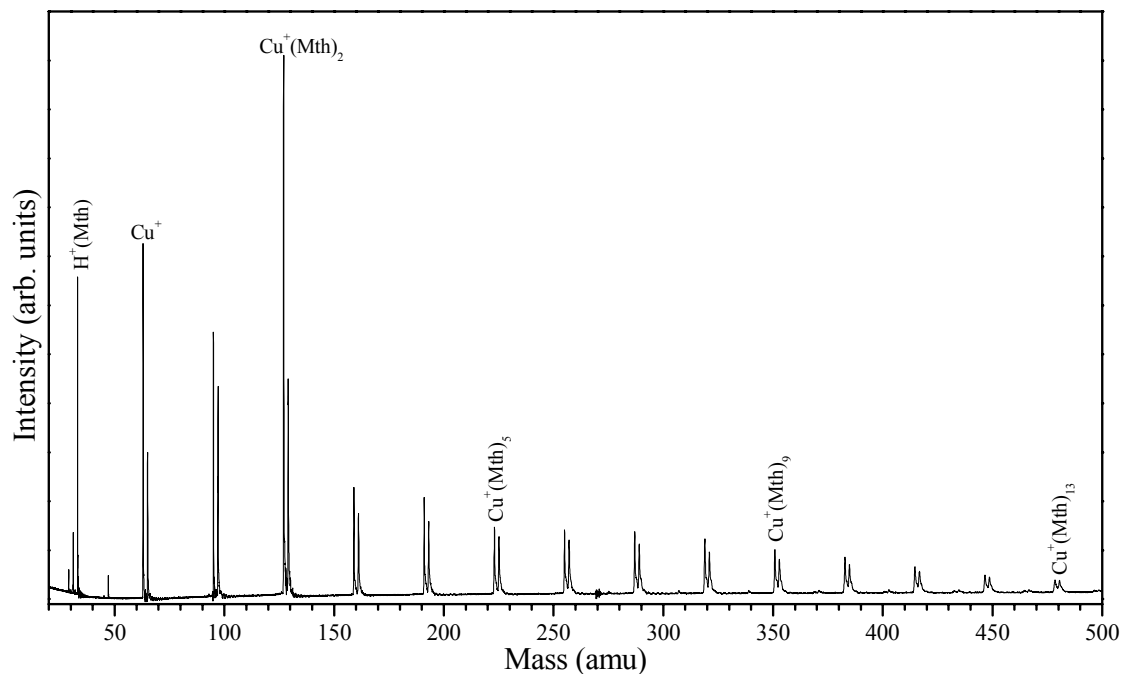


Figure 97: Time of Flight (TOF) mass spectrum of  $\text{Cu}^+(\text{CH}_3\text{OH})_n$  clusters. Here, the Nd:YAG laser was timed to fire  $564 \mu\text{s}$  after the nozzle opened ( $t_0$ ). The acceleration plates were pulsed  $1.04 \text{ ms}$  after  $t_0$ . Pressure of the first chamber was  $1.7 \times 10^{-5}$  Torr. Helium stagnation pressure was 11 PSI and methanol temperature was  $27^\circ \text{C}$ .

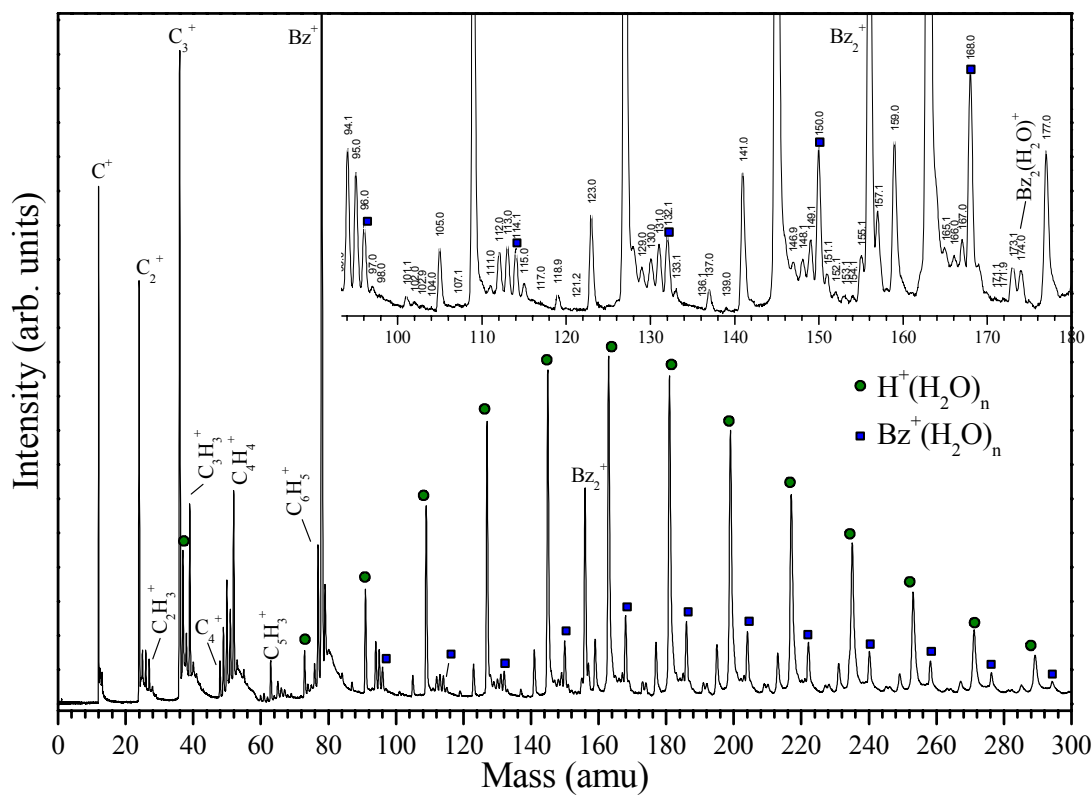


Figure 98: TOF mass spectrum of photoionized benzene/water clusters. Helium pressure was 70 PSI and the water and benzene temperatures were  $-78.5^\circ\text{C}$  and  $27^\circ\text{C}$  respectively.

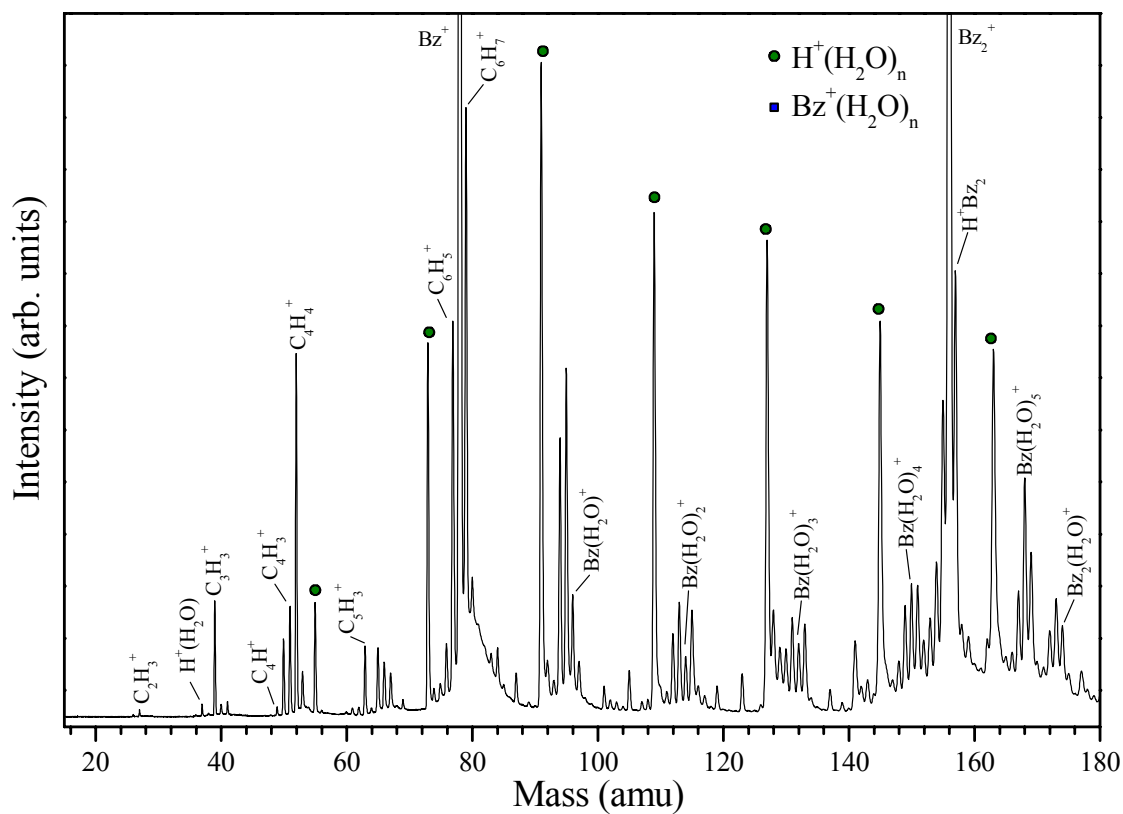


Figure 99: TOF mass spectrum of photoionized benzene/water clusters. Helium pressure was 20 PSI and the water and benzene temperature was 27° C. Benzene and water are mixed in the bubbler.

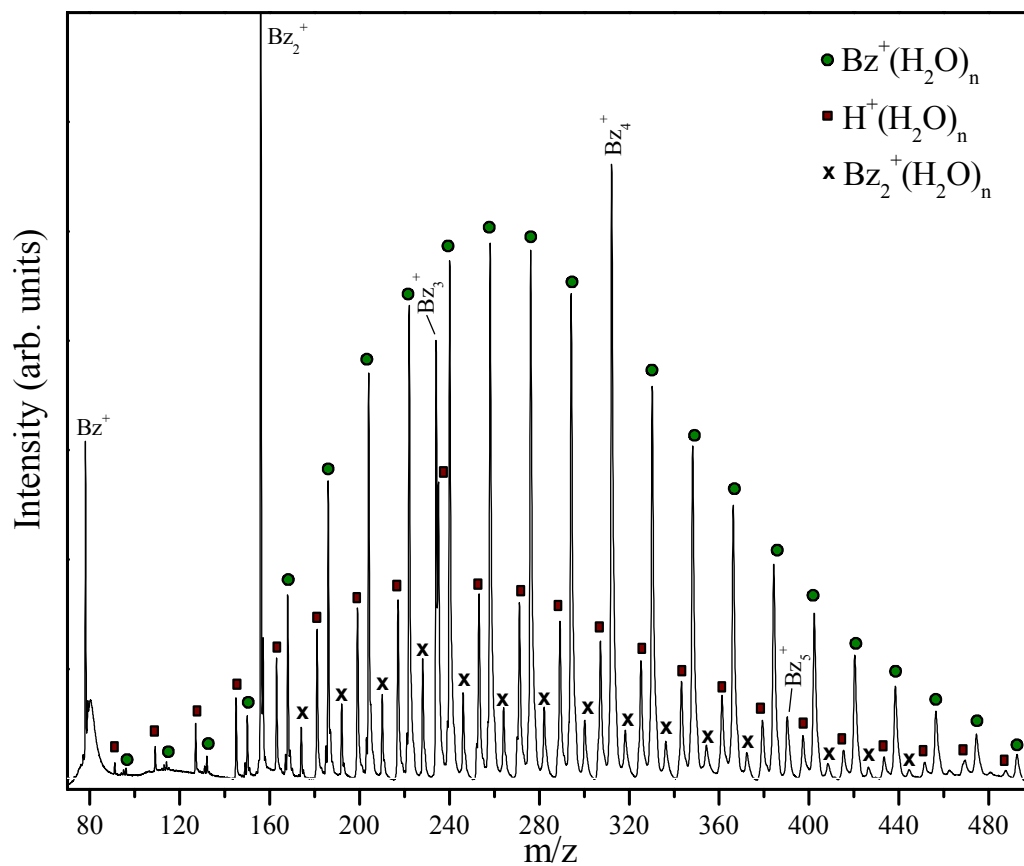


Figure 100: TOF mass spectrum of photoionized benzene/water clusters. Helium pressure was 70 PSI and the water and benzene temperature was 27° C. Benzene and water are mixed in the bubbler.



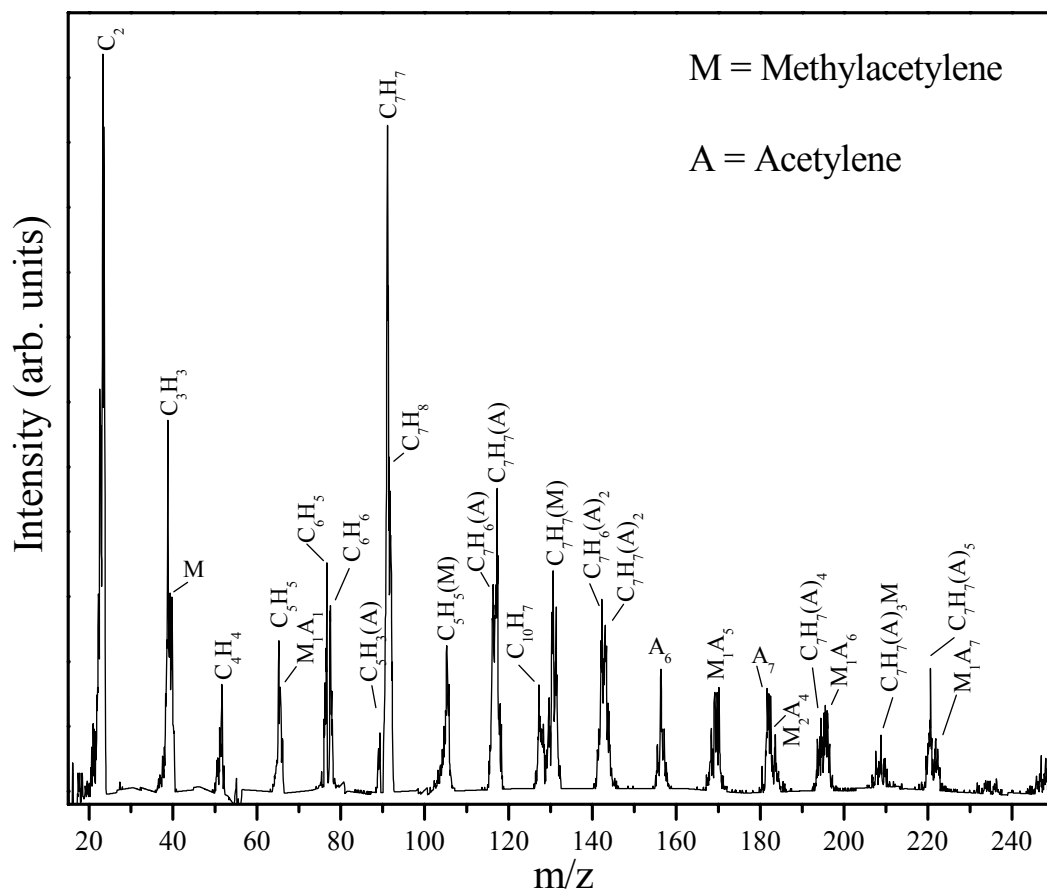


Figure 101: Electron Impact (EI) ionized mass spectrum of acetylene/methylacetylene clusters. Helium stagnation pressure was 60 PSI and electron energy was 74 eV.

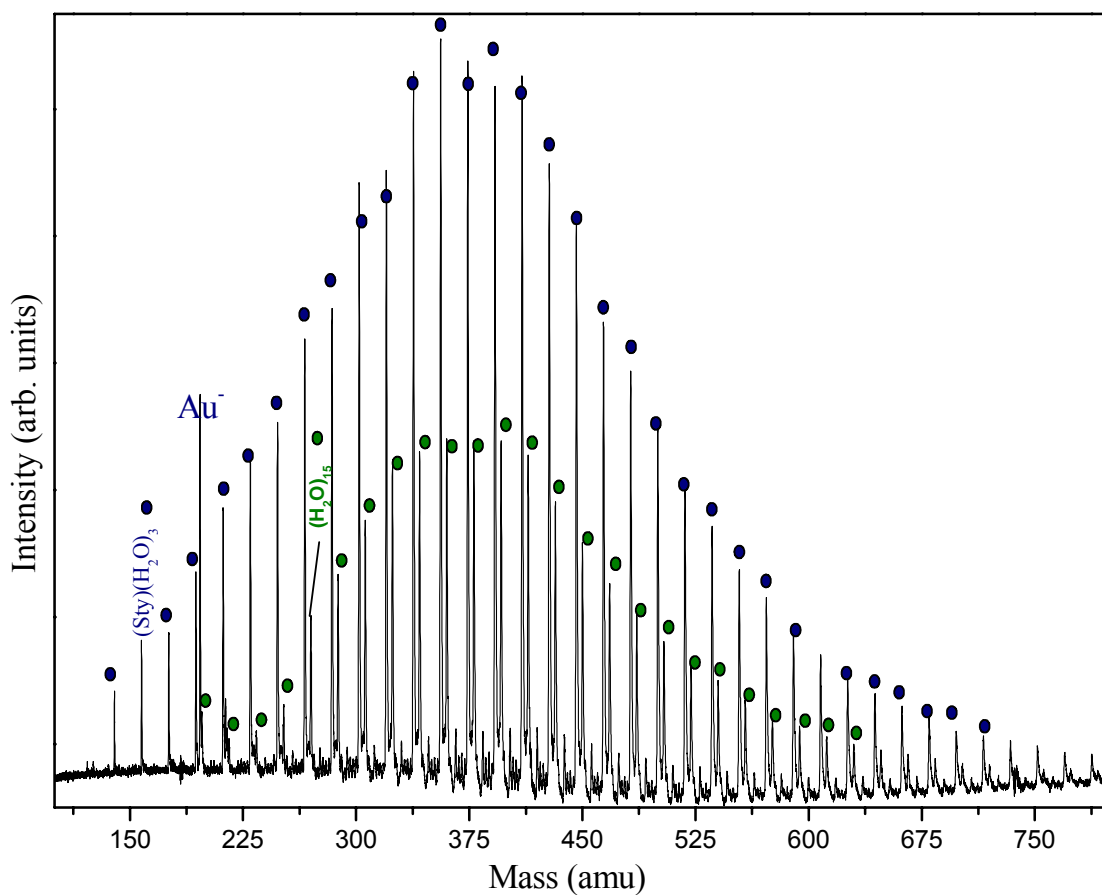


Figure 102: Time of Flight (TOF) mass spectrum of negative Au/styrene/water clusters. Here, the Nd: YAG laser was timed to fire  $500 \mu\text{s}$  after the nozzle opened ( $t_0$ ). The acceleration plates were pulsed  $920 \mu\text{s}$  after  $t_0$ . Pressure of the first chamber was  $1.1 \times 10^{-5}$  Torr. Helium stagnation pressure was 30 PSI and the styrene and water temperature was  $27^\circ \text{C}$ .

## VITA

Paul Ogheneigah Momoh was born on December 3, 1977, in Benin City, Edo State (then Bendel State), Nigeria. In February 1995, he immigrated to the United States to attend college. Paul developed an interest in chemistry and subsequently obtained a Bachelors of Science degree in this field. Some notable awards he received as an undergraduate student include, “Chemistry Student of the Year” award (2001) and winner of the Beta Kappa Chi (BKX) national undergraduate research presentation (58<sup>th</sup> annual meeting of the National Institute of Science (NIS), 2001).

Paul joined the lab of Professor M. Samy El-Shall at Virginia Commonwealth University to pursue a doctorate degree in chemistry. Shown below is a summary of his graduate work.

### **EDUCATION**

Ph.D. in Physical Chemistry, May 2007  
Virginia Commonwealth University

Bachelor of Science in Chemistry June 2002  
Fort Valley State University

## AWARDS ACCOMPLISHMENTS

Research highlight reported in *Chemical & Engineering News* (vol.84, num.37, pp.30, September 11, 2006)

“*Chemistry Student of the Year*” Award, Fort Valley State University (2002)

*1<sup>st</sup> place prize* in the National Undergraduate Research Presentation, 58<sup>th</sup> National Institute of Science (NIS) and Beta Kappa Chi National Scientific Honor Society Symposium (2001)

## RESEARCH EXPERIENCE

*Advisor:* M. S. El-Shall

*Dissertation:* “Structures and Reactivities of Ionized and Metal Cation-Containing Acetylene Clusters”

*Research Projects:* (1) Investigation of the structures and reactivities of intracuster polymerization products in acetylene clusters using the ion-mobility technique and quantum chemical calculations.

(2) Investigation of suspect reactions and structures of acetylene solvated transition metal cations using time of flight (TOF) mass spectrometry and density functional (DFT) calculations

## PUBLICATIONS

*Polymerization of Ionized Acetylene Clusters into Covalent Bonded Ions: Evidence for the Formation of Benzene Radical Cation*, **P. O. Momoh**, S. A. Abrash, M. S. El-Shall, *Journal of the American Chemical Society*, **128**, 12408 (2006)

*Stepwise Hydration of Ionized Acetylene Trimer. Further Evidence for the Formation of Benzene Radical Cation*, **P. O. Momoh**, M. S. El-Shall, *Journal of Chemical Physics*, **436**, 25 (2006)

*Development of a Multiple-Element Flame Emission Spectrometer Using CCD Detection*, C. S. Seney, K. V. Sinclair, R. M. Bright, **P. O. Momoh**, A. D. Bozeman, *Journal of Chemical Education*, **82**, 1826 (2005)

## PRESENTATIONS

“*The Missing Link: Generation of Benzene Cations from Ionized Acetylene Clusters*” American Chemical Society Regional Meeting (SERMACS), Nov. 1-4, 2006, Augusta, GA.

*“Reaction of Transition Metal (Ni, Co, and Fe) Cations with Acetylene Clusters  $[M^+(C_2H_2)_n]$ ”* Gordon Research Conference, Feb. 27-March 4, 2005, Ventura, CA.

*“Solvated Iron and Nickel Ions,  $Fe^+(H_2O)_n$ ,  $Ni^+(H_2O)_n$  using Time-of-Flight Mass Spectrometry (TOF-MS)”* American Chemical Society National Meeting, April 7, 2002, FL.